Catalytic Water Oxidation with Functionalized Ruthenium Macrocycles

Dissertation zur Erlangung des
naturwissenschaftlichen Doktorgrades
der Julius-Maximilians-Universität Würzburg

vorgelegt von
Ana Lucia Meza Chincha
aus Lima, Peru

Würzburg, 2020

Eingereicht bei der Fakultät für Chemie und Pharmazie am:
15.06.2020

Gutachter der schriftlichen Arbeit:

1. Gutachter: Prof. Dr. Frank Würthner
2. Gutachter: Prof. Dr. Christoph Lambert

Prüfer des öffentlichen Promotionskolloquiums:

1. Prüfer: Prof. Dr. Frank Würthner
2. Prüfer: Prof. Dr. Christoph Lambert
3. Prüfer: Prof. Dr. Udo Radius

Datum des öffentlichen Promotionskolloquiums:
24.07.2020

Doktorurkunde ausgehändigt am:

_____

Para Eduardo

Abbreviations

APT	atom-proton transfer
a.u.	arbitrary units
ax	axial
bda	2,2'-bipyridine-6,6'-dicarboxylic acid
Bpin	4,4,5,5-tetramethyl-1,3,2-dioxaborolan-2-yl
bpb	1,4-bis(pyridin-3-yl)benzene
bpy	2,2'-bipyridine
CAN	ceric ammonium nitrate
COSMO	conductor-like screening model
COSY	correlation spectroscopy
Cp*	1,2,3,4,5-pentamethylcyclopentadienyl
CV	cyclic voltammetry
d	doublet
DCM	dichloromethane
DCTB	*trans*-2-[3-(4-*tert*-butylphenyl)-2-methyl-2-propenylidene]malononitrile
DFT	density functional theory
DME	dimethoxyethane
DMF	*N*,*N*-dimethylformamide
dmso	dimethyl sulfoxide
DOSY	diffusion-ordered spectroscopy
dppf	1,1'-bis(diphenylphosphino)ferrocene
DPV	differential pulse voltammetry
engl.	english
EPR	electron paramagnetic resonance
eq.	equation
equiv	equivalent
ESI	electrospray ionization
EWG	electron withdrawing group
ex	excitation
EXAFS	extended X-ray absorption fine structure
Fc	ferrocene
HMBC	heteronuclear multiple bond coherence
HOMO	highest occupied molecular orbital
HR	high resolution

HSQC	heteronuclear single quantum coherence
I2M	interaction of two metal-oxyl radicals
ITO	indium tin oxide
LHE	light-harvesting efficiency
LUMO	lowest unoccupied molecular orbital
m	multiplet
MALDI	matrix-assisted laser desorption ionization
MLCT	metal-to-ligand charge-transfer
MOF	metal-organic framework
MS	mass spectrometry
NHC	N-heterocyclic carbene
NHE	normal hydrogen electrode
NMR	nuclear magnetic resonance
NOESY	nuclear Overhauser effect spectroscopy
norm	normalized
OD	optical density
OEC	oxygen evolving complex
OEG	oligoethylene glycol
ORTEP	Oak Ridge thermal-ellipsoid plot
pda	1,10-phenanthroline-2,9-dicarboxylic acid
phth	phthalazine
pic	4-picoline
ppm	parts per million
PS	photosensitizer
PTFE	polytetrafluoroethylene
PXRD	powder X-ray diffraction
py	pyridine
ref.	reference
rt	room temperature
s	singlet
t	triplet
tda	2,2′:6′,2″-terpyridine-6,6″-dicarboxylic acid
TFE	2,2,2-trifluoroethanol
THF	tetrahydrofuran
TLC	thin layer chromatography
toe	tonne of oil equivalent
TOF	turnover frequency

TON	turnover number
UV	ultraviolet
Vis	visible
vs.	versus
WNA	water nucleophilic attack
WOC	water oxidation catalyst
XANES	X-ray absorption near edge structure
XAS	X-ray absorption spectroscopy

Variables and Constants

c	concentration
δ	chemical shift
d	distance
E	potential
g	EPR *g*-factor
I	current
$\mathcal{I}$	intensity
J	NMR coupling constant
k_{ET}	rate constant of electron transfer
k_q	rate constant of emission quenching
λ	wavelength
n	amount of substance
Φ	torsion angle
p	pressure
R	ideal gas constant (8.314 J K^{-1} mol^{-1})
θ	rotation angle
τ	lifetime
T	temperature
V	volume

Table of Contents

Chapter 1 – Aim of the Thesis

"[…] *how to fix solar energy through suitable photochemical reactions. To do this it would be sufficient to be able to imitate the assimilating process of plants.* […] *And if in a distant future the supply of coal becomes exhausted, […] life and civilization will continue as long as the sun shines!"* – G. Ciamician, 1912.[1]

Italian chemist Giacomo Ciamician was ahead of his time when he envisioned the possibility of mimicking the process of natural photosynthesis to enable a transition to a carbon-neutral economy.[1] This concept is now known as "artificial photosynthesis" and is based on the idea of exploiting sunlight, in a similar way as plants, to oxidize water and use the obtained reducing equivalents for the production of hydrogen or other solar fuels which can be stockpiled and transported.[2] Due to the continuous increase in energy demand, that is still mainly met by the combustion of fossil fuels (Figure 1a),[3] renewable energy approaches like artificial photosynthesis are gaining much attention due to their potential to reduce carbon emissions and thus prevent climate change.[4] In the last years, much efforts have been devoted to the development of wind and solar energy which are now able to produce more than 136 million tonnes of oil equivalent (toe) per year (Figure 1b).[5] However, considering the current global energy consumption of about 14 billion toe per year,[6] that is even forecast to double by 2050,[7] further development of renewable energy sources is still very much needed.

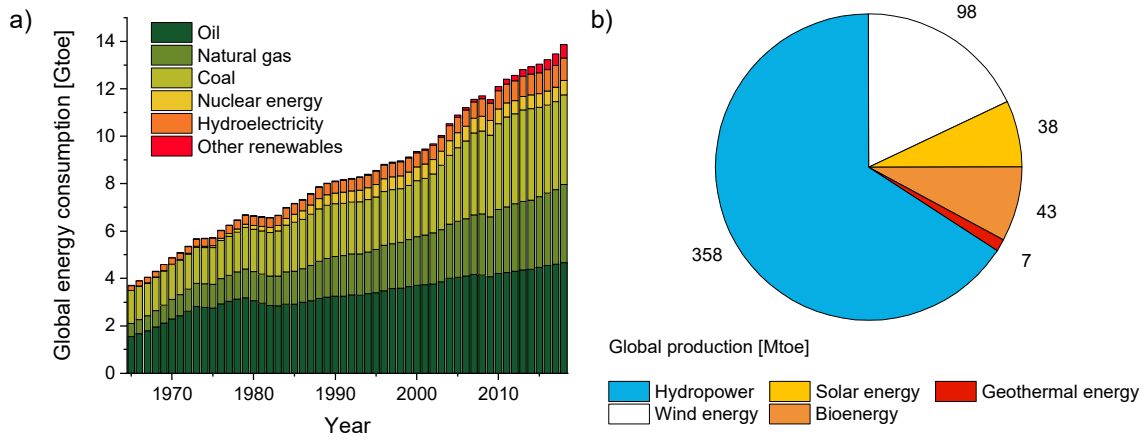

Figure 1. a) Global energy consumption between 1965 and 2018. Data from BP Statistical Review of World Energy 2019.[3] b) Global production of renewable energy in 2017. Data from IRENA, Renewable Energy Statistics 2019.[5]

Over the last decades, significant knowledge has been accumulated on the individual components that would be required for the production of solar fuel devices.[2b, 8] Nevertheless, artificial photosynthesis remains at the level of basic research mainly due to the lack of efficient water oxidation catalysts (WOCs). Water oxidation is a very complex process as it involves not only the transfer of four electrons and four protons but also the presence of several catalytic intermediates.[9] In the last years, promising results have been obtained using oxides and hydroxides of various transition metals as heterogeneous catalysts.[10] However, to achieve a thorough understanding of operating mechanisms and underlying principles determining the efficiency of water oxidation further fundamental research with molecular catalysts is required that might culminate in better suited catalytic systems.[11]

Since the discovery of the "blue dimer" by Meyer and co-workers almost four decades ago,[12] tremendous progress has been achieved in the field of homogeneous water oxidation. This has resulted in the development of a plethora of new catalysts based on Ru, Ir and first row transition metals like Mn, Fe, Co, Ni and Cu.[13] Among ruthenium catalysts, Ru(bda) WOCs (bda: 2,2'-**b**ipyridine-6,6'-**d**icarboxylic **a**cid) have attracted particular attention as some of these catalysts exhibit impressive catalytic activities in chemical water oxidation that are comparable to those of the oxygen-evolving complex of photosystem II.[14] However, chemical water oxidation is studied in most cases using one-electron oxidant ceric ammonium nitrate (CAN) which is only stable at low pH values. This restricts the analysis of the catalytic activities of WOCs to pH 1.[15] In contrast, photocatalytic water oxidation is generally performed under neutral conditions that would be more suitable for the development of solar fuel devices.[16] Given that most homogeneous WOCs, including Ru(bda) catalysts exhibit only poor catalytic activities under photocatalytic conditions,[17] there is a need for new catalytic systems enabling efficient water oxidation under solar light exposure.

Würthner and co-workers reported 2016 supramolecular ruthenium macrocycle **MC3** bearing three catalytically active Ru(bda) units in a cyclic arrangement (Figure 2).[18] This trinuclear WOC showed a remarkably high catalytic efficiency in chemical water oxidation which, based on theoretical simulations, was ascribed to the presence of a hydrogen-bonded network of preorganized water molecules in the macrocyclic cavity.[19] However, no experimental evidence for the proposed water network could be provided. Furthermore, kinetic studies and ^{18}O labelling experiments confirmed a monomolecular mechanism of water oxidation for macrocycle **MC3**.[18] Accordingly, O-O bond formation takes place upon nucleophilic attack of water on highly reactive Ru^{V}-oxo intermediates. Moreover, the rate-determining step of catalytic water oxidation with WOC **MC3** was found to be the oxidation of Ru^{IV} to Ru^{V}.

The aim of this thesis was the study of catalytic water oxidation with functionalized Ru(bda) macrocycles (Figure 2). Hereby, the introduction of electron donating substituents either in the bridging or equatorial bda ligand was designed to increase the electron density at the Ru centers and, as a result, decrease the $Ru^{V/IV}$ oxidation potential and accelerate the rate of oxygen formation compared to parent macrocycle **MC3**. In addition, the role of steric effects on the catalytic activities of regioisomeric *meta* (*m*) and *para* (*p*)-substituted Ru(bda) WOCs should be investigated. Furthermore, in-depth studies on photocatalytic water oxidation with **MC3** and water soluble derivative ***m*-CH_2NMe_2-MC3** should be conducted to elucidate factors that influence the efficiency of photocatalysis with this class of supramolecular catalysts. Although the catalytic activity of ***m*-CH_2NMe_2-MC3** in chemical water oxidation has been reported previously,[20] its catalytic properties under light-driven conditions remained unexplored.

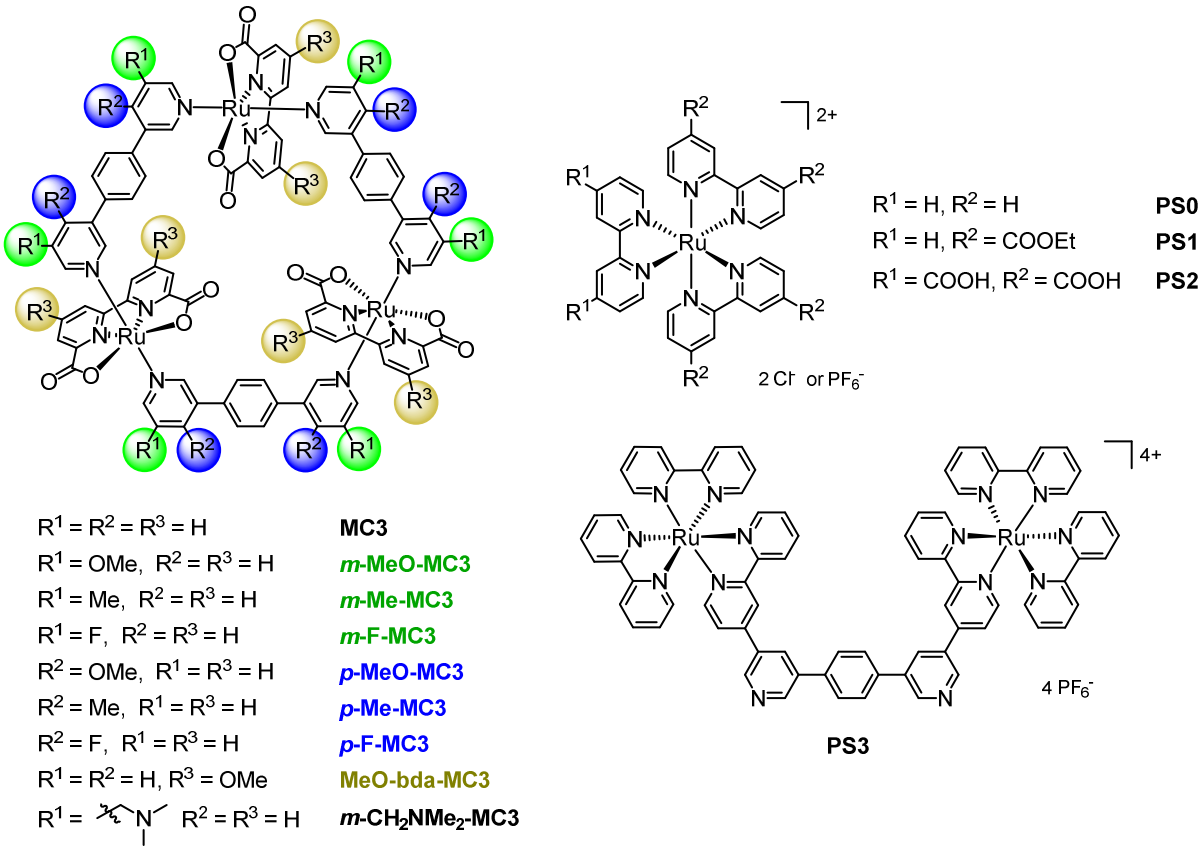

Figure 2. Chemical structures of **MC3** macrocycles functionalized at equatorial or axial ligands and ruthenium tris(bipyridine) photosensitizers **PS0–3** studied within this thesis.

Chapter 2 provides a brief overview on the process of natural photosynthesis focusing on the oxygen-evolving complex of photosystem II as a prime example of a water oxidation catalyst that is product of billions of years of evolution. After an introduction into artificial photosynthesis, the development of homogeneous WOCs is discussed in detail. Hereby, emphasis

is given on the Ru(bda) catalyst family which inspired the design of supramolecular macrocycles by Würthner and co-workers.[18-21] The last part of this chapter deals with current knowledge on photocatalytic water oxidation with Ru(bda) WOCs.

In *Chapter 3*, a series of trinuclear Ru(bda) macrocycles bearing different substituents at axial and equatorial ligands is presented which enabled the study of substitutent effects on molecular properties and catalytic activities in chemical and photocatalytic water oxidation. Detailed studies by X-ray crystal structure analysis and theoretical simulations were performed to explain the observed variations in catalytic activities.

Chapter 4 is focused on light-driven water oxidation with trinuclear Ru(bda) macrocycles **MC3** and ***m*-CH_2NMe_2-MC3** using a series of ruthenium tris(bipyridine) photosensitizers **PS0–3** (Figure 2) and sodium persulfate as sacrificial electron acceptor. Hereby, new insights into the effects of photosensitizers and reaction media on the efficiency of photocatalysis were obtained by steady-state emission quenching and nanosecond flash photolysis.

Chapters 5 and 6 summarize the results of this thesis in English and German.

Chapter 7 describes the used materials and methods and provides additional information on synthetic procedures and characterization of new compounds.

Chapter 2 – Literature Survey

2.1 Natural Photosynthesis

Cyanobacteria, algae and green plants convert light energy into chemical energy in a complex process known as photosynthesis. Hereby, the solar energy is used to oxidize water to molecular oxygen and reduce carbon dioxide to glucose or other carbohydrates according to the general equation:[22]

$$6\,H_2O + 6\,CO_2 \xrightarrow{h\nu} C_6H_{12}O_6 + 6\,O_2$$

In green plants, photosynthesis takes place in cell organelles known as chloroplasts. These are equipped with a special enzymatic machinery tailored to perform a series of light-induced and dark reactions as graphically illustrated in Figure 3. During the light reactions, electrons obtained from the oxidation of water are used to produce NADPH (reduced **n**icotinamide **a**denine **d**inucleotide **p**hosphate) as a reducing agent and also generate a proton gradient needed to trigger the production of energy carrier ATP (**a**denosine **t**ri**p**hosphate).[22, 23] Both components are required to reduce carbon dioxide in a light-independent multi-step process known as Calvin cycle.[24]

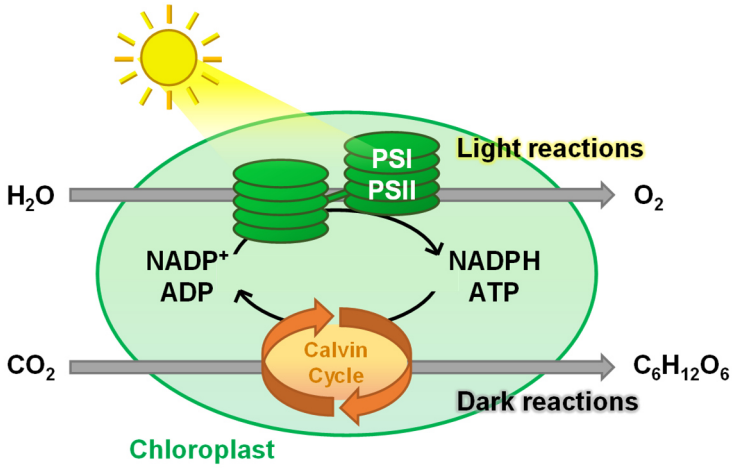

Figure 3. Graphical illustration of photosynthetic processes with light and dark reactions for the conversion of water and carbon dioxide to molecular oxygen and carbohydrates, respectively.

2.1.1 Light-Dependent Reactions

Over billion years nature has developed a highly efficient electron-transfer system for the photosynthetic production of NADPH and ATP which is based on light capture and charge separation in large protein complexes known as photosystems I and II.[25] In these photosystems, light is collected by so-called light-harvesting complexes (LHCs) bearing specific arrays of proteins and pigments such as chlorophyll *a* and *b* as well as carotenoids.[26] The captured light energy is funneled to reaction centers which contain a special pair of chromophores for charge separation.[27] As shown in Figure 4 for the light reactions taking place in green plants,[28] upon excitation of a chlorophyll *a* dimer in photosystem II, which is also known as pigment P680 due to its absorption maximum at 680 nm, electrons are rapidly transferred over a series of cofactors and coenzymes leading to efficient charge separation. Radical cation $[P680]^{\cdot+}$ is reduced by a nearby tyrosine (Y_z) which acts as a redox shuttle. Y_z is then recovered by electron transfer from the oxygen-evolving complex (OEC). Similarly, the holes generated upon excitation of reaction center P700 in photosystem I are filled with electrons transferred from copper-based protein plastocyanin. After transfer of electrons over Fe-S proteins and ferredoxin to enzyme $NADP^+$ reductase, reducing cofactor NADPH is produced. As mentioned before, a transmembrane proton gradient is built during electron transfer between photosystems II and I which is used by enzyme ATP synthase to produce ATP from ADP (**a**denosine **di**phosphate). Importantly, during light-dependent reactions holes are accumulated in the OEC which is recovered upon four-electron oxidation of water to molecular oxygen.[29]

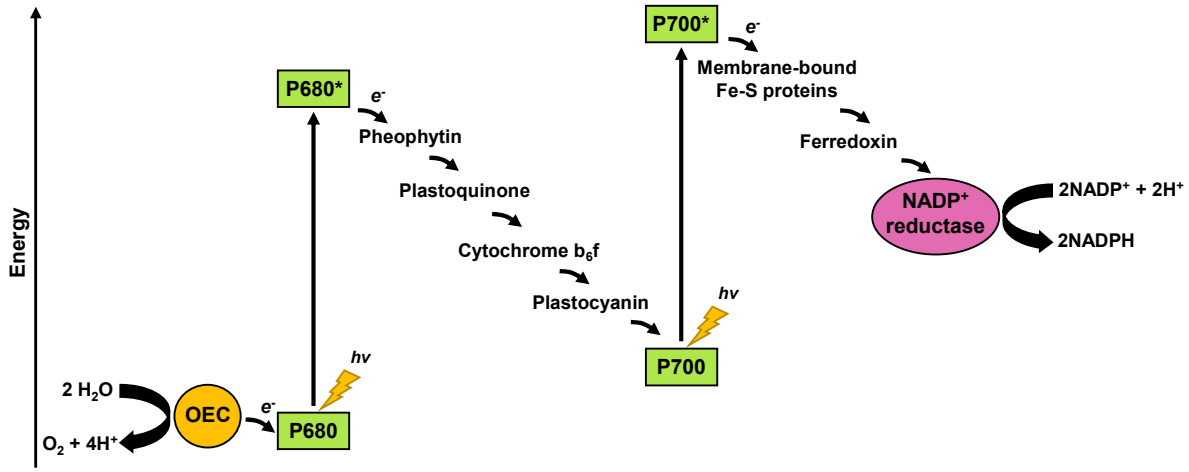

Figure 4. Schematic representation of light reactions of photosynthesis in green plants involving electron transfer from the OEC over several components to $NADP^+$ reductase.

2.1.2 Oxygen Evolving Complex

A tetramanganese calcium cluster is found in the core of the OEC in photosystem II. This Mn_4CaO_5 cluster exhibits a distorted cubane structure with three manganese, one calcium and four oxygen atoms in its corners and a fourth “dangler” manganese atom which is covalently linked to the heterocubane by a di-μ-oxo bridge (Figure 5a).[30] Manganese as an abundant element with rich redox chemistry is strongly complexed in its Mn^{III} and Mn^{IV} oxidation states by O^{2-} ions forming robust metal-oxo bonds.[31] This might explain why nature chose this element for stabilization of the water oxidizing complex. The role of the redox inert Ca^{2+} ion has not yet been fully elucidated. On the one hand, it has been proposed that this metal might function as a Lewis acid for activation of substrate water molecules.[32] On the other hand, it might play a role in proton-coupled electron transfer (PCET) between the Mn_4CaO_5 cluster and tyrosine Y_z.[33] Interestingly, upon replacing Ca^{2+} with Sr^{2+} a reduction of the catalytic activity of the resulting metal cluster was observed.[28] Shen and co-workers have ascribed this effect to an elongated distance between Sr and a coordinated water molecule W3 in comparison to the Ca^{2+} containing cluster.[34] In nature, two water molecules each are bound to the calcium (W3 and W4) and dangler manganese (W1 and W2) atoms of the cluster (Figure 5a). In addition, as shown in Figure 5b, the Mn_4CaO_5 cluster is embedded in a complex protein matrix with six carboxylate groups and one imidazole ring of neighboring amino acid residues acting as direct ligands.[30] Several studies have been performed on artificial Mn_3CaO_4 cubane systems as catalysts for water oxidation.[35] For example, Zhang *et al.* reported a Mn_4CaO_5 cluster which was coordinated to carboxylic acid groups of pivalic acid and a pyridine ligand.[36] Importantly, although this artificial system closely resembles the structure of the multimetallic OEC core, it was unable to perform water oxidation presumably due to the lack of the protein matrix providing the metal cluster with preorganized water molecules. This underlines the importance of the organic ligand environment for the catalytic activity of the Mn_4CaO_5 cluster in nature. Furthermore, the OEC is connected to bulk water around photosystem II by several channels formed by amino acid residues specifically arranged to preorganize water molecules in long-range hydrogen-bonded networks (Figure 5c).[37] These channels most likely play a role not only for fast diffusion of substrate water to the Mn_4CaO_5 cluster, which takes place at an estimated transport rate of around 5000 water molecules per second,[38] but also for proton transport, oxygen evacuation and even regeneration of the OEC upon oxidative damage caused by reactive oxygen species (ROS).[39] These ROS, which are generated as a by-product during water oxidation, limit the lifetime of the OEC to about 30 min under normal light irradiation conditions.[29]

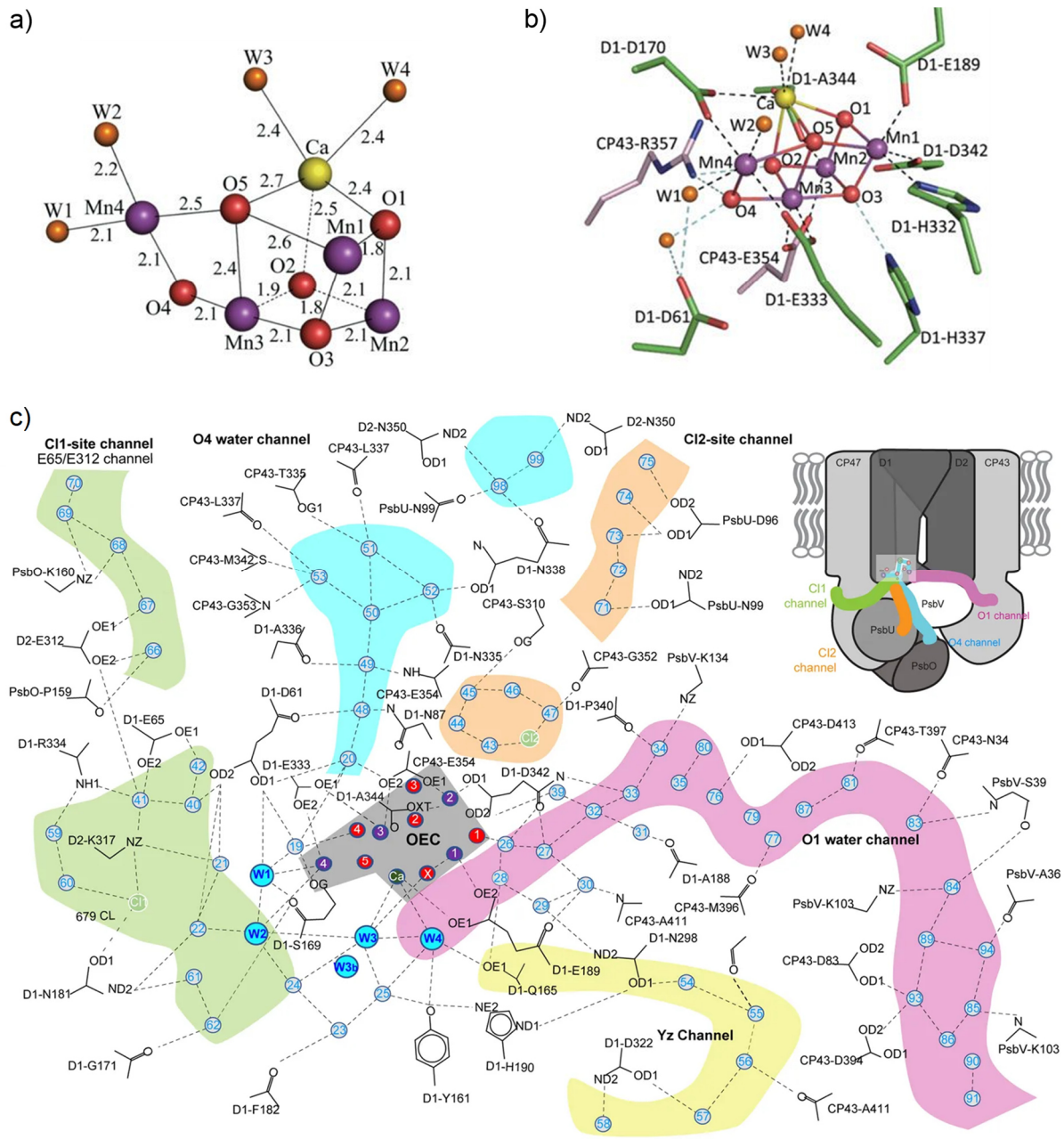

Figure 5. a) X-ray crystal structure of Mn_4CaO_5 cluster at a resolution of 1.9 Å showing distances in Å between different atoms.[30] b) Amino acid environment around OEC.[30] c) Schematic representation of water molecules preorganized in channels, which connect the OEC with bulk water around photosystem II.[37b] Mn and O atoms as well as water molecules are depicted as numbered purple, red and blue circles, respectively. Figures 5a) and 5b) are reproduced with permission from ref. [30]. Copyright 2011 Nature Publishing Group. Figure 5c) is reproduced with permission from ref. [37b]. Copyright 2018 Nature Publishing Group.

The OEC produces oxygen at a turnover frequency (TOF) of around 500 s^{-1} and reaches high turnover numbers (TON) of more than 10^5.[40] The process of water oxidation with accumulation of four holes at the Mn_4CaO_5 cluster prior to actual oxidation of water to molecular oxygen was first proposed by Kok and co-workers.[41] These authors suggested a stepwise oxidation of the multimetallic core in a five state cycle also known as S_n-state cycle (Figure 6). Hereby, n = 0 – 4 denotes the number of stored oxidizing equivalents. Accordingly, S_0 and S_4 represent the most reduced and most oxidized intermediates of the Mn_4CaO_5 cluster, respectively. The S_n-state cycle is driven by the absorption of four photons, which trigger the transfer of electrons from the metal cluster to oxidized tyrosine radical $Y_Z^{\cdot}$ formed upon reduction of $[P680]^{\cdot+}$ (see above). Three PCET processes prevent the accumulation of positive charges during water oxidation.[29] Interestingly, while the redox valences of the S_0 – S_3 states ($Mn^{III}_3Mn^{IV}$ to Mn^{IV}_4, respectively) have been unambiguously determined by X-ray diffraction,[30, 42] X-ray free electron laser (XFEL),[37b, 43] extended X-ray absorption fine structure (EXAFS)[44] and electron paramagnetic resonance (EPR)[29] techniques in combination with theoretical calculations,[45] the redox valences of the transient S_4 intermediate are still unknown.

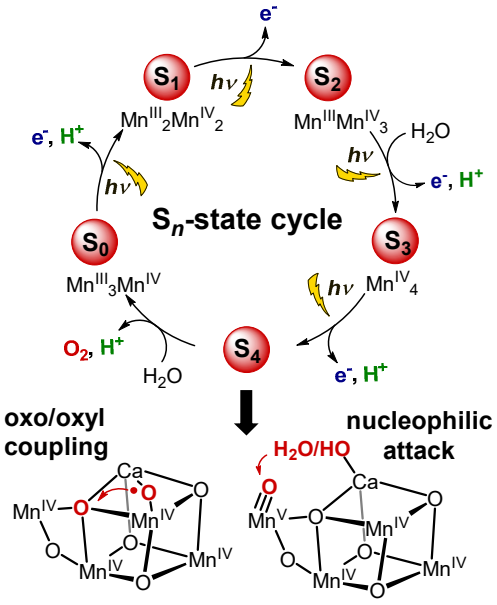

Figure 6. Illustration of the catalytic S_n-cycle of oxygen evolution by Mn_4CaO_5 cluster with two proposed structures of highly reactive S_4 state. Adapted with permission from ref. [21]. Copyright 2017 Wiley-VCH.

Molecular oxygen is evolved directly after formation of the short-lived S_4 state. The lack of experimental data owing to the elusive nature of this intermediate has prevented the conclusive study of the precise mechanism of O-O bond formation. Based on indirect evidence as well as theoretical simulations, two pathways of oxygen formation have been mainly

discussed in literature. In the so-called water nucleophilic attack (WNA) mechanism proposed amongst others by the groups of Barber,[46] Brudvig[47] and Pecoraro,[48] a Mn^{V}-oxo species (which might have a substantial Mn^{IV}-oxyl character) is attacked by a nucleophilic water molecule or hydroxyl group attached to the Ca^{2+} ion of the Mn_4CaO_5 cluster. In contrast, Siegbahn proposed oxygen formation by an intramolecular radical coupling of two Mn^{IV}-oxyl units as depicted in Figure 6.[49] Very recently, Sun and co-workers proposed a different mechanism involving O-O bond formation within a Mn^{VII}-dioxo intermediate formed at the position of the dangler Mn by disproportionation of the four Mn^{IV} centers in the S_3 state.[50] Thus, further investigations will be required for conclusive elucidatation of the mechanism of O-O bond formation by the OEC. Undoubtedly, understanding of this mechanism will be essential for the development of efficient artificial photosynthesis systems for water oxidation to produce solar fuels.

2.2 Artificial Photosynthesis

Over the last decades, several approaches have been considered to replace fossil fuels with environmentally benign, carbon-neutral and sustainable energy sources. In this context, artificial photosynthesis as a biomimetic concept aims to convert solar energy into chemical energy storing the latter in the bonds of so-called “solar fuels” such as molecular hydrogen, methanol or other compounds generated by reduction of CO_2 (Figure 7).[8, 51] As in natural photosynthesis, the oxidation of water should provide the required reducing equivalents in artificial photosynthesis.

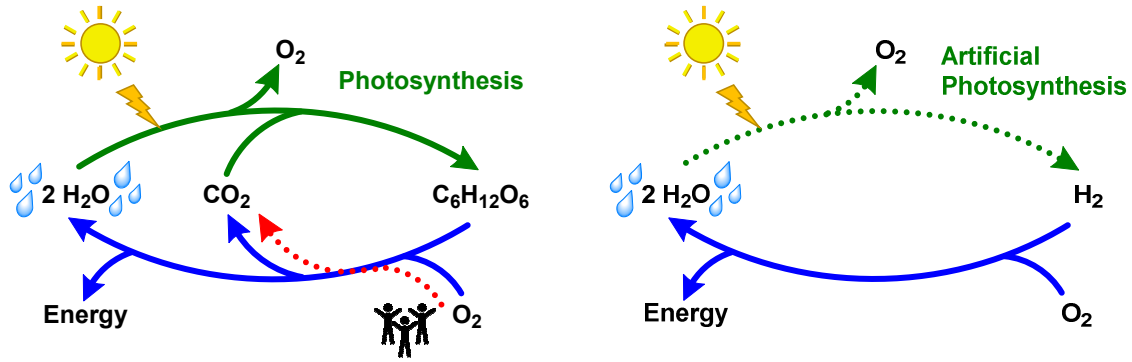

Figure 7. Schematic illustration of natural and artificial carbon-free photosynthesis for comparison, the latter process leads to generation of molecular hydrogen as an example of “solar fuel”.

Figure 8 shows the assembly of components needed for fabrication of functional solar fuel devices.[27, 52] These are: (i) a light-harvesting antenna which should capture sunlight over a

wide range of wavelengths and subsequently funnel the absorbed energy to a photosensitizer, (ii) a photosensitizer for charge separation (electron-hole pair generation), (iii) an O_2 evolving catalyst able to gain electrons from the oxidation of water and (iv) a H_2 evolving (or CO_2 reducing) catalyst to store the obtained energy in form of molecular hydrogen (or other compounds produced by reduction of CO_2). Despite considerable knowledge on each of these components has been accumulated over the past years leading to a tremendous development and optimization of the properties of individual components, the construction of fully functioning solar fuel devices is still very challenging. Two main strategies for the realization of such devices comprise the integration of components in photoanodes and photocathodes of photoelectrochemical (PEC) cells or the use of photovoltaic-coupled electrolyzers (PVE) which rely on solar cells instead of photosensitizers to generate the potentials needed to drive water splitting.[8, 53] Recent reviews summarize the significant developments achieved over the last years in this field,[8, 54] which is beyond the scope of this literature survey. Nevertheless, it should be mentioned that back electron transfer as well as difficult tuning of the properties of all components in a single device constitute considerable challenges preventing realization of efficient solar fuel devices.[8, 51, 53] Moreover, compared to cathodic proton reduction, water oxidation at the anode with sluggish kinetics and a high energy demand represents an additional bottleneck hindering a broad application of water splitting technologies.[9]

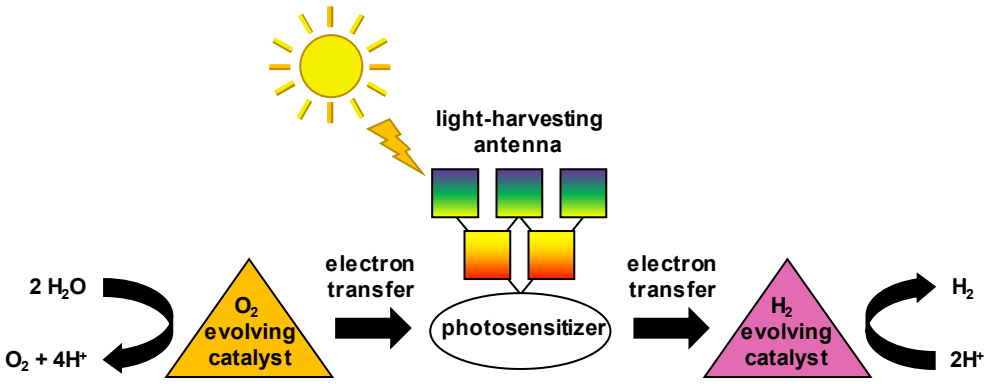

Figure 8. Illustration of assembly of main components required for artificial photosynthesis.

2.2.1 Water Oxidation Catalysis

The development of catalysts for water oxidation has been a subject of intense research due to the complexity of this energetically demanding oxidation reaction involving the transfer of four electrons and four protons (as shown in the following equation) as well as the presence of several highly oxidized catalytic intermediates.[13a, 16]

$$2\,H_2O \longrightarrow O_2 + 4\,H^+ + 4\,e^-$$

Thus, there is a need for efficient water oxidation catalysts (WOCs) able to perform this reaction at low overpotentials.[13d, 55] Transition metal oxides, oxo/hydroxides, phosphides, nitrides and chalcogenides as well as binary, ternary and metal/carbon hybrid materials have been investigated as heterogeneous catalysts for the oxygen evolution reaction (OER) over the entire pH range.[9, 56] These heterogeneous materials offer technical advantages over homogeneous catalysts due to their more straightforward large-scale preparation and higher stability under water oxidation conditions. However, the study of their operating mechanisms of water oxidation, which is vital for the improvement of their catalytic properties, is rather difficult.[11b, 57] In this regard, homogeneous molecular WOCs are ideal to accomplish such profound understanding of mechanistic aspects as these catalysts and their intermediates can be readily characterized by several spectroscopic, analytical and electrochemical methods. Moreover, the use of theoretical simulations as a further very powerful tool to study water oxidation is mainly limited to such small molecular systems.

Numerous homogeneous WOCs including molecular complexes based on Ru, Ir and first-row transition metals[13a, 13b, 58] as well as polyoxometalates[59] have been developed over the last decades. Selected examples of highly efficient molecular catalysts or catalyst precursors containing transition metals other than Ru are shown in Figure 9 (Ru WOCs will be discussed separately). Ir^{III} complex **1** is a confirmed catalyst precursor, which upon oxidation and *in situ* cleavage of the Cp* ligand (Cp*: 1,2,3,4,5-pentamethyl**c**yclo**p**entadienyl) generates a oxo-bridged Ir^{IV} dinuclear species known as “blue solution”.[60] This solution was able to evolve molecular oxygen with a TOF of 1.8 s^{-1} in chemical water oxidation using sodium periodate as an oxidant. The structure of the actual dinuclear catalyst was elucidated by a combination of EPR, resonance Raman, UV-vis absorption and ^{17}O nuclear magnetic resonance (NMR) spectroscopy along with EXAFS and theoretical simulations. For this WOC, a water oxidation mechanism involving nucleophilic attack of water to a bis(Ir^{V}-$O^{\cdot}$) intermediate was proposed. For pentanuclear iron complex **2** bearing six 3,5-**b**is(2-**p**yridyl)-**p**yrazole (Hbpp) and a μ_3-oxo ligand, a very high TOF of 1900 s^{-1} and a TON of 10^6 – 10^7 were measured in electrochemical water oxidation.[61] However, water oxidation experiments were performed in MeCN/H_2O 10:1 due to instability of the WOC in mixtures containing higher amounts of water. Interestingly, for this catalyst a similar water oxidation mechanism to that of the oxygen-evolving complex (OEC) in natural photosynthesis was proposed. Accordingly, upon four one-electron oxidations with subsequent coordination of two water molecules and deprotonation the O-O bond is presumably formed by intramolecular coupling of two Fe^{IV}=O centers. The highly electron-deficient cationic Co^{III} porphyrin **3** was studied in electrochemical water oxidation in phosphate buffer saline (PBS) at pH 7.[62] Under these conditions, this WOC exhibited a high TOF of 1400 s^{-1} at a low overpotential of 380 mV. The proposed mechanism of O-O bond

formation involved nucleophilic attack of water on a Co^{IV}=O intermediate bearing an oxidized porphyrin radical. Ni-PY5 (PY5: 2,6-bis(1,1-bis(2-pyridyl)ethyl)pyridine)) complex **4** was found to oxidize water under electrochemical conditions with a maximal TOF of 2000 s^{-1} at pH 10.8.[13c] Notably, the catalytic properties of this WOC are significantly dependent on the concentration of the used phosphate buffer. Thus, the maximal TOF was observed at a buffer concentration of 1.0 M, while a more moderate value of 145 s^{-1} was obtained in a 0.2 M solution. To explain this dependency on buffer concentration, an atom-proton transfer (APT)[63] assisted WNA mechanism was proposed. Hereby, the rate-determining step of O-O bond formation by the attack of water on a Ni^{V}=O intermediate is facilitated by using phosphate as a proton acceptor. The pyrene-functionalized Cu complex **5** was studied in electrochemical water oxidation both as a homogeneous WOC and upon heterogenization with graphene onto glassy carbon electrodes.[64] Interestingly, a higher TOF of 540 s^{-1} was measured for the heterogenized catalyst compared to a TOF of 128 s^{-1} obtained in solution. The higher catalytic activity under heterogeneous condition was ascribed to a fast oxidation of the WOC on the electrode surface facilitated by anchoring of the catalyst through pyrene functionality.

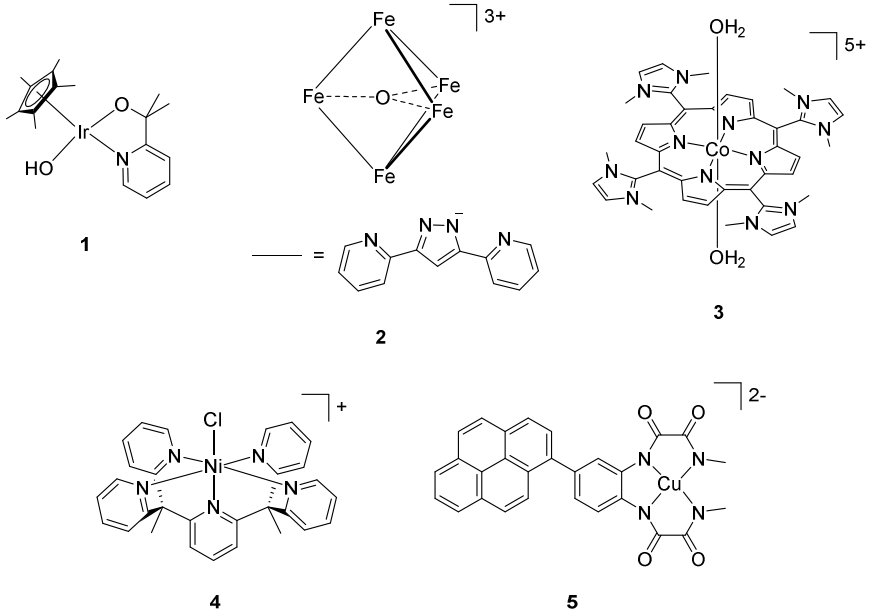

Figure 9. Selected examples of highly reactive homogeneous catalysts and catalyst precursors for water oxidation.

2.2.2 Ruthenium-Based Water Oxidation Catalysts

The development of Ru complexes as catalysts for water oxidation started almost four decades ago with the discovery of dinuclear μ-oxo-bridged Ru complex **6** by Meyer and co-workers (Figure 10).[12] The catalytic activity of this complex, also known as “blue dimer” due to its characteristic blue color, was studied in chemical water oxidation using ceric ammonium

nitrate (CAN) as an oxidant. Although low TOF and TON values of 0.004 s^{-1} and 13.2, respectively, were obtained,[65] this pioneering work showed for the first time that the rich redox chemistry of Ru with possible oxidation states ranging from -2 to +8[66] could be used to generate artificial systems for water oxidation emulating the properties of the OEC. Oxygen formation with the "blue dimer" has been proposed to occur upon three or four one-electron oxidations of the catalyst *via* WNA on a $Ru^{V}ORu^{IV}$ or $Ru^{V}ORu^{V}$ species, respectively.[67] Oxidatively stable ligands are particularly important for the design of successful WOCs. Therefore, most of the Ru WOCs were prepared using oxidatively robust aromatic N-heterocycles such as pyridine as ligand (Figure 10).[16, 68]

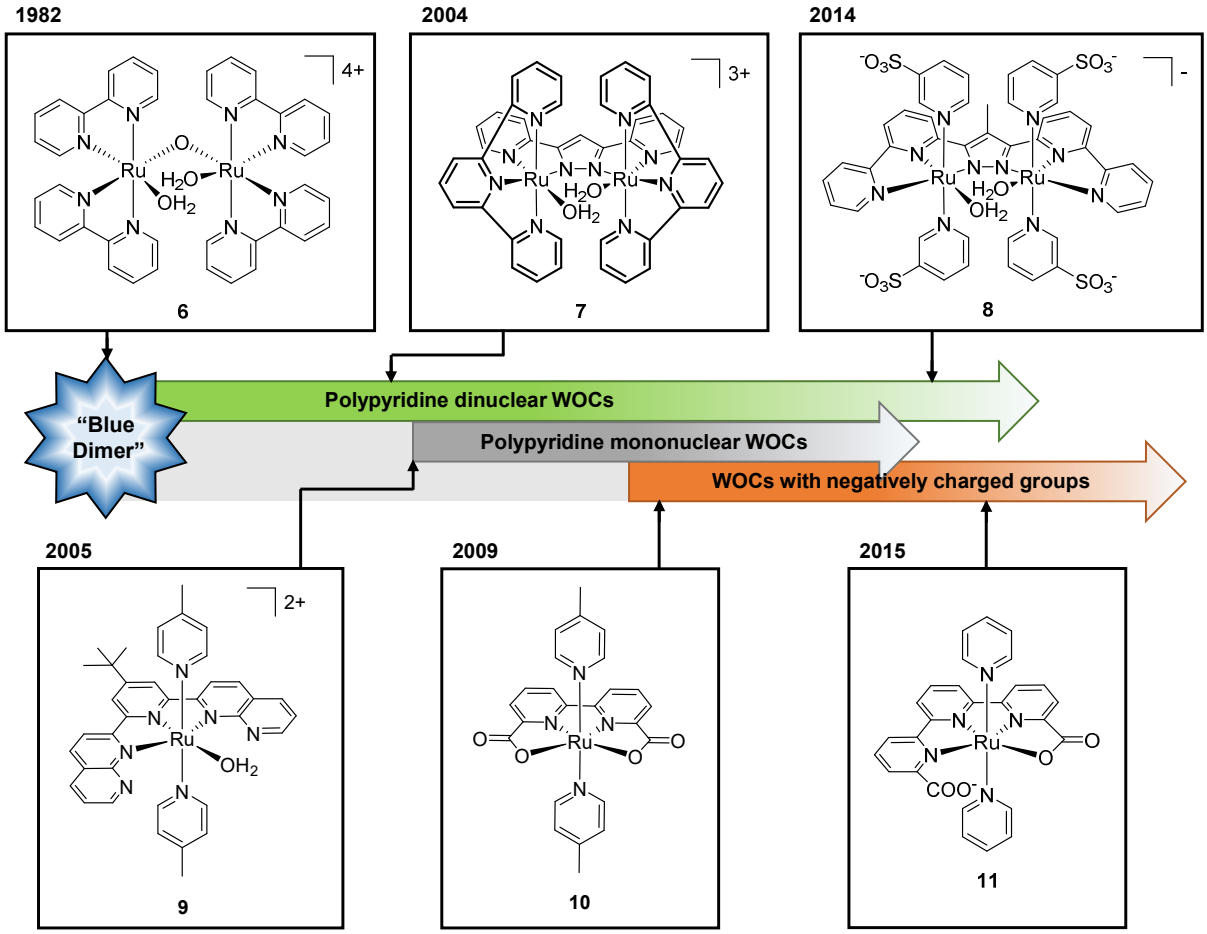

Figure 10. Development of homogeneous Ru WOCs since the discovery of the "blue dimer" in 1982.

Dinuclear complex **7** was the first Ru WOC bringing two Ru centers in close proximity without a μ-oxo bridge, which was allegedly responsible for the low stability of preceding catalysts.[69] The catalytic activity of **7** was investigated in chemical water oxidation using CAN as oxidant leading to a TOF of 0.014 s^{-1} and a TON of 18.6. Kinetic studies combined with ^{18}O labeling experiments and theorical calculations led to the conclusion that the design of this WOC facilitated O-O bond formation by an intramolecular coupling of two Ru=O units in a

mechanism later named I2M (**i**nteraction of **two m**etal-oxyl radicals).[70] Related complex **8** bearing a methylated pyrazole ring showed an improved TOF of 0.068 s^{-1} and a significantly increased TON of 211 compared to complex **7** in chemical water oxidation using oxidant CAN.[71] WOC **8**, however, performed water oxidation by a WNA mechanism. Thus, the authors concluded that the subtle changes in the position of the Ru=O units resulting from the modification of the equatorial ligand induced the observed switch of water oxidation mechanism. The catalytic activity of WOC **8** was also studied in light-driven water oxidation using a ruthenium tris(bipyridine) derivative as photosensitizer and sodium persulfate as electron acceptor. In this experiment, **8** exhibited a higher TOF of 11 s^{-1} and a TON of 5300 which were ascribed to the increased stability of the dinuclear complex in phosphate buffer at pH 7 compared to the pH 1 aqueous solution needed for chemical water oxidation using oxidant CAN (see Chapter 2.4).[72]

A major breakthrough in the field of homogeneous water oxidation was achieved in 2005 with the first irrefutably confirmed mononuclear WOC **9** by the group of Thummel.[73] Previously, it was a generally accepted notion that, similarly to the OEC, artificial catalysts required more than one metal center to be able to perform water oxidation. This significantly restricted the design of new WOCs, which were to that time exclusively based on Mn or Ru. Single-site Ru catalyst **9** reached TOF and TON values of 0.014 s^{-1} and 260, respectively, in chemical water oxidation using CAN as an oxidant.[74] A WNA mechanism involving water attack on a Ru^{V}=O or Ru^{IV}=O intermediate formed upon a series of consecutive PCETs was proposed for this catalyst.[75] Hereby, the non-coordinating N-atoms of the 1,8-naphthyridyl moieties were initially suggested to stabilize the complex by engaging in hydrogen bonding with the aqua ligand. Later, formation of N-O bonds by oxygen transfer to these uncoordinated N-atoms was detected.[76] However, the role of these N-O groups for the catalytic activity of the WOC has not yet been elucidated.

The introduction of negatively charged groups such as carboxylic acids into the ligand framework of Ru complexes was shown to reduce the oxidation potentials of Ru in seminar work by Åkermark and co-workers.[77] This effect was also observed for a dinuclear Ru WOC bearing a bis(pyridyl)pyridazine ligand.[78] This inspired the design of a new 2,2'-**b**ipyridine-6,6'-**d**icarboxylic **a**cid ligand commonly known as bda ligand by Sun and co-workers in 2009.[79] They reported Ru(bda)$(pic)_2$ complex **10** (pic: 4-picolin) which was able to oxidize water with a remarkably high TOF of 41.2 s^{-1} and a TON of 2000 in chemical water oxidation using CAN.[80] Further details emphasizing on the significance of this work for the development of a new generation of highly efficient molecular WOCs will be discussed in the following Chapter 2.3. However, it should be mentioned that the outstanding catalytic properties of **10**

and related Ru(bda) catalysts inspired the design of further polypyridine ligands bearing carboxylate groups such as tda ligand (tda: 2,2′:6′,2″-**t**erpyridine-6,6″-**d**icarboxylic **a**cid) by Llobet and co-workers.[81] This group has reported that Ru(tda) complex **11** is a confirmed precursor of active catalyst Ru^{IV}=O(tda)$(py)_2$ (py: pyridine) which in electrochemical water oxidation at pH 7 reaches an extremely high TOF of 8000 s^{-1} and an estimated TON of 27 million.[81] In photocatalytic water oxidation using a ruthenium tris(bipyridine) derivative as photosensitizer and sodium persulfate as electron acceptor, Ru^{IV}=O(tda) WOC exhibited a more moderate catalytic activity with a TOF of 50 s^{-1} and TON of 1050.[82] Very recently, the same group has reported a derivative of Ru(tda) complex **11** bearing phosphonic acid instead of carboxylic acid groups.[83] Interestingly, upon insertion of an oxygen atom into the tpa ligand (tpa: 2,2′:6′,2″-**t**erpyridine-6,6″-di**p**hosphonic **a**cid) the generated active species was able to oxidize water with an impressive TOF of 16000 s^{-1} and an estimated TON of 42 million in electrochemical experiments performed under neutral conditions.

2.3 Ru(bda) Catalyst Family

The discovery of the Ru(bda) catalyst family with a rather uncomplicated synthesis, readily isolation as a neutral molecule in the Ru^{II} oxidation state and very high catalytic activities marked a major milestone in the field of homogeneous water oxidation. The bda ligand with two carboxylate groups attached to a bipyridine moiety was designed to facilitate the access to high valent Ru=O species by decreasing the oxidation potentials of Ru.[79, 84] Such metal-oxo species play an essential role during catalysis and are stabilized by the presence of negatively charged groups.[11a] Further, the adaptability of the equatorial bda ligand is decisive for the high catalytic efficiency of Ru(bda) WOCs.[85] In the Ru^{II} oxidation state, Ru(bda) complexes exhibit a distorted octahedral geometry with bda ligand acting in a tetradentate fashion. X-ray analysis of complex Ru^{II}(bda)$(pic)_2$ **10** showed the formation of a large O_{bda}-Ru-O_{bda} angle of 123° in the equatorial plane, which is extended upon oxidation to Ru^{III} and Ru^{IV} to 126° and 145°, respectively (Figure 11).[79, 86] This angle expansion is vital for coordination of substrate water molecules to the Ru center of the WOC leading to formation of seven-coordinated species with pentagonal bipyramidal geometry. Figure 11 shows a dimeric Ru^{IV}(OH) species stabilized by the formation of hydrogen bonds.

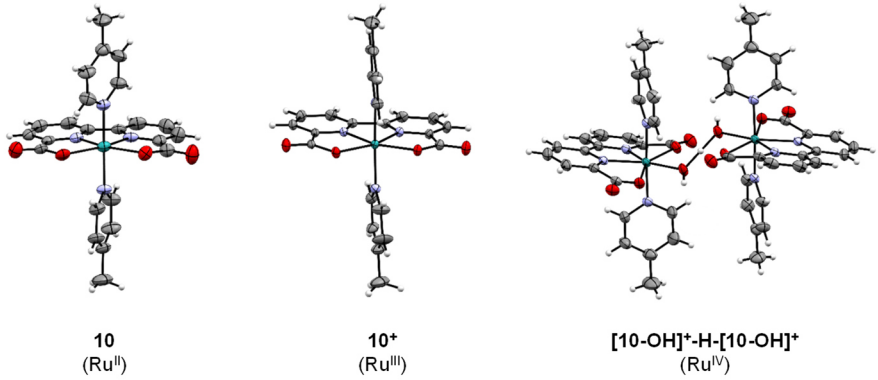

Figure 11. Structures of Ru(bda)(pic)$_2$ **10** with Ru center in oxidation states II,[79] III[86] and IV[79] obtained by single-crystal X-ray diffraction (ORTEP diagram with thermal ellipsoids set at 50% probability; grey: carbon, white: hydrogen, red: oxygen, lavender: nitrogen, turquoise: ruthenium). Counteranions and solvent molecules were omitted for clarity. Crystallographic data are reproduced with permission from ref. [79]. Copyright 2009 American Chemical Society and ref. [86]. Copyright 2015 Royal Society of Chemistry.

A complex equilibrium between six- and seven-coordinated Ru(bda) catalytic intermediates results from the coordinative flexibility of the bda ligand (Figure 12). Interestingly, some of the six-coordinated species bear pendant carboxylate groups (e.g. structures **E**, **F**, **G**, **H**). Such tridentate coordination of the bda ligand was initially proposed by DFT calculations based on the loss of symmetry observed in NMR spectra of Ru(bda) complexes in solvent mixtures containing acetonitrile.[86, 87] Coordination of acetonitrile molecules to Ru(bda) complexes with concomitant detachment of one carboxylate group was found to be energetically favored compared to coordination of other solvent molecules such as trifluoroethanol.[87b]

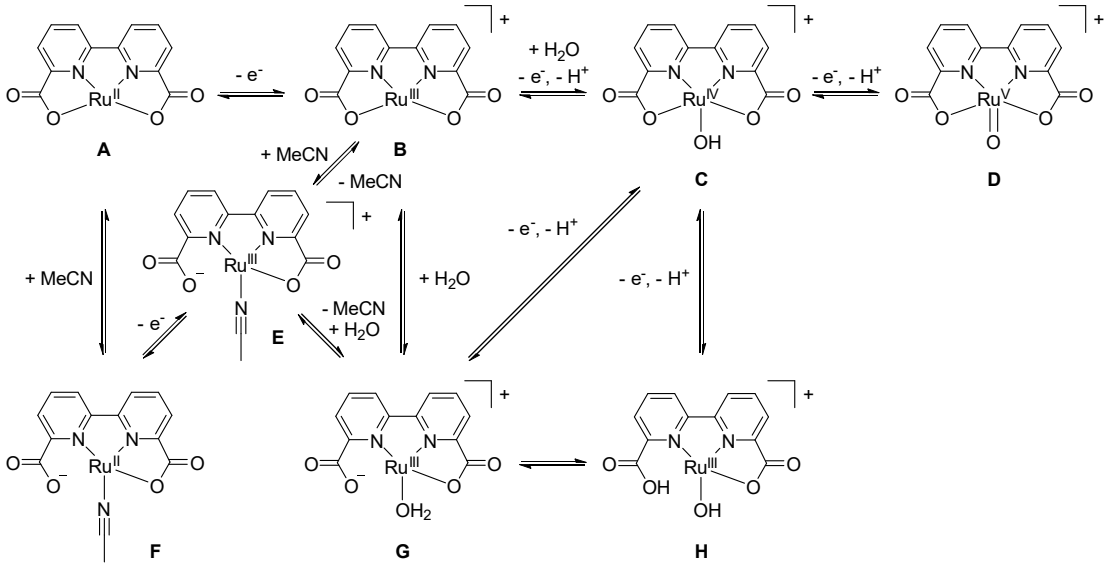

Figure 12. Equilibria between six- and seven-coordinated Ru(bda) catalytic intermediates in MeCN/H$_2$O mixtures. Axial ligands are omitted for clarity.

Confirmation of this κ^3-coordination mode (κ: denticity) of bda was later achieved by X-ray analysis of Ru^{II}(bda) complexes bearing isoquinoline (isoq)[88] or 4-(pyridin-4-yl)aniline[89] axial ligands (**F**-type structures). Meyer and co-workers proposed that oxidation of species **F** leads to intermediate **E** and the MeCN ligand is readily replaced by water to yield **G**-type Ru(bda) complexes with a dangling carboxylate group.[88] These **G** complexes most likely exist in equilibrium with **B** species bearing Ru^{III} centers attached to κ^4-bda in the absence of an additional aqua ligand. Indeed, EPR studies with a water soluble Ru(bda) WOC showed the formation of two Ru^{III} species.[90] Considering the EPR spectral width, a "narrow" spectrum with g-tensors $g_{xx} = 2.31$, $g_{yy} = 2.19$ and $g_{zz} = 1.85$ was assigned to a symmetric **B**-type complex. In contrast, a "wide" spectrum with $g_{xx} = 2.58$, $g_{yy} = 2.30$ and $g_{zz} = 1.68$ was proposed to belong to a less symmetric species. Although the authors assigned the latter set of signals to a seven-coordinated $Ru^{III}(OH_2)(\kappa^4$-bda) species, theoretical calculations by Concepcion and co-workers suggested that such a 19-electron complex would be significantly less stable in solution compared to a 17-electron **G** species with pendant carboxylate.[91] Further, the Concepcion group proposed an acid-base equilibrium between **G** and **H** species of Ru(bda) complexes, the latter generated by proton transfer from the aqua ligand to the dangling carboxylate group.[92] Based on theoretical calculations, a more facile oxidation of such **H** intermediates to yield Ru^{IV} species **C** is expected compared to oxidation of a **G** intermediate to form **C**.[91] Notably, upon oxidation to d^4 Ru^{IV} 7th coordination of the metal center is favored as it results in stable 18-electron Ru(κ^4-bda) complex **C**.[91] One-electron oxidation of **C** leads to the formation of ultimate reactive catalyst Ru^{V}=O species **D**.

Figure 13 illustrates the splitting of d-orbitals of a Ru(bda) WOC in the oxidation states Ru^{II} and Ru^{IV}.[93] Accordingly, Ru^{II}(bda) complexes with octahedral geometry (C_{2v} symmetry) and d^6 low spin configuration as well as Ru^{IV}(bda) intermediates with a pentagonal bipyramidal geometry (D_{5h} symmetry) and four d-electrons are diamagnetic species.[58b] In contrast, d^5 Ru^{III} and d^3 Ru^{V}(bda) intermediates are paramagnetic.

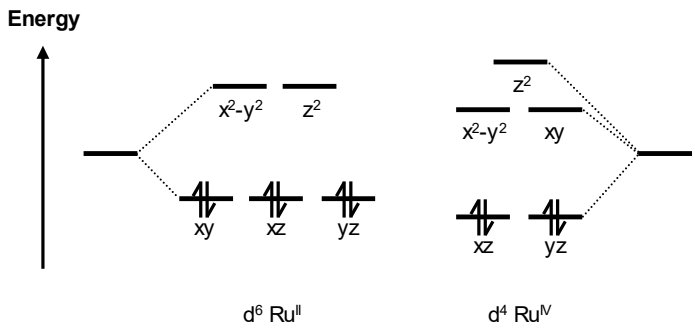

Figure 13. Qualitative energy-splitting of d-orbitals of a Ru(bda) WOC in Ru^{II} and Ru^{IV} oxidation states with octahedral and pentagonal bipyridamidal geometry, respectively.[93]

The catalytic activities of parent complex Ru(bda)(pic)$_2$ **10** have been studied by chemical, electrochemical and photochemical methods. In chemical water oxidation at pH 1, high TOF and TON values of 41.2 s^{-1} and 2000, respectively, were observed using CAN as an oxidant.[80] In electrochemical experiments, a pH-independent TOF of 11 s^{-1} was observed.[94] Markedly lower TOF and TON values of 0.15 s^{-1} and 100, respectively, were obtained for WOC **10** in photocatalytic water oxidation under neutral conditions using ruthenium tris(bipyridine) as photosensitizer and $[Co^{III}(NH_3)_5Cl]Cl_2$ as electron acceptor.[95] Replacing this cobalt salt by sodium persulfate ($Na_2S_2O_8$) as electron acceptor led to a higher TOF of 0.35 s^{-1} but a reduced TON of 10.[95]

Several studies have been performed on the mechanism of water oxidation by Ru(bda) complexes. Based on kinetic measurements and theoretical calculations, Sun and co-workers proposed an I2M mechanism for WOC Ru(bda)(pic)$_2$ **10** (Figure 14).[14a] Accordingly, upon fast one-electron oxidation of **10** and coordination of a water molecule a $[Ru^{III}\text{-}OH_2]^+$ intermediate is generated. Coordination of the aqua ligand is essential to enable subsequent proton-coupled oxidations (i.e. PCET processes) to obtain a $[Ru^{IV}\text{-}OH]^+$ and then a $[Ru^{V}{=}O]^+$ intermediate. These PCET steps allow for oxidation of Ru without the buildup of positive charges.[63] Theoretical studies have further shown that $[Ru^{V}{=}O]^+$ species exhibit a distinct radical character and thus can also be described as $[Ru^{IV}\text{-}O^{\cdot}]^+$.[96] Dimerization of two Ru oxyl units yields dinuclear $[Ru^{IV}\text{-}O\text{-}O\text{-}Ru^{IV}]^{2+}$ peroxo intermediate from which molecular oxygen is then released. Under acidic conditions using an excess of oxidant CAN, dimerization of two high-valent $[Ru^{V}{=}O]^+$ intermediates of WOC Ru(bda)(pic)$_2$ **10** was found to be the rate-determining step of catalysis.[14a] For a long time, there was some controversy over the existence of $[Ru^{V}{=}O]^+$ intermediates. However, experimental evidence for the formation of $Ru^{V}{=}O$(bda) was recently obtained by *in situ* X-ray absorption spectroscopy (XAS) studies on a phosphonate functionalized Ru(bda) complex immobilized on an ITO surface.[97] Interestingly, theoretical simulations by Ahlquist and co-workers suggested an unexpected hydrophobic character for the oxo group of $Ru^{V}{=}O$(bda) based on the absence of hydrogen bonding observed between the oxo ligand and surrounding water molecules.[98] This hydrophobicity was proposed as the driving force for the attractive interaction of two Ru^{V}-oxo units with a predetermined orientation favorable for formation of peroxo species in solution.

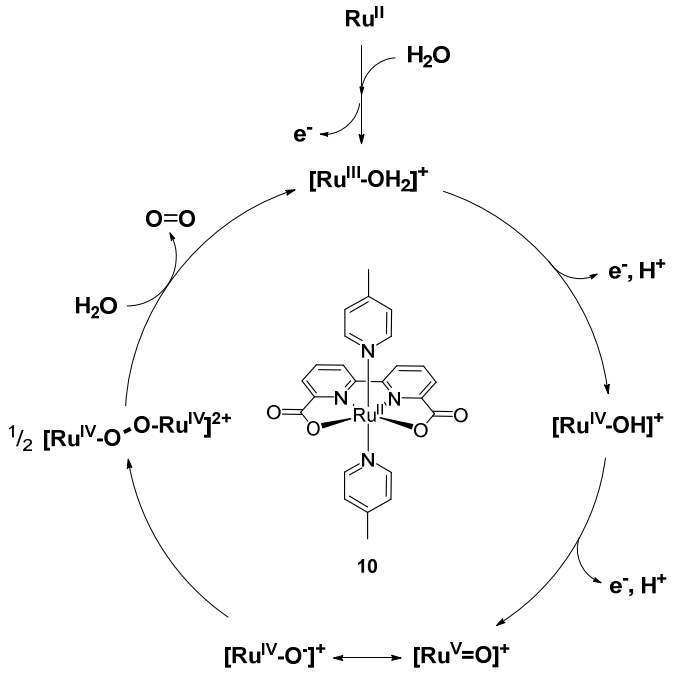

Figure 14. Proposed I2M mechanism of water oxidation for Ru(bda)(pic)$_2$ **10**.[14a]

Over the last years, two main strategies have been developed to tune the properties of parent catalyst Ru(bda)(pic)$_2$ **10** and achieve faster rates of O-O bond formation. On the one hand, the rather uncomplicated manipulation of the axial ligands, given that picoline can be readily replaced by other N-heterocyclic compounds of varying electronic nature, has enabled the synthesis of several mononuclear Ru(bda) WOCs. Some studies have also been performed on Ru(bda) catalysts bearing functionalized bda ligands. On the other hand, supramolecular approaches such as encapsulation of mononuclear Ru(bda) WOCs to reach high local concentrations and assembly of Ru(bda) units into diverse supramolecular architectures have been pursued as well. Both strategies are discussed in the following.

2.3.1 Functionalized Mononuclear Catalysts

As already mentioned, the rate-determining step of water oxidation with WOC Ru(bda)(pic)$_2$ **10** is the reaction of two high-valent $[Ru^{V}=O]^{+}$ intermediates to form a $[Ru^{IV}\text{-}O\text{-}O\text{-}Ru^{IV}]^{2+}$ peroxo species.[14a] The exchange of picoline by isoquinoline (isoq) axial ligands has been proven to be a very successful approach to increase the rate of this dimerization. Catalyst Ru(bda)(isoq)$_2$ **12** (Figure 15a) reached a remarkable TOF of 303 s^{-1} and a TON of 8360 in chemical water oxidation compared to 41.2 s^{-1} and 2000 for WOC **10**.[14a] The high catalytic activity of **12** was ascribed to π-π interactions facilitating the formation of the peroxo intermediate as shown in Figure 15b. Based on theoretical calculations it has been shown that

this effect is greatly dependent on the solvent environment.[98, 99] Fast dimerization is observed in aqueous solutions, while no π-stacking between **12** complexes is detected in the gas phase.

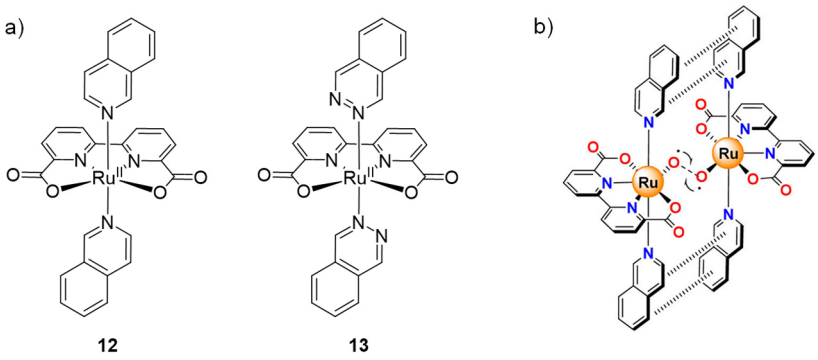

Figure 15. a) Catalysts Ru(bda)(isoq)$_2$ **12** and Ru(bda)(phth)$_2$ **13** bearing isoquinoline and phthalazine axial ligands, respectively. b) Non-covalent π-π interactions between two Ru^V-oxo intermediates of WOC **12**. Figure 15b) is reproduced with permission from ref. [16]. Copyright 2014 American Chemical Society.

Deactivation of Ru(bda) WOCs is usually associated with the loss of the axial ligands. Indeed, based on DFT analysis an interesting relationship was found between the HOMO energy of these ligands and the Gibbs free energy for their dissociation from Ru center.[14b] Thus, ligands with higher HOMO energies, compared to picoline, such as phthalazine (phth) should lead to more stable Ru(bda) complexes. This is indeed the case as Ru(bda)(phth)$_2$ **13** (Figure 15a) reached a TOF of 286 s^{-1} and an impressive TON of 55400 in chemical water oxidation,[14b] while Ru(bda)(pic)$_2$ **10** performed with TOF of 41.2 s^{-1} and TON of 2000.[80]

In the last years, several studies have been reported on the effect of substituents on the catalytic performance of monomeric Ru(bda) WOCs. Often has been reported that catalysts bearing electron-withdrawing groups (EWGs) at the 4-position of axial picoline ligands exhibited higher catalytic activities in chemical and light-driven water oxidation than parent WOC Ru(bda)(pic)$_2$ **10** and derivatives bearing electron-donating groups.[87a, 100] This effect was explained by destabilization of Ru^V=O catalytic intermediates resulting from ligand functionalization with EWGs which led to enhanced rates of dimerization. Voltammetry measurements further showed that the introduction of substituents significantly affected the Ru$^{III/II}$ oxidation potential of the WOCs.[87a, 100] However, higher oxidation potentials leading to the formation of Ru^V=O were less affected. Recent investigations on halogenation of picoline, isoquinoline and phthalazine axial ligands of mononuclear Ru(bda) WOCs have emphasized the pivotal role of non-covalent interactions on the catalytic efficiency of this catalyst class.[87b, 101] The introduction of hydrophobic halogens at the 4-position of picoline or 6-position of

isoquinoline and phthalazine ligands favors the formation of $[Ru^{IV}\text{-O-O-}Ru^{IV}]^{2+}$ peroxo intermediates in aqueous solution due to halogen-π and dipole-induced dipole interactions which lower the activation barrier for dimerization. Interestingly, functionalization of isoquinoline axial ligands with electron-donating methoxy groups was also found to increase the catalytic activity in chemical water oxidation leading to a TOF of 923 s^{-1} compared to 303 s^{-1} for undecorated WOC Ru(bda)$(isoq)_2$ **12**.[102] Based on DFT calculations, this effect was ascribed to a favorable off-center π-stacking geometry of the axial ligands in the transition state forced by the introduction of the methoxy groups.

Sparse examples of modifications on the equatorial bda ligand have been reported presumably due to its higher synthetic complexity. A derivative of WOC Ru(bda)$(isoq)_2$ **12** bearing additional carboxylic acid groups at the 4-position of bda was immobilized on an ITO electrode leading to a TOF of 0.41 s^{-1} and a TON of 15000 in electrochemical water oxidation at pH 7.[103] Furthermore, studies were performed on Ru(bda) catalyst bearing bromo[104] and trifluoromethyl[105] functionalized bda ligands. These studies revealed that the introduction of electron-withdrawing substituents at the 4-position of bda increases the $Ru^{III/II}$ and $Ru^{IV/III}$ oxidation potentials of the WOCs. Reduced TOF and TON values were obtained for dibromo-functionalized Ru(bda)$(pic)_2$ and Ru(bda)$(isoq)_2$ complexes compared to the respective unsubstituted WOCs.[104]

In addition to pyridine, isoquinoline and phthalazine, various imidazoles,[80] pyrazoles[106] and even 1,3-dimethylimidazolium-2-ylidene as a N-heterocyclic carbene (NHC)[107] have been used as axial ligands for Ru(bda) WOCs as well. While Ru(bda) complexes bearing imidazole and pyrazole axial ligands exhibit similar catalytic activities as those reported for parent Ru(bda)$(pic)_2$ **10**, the introduction of NHC ligand resulted in a drastic decrease in catalytic performance with an observed TOF of 0.04 s^{-1} in chemical water oxidation.[107] This strongly reduced catalytic efficiency was explained by a change in operating mechanism of water oxidation from I2M to WNA.

2.3.2 Supramolecular Approaches

One of the first supramolecular strategies used to accelerate the rate-determining dimerization of Ru(bda)$(pic)_2$ **10** comprised its encapsulation into the nanocages of mesoporous silica (SBA-16) with an average pore diameter of 5.9 nm.[108] As shown in Figure 16a, irreversible confinement of **10** within the pores was achieved by reducing the size of the pore entrances after encapsulation using a silylation reagent. Investigations on the catalytic activity of the Ru loaded material in chemical water oxidation showed that increasing the number of **10**

complexes per nanocage from one to seven resulted in an increase in TOF values from 1.2 s^{-1} to 8.7 s^{-1}, respectively. This effect was not observed upon encapsulation of variable amounts of WOC Ru(pda)$(pic)_2$ **15** (pda: 1,10-phenanthroline-2,9-dicarboxylic acid), which was previously demonstrated to perform water oxidation by a monomolecular WNA mechanism (Figure 16b).[109] Accordingly, the variations in TOF values observed using Ru(bda) complex **10** were ascribed to an increased probability for dimerization resulting from confinement of the WOC in pores of limited size. In contrast, the constant TOF obtained for Ru(pda) complex **15** independent of the number of trapped catalyst units per nanocage was explained based on its WNA mechanism, which does not require close contact of two Ru^{V}=O units in the rate-determining step.

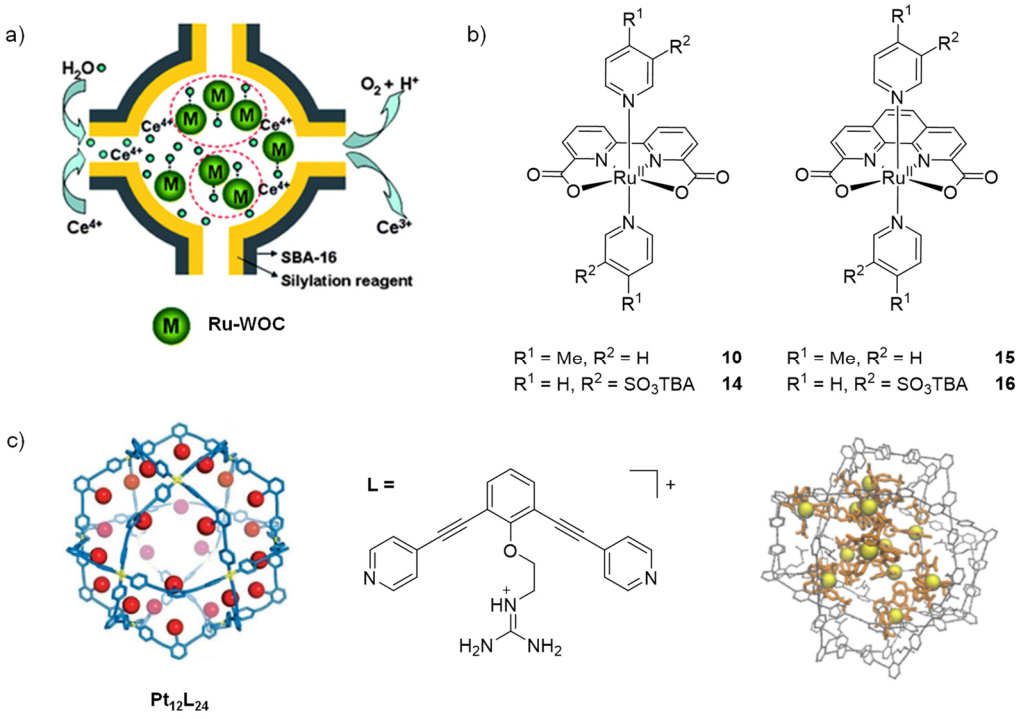

Figure 16. a) Schematic illustration of Ru WOCs confined in mesoporous silica (SBA-16). b) Structures of mononuclear Ru(bda) (**10** and **14**) and Ru(pda) (**15** and **16**) catalysts used in encapsulation studies. c) Supramolecular $\mathbf{Pt_{12}L_{24}}$ cage used for trapping of Ru WOCs and illustration of host-guest complex formed upon encapsulation of twelve sulfonated Ru complexes. Figure 16a) is reproduced with permission from ref. [108]. Copyright 2012 Royal Society of Chemistry and Figure 16c) is adapted with permission from ref. [110]. Copyright 2018 Wiley-VCH.

Reek and co-workers used a similar strategy to accelerate the rate of water oxidation of sulfonated Ru(bda) WOC **14** (Figure 16b).[110] Hereby, a $Pt_{12}L_{24}$ nanosphere endohedrally functionalized with guanidinium groups was used to encapsulate up to twelve **14** complexes as it was confirmed by ^{1}H and DOSY NMR spectroscopy as well as mass spectrometry (Figure 16c). Remarkably, using this approach high local concentrations of catalyst **14** of up

to 0.54 M were achieved within the nanospheres leading to a high TOF value of 125 s^{-1} in electrochemical water oxidation. Furthermore, the relationship between the local concentration of Ru(bda) catalyst **14** and the rates of water oxidation was investigated. Thus, up to 0.27 M (i.e. six catalyst molecules pro cage) a second-order dependence of these rates on the WOC concentration was observed which changed to first-order at higher concentrations. Accordingly, the authors proposed that below 0.27 M encapsulation of **14** facilitated the rate-determining dimerization of two Ru^{V}=O units. Further acceleration of this dimerization reaction at higher local concentrations led to a change in rate-determining step of catalysis to oxidation of the WOC from Ru^{IV}-OH to Ru^{V}=O. Encapsulation studies with Ru(pda) complex **16** operating by a WNA mechanism showed rather constant rates of water oxidation independent of the changes in local concentration.

Würthner and co-workers have studied the aggregation behavior and catalytic water oxidation propensity of Ru(bda) complex **17** bearing axial perylene bisimide (PBI) ligands functionalized with oligoethylene glycol (OEG) chains (Figure 17).[111] In a mixture of MeCN/H_2O 1:1, the strong π-π interactions between the axial PBI ligands of **17** facilitated self-assembly into supramolecular nanofibers with a length of up to 300 nm. The catalytic activity of these fibers was investigated in chemical water oxidation using CAN as oxidant leading to an increased TON of 826 compared to 632 for mononuclear Ru(bda)$(pic)_2$ under identical conditions. This was explained by partial prevention of axial ligand dissociation within the supramolecular nanofibers.

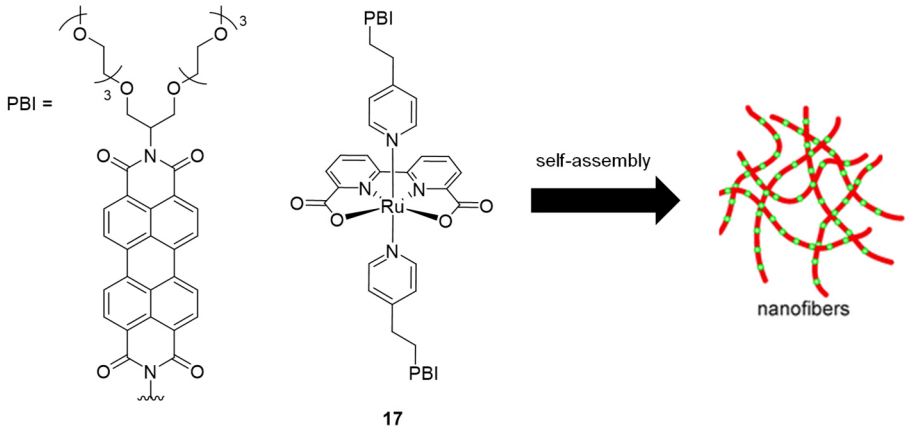

Figure 17. Ru(bda) complex **17** bearing PBI functionalized axial ligands to enable self-assembly into supramolecular nanofibers (green: Ru(bda) units, red: PBI functionalized ligands). Adapted with permission from ref. [111]. Copyright 2015 Royal Society of Chemistry.

A different aggregation behavior was reported for sulfonated Ru(bda) complex **14** (Figure 16b) and a derivative of it bearing OEG chains which upon reaching a critical concentration in water

formed vesicles with a diameter of about 100 nm.[112] The catalytic activity of these supramolecular vesicles was studied in chemical water oxidation with standard oxidant CAN. Interestingly, a linear relationship between the catalyst concentration and the initial rate of catalysis was found for vesicles of the OEG complex, while for **14** a second-order dependence of these rates on the catalyst amount was observed. This was interpreted as the result of different aggregation modes which led to a closer packing of the Ru centers in the case of **14**, thus facilitating the oxidation of water by I2M mechanism. Within the vesicles of the OEG derivative, a larger distance between the Ru centers forced the WOC to perform water oxidation *via* WNA.

A few studies have been conducted on the introduction of Ru(bda) units into large supramolecular polymers. Cross-linked polymer **18** showed a moderate catalytic efficiency as a heterogeneous WOC with a TOF value of 4.6 s^{-1} and a TON of 750 in chemical water oxidation (Figure 18a).[113] Kinetic studies suggested that this catalyst operates by a mononuclear WNA mechanism. Polymer family **19** bearing variable amounts of Ru(bda) units reached a high solubility in acidic aqueous solution due to protonation of the uncoordinated pyridines (Figure 18a).[114] Thus, these polymers were studied as homogeneous WOCs in chemical water oxidation reaching a maximal TON of 1700. Figure 18b shows the formation of a Ru(bda) supramolecular polymer by step-growth polymerization of monomer **21** on an ITO electrode.[115] Hereby, after initial immobilization of phosphonate functionalized Ru(bda) complex **20**, electrochemical stimuli were used to alternately induce reductive coupling of vinyl or oxidative coupling of carbazolyl substituents. The catalytic properties of the formed molecular wires were studied in electrochemical water oxidation resulting a maximal current density of 66.2 μA cm^{-2}. A few bimetallic Ru(bda) systems are also known in literature.[116] One interesting example was recently reported by Ott and co-workers who successfully performed post-synthetic modification of metal-organic framework (MOF) MIL-101 (Cr) to covalently attach variable amounts of Ru(bda) units in the pores of the MOF (Figure 18c).[116b] Ru-functionalized MIL-101 (Cr) MOF **22** exhibited a maximum TON value of 1500 in chemical water oxidation using CAN.

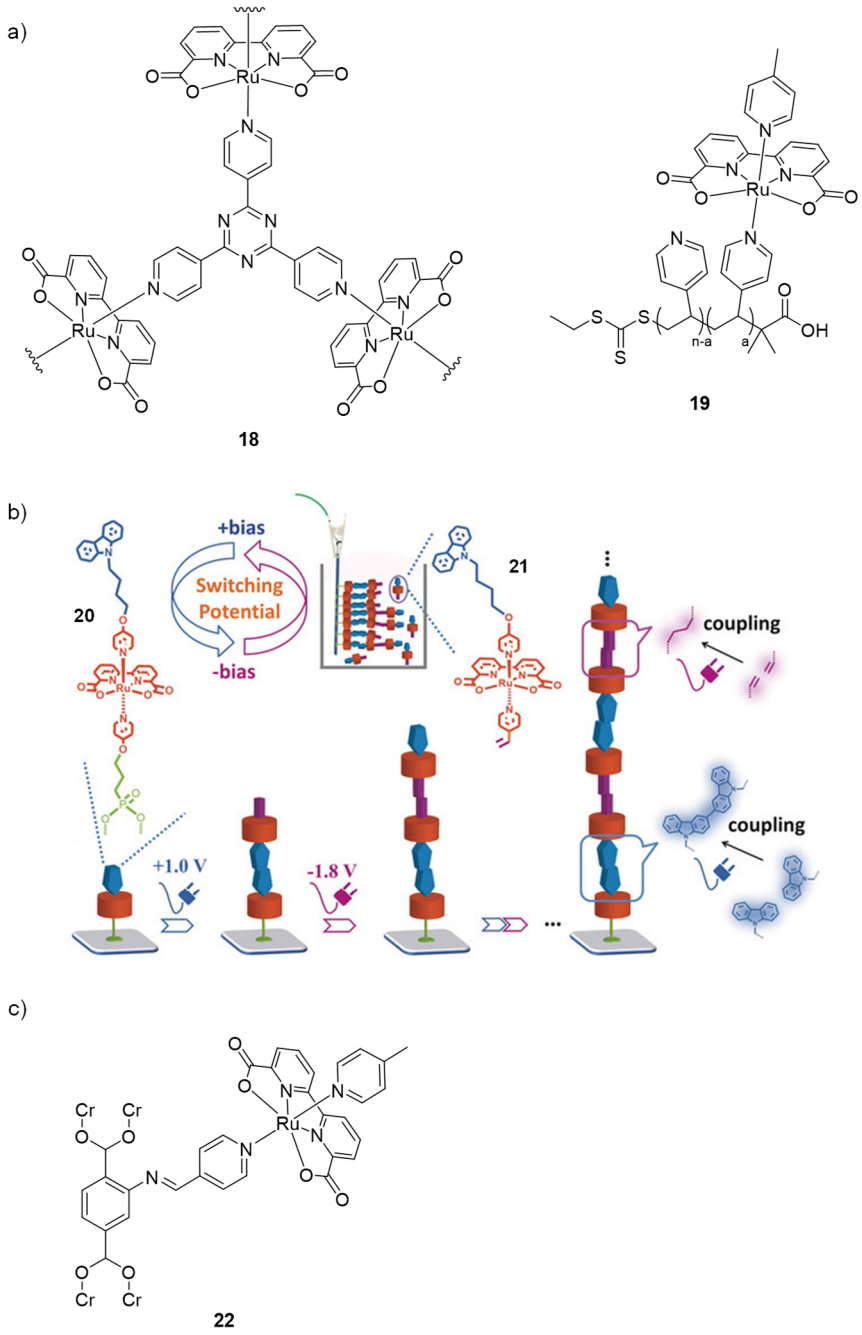

Figure 18. a) Structures of cross-linked Ru(bda) polymer **18** and polymer family **19** bearing variable amounts of Ru(bda) units (polymer length n = 21, 42, 74 and 198, Ru loading between 2.8 – 3.5%). b) Schematic illustration of step-growth polymerization of Ru(bda) complex **21** on an ITO surface. c) Structure of Ru(bda) MOF **22**. Figure 18b) is adapted with permission from ref. [115]. Copyright 2018 Wiley-VCH.

A different supramolecular strategy to improve the catalytic performance of Ru(bda) WOCs pursued by introduction of Ru(bda) units into defined di- or trinuclear complexes such as those shown in Figure 19. Rigid dinuclear complex **23** bearing a xanthene bridging ligand was designed to bring two Ru(bda) units in close proximity and thus increase the rate of

dimerization of Ru^{V}=O intermediates.[117] The use of a ditopic bridging ligand was further expected to increase the stability of the WOC compared to mononuclear catalyst Ru(bda)$(pic)_2$ **10**. However, only a moderate TON of 900 was reached with catalyst **23** in chemical water oxidation compared to a TON of 2000 for mononuclear reference complex **10**. Based on kinetic analysis, a less efficient WNA mechanism instead of I2M was proposed for dinuclear WOC **23**. This was explained by the steric constraint imposed by the rigid xanthene bridge which did not have the ideal geometry to promote intramolecular coupling of two Ru^{V}=O units. In contrast, more flexible dinuclear catalysts **24** and **25** reached significantly higher TON values of about 20800[118] and 44400[119] in chemical water oxidation, respectively. Kinetic studies revealed in both cases a linear relationship between the rates of water oxidation and the amount of catalyst present which was indicative of an intramolecular I2M mechanism. A remarkable TON of 86500 was obtained with trinuclear Ru(bda) WOC **26**, which also reached an impressive TOF of 126 s^{-1} in chemical water oxidation using oxidant CAN. For comparison, TOF values of 68 s^{-1} and 41.2 s^{-1} were obtained for the dinuclear WOC **25** and mononuclear Ru(bda)$(pic)_2$ complex **10**, respectively.[119] The authors proposed that the high catalytic activity of trinuclear WOC **26** was the result of an increased probability for intramolecular O-O bond formation owing to the increased number of Ru(bda) units per molecule.

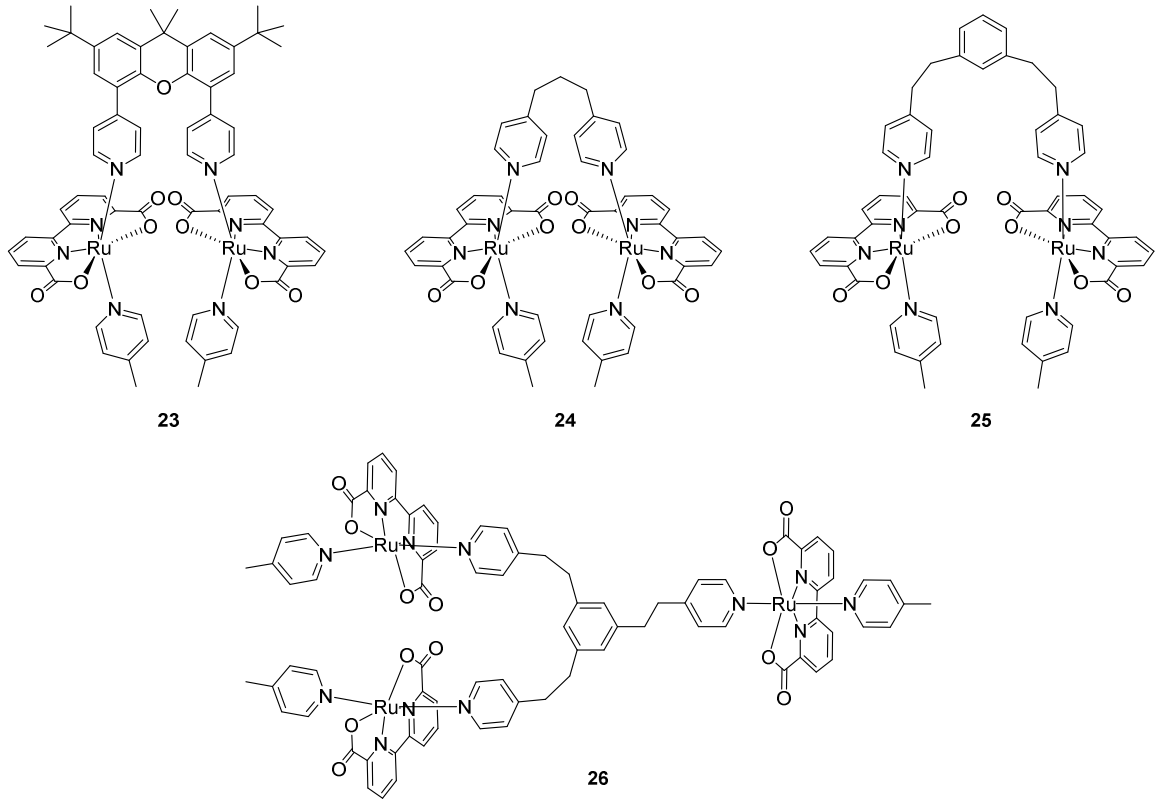

Figure 19. Structures of di- and trinuclear Ru(bda) complexes **23** – **26**.

The introduction of Ru(bda) units into a macrocyclic structure was first reported 2015 in a chinese patent.[120] The structure of dinuclear macrocycle **27** bearing 1,3,4-oxadiazole bridging ligands was confirmed by X-ray analysis which showed coordination of a CO ligand to one of the Ru centers (Figure 20). However, neither TOF nor TON values were reported for this molecule, albeit it was mentioned that it could be used for water oxidation using CAN as an oxidant.

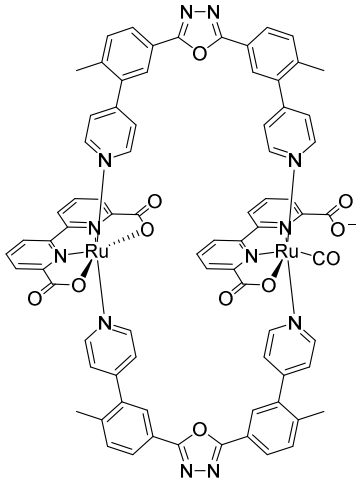

27

Figure 20. Structure of dinuclear Ru(bda) macrocycle **27** bearing 1,3,4-oxadiazole bridging ligands.

Catalytic water oxidation by macrocyclic Ru(bda) complexes was explored for the first time by the Würthner group.[18] Catalytic activities of a series of trinuclear Ru(bda) macrocycles **MC1–4** bearing ditopic bridging ligands of variable lengths were studied in chemical water oxidation using oxidant CAN (Figure 21a).[19] Interestingly, middle-sized macrocycle **MC3** showed the highest catalytic efficiency of this series reaching an impressive TOF of 150 s^{-1} and a TON of 7400.[18] Based on molecular dynamics simulations, the formation of a hydrogen-bonded network of water molecules inside the cavity of **MC3** was proposed.[19] Theoretical studies suggested that cooperative proton abstractions between the Ru centers of **MC3** might be facilitated by this preorganized water network, thus reducing activation barriers for proton-coupled steps and increasing the rates of catalysis. Notably, macrocycle **MC3** was the only one of the **MC1–4** series with an ideal size to allow for formation of such an ordered network of water molecules in its cavity. Kinetic studies and ^{18}O labelling experiments have confirmed that WOC **MC3** performs water oxidation by a WNA mechanism in which the oxidation of Ru^{IV} to Ru^{V} is the rate-determining step (Figure 21b).[18] Accordingly, O-O bond formation occurs by the attack of water on a highly oxidized Ru^{V}=O intermediate. Thus, **MC3** is one of the most active Ru(bda) WOCs known to date that perform water oxidation *via* WNA. Previous reports on immobilization of mononuclear Ru(bda) catalysts on electrode surfaces have shown a drastic reduction of the catalytic activities of such WOCs upon anchoring.[121] This effect was

explained based on a hindered diffusion of the Ru catalysts on surfaces which prevented the efficient formation of dimeric peroxo intermediates. Therefore, supramolecular Ru macrocycles that perform catalytic water oxidation efficiently by a monomolecular WNA mechanism are interesting for potential application in solar fuel devices.

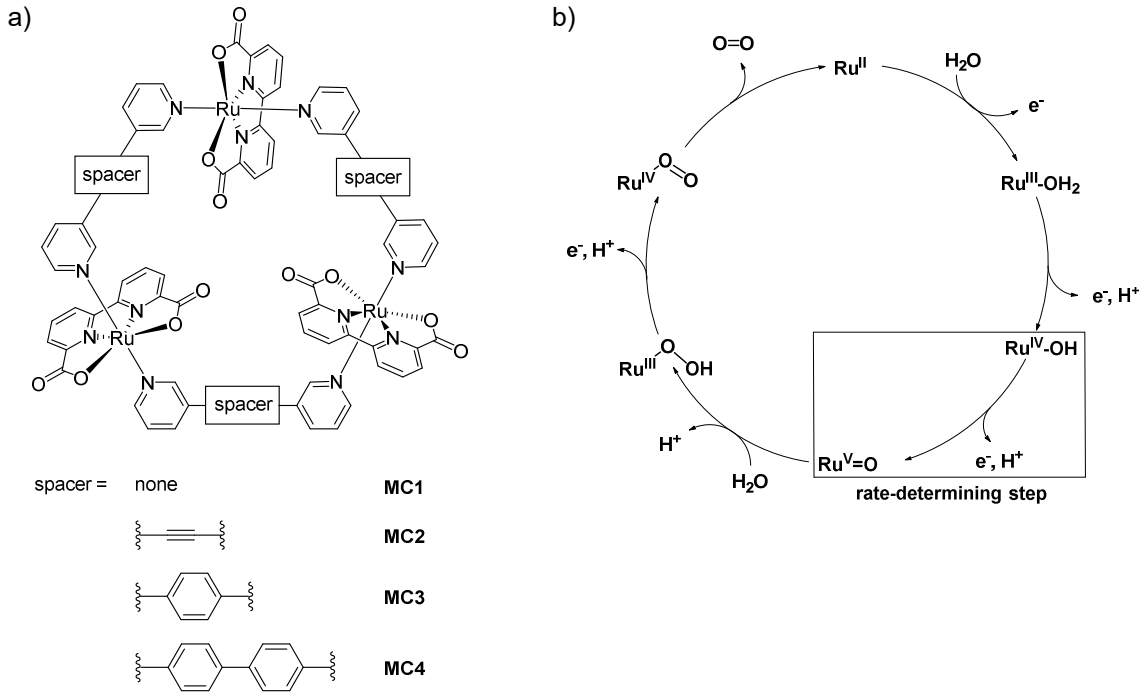

Figure 21. a) Structures of trinuclear Ru(bda) macrocycles **MC1–4** bearing bridging ligands of variable lengths. b) Simplified proposal for WNA water oxidation mechanism of **MC3** macrocycle. After liberation of molecular oxygen, Ru^{II} species might be oxidized by neighboring Ru^{IV} centers by comproportionation.

Due to the rather hydrophobic nature of macrocycle **MC3**, chemical water oxidation was studied in a MeCN/H_2O 6:4 mixture (i.e. in 60% MeCN). To increase the solubility of the WOC in water, OEG and trialkylamine groups were introduced (Figure 22).[20] Studies with ***m*-OEG-MC3** and ***m*-CH_2NMe_2-MC3** using standard oxidant CAN showed that the catalytic activities of these functionalized macrocycles in 30% and 20% MeCN, respectively, were comparable to those of parent compound **MC3**.

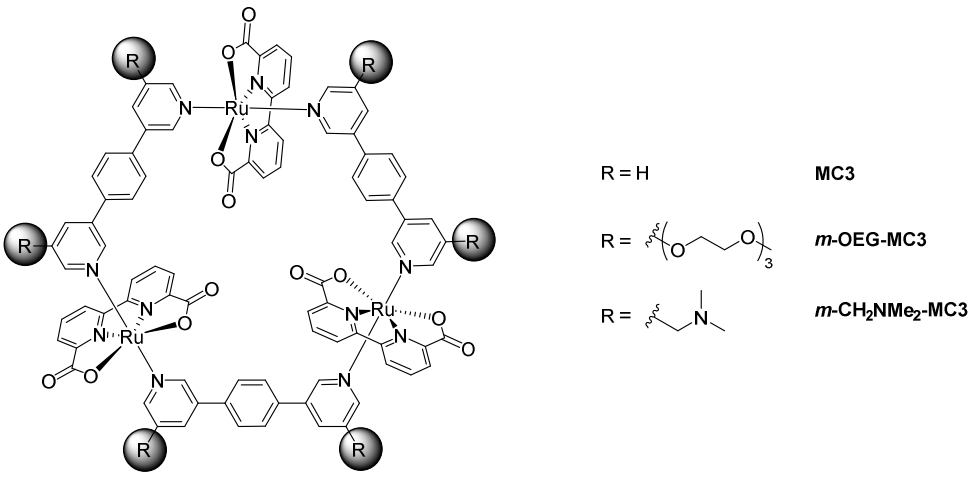

Figure 22. Structures of functionalized **MC3** macrocycles for increased solubility in water.

2.4 Photocatalytic Water Oxidation with Ru(bda) Catalysts

The catalytic activity of the majority of Ru(bda) WOCs has been investigated by chemical methods using one-electron oxidant CAN (see above). Chemical water oxidation is a convenient technique to assess the catalytic efficiency of a WOC as it only requires the presence of a sacrificial oxidant and the catalyst itself. However, the use of CAN which is only stable at low pH values restricts the study of the catalytic activities of the WOCs to pH 1.[15] In contrast, photocatalytic water oxidation is generally performed under neutral conditions using a photosensitizer (PS) and a compatible sacrificial electron acceptor. In light-driven water oxidation WOCs are activated by oxidants which are generated by irradiation of a sensitizer,[16] thus mimicking the photosynthetic process of water oxidation. Reported investigations on the photocatalytic activities of Ru(bda) WOCs have been conducted using ruthenium tris(bipyridine) derivatives as photosensitizers and sodium persulfate ($Na_2S_2O_8$) or $[Co^{III}(NH_3)_5Cl]Cl_2$ as electron acceptors. Due to their good absorption of visible light and efficient generation of excited triplet state, ruthenium tris(bipyridine) complexes are excellent photosensitizers for activation of Ru(bda) catalysts.[122] Mechanistic details of photocatalytic water oxidation with this sensitizer are discussed in Chapter 4. In short, oxidative quenching of excited ruthenium tris(bipyridine) leads to *in situ* generation of oxidant $[Ru(bpy)_3]^{3+}$ which extracts an electron from the WOC. Once four electrons are transferred, water is oxidized to molecular oxygen.[16]

Photocatalytic water oxidation with $Ru(bda)(pic)_2$ **10** using ruthenium tris(bipyridine) as photosensitizer and $[Co^{III}(NH_3)_5Cl]Cl_2$ as sacrificial electron acceptor led to a TOF of 0.15 s^{-1} and a TON of 100.[95] A slightly higher TOF of 0.35 s^{-1} but a reduced TON of 10 was obtained

using sodium persulfate ($Na_2S_2O_8$) as electron acceptor. As mentioned before, deactivation of Ru(bda) WOCs usually occurs by dissociation of the axial monodentate ligands.[14b] However, investigations with catalyst **10** showed that at pH 7 decomposition of the WOC also resulted in formation of a bis(μ-oxo) bridged trinuclear species **28** with a characteristic absorption band at 690 nm (Figure 23).[123] Sun and co-workers proposed that the formation of this decomposition product could be prevented by decreasing the pH of the solution.[123a] Indeed, at pH 5 analysis of the absorption at 690 nm revealed a reduced formation of **28** which resulted in an increased TOF of 0.48 s^{-1} compared to 0.15 s^{-1} at pH 7 for the photocatalytic system based on catalyst **10**, ruthenium tris(bipyridine) and $[Co^{III}(NH_3)_5Cl]Cl_2$. Brudvig, Sakai and co-workers succeeded in isolating trinuclear compound **28** and they studied its catalytic activity in photocatalytic water oxidation.[123b] A maximum TOF and TON of 0.9 s^{-1} and 610, respectively, were reached at pH 8 using $[Ru(bpy)_3](NO_3)_2$ as sensitizer and sodium persulfate as electron acceptor.

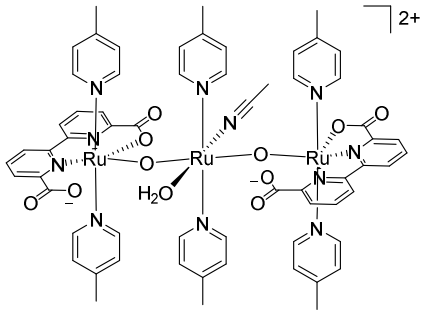

28

Figure 23. Structure of trinuclear complex **28** formed by decomposition of WOC Ru(bda)(pic)$_2$ **10** at pH 7.

Very recently, photocatalytic water oxidation was also reported at pH 1 using WOC Ru(bda)(isoq)$_2$ **12** (see Figure 15 for structure) in combination with sodium persulfate and ruthenium tris(bipyridine) derivatives functionalized with trifluoromethyl or phosphonic acid groups.[124] Although similar TOF and TON values as those obtained for the catalyst **10** were achieved with **12**, at this pH the formation of decomposition product **28** was not observed. Photocatalytic water oxidation of dinuclear Ru(bda) complex **24** (see Figure 19 for structure) using ruthenium tris(bipyridine) and sodium persulfate as PS and electron acceptor, respectively, at pH 7 has also been recently reported.[125] Under these conditions, WOC **24** reached a TON of 640.

A few studies have been performed on the integration of Ru(bda) complexes in supra-molecular catalyst-photosensitizer assemblies for light-driven water oxidation. The main advantage of such assemblies should be a more efficient electron transfer between the WOC and the photosensitizer compared to the standard multi-component system which is limited

by diffusion rates. A fast regeneration of the sensitizer should increase its stability during catalysis and lead to higher TONs as, typically, degradation of oxidant $[Ru(bpy)_3]^{3+}$ represents the major deactivation pathway of light-driven water oxidation.[126] Figure 24 shows selected examples of covalent catalyst-photosensitizer assemblies containing Ru(bda) WOCs.

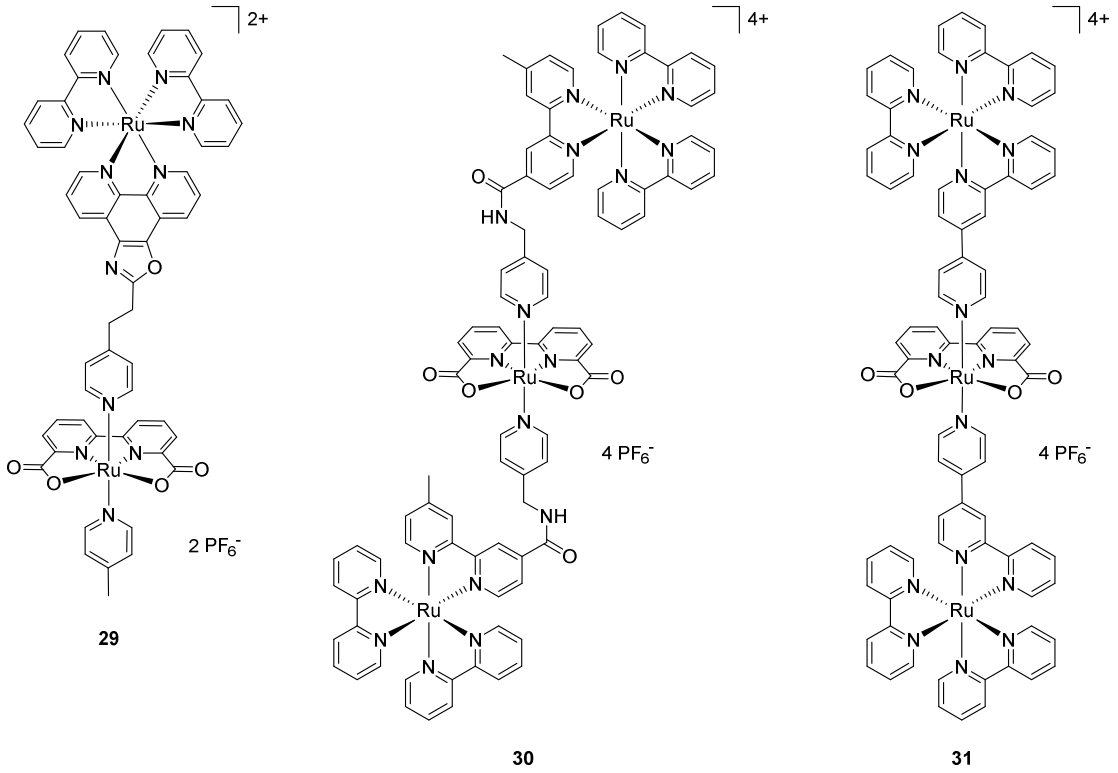

Figure 24. Structures of covalent catalyst-photosensitizer assemblies based on Ru(bda) WOCs.

Dyad **29**[127] bearing an oxazole-functionalized ruthenium sensitizer and triad **30**[128] with an amide linkage between photosensitizer and Ru(bda) WOC reached a TON of 34 and 38, respectively, in photocatalytic water oxidation using sodium persulfate as electron acceptor. Under identical conditions, a TON of 8 was obtained for catalyst $Ru(bda)(pic)_2$ **10**.[128] Thus, the attachment of Ru(bda) WOCs to ruthenium tris(bipyridine) photosensitizers indeed increased the stability of the photocatalytic systems. Upon shortening the bridge between catalyst and sensitizer, assembly **31** reached a significantly higher TON of 209 in photocatalytic water oxidation.[126] In-depth investigations by transient absorption spectroscopy revealed faster rates of sensitizer regeneration within this triad compared to the individual component system. However, unproductive quenching of the PS unit by intra-molecular energy transfer from the sensitizer to the WOC was also detected.

A non-covalent approach was followed by Sun and co-workers to design assembly **32**, in which a phenyl functionalized Ru(bda) catalyst is connected with a ruthenium tris(bipyridine) photosensitizer through a cyclodextrin ring by supramolecular host-guest interactions

(Figure 25).[129] By isothermal titration calorimetry (ITC), a 1:1 ratio of components was observed, although in principle two sensitizer units could bind to one phenyl functionalized Ru(bda) complex. In photocatalytic water oxidation, assembly **32** reached a TOF of 0.13 s^{-1} and a TON of 267. Control experiments with the separated components confirmed once again the higher stability of the ruthenium tris(bipyridine) moiety within the triad system.

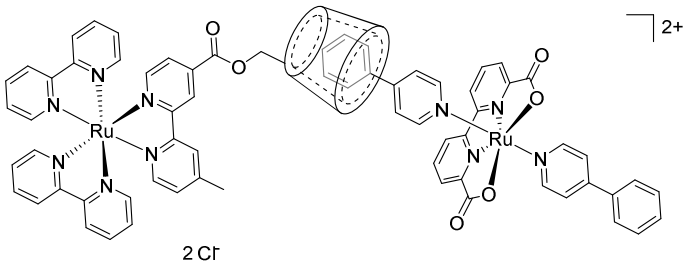

32

Figure 25. Structure of non-covalent catalyst-photosensitizer assembly **32** containing a Ru(bda) catalytic unit.

Chapter 3

Impact of Substituents on Molecular Properties and Catalytic Activities of Trinuclear Ru Macrocycles in Water Oxidation[1]

3.1 Introduction

During the last decade, some insightful studies have been performed on the effect of substituents on the catalytic activity of monomeric Ru(bda) WOCs.[87, 100-105] Hereby, uncomplicated manipulations of the axial ligands have enabled the synthesis of a plethora of catalysts within the family of mononuclear Ru(bda) WOCs. On the contrary, there are only sparse examples of modifications on the equatorial bda backbone presumably due to its higher synthetic complexity. These studies mainly focused on the electronic properties and non-covalent interactions of catalysts imparted by the substituents and how these affect the operating mechanism of water oxidation. However, the conformational effect imposed by ligand substituents on the accessibility of water molecules to the 7th coordination site of Ru and thus on the catalytic activity of WOCs still remained unadresssed.

Würthner and co-workers have previously reported that the supramolecular ruthenium macrocycle **MC3** (Scheme 1) is a highly efficient catalyst for chemical water oxidation using ceric ammonium nitrate (CAN) as an oxidant under acidic conditions.[18] Based on molecular dynamics simulations, the authors recently proposed that the formation of a hydrogen-bonded water network inside the macrocyclic cavity promoted a cooperative proton abstraction which resulted in the high catalytic activity of the catalyst.[19] Kinetic studies with **MC3** have further shown that the oxidation of Ru^{IV} to Ru^{V} is the rate-determining step in this catalytic water oxidation.[18] Thus, electron donating substituents either in the bridging or equatorial ligand might increase the electron density at the Ru centers and, accordingly, decrease the $Ru^{V/IV}$ oxidation potential and accelerate the rate of oxygen formation. Guided by this hypothesis, I

[1] This chapter was partly communicated in [130] A.-L. Meza-Chincha, J. O. Lindner, D. Schindler, D. Schmidt, A.-M. Krause, M. I. S. Röhr, R. Mitrić, F. Würthner, *Chem. Sci.* **2020**. DOI: 10.1039/ D0SC01097A (Reproduced with permission, Copyright 2020 Royal Society of Chemistry).

have synthesized a series of **MC3** derivatives that contain different substituents of varied electronic nature either at axial or equatorial ligands. The present series of Ru macrocyclic WOCs provided the unique opportunity to explore the steric impact of the substituents on the catalytic performance of regioisomeric **MC3** macrocycles. Here I report the synthesis of a series of **MC3** derivatives that bear methoxy, methyl or fluoro substituents either in the bridging or equatorial bda ligand (Schemes 1 and 2). The catalytic activities of these diversely substituted Ru macrocycles were studied in chemical water oxidation with Ce^{IV} as oxidant and under photochemical conditions using a three-component system based on a photosensitizer, a sacrificial electron acceptor and the supramolecular catalyst at a neutral pH. The distinct differences in the water oxidation performance of the regioisomeric macrocycles were analized based on experimental evidence as well as on molecular dynamics simulations. Moreover, Ru species at different oxidation states were identified by EPR and XAS techniques, both very powerful tools to obtain information on Ru at high oxidation states. Notably, for the first time crystallographic evidence for the **MC3** macrocyclic structure as well as an indication for a hydrogen-bonded water network in its cavity could be obtained.

3.2 Results

3.2.1 Synthesis and Structural Characterization of Functionalized Ru Macrocycles

Two strategies were followed to achieve the desired functionalization of the **MC3** macrocycles. On the one hand, methoxy, methyl and fluoro groups were introduced into the pyridyl rings of the bpb (1,4-**b**is(**p**yridin-3-yl)**b**enzene) bridging ligand. Hereby, the use of 3-bromopyridines **34** with substituents either in 4- (*para*) or 5-position (*meta*) enabled the synthesis of a series of regioisomeric trinuclear Ru macrocycles. On the other hand, a **MC3** macrocycle containing a methoxy decorated bda (2,2'-**b**ipyridine-6,6'-**d**icarboxylic **a**cid) ligand was also prepared.

The new **MC3** derivatives bearing methoxy, methyl or fluoro groups in the *meta* or *para*-position of the bridging ligands were synthesized according to the route displayed in Scheme 1. The substituted bridging ligands ***m*-X-bpb** or ***p*-X-bpb** (X: MeO, Me or F) were readily accessible by Suzuki-Miyaura cross-coupling reactions followed by purification *via* column chromatography. The macrocycles were then obtained by self-assembly of the ruthenium precursor [Ru(bda)$(dmso)_2$] **35** and the respective bridging ligand in a chloroform/methanol mixture under a nitrogen atmosphere. Oligomeric side products as well as macrocycle fragments were removed by column chromatography over Al_2O_3 or SiO_2 to yield

the desired **MC3** derivatives in moderate to good yields for this type of reaction (21–55%). Detailed synthetic procedures and characterization data of ligands and macrocycles are reported in the Experimental Section (Chapter 7).

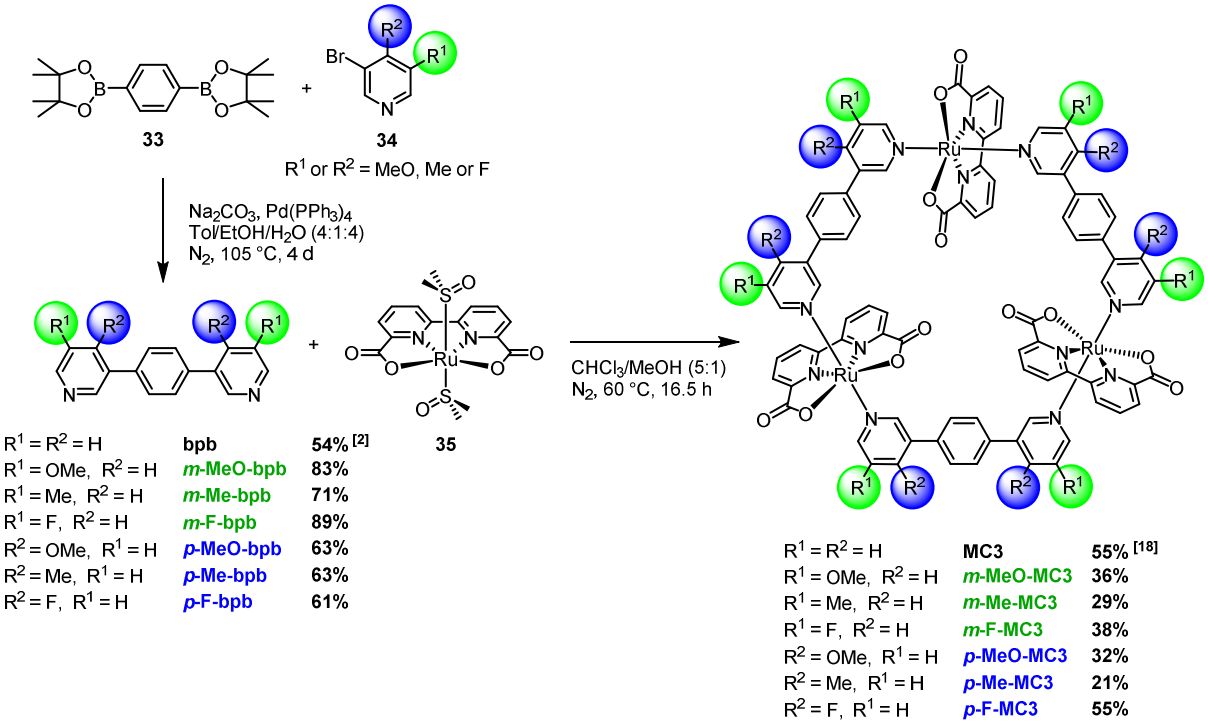

Scheme 1. Synthesis of **MC3** macrocycles functionalized at the bridging ligand in *meta*- or *para*-position.

The synthetically more challenging **MeO-bda-MC3** macrocycle containing methoxy groups in the equatorial bda ligand was prepared in a four-step synthesis as depicted in Scheme 2. Starting from 6,6'-dibromo-4,4'-dimethoxy-2,2'-bipyridine **36**, which was prepared according to literature procedures,[131] divinylbipyridin **38** was obtained by reaction with trivinylcyclotriboroxane **37** in a DME/water mixture under Suzuki coupling conditions.[132] The methoxy-bda ligand **39** was then prepared by subsequent oxidation with potassium dichromate in acidic media and purified by precipitation. Afterwards, the synthesis of the Ru precursor **40** was achieved by reaction of the ligand with $[RuCl_2(dmso)_4]$ according to the procedure described in the literature for **35**.[133] Finally, the macrocycle **MeO-bda-MC3** was obtained by self-assembly of **35** with the unsubstituted bpb ligand and purified by column chromatography over Al_2O_3. Detailed synthetic procedures and characterization data of all new compounds are provided in the Experimental Section (Chapter 7).

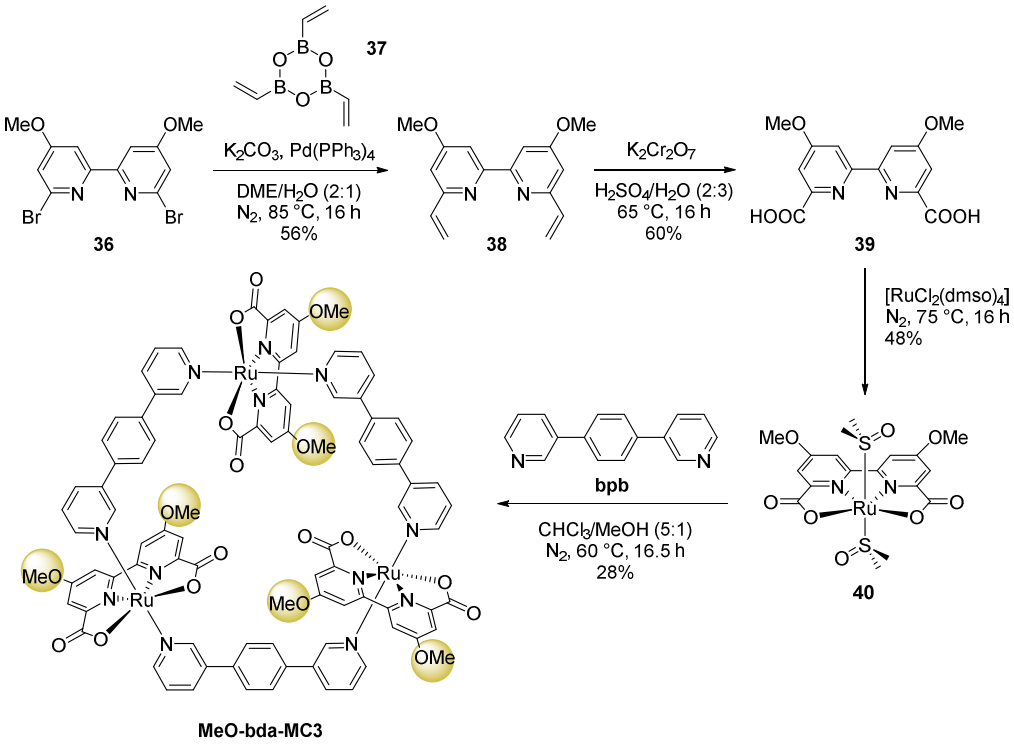

Scheme 2. Synthesis of **MeO-bda-MC3** macrocycle functionalized at the equatorial bda ligand.[2]

Single crystals of ***m*-F-MC3** and ***p*-F-MC3** suitable for X-ray analysis were obtained by slow evaporation of their respective solutions in not dried dichloromethane/methanol 5:1 mixture under argon atmosphere.[3] The crystal structures of ***m*-F-MC3** and ***p*-F-MC3** unequivocally confirmed the formation of macrocyclic trimeric Ru complexes (Figure 26). After refining the structure of ***m*-F-MC3** as a two-component twin, diffuse electron density originating from solvent molecules was located inside the macrocyclic cavity. Water molecules were assigned to the maxima of electron density, although the origin of these Q-peaks could not be elucidated unambiguously. However, the resulting hydrogen bonding network is in good agreement with the performed molecular dynamic simulations.[19] I can be assumed that the high hydrophilicity of the cavity constitutes the driving force for the accumulation of water molecules from not dried solvent in the macrocyclic cavity. The macrocyclic structure of the para-derivative ***p*-F-MC3** was refined as a two-component twin similarly to ***m*-F-MC3**. However, in this case residual electron density could not be modeled satisfactorily indicating the lack of ordered solvent molecules in the cavity and was therefore removed. Pleasingly, the remaining structure could be refined adequately.

---

[2] Synthesis and characterization of **MeO-bda-MC3** was performed by M. Sc. Dorothee Schindler, Universität Würzburg.

[3] Single-crystal X-ray structure analysis of ***m*-F-MC3** and ***p*-F-MC3** was performed by Dr. David Schmidt and Ana-Maria Krause, Universität Würzburg.

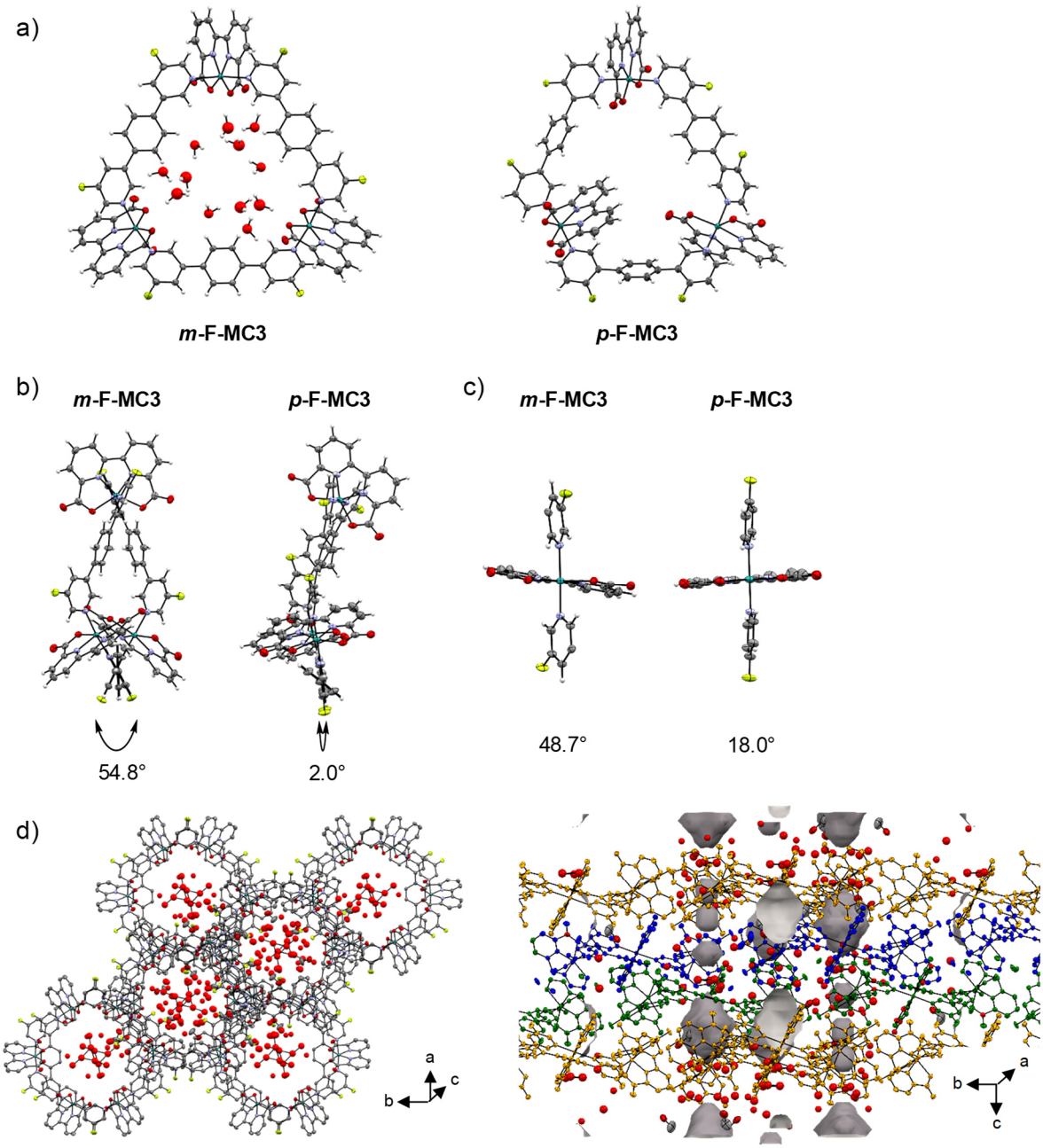

Figure 26. a) Crystal structures of ***m*-F-MC3** and ***p*-F-MC3** determined by single crystal X-ray diffraction (ORTEP diagram with thermal ellipsoids set at 50% probability; grey: carbon, white: hydrogen, red: oxygen, lila: nitrogen, turquoise: ruthenium, green-yellow: fluorine). The crystals were grown from a DCM/methanol solvent (not dried) mixture. b,c) Comparison of the X-ray crystal structures regarding the torsion angle between the terminal pyridyl rings within a single bridging ligand (b) and the torsion between two axial ligands coordinated to one Ru center (c). Only one Ru center with its coordinated pyridyl rings is shown for each macrocycle in c) for clarity. d) Crystal packing of ***m*-F-MC3**. Left: View along axis *c* with water and methanol molecules in the pores. Right: View along axis *a* showing three layers of macrocycles (depicted in yellow, green and blue) and voids interrupted by solvent molecules in the pores. a = 23.4927(5) Å, b = 23.4927(5) Å, c = 32.5166(7) Å, α = 90°, β = 90°, γ = 120°.

Macrocycle ***m*-F-MC3** crystallizes in the trigonal space group *R*-3 with a slipped stacked arrangement leading to the formation of one-dimensional pores (Figure 26d). The distance between Ru center and the axially coordinated pyridyl rings are 2.081(5) Å and 2.084(4) Å. These values are comparable to those of the previously reported acyclic mononuclear complex [Ru(bda)(pic)$_2$] (2.070(6) Å and 2.084(6) Å)[79] and a larger macrocycle **MC4** (2.066(5) Å and 2.078(7) Å)[19] that contains an additional phenyl ring in its bridging ligand. The distorted octahedrally coordinated Ru centers present an obtuse O-Ru-O angle of 122.8(2)°. Similarly to **MC4**, the axial pyridyl rings of ***m*-F-MC3** attached to one Ru center form a N_{ax}-Ru-N_{ax} angle of 172.5(2)° and are torsionally twisted by 48.7° (Figure 26c), thus leaving largely available Ru active sites for coordination of water molecules. In addition, Figure 26b shows the torsion of 54.8° between the terminal pyridyl rings within one single bridging ligand. The intramolecular distance between two Ru centers of 12.057(9) Å and, more importantly, the open coordination sites of all Ru centers point to the interior of the macrocyclic cavity that should be favorable for the water oxidation process by preorganization of water molecules in the cavity.

Macrocycle ***p*-F-MC3** crystallizes in the triclinic *P*-1 space group. The distances between the Ru centers and the axial pyridyl rings as well as the obtuse O-Ru-O and the N_{ax}-Ru-N_{ax} angles are all very similar to those of the *meta*-substituted macrocycle ***m*-F-MC3** (Table S1). The crystal structure of ***p*-F-MC3** features one Ru center whose open coordination site points to the exterior of the macrocyclic cavity. In addition, also in strong contrast to the structure of ***m*-F-MC3**, the terminal pyridyl rings within the individual bridging ligands coordinated to the inverted Ru(bda) moiety present only a slight torsion of 2.0° and 5.3° (Figure 26b). Moreover, the axial pyridyl rings attached to two of the Ru centers are torsionally twisted by only 29.0° and 18.0° as depicted in Figure 26c, thus suggesting a more restricted access of water molecules to the 7th coordination site of these Ru centers.

3.2.2 Redox and Optical Properties

After successful synthesis of the functionalized Ru macrocycles, their redox properties were characterized by cyclic voltammetry (CV) and differential pulse voltammetry (DPV). Due to the poor solubility of these **MC3** derivatives in pure water, the electrochemical studies were performed using 2,2,2-trifluoroethanol (TFE) as a non-coordinating co-solvent. The measurements were performed at pH 1 and pH 7 to resemble the conditions of the chemical and photocatalytic water oxidation experiments, respectively (see below). The redox properties observed in acidic and neutral media are summarized in Tables 1 and S2,

respectively, and the voltammograms are displayed in Figures S1–S15 (see Appendix – Chapter 8).

Table 1. Summary of redox properties of the macrocyclic **MC3** derivatives at pH 1.[a]

Macrocycle	*E vs.* NHE [V]			
	$Ru^{III}{}_3/Ru^{II}{}_3$	$Ru^{III}{}_2Ru^{IV}/Ru^{III}{}_3$	$Ru^{III}Ru^{IV}{}_2/Ru^{III}{}_2Ru^{IV}$	$Ru^{IV}{}_3/Ru^{III}Ru^{IV}{}_2$
MC3	+0.71	+0.94	+1.17	+1.36
***m*-MeO-MC3**	+0.73	--- [b]	+1.17	+1.35
***m*-F-MC3**	+0.82	--- [b]	+1.17	+1.40
***m*-Me-MC3**	+0.70	--- [b]	+1.17	+1.35
***p*-F-MC3**	+0.75	--- [b]	+1.17	+1.39
***p*-MeO-MC3**	+0.65	+0.94	+1.17	+1.36
***p*-Me-MC3**	+0.67	+0.94	+1.17	+1.35
MeO-bda-MC3	+0.60	+0.87	+1.14	+1.35

[a] CV and DPV in TFE/H_2O 1:1 (pH 1, triflic acid), c = 0.25 mM. [b] Not detectable due to low intensity and overlap with neighboring waves.

Under acidic conditions four reversible oxidation processes were detected which correspond to an initial three-electron $Ru^{III}{}_3/Ru^{II}{}_3$ oxidation followed by three subsequent one-electron oxidation events leading to the formation of a $Ru^{IV}{}_3$ state. The final oxidation to Ru^{V} could not be observed, presumably due to overlap with the water oxidation current. The differences in peak current intensity observed in CV and DPV for the single redox processes (Figures S1-S7) might be explained based on the number of transferred electrons and the kinetic hindrance resulting from proton coupling to the electron transfer processes. These made it challenging to assign the $Ru^{III}{}_2Ru^{IV}$/ $Ru^{III}Ru^{IV}{}_2$ oxidation potential for all macrocycles, albeit the electrochemical trend is clear. Contrary to the expectations, the introduction of substituents to the bridging ligand affected the $Ru^{III}{}_3/Ru^{II}{}_3$ redox potential but had a negligible impact on the higher oxidations. The methoxy groups on the bda ligand of **MeO-bda-MC3** had a more pronounced effect on the redox properties of the macrocycle, however, only up to the $Ru^{III}Ru^{IV}{}_2$/ $Ru^{III}{}_2Ru^{IV}$ oxidation.

Under neutral conditions (pH 7), three three-electron oxidation events were observed for the **MC3** derivatives (Figures S8-S15). These were assigned to the reversible electron redox couples $Ru^{III}{}_3/Ru^{II}{}_3$, $Ru^{IV}{}_3/Ru^{III}{}_3$ and $Ru^{V}{}_3/Ru^{IV}{}_3$ in accordance to the measured Pourbaix diagram (Figure S16). At this pH, the introduction of substituents again mainly affected the initial $Ru^{III}{}_3/Ru^{II}{}_3$ oxidation (Table S2). This is in agreement with previous reports by Llobet[11a, 102] and Sun[85] and co-workers. These authors independently stated that, although it is possible to affect the $Ru^{III/II}$ potential of monomeric Ru(bda) WOCs *via* the introduction of

substituents to the axial ligand, the lower participation of these ligands in the HOMO/LUMO at higher oxidation states of Ru leads to a limited effect on the $Ru^{IV/III}$ and $Ru^{V/IV}$ oxidations. Surprisingly, functionalization of the bda moiety, which was expected to have a more prominent effect on the redox properties of the macrocycle, led to similar results.

UV/vis absorption spectroscopy of the **MC3** macrocycles at the Ru^{II}_3 state revealed that the substituents at bridging ligand have negligible effect on the optical properties of the WOCs under acidic and neutral conditions (Figure 27). Under both conditions, the strong band at around 300 nm corresponds to the π-π* ligand-centered transitions whereas the broad bands between 350 nm and 550 nm can be assigned to metal-to-ligand charge transfer (MLCT) processes.[86, 100a] According to theoretical calculations,[19] the higher energy MLCT band at around 350 nm can be assigned to the transition from the Ru d-orbital to the π*-orbital of the axial ligand. The less energetic bands between 450 nm and 550 nm are characteristic for the transition from the Ru d-orbital to the π*-orbital of the bda ligand. As it can be seen in Figure 27, the absorption spectra of all macrocycles are very similar with only slight differences with regard to the position of the higher energetic MLCT band as expected after functionalization of the axial ligands. Additionally, spectroelectrochemistry was performed to analyze the absorption spectra of the oxidized macrocycles upon increasing the set potential from 500 mV to approximately 750 mV and then to 1000 mV (Figure S18). Here again, only modest shifts of the characteristic bands at 700 nm and 550 nm for the Ru^{III}_3 and Ru^{IV}_3 states, respectively, were observed. Detailed spectroelectrochemistry data of the **MC3** derivatives are presented in Figures S19–S22 (see Appendix – Chapter 8).

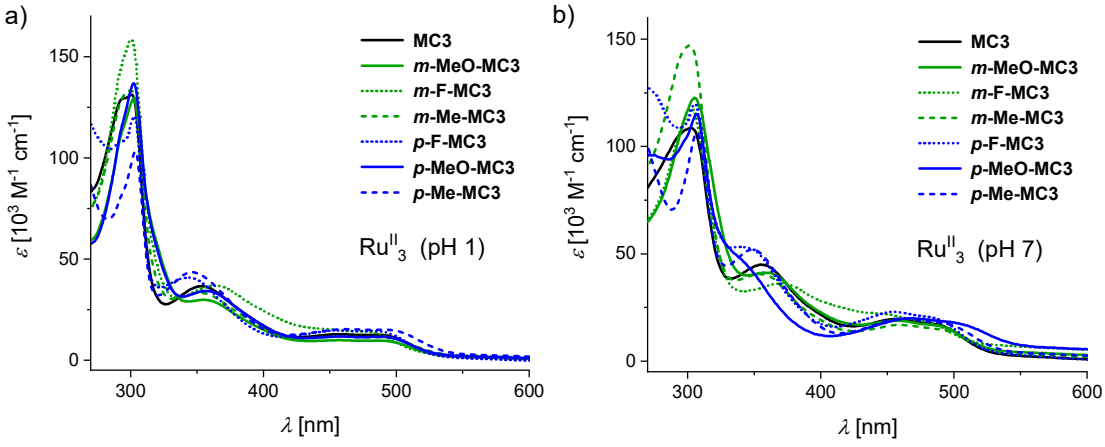

Figure 27. UV/Vis absorption spectra of the macrocyclic **MC3** derivatives at the Ru^{II}_3 state in MeCN/H_2O 1:1 at pH 1 (a) and pH 7 (b), *c* = 10 µM.

3.2.3 Characterization of Catalytic Intermediates by EPR and XAS

In order to further characterize the **MC3** macrocycles in their Ru^{III} and Ru^{IV} oxidation states electron paramagnetic resonance (EPR) and X-ray absorption spectroscopy (XAS) studies were carried out at Purdue University.[4] For this purpose, samples were prepared by stopped-flow freeze-quench techniques to enable tracking of the reactive intermediates.

Time-dependent EPR measurements upon oxidation of the EPR silent parent Ru^{II} complex **MC3** with an excess CAN (20 equiv per macrocycle) revealed the formation of a rhombic signal with g_{xx} = 2.29, g_{yy} = 2.16 and g_{zz} = 1.86, which is characteristic of a Ru^{III}(bda) S = ½ species (Figure 28a).[90, 97] After addition of the oxidant, the intensity of this signal increased until 30 s and then decreased at 5 min. Interestingly, this decay was accompanied by an evident color change of the sample from green to purple. It should be noted that, while d^5 Ru^{III} and d^3 Ru^{V} species can be detected by EPR due to the presence of unpaired electrons, both Ru^{II} as well as Ru^{IV} species are EPR silent. Therefore, in agreement with previous reports by Würthner and co-workers[18] the observed color change indicates the accumulation of Ru^{IV} over time. The fact that a strong Ru^{III} signal was still present in the purple sample taken at 5 min might be explained by the presence of some mixed-valenced $Ru^{III}_xRu^{IV}_{3-x}$ states. Further, *g*-tensors corresponding to a Ru^{V}(bda) intermediate[97] could not be observed at any point, presumably due to the very short-lived nature of this highly reactive species in solution. Similar results were obtained for the derivative ***p*-MeO-MC3** (Figure S23). For this reason, all further XAS studies were only performed on **MC3** due to its more straightforward synthesis and availability in larger quantity.

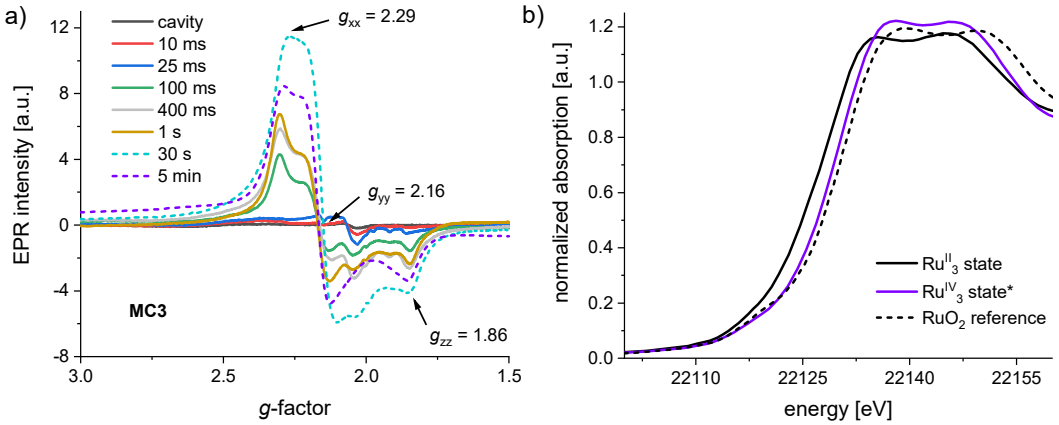

Figure 28. a) Time-dependent X-band EPR spectra (9.47 GHz) of **MC3** after addition of excess CAN. b) Ru K-edge XANES of **MC3** indicating the formation of a Ru^{IV} species after oxidation with CAN. EPR and XANES in MeCN/H_2O 1:1 (pH 1, nitric acid), *c*(**MC3**) = 1 mM. * Although minor Ru^{III} fraction could still be detected in EPR, sample contained mostly Ru^{IV}.

[4] EXAFS fits were performed by Prof. Dr. Yulia Pushkar, Purdue University.

For the characterization of Ru^{IV} species of **MC3** macrocycle and elucidation of the coordination environment of Ru at this oxidation state, X-ray absorption near-edge spectroscopy (XANES) and extended X-ray absorption fine structure (EXAFS) analysis were exploited. For this purpose, "purple samples" were prepared as detailed above by addition of CAN to a **MC3** solution with a mixing time of 5 min. Subsequently, these samples were freeze-quenched at 10 ms after addition of further CAN to reach a more complete conversion toward the Ru^{IV}_3 state. Accordingly, EPR showed that indeed this process resulted in significant reduction of the Ru^{III} content (Figure S24). In addition, as illustrated by the XANES plot in Figure 28b, an increase of Ru K-edge energy can be clearly observed in the oxidized sample which corroborates the presence of Ru^{IV} by comparison with the reference compound $Ru^{IV}O_2$.

Multiple XAS spectra of the macrocycle **MC3** in both its initial Ru^{II} and oxidized Ru^{IV} state were recorded without detectable changes in the absorption spectra during consecutive scans. EXAFS data were fitted using an available DFT structure of the Ru(bda) WOC [Ru(bda)$(isoq)_2$] as a model with comparable geometries and Ru coordination environment to the supra-molecular **MC3** catalyst. In agreement with a previous report by Copéret and Pushkar and co-workers,[97] a satisfactory fit could be obtained for the Ru^{II} form of **MC3** using six identical nitrogen atoms in the first and ten (6 + 4) carbon atoms in the second coordination shell of Ru (Table 1, Fit 3; Figures S26 and S27). Indeed, the calculated Ru-N distance of 2.10 Å is very similar to the average Ru-N/O distance of 2.07 Å of the crystal structure of ***m*-F-MC3**. More interestingly, analysis of the EXAFS data of the oxidized sample revealed that an additional backscatter hat to be added to the first coordination shell in order to achieve a good fit (Fit 6). This clearly correlates to formation of a seven-coordinated Ru(bda) moiety. Further, in this case splitting of the first coordination shell into each equivalent four nitrogen, two oxygen and an additional oxygen atom resulted in an excellent fit for these data (Fit 7, Figures S28 and S29). Accordingly, a Ru-O bond distance of 1.88 Å was determined. Notably, this distance is distinctly longer than that reported for a surface attached [$(isoq)_2Ru^{V}$(bda)=O] derivative (1.75 Å)[97] and also shorter than 2.07 Å and 1.96 Å corresponding to a DFT modeled [$(pic)_2Ru^{III}$(bda)-OH_2][90] and to the X-ray crystal structure of [$(pic)_2Ru^{IV}$(bda)-OH],[79] respectively. However, the obtained Ru-O distance perfectly agrees with a DFT calculation of **MC3** including 18 explicit water molecules in which a value of 1.89 Å was determined for the Ru^{IV}-OH bonds (Figure S56). Importantly, this bond distance is strongly dependent on the presence of the explicit water network in the macrocyclic cavity. It is noteworthy that in the absence of hydrogen bonding the calculated Ru^{IV}-OH distance elongates to 1.95 Å.

Table 2. EXAFS fits of **MC3** in its initial Ru^{II} and oxidized Ru^{IV} form.

	Fit	shell, N [a]	R [Å] [b]	σ^2 [10^{-3} Å^2] [c]	R-factor	reduced X^2
MC3 Ru^{II} state	1	Ru-N, 6	2.10	5.7	0.38	3597
3.8-13.9 k-space	2	Ru-N, 6	2.11	5.6	0.07	908
1.3-3.0 R-space		Ru-C, 10	3.02	10.2		
	3	Ru-N, 6	2.10	5.6	0.05	699
		Ru-C, 6	2.96	3.5*		
		Ru-C, 4	3.11	3.5*		
MC3 Ru^{IV} state	4	Ru-N, 6	2.08	1.7	0.20	3217
3.6-14.2 k-space	5	Ru-N, 6	2.08	1.8	0.05	1353
1.4-3.2 R-space		Ru-C, 10	3.02	6.1		
	6	Ru-N, 7	2.09	2.6	0.04	700
		Ru-C, 8	3.03	3.3		
		Ru-C, 2	3.25	3.3		
	7	Ru-O, 1	1.88	2.7*	0.01	448
		Ru-O, 2	2.04	1.0		
		Ru-N, 4	2.14	2.7*		
		Ru-C, 8	3.05	3.7*		
		Ru-C, 2	3.26	3.7*		

[a] N: coordination number. [b] R: distance between absorber and backscatter atoms. [c] σ^2: Debye-Waller parameter (* indicates that the same parameter was used for multiple shells). Amplitude reduction factor S_0^2 was set to 1.

3.2.4 Catalytic Water Oxidation with Chemical Oxidant in Acidic Aqueous Solutions

Catalytic activities of the functionalized **MC3** macrocycles toward water oxidation were first explored by using ceric ammonium nitrate (CAN) as a strong one-electron oxidant. Hereby, a solution of the respective macrocycle was injected into a sealed Schlenk vial containing a fresh solution of CAN in acetonitrile (MeCN)/water mixtures (pH 1, triflic acid). As described in previous reports by Würthner and co-workers,[18-20] acetonitrile was used as an organic co-solvent due to its known robustness under oxidative conditions.[87a, 134] The amount of evolved oxygen was determined by the increase of pressure in the vials after catalyst injection as detected by attached pressure sensors. Further, gas composition of the headspace in each reaction vial at the end of catalysis was evaluated by gas chromatography (GC).

Initially, chemical water oxidation experiments with the **MC3** derivatives as catalysts were performed in variable amounts of acetonitrile (Table S3). This organic solvent, though

necessary to achieve solubility of the macrocycles in aqueous mixtures, is known for its ability to compete with water for the binding sites of Ru(bda) WOCs and thus reduce their catalytic performance.[87a] Therefore, prior to conducting detailed concentration-dependent experiments the optimal solvent composition for each **MC3** macrocycle was determined. Interestingly, while the highest catalytic activity of the unsubstituted **MC3** compound is reached in aqueous mixtures containing 60% of MeCN,[18] the functionalized macrocycles showed their best performance at 50%. Accordingly, all further experiments were carried out in MeCN/H_2O 1:1 solvent mixture.

Water oxidation at varying WOC concentrations was performed for accurate determination of TOF and TON values for each of the Ru macrocycles, including the parent compound **MC3** as a reference. As exemplarily depicted in Figure 29a for ***m*-MeO-MC3** (see Figures S30–S37 for other compounds), the amount of evolved oxygen is clearly dependent on the concentration of the catalyst. Further, a linear relationship between the catalyst amount and the initial rates of catalysis was observed (Figure 29b). The initial rates were determined in the first two seconds after injection of the WOC and the observed linear relationship complies with the first order kinetics of the previously proposed WNA mechanism for the unsubstituted **MC3** macrocycle.[18] The calculated linear regressions in Figure 29b represent the averaged TOF value of the respective **MC3** derivative. Additionally, a TON was calculated for each concentration and the highest TON is reported in Table 3.

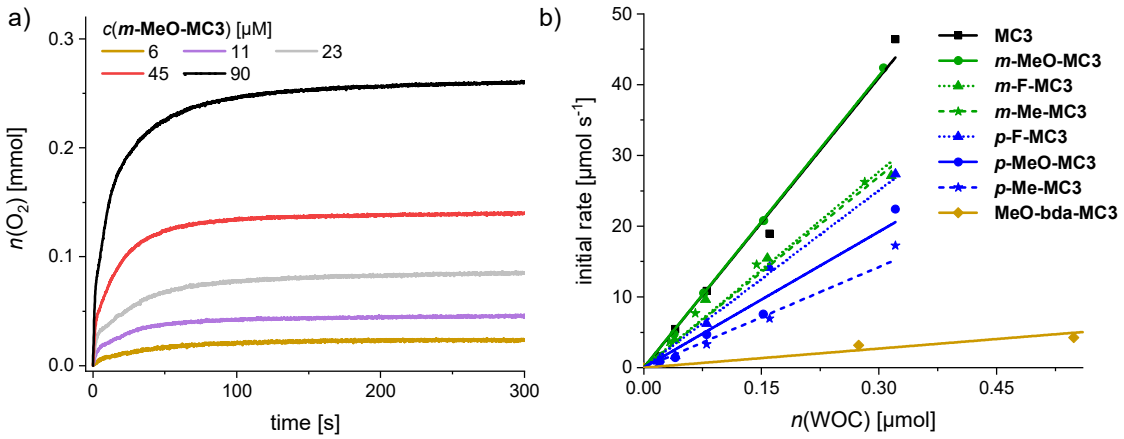

Figure 29. a) Oxygen evolution curves of ***m*-MeO-MC3** at variable concentrations in MeCN/H_2O 1:1 (pH 1, triflic acid), *c*(CAN) = 0.6 M. b) Concentration-dependent initial rates of all macrocycles including linear regression for determination of averaged TOF.

Table 3. Catalytic activity of the macrocyclic **MC3** derivatives in chemical water oxidation.[a]

Macrocycle	TOF [s^{-1}]	TON
MC3	136 ± 2	5300 ± 800
***m*-MeO-MC3**	138 ± 1	1300 ± 100
***m*-F-MC3**	92 ± 6	4700 ± 800
***m*-Me-MC3**	90 ± 4	3700 ± 500
***p*-F-MC3**	84 ± 4	2500 ± 400
***p*-MeO-MC3**	64 ± 5	2200 ± 400
***p*-Me-MC3**	47 ± 6	2300 ± 450
MeO-bda-MC3	10 ± 1	1000 ± 150

[a] Experiments were performed in MeCN/H_2O 1:1 (pH 1, triflic acid); *c*(CAN) = 0.6 M, *c*(WOC) = 5-322 µM.

The data in Table 3 revealed that the introduction of substituents in either the bridging or equatorial bda ligand did not result in an improvement of the catalytic activities of the functionalized macrocycles in chemical water oxidation compared to the unsubstituted **MC3** WOC (TOF = 136 s^{-1}, TON = 5300). This is in line with the observed redox properties of the macrocycles in acidic medium (see Table 1). However, there are some distinct differences with regard to the catalytic performance of the **MC3** derivatives that can not be explained based on the redox properties of the catalysts. For instance, independent of the introduced substituents the *meta*-substituted macrocycles reached in all cases higher TOF values than their *para*-substituted counterparts. This regioisomer effect on catalytic activity is more pronounced for the methoxy and methyl-substituted macrocycles as the TOF values of the *para*-derivatives are halved compared to those of the respective *meta*-**MC3** macrocycles. Further, functionalization of the bda ligand with methoxy groups led to a decrease in catalytic efficiency of more than one order of magnitude compared to parent compound **MC3** (see Table 3). Control experiments have shown that Ru precursors $RuCl_2(dmso)_4$ and $Ru(bda)(dmso)_2$ do not exhibit any significant catalytic activities for water oxidation under identical experimental conditions (Figure S55).

The reduction in TON of the **MC3** derivatives might be attributed to the diminished stability of the functionalized ligands under strong oxidative conditions. As it was demonstrated by CV and DPV (Figure S17), the modified bridging ligands indeed undergo an irreversible oxidation whereas the unsubstituted **bpb** ligand remains intact within the same electrochemical window. The lowest TON (reflects the stability of the catalyst) values obtained for the methoxy-functionalized macrocycles compared to the methyl and fluoro **MC3** derivatives can be attributed to a higher lability of the methoxy bearing ligands in acidic media. However, there

is no apparent correlation between the TOFs and TONs of the functionalized macrocycles as ***m*-MeO-MC3** with the second lowest TON of 1300 reached the highest TOF value in the series with 138 s^{-1}. GC analysis of each reaction headspace confirmed that oxygen was the only gaseous product formed during catalysis (Figures S38–S45). Thus, it can be assumed that catalyst deactivation involves to some extent oxidative decomposition of the ligands without the release of CO or CO_2 in addition to the disassembly of the macrocycles by loss of the axial ligands, which is usual deactivation pathway for Ru(bda) WOCs[14b] and the previously reported Ru macrocycles.[18-20]

3.2.5 Photocatalytic Water Oxidation under Neutral Conditions

A sustainable catalyst for application in artificial photosynthesis water splitting devices should perform water oxidation efficiently not only under chemical conditions but also under solar light exposure. Therefore, the catalytic reactivity of the **MC3** macrocycles was further investigated in photocatalytic water oxidation using a three-component system based on ruthenium tris(bipyridine) as a photosensitizer (PS), sodium persulfate as sacrificial electron acceptor and the **MC3** derivatives as WOC (a general scheme is shown in Figure 30). In these experiments, the mild oxidant $[Ru(bpy)_3]^{3+}$ is photogenerated *in situ* by oxidation of the excited PS* in ^{3}MLCT state by the sacrificial electron acceptor.[15, 135] Upon one electron reduction, the persulfate ion splits into a SO_4^{2-} anion and a $SO_4^{\bullet -}$ radical. The latter is able to oxidize a second PS molecule or even the WOC.[72] Subsequently, the PS is regenerated through one-electron oxidation of the WOC by PS^+.[72] This process is repeated until the catalyst reaches the Ru^V oxidation state which finally oxidizes water to molecular oxygen. Note the higher complexity of the present system for which due to the presence of three Ru centers com- or disproportionations may play a role.

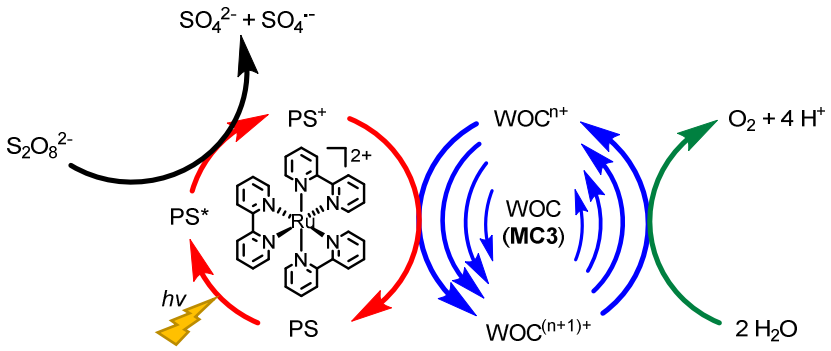

Figure 30. Illustration of the catalytic cycle of photocatalytic water oxidation using $Na_2S_2O_8$ as sacrificial electron acceptor, $[Ru(bpy)_3]^{2+}$ as PS and **MC3** derivatives as WOC.

Photocatalytic water oxidation was performed in phosphate buffer at pH 7, using again acetonitrile as an oxidatively stable co-solvent to circumvent the poor water solubility of the macrocycles. Hereby, a 1:1 ratio of MeCN/H_2O was used as for chemical water oxidation. Samples were irradiated using a xenon lamp carefully calibrated to an irradiation power of 100 mW cm^{-2} (Figure S46) and the generated oxygen was detected with a Clark electrode set-up. The catalytic activities of the **MC3** derivatives were studied under identical conditions to enable a reliable comparison of the results. Accordingly, in all experiments a large excess of PS (up to $2.5x10^3$ equiv) and $Na_2S_2O_8$ ($6.0x10^5$ equiv) was used. Both components were dissolved in the dark and mixed with the respective **MC3** macrocycle directly in the experiment chamber, which was kept in the dark at 20 °C for 50 s prior to irradiation. As for chemical water oxidation, the amount of evolved oxygen was measured at variable WOC concentrations. Figure 31a shows the oxygen evolution curves of ***m*-MeO-MC3** as a representative example (see Figures S47-S54 for other catalysts). Note that after reaching a plateau of maximal O_2 concentration, some of the dissolved oxygen is released into the gas phase leading to a reduction in the amount of gas detected by the Clark electrode. As in chemical water oxidation, both the amount of oxygen and the initial rates of oxygen generation in photocatalytic oxidation are dependent on the concentration of the WOC. The initial rates were determined from the linear part of the curves at the beginning of catalysis between 55–70 s. An averaged TOF value for each macrocycle was then obtained from a linear regression in the plot of the initial rates *vs*. the amount of catalyst (Figure 31b). The TON was calculated from the maximum amount of oxygen produced by each WOC during the experiments. As before, the reported TON is the highest value obtained for each macrocycle (Table 4).

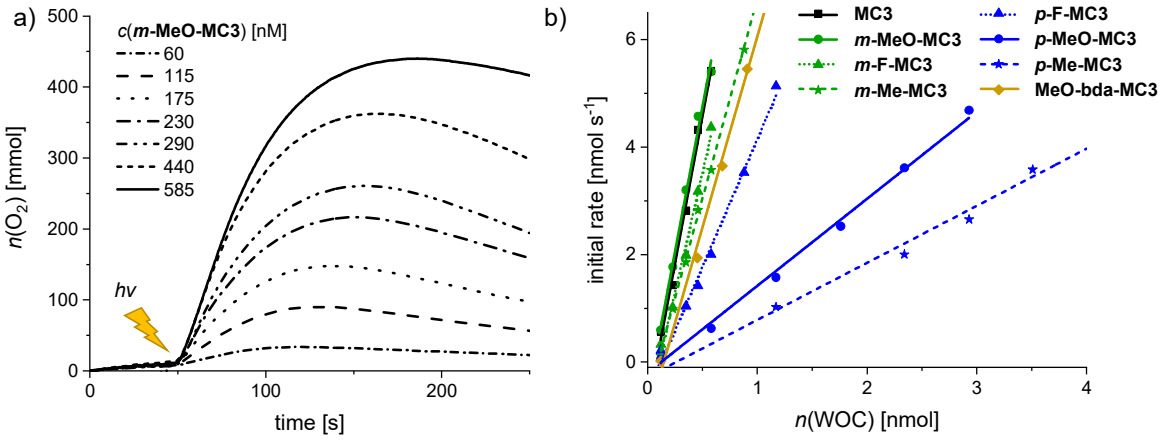

Figure 31. a) Concentration-dependent oxygen evolution curves of ***m*-MeO-MC3** in MeCN/H_2O 1:1 (pH 7, phosphate buffer), c(PS) = 1.5 mM, c($Na_2S_2O_8$) = 37 mM. The lighting symbol indicates the start of sample irradiation at t = 50 s. b) Initial rates of all macrocycles with linear regression for the determination of averaged TOF.

Table 4. Catalytic activity of the macrocyclic **MC3** derivatives in photochemical water oxidation.[a]

Macrocycle	TOF [s^{-1}]	TON
MC3 [b]	10.9 ± 0.5	430 ± 20
***m*-MeO-MC3**	10.8 ± 0.6	480 ± 20
***m*-F-MC3**	9.1 ± 0.7	400 ± 10
***m*-Me-MC3**	7.8 ± 0.3	380 ± 20
***p*-F-MC3**	4.8 ± 0.3	260 ± 20
***p*-MeO-MC3**	2.0 ± 0.1	170 ± 20
***p*-Me-MC3**	1.7 ± 0.2	120 ± 10
MeO-bda-MC3	7.8 ± 0.1	120 ± 20

[a] Photochemical water oxidation in MeCN:H_2O 1:1 (pH 7, phosphate buffer), *c*(PS) = 1.5 mM, *c*(Na2S2O8) = 37 mM, *c*(WOC) = 60-600 nM. [b] In a previous publication (ref. [18]) different catalytic values were reported for **MC3** (TOF > 13.1 s^{-1}, TON > 1255). This discrepancy might be attributed to contamination of the Clark electrode or not properly accounted intensity fluctuations of the light source in the previous work.

Under photocatalytic conditions a similar trend was observed for the catalytic activities of the functionalized **MC3** macrocycles as for chemical water oxidation, with the exception that **MeO-bda-MC3** exhibits here a comparatively high TOF of about 8 s^{-1} while in chemical catalysis this WOC exhibited the lowest activity in the series. Otherwise, independent of the nature of the substituents at the bridging ligand, the meta-substituted derivatives showed similar TOFs as the parent **MC3** macrocycle (TOF = 11 s^{-1}) and also reached in all cases higher values than the respective *para*-**MC3** WOCs (Table 4). It is noteworthy that the difference in TOF comprises nearly one order of magnitude in the most extreme case of the methoxy **MC3** derivatives (TOF $_{m\text{-MeO-MC3}}$ = 11 s^{-1}, TOF $_{p\text{-MeO-MC3}}$ = 2 s^{-1}). It should be noted that the reported photocatalytic TOFs are distinctly lower than those measured under chemical conditions. This can be attributed to the limited stability of the PS[136] and to the general complexity inherent to the applied three-component system as it has been extensively discussed in the literature.[82, 137] However, it should be emphasized that all functionalized macrocycles exhibit higher photocatalytic activity in water oxidation than most of the so far reported homogeneous Ru catalysts, including Ru(bda) WOCs that do not reach TOFs above 1 s^{-1}.[17] Control experiments with Ru precursors revealed that the measured catalytic activities are originated from trinuclear Ru(bda) catalysts (Figure S55). Under photocatalytic conditions the *meta*-substituted macrocycles exhibit similar TON values as the parent compound **MC3** (TON ≥ 380), whereas the *para*-derivatives show significantly lower TONs compared to the reference and their *meta* congeners as well. The results clearly indicate that the catalytic activities in terms of TOFs could be influenced by the stabilities of the functionalized macrocycles under

photocatalytic conditions. However, MeO-bda-MC3 with the lowest TON of the series (120) exhibits a rather high catalytic activity reaching a TOF of 7.8 s^{-1}. In both chemical and photocatalytic water oxidation experiments, **MeO-bda-MC3** was least stable which is in agreement with a previous report by Liu and co-workers where a drastic decrease in TON was also observed by functionalization of the bda ligand of Ru WOCs at the same position.[104]

3.3 Discussion

The performed detailed studies on chemical and photocatalytic water oxidation with a series of Ru(bda) macrocycles revealed that the catalytic activities are strongly influenced by the substituents at axial or equatorial ligands. However, the introduction of methoxy, methyl or fluoro substituents did not achieve the expected modification of the redox properties of the macrocycles neither at pH 1 nor pH 7 (see Tables 1 and S2). Moreover, a linear relationship between the catalyst amount and the initial rates of catalysis was observed for all **MC3** macrocycles in both chemical and photocatalytic water oxidation which complies with the first order kinetics of the previously proposed WNA mechanism (Figure 32) for the unsubstituted **MC3** macrocycle, facilitated by network of hydrogen-bonded water molecules in the cavity.[18-19] Thus, the observed trends in catalytic performance revealing a higher catalytic activity of all *meta*-substituted macrocycles compared to their *para*-substituted counterparts can neither be ascribed to a modification of the electronic properties of the macrocycles nor to a change in operating mechanism of water oxidation. Based on these results, conformational changes imparted by the ligand substituents were considered as the probable reason for diverse catalytic activities of the Ru macrocycles. Therefore, theoretical calculations were performed to substantiate this notion that are discussed in the following.[5]

[5] Molecular dynamics simulations and DFT calculations were performed by Dr. Joachim O. Lindner, Universität Würzburg.

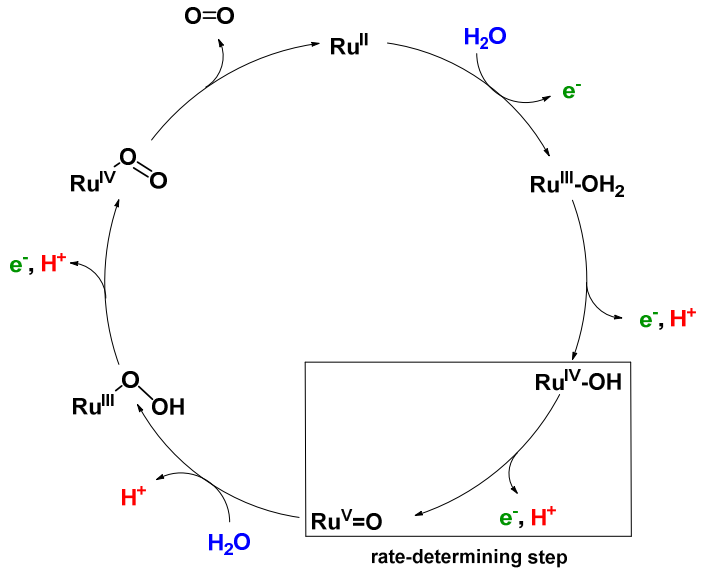

Figure 32. Simplified proposal for WNA mechanism of water oxidation for **MC3** macrocycle.[18] Presumably, after liberation of O_2 the Ru^{II} species is instantaneously oxidized by neighboring Ru^{IV} centers by comproportionation.

3.3.1 Characterization of the Water Network inside the Cavity

For the unsubstituted **MC3**, molecular dynamics simulations revealed that carboxy groups of the bda ligands can act as proton relays through a network of hydrogen-bonded water molecules. This facilitates proton-coupled electron transfer (PCET)[63] processes during catalysis, such as the rate-determining oxidation of the Ru^{IV} species of the WOC (Figure 32).[19] Interestingly, the crystal structure of ***m*-F-MC3** provided the first experimental indication for a hydrogen-bonded water network in the inner cavity of trinuclear macrocycles (see Figure 26a). It can be assumed that this is only possible when the hydrophilic carboxy groups of all Ru(bda) moieties are rotated into the inside of the cavity, since no highly organized water network was found in the crystal structure of ***p*-F-MC3** where most of the carboxy groups of Ru(bda) are directed outwards. Since the positions of hydrogen atoms are not available from the crystal structure, in order to investigate the intermolecular interactions in the water network, the ***m*-F-MC3** structure obtained in the solid state was refined on the DFT level including additional implicit solvation (see Chapter 7 for details). For this purpose, nine water molecules with shortest distance to Ru were selected and an additional water molecule was placed in the center of the macrocycle where some diffuse electron density could not be assigned unambiguously in the XRD data. The resulting locally optimized structure depicted in Figure 33a shows that the three catalytic sites are connected by a network of nicely ordered water molecules with H-bonding distances below 1.9 Å. This clearly

indicates that the water molecules, as located in the crystal structure, are appropriately arranged to form strong networks.

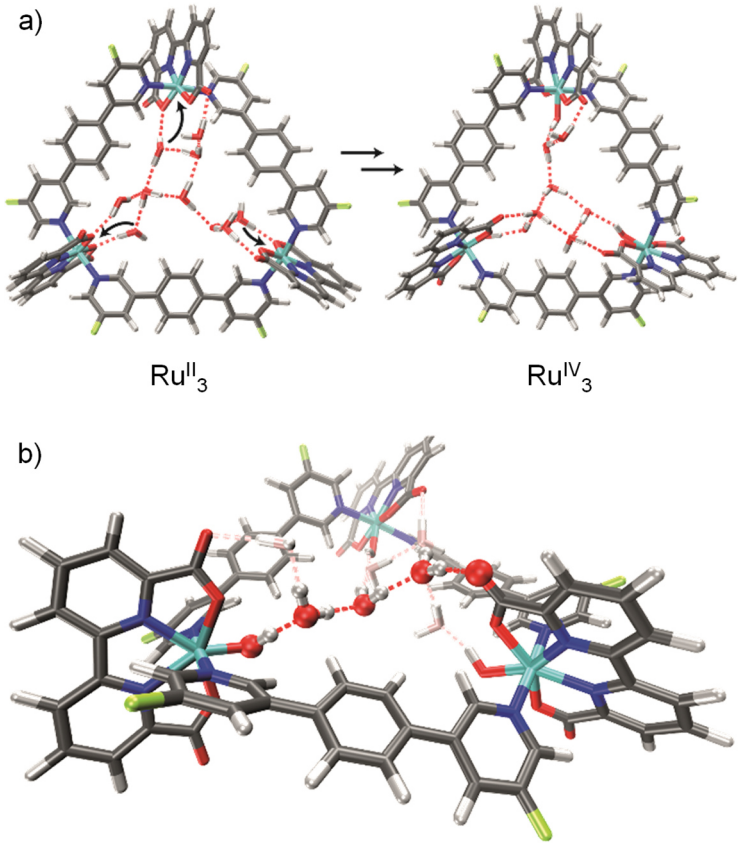

Figure 33. a) DFT-refined structure of the water network inside the cavity of ***m*-F-MC3** in the Ru^{II}_3 and Ru^{IV}_3 oxidation states derived from the crystal structure depicted in Figure 26a. The coordination of water molecules needed to form higher oxidation states is indicated by black arrows. b) Zoomed perspective view on the three water molecules connecting two catalytic centers optimized in the Ru^{IV}_3 state. The other water molecules are grayed out for clarity.

This also holds true upon oxidation of the macrocycle to the Ru^{IV}_3 oxidation state. A structure of ***m*-F-MC3** in this oxidation state was obtained by coordination of one water molecule to each Ru center accompanied by removal of three protons and re-optimization. The resulting $[Ru^{IV}\text{-}OH]_3$ species features a hydrogen-bonded water network that connects the hydroxo protons of each Ru^{IV} center with the carboxy groups of the remaining Ru(bda) moieties by only three water molecules. Stabilization of oxidized WOC intermediates by hydrogen bonds was also observed for other Ru catalysts such as Ru^{IV}=O(damp)(bpy) (damp: bis((dimethylamino)-methyl)pyridine)[138] and recently for a Cu(II)-based WOC in photocatalytic water oxidation.[139] As illustrated in Figure 33b, preorganization of water molecules in the cavity of the macrocyclic WOCs presumably allows for efficient proton transfer following a Grotthuss-type mechanism.[140] Therefore, the performed studies suggest that proton abstraction in the rate-

determining oxidation of Ru^{IV} to Ru^{V} (Figure 32) could be facilitated if the macrocycles adopt in solution a conformation close to that found in the crystal structure of ***m*-F-MC3** which promotes the formation of a highly organized water network. Remarkably, in nature the function of several enzymes as well as of the oxygen-evolving complex Mn_4CaO_5 of photosystem II also relies on such preorganized water networks to facilitate PCET processes and accelerate the rates of catalysis.[37b, 141]

3.3.2 Conformational Effects of Axial Ligand Substituents

Several different conformations of the newly designed Ru macrocycles are likely to be present in solution as a result of twisting of the bridging ligands or by rotation of the Ru(bda) units. Representative examples of symmetric conformers bearing either “flat” or “twisted” bridging ligands and Ru(bda) moieties with the open coordination site pointing to the in- or outside of the macrocyclic cavity are depicted in Figure 34. Structures of mixed character between these extremes are omitted for simplicity. To gain insight into these conformations of the macrocycles in solution, which might provide some rational for the reserved superior catalytic activities of *meta*-substituted derivatives compared to *para*-macrocycles, theoretical studies were performed on the basis of semi-empirical calculations (see Chapter 7 for details). For this purpose, the methylated **MC3** derivatives ***m*-Me-MC3** and ***p*-Me-MC3** at the Ru^{II}_3 oxidation state were chosen as model compounds due to their particularly distinct catalytic activities in higher oxidation states (see Tables 3 and 4). It can be assumed that the steric influence of the substituents on the macrocyclic structure should be independent of the oxidation state of Ru. Calculations on both methylated **MC3** macrocycles showed that structures bearing three Ru(bda) moieties with the open coordination sites rotated to the outside of the cavity (cf. structures **C** and **D** in Figure 34) are very unlikely (Table S4). More interestingly, the most stable conformation of ***m*-Me-MC3** and reference compound **MC3** was found to be the structure **B** with calculated energy of -22.5 kJ mol^{-1} relative to **A**. Notably, this is also the solid-state conformation of ***m*-F-MC3**. In the case of ***p*-Me-MC3**, the structures **A** and **B** are nearly isoenergetic. Metadynamics simulations in the conformational space of the bridging ligands (see Figure S57) revealed that functionalization at the *para*-position indeed induces a more drastic twisting of these ligands with a concomitant raise of macrocyclic ring strain in **B**. As a result of the destabilization of **B**, **A** and **B** conformers of the *para*-macrocycles are likely to be present in similar concentrations in solution. In contrast, the *meta*-derivatives most probably exist in the **B** conformation as this conformation is energetically favored compared to **A** (Table S4). The significance of this conformational effect on catalytic activity will be discussed in the following.

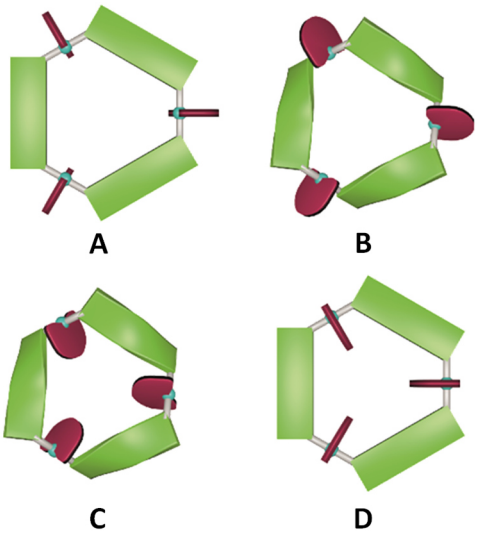

Figure 34. Schematic illustration of conformational equilibrium of **MC3** derivatives in solution displaying four possible conformations **A**-**D**; turquoise: ruthenium, red: bda ligands, green: bridging ligands.

To assess the rotation of the Ru(bda) units around the N_{ax}-Ru-N_{ax} bond in solution additional metadynamics simulations were conducted. The resulting free energy profiles (see Figure 35a and S58) show that in structure **A** rotation of one of the bda ligands to the inside of the cavity requires 11 kJ mol^{-1}, while 22 kJ mol^{-1} are needed in the case of **B**. Thus, it can be concluded that conformations similar to the solid state structure of ***p*-F-MC3** with one open coordination site of Ru pointing to the exterior of the cavity could indeed be found in solutions of the *para*-substituted macrocycles as these exist in an equilibrium between the **A** and **B** structures. In the case of *meta*-WOCs, such a rotation of the Ru(bda) units is rather unlikely since these macrocycles mostly adapt the **B** conformation in solution which does not allow for such a rotation. However, it should be mentioned that conformers of the *para*-macrocycles bearing rotated Ru(bda) moieties which would do not support an inner hydrogen-bonded water network represent most probably only a minor fraction in solution. The performed studies indicate that such structures exist in equilibrium with more abundant structures containing Ru(bda) units with the open coordination sites oriented to the inside of the macrocyclic cavity.

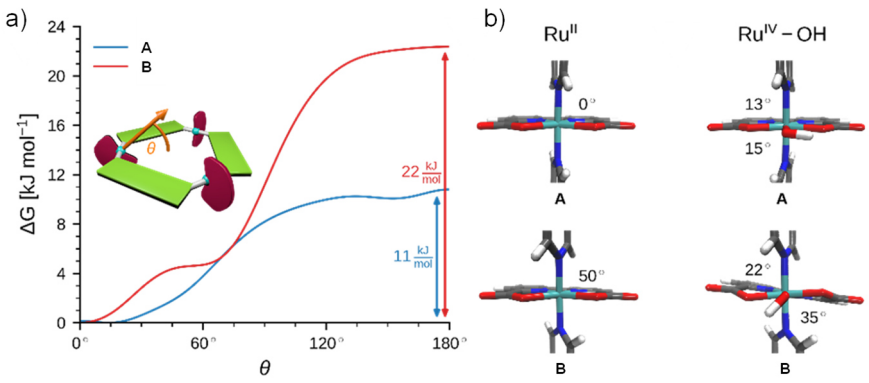

Figure 35. a) Free energy profiles obtained from metadynamics studies of ***p*-Me-MC3** using the angle *θ* for the rotation of the Ru(bda) unit as collective variable. b) Study of C-N_{ax}-N_{ax}-C (left) and C-N_{ax}-Ru-O (right) torsion angles between the axial ligands as well as axial and hydroxo ligand in DFT optimized structures of **MC3** in the Ru^{II}_3 or Ru^{IV}_3 oxidation states, respectively.

DFT optimizations (see Chapter 7 for details) of both **A** and **B** conformations of **MC3** were performed to get deeper insight into the direct ligand environment around Ru, which presumably defines the accessibility of the catalytic centers for water molecules. As depicted in Figure 35b, **A** exhibits a C-N_{ax}-N_{ax}-C torsion of 0°, whereas an opening angle of 50° is observed in **B**. Further, in the Ru^{IV}_3 oxidation state where a hydroxo ligand is attached to Ru on the equatorial plane as confirmed by XAS (see above), the C-N_{ax}-Ru-O torsion angles are distinctly larger in **B** than in **A** which is reflected in a stabilization energy of 35 kJ mol^{-1} of **B** over **A** (Table S5). Therefore, it can be concluded that the conformation **B** of the Ru macrocycles plays a crucial role in their catalytic efficiency since the critical access of water molecules to the 7th coordination site of Ru(bda) WOCs in only possible in this conformation. Accordingly, the *meta*-substituted **MC3** macrocycles which are predominantly present in **B**-type structures in solution show higher catalytic reactivities than the *para*-derivatives. For the latter, the observed lower catalytic activities in both chemical and photocatalytic water oxidation might be due to the presence of an equilibrium between unfavorable and favorable conformations as predicted by calculations. In unfavorable conformations, the access of water molecules to the 7th coordination site of the Ru centers of the *para*-macrocycles is restricted, thus resulting in a reduced efficiency for water oxidation catalysis by a WNA mechanism.

3.3 Conclusions

A series of Ru(bda) macrocycles bearing different substituents at both axial and equatorial ligands were synthesized and their molecular properties were studied. More importantly, I have explored here the catalytic activities of the newly synthesized series of Ru macrocycles (**MC3** derivatives) in chemical and photocatalytic water oxidation to gain insight into the electronic and steric impact of the substituents on their catalytic efficiencies. For the first time, crystallographic evidence for the **MC3** macrocyclic structure was obtained. Interestingly, one of the crystal structures provided the first experimental indication for a hydrogen-bonded water network in the macrocyclic cavity that was considered to be essential for the high catalytic efficiency for a WNA mechanism according to theoretical calculations reported previously.[18-19] This strengthens the hypothesis that the high catalytic activity of the **MC3** macrocycles is closely related to the presence of such a network of preorganized water molecules which induce efficient cooperative proton abstraction processes during water oxidation. Moreover, Ru species at different oxidation states were successfully characterized by EPR and XAS techniques. The latter method further confirmed the importance of the water network in the macrocyclic cavity as the Ru^{IV}-OH bond lengths could only be satisfactory fitted under this consideration.

Contrary to the expectations, neither the modification of the axial nor the bda ligands resulted in the desired tuning of the oxidation potentials of the Ru macrocycles to modulate the formation of catalytically active Ru^{V} oxidation state. However, the performed studies clearly revealed that the catalytic performance of the **MC3** macrocycles is dependent on the position at which the substituents are introduced. Thus, the macrocyclic nature of the catalysts provided the unique opportunity to perform to date unprecedented studies on the role of steric effects on the catalytic activity of regioisomeric *meta* and *para*-substituted Ru(bda) WOCs. Accordingly, the presented detailed investigation by X-ray crystal structure analysis as well as metadynamics simulations has convincingly shown that functionalization of the macrocycles at the *para*-position induces conformational changes with partial rotation of one of the Ru(bda) active centers to the outside of the macrocyclic cavity. The reduced catalytic performance of these *para*-WOCs in both chemical and photochemical water oxidation cannot be ascribed to this rotation as it could be demonstrated that it only plays a minor role in solution. Instead, it is proposed that the more restricted access of water molecules to the 7^{th} coordination site of Ru of these *para*-macrocycles resulting from parallel orientation of the axial pyridyl ligands leads to their diminished water oxidation efficiency, presumably, due to loss of contact with the inner network of preorganized water molecules. In contrast, in *meta*-substituted macrocycles and parent **MC3** WOC the twisted orientation of the axial ligands results in

available Ru centers for coordination of water molecules which reflects in their significantly higher catalytic performance both in chemical and photocatalytic water oxidation. Therefore, rigidification of supramolecular catalysts by a strategic modification of the ligands that kept the Ru active centers permanently accessible and in contact with each other *via* a hydrogen-bonded water network would lead to high performance water oxidation catalysts.

Chapter 4

Effects of Photosensitizers and Reaction Media on Light-Driven Water Oxidation with Trinuclear Ru Macrocycles

4.1 Introduction

Catalytic water oxidation by molecular water oxidation catalysts (WOCs) can be accomplished by chemical, electrochemical and photochemical methods.[16] The latter method is of pivotal importance for the application of WOCs in solar fuels devices. As in natural photosynthesis, a key process in light-driven water oxidation is the activation of the WOC by oxidants generated by irradiation of a photosensitizer. Thus, the photocatalytic activities of homogeneous WOCs are generally studied by means of a three-component system comprising a photosensitizer (PS), a sacrificial electron acceptor and the catalyst. As shown in Figure 36, after activation of the PS to the excited state PS* by light (eq. 1), the oxidant PS^+ is produced by one-electron transfer from PS* to the electron acceptor (eq. 2) and PS is then regenerated by oxidation of the WOC (eq. 5). Upon transfer of four electrons in a photocatalytic cycle, water is oxidized to molecular oxygen and four protons and four electrons are released (eq. 6). Although several PS and electron acceptor systems have been applied in photocatalytic water oxidation,[137b] ruthenium tris(bipyridine) as PS and sodium persulfate as electron acceptor has become a standard combination for light-driven water oxidation by homogeneous WOCs. On the one hand, ruthenium tris(bipyridine) complexes are excellent sensitizers due to their good absorption of visible light, efficient generation of a long-lived triplet metal-to-ligand charge transfer (^{3}MLCT) state and relatively high oxidation potential of their oxidized form PS^+, which enables oxidation of the WOC to higher oxidation states.[122] On the other hand, the irreversible splitting of the persulfate ion upon one-electron reduction into a sulfate ion and a sulfate radical anion (Figure 36, eq. 2) limits competitive recombination processes which can reduce the efficiency of photocatalytic water oxidation. In addition, the strong oxidant nature of the sulfate radical anion leads to the generation of a second equivalent PS^+ from PS as indicated in eq. 3.

Accordingly, two PS molecules are oxidized by one persulfate ion upon light irradiation in a two-step process (eq. 4).[142] While the initial oxidation of the excited PS* takes place in the ns time regime, the dark thermal quenching by the sulfate radical is observed in the µs range.[82, 143]

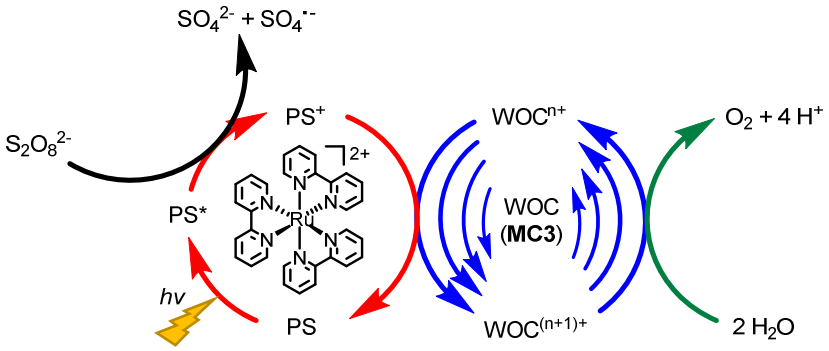

$$PS \xrightarrow{hv} PS^* \quad (1)$$

$$PS^* + S_2O_8^{2-} \longrightarrow PS^+ + SO_4^{2-} + SO_4^{\bullet-} \quad (2)$$

$$PS + SO_4^{\bullet-} \longrightarrow PS^+ + SO_4^{2-} \quad (3)$$

$$2\ PS + S_2O_8^{2-} \xrightarrow{hv} 2\ PS^+ + 2\ SO_4^{2-} \quad (4)$$

$$PS^+ + WOC^{n+} \longrightarrow PS + WOC^{(n+1)+} \quad (5)$$

$$2\ H_2O \xrightarrow{WOC^{(n+1)+}} O_2 + 4\ H^+ + 4\ e^- \quad (6)$$

Figure 36. Schematic illustration of the catalytic cycle of photocatalytic water oxidation using ruthenium tris(bipyridine) as PS, $Na_2S_2O_8$ as sacrificial electron acceptor and trinuclear Ru complexes (e.g. **MC3**) as WOC. The individual steps leading to oxidation of water are indicated in equations 1-6.[16, 68b]

Notably, light-driven water oxidation is a very complex process not only due to the involvement of the three essential components (WOC, PS and electron acceptor), but also due to the interplay of several additional factors that can drastically affect its efficiency as well. These include, e.g. light intensity,[137a, 143a] pH of the solution,[81, 82, 144] chosen buffer system[143a, 145] and its concentration.[72, 145b, 146] Polyansky and Fujita and co-workers reported a two-fold decrease in the initial rate of oxygen generation by Ru(NPM)(H_2O)($pic)_2$ (NPM: 4-*tert*-butyl-2,6-di-(1',8'-naphthyrid-2'-yl)-pyridine) WOC upon decreasing the light power from 25 mW to 13 mW.[143a] Similarly, Bonnet and co-workers reported a notable reduction in TOF from about 0.5 s^{-1} to less than 0.05 s^{-1} for the catalyst Ru(bda)($isoq)_2$ upon decreasing the light intensity from 136 mW cm^{-2} to 26 mW cm^{-2}.[137a] This was explained by the high catalytic activity of the monomeric Ru(bda) WOC, which at lower light intensities can produce oxygen at a higher rate than that of photogeneration of PS^+ due to the limited amount of photons. Further studies have

shown the importance of maintaining a constant pH in photocatalytic water oxidation with a properly chosen buffer concentration. On the one hand, it has been reported that lower pH values deactivate photocatalytic systems by decreasing the rates of electron transfer due to loss of thermodynamic driving force.[81, 82, 145b] On the other hand, increasing the concentration of the buffer above the amount needed for pH regulation results in unnecessarily high ionic strengths which can have a negative impact on the formation of ion pairs between the PS and sodium persulfate.[142, 143, 147]

It has been reported in literature that catalytic performance (that means TOF and TON values) of homogeneous WOCs under light-driven conditions is typically inferior than under chemical or electrochemical conditions.[82, 137a] Indeed, this is also the case for trinuclear Ru(bda) macrocycle **MC3**, which reached a remarkable TOF value of 150 s^{-1} using CAN as chemical oxidant in acidic medium while a more moderate TOF of 11 s^{-1} was observed for photocatalytic water oxidation (Chapter 3.1).[18, 130] This motivated me to address the unveiled question, why photocatalytic activities of Ru macrocycles are less efficient than those of chemical counterpart and which factors influence the photocatalytic activities of Ru(bda) macrocycles. Therefore, I have now explored the photocatalytic activities of **MC3** and its derivative ***m*-CH_2NMe_2-MC3**[20] as prime examples for the class of Ru(bda) macrocyclic WOCs under different reaction conditions using a series of ruthenium tris(bipyridine) **PS0–3** as photosensitizers and sodium persulfate as electron acceptor (Figure 37).

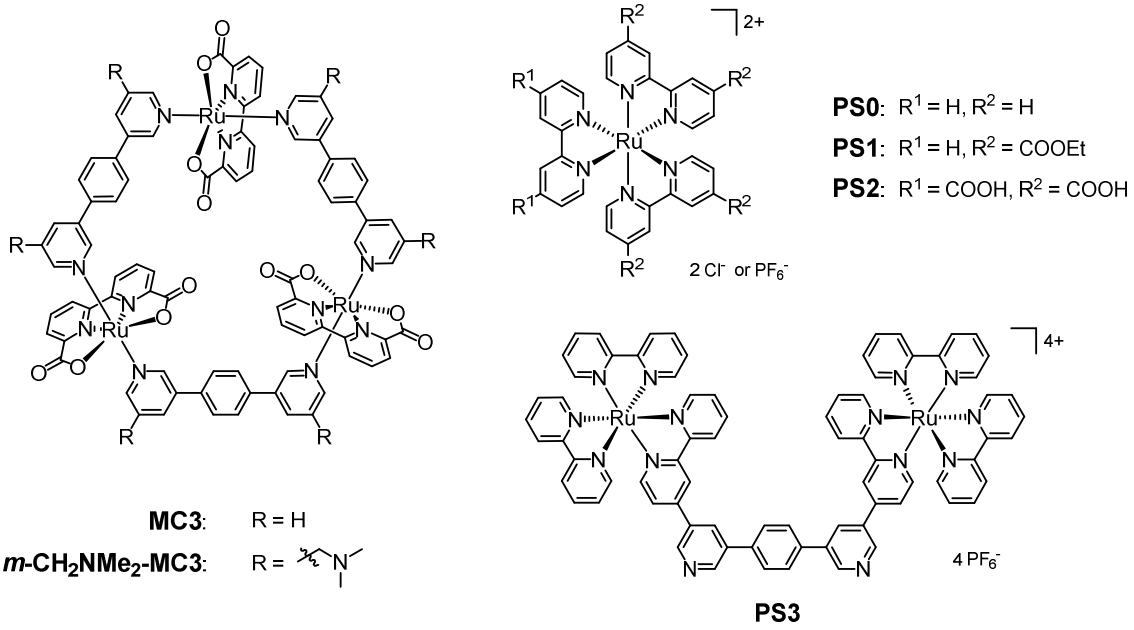

Figure 37. Chemical structures Ru(bda) macrocycles **MC3** and ***m*-CH_2NMe_2-MC3** and ruthenium tris(bipyridine) sensitizers **PS0-3** used in photocatalytic water oxidation.

Macrocycle ***m*-CH_2NMe_2-MC3**, bearing six trialkylamine groups in axial ligands, was chosen as WOC to study the effect of the reaction media, particularly content of organic co-solvent, on the efficiency of photocatalysis as its solubility in water is significantly higher compared to parent **MC3**. Although, chemical water oxidation with this water-soluble derivative has been reported previously,[20] its catalytic properties under light-driven conditions remained unexplored. Now I have studied the photocatalytic activities of ***m*-CH_2NMe_2-MC3** and **MC3** in water oxidation in a comparative manner. For these studies, the photosensitizer selection includes the standard, parent ruthenium tris(bipyridine) complex **PS0**, derivatives **PS1** and **PS2** bearing electron withdrawing groups to increase PS^+/PS oxidation potentials and thermodynamic driving force for activation of the WOC[72, 146a] as well as a newly designed bichromophoric sensitizer **PS3** bearing a dipyridyl phenyl bridge. The kinetic processes that determine the efficiency of photocatalysis were analyzed by steady-state and transient spectroscopic techniques. Here I report that the photocatalytic performances of Ru(bda) macrocycles are strongly dependent on the applied photosensitizer and reaction media, in particular, amount of organic co-solvent used. These findings are explained based on detailed analysis of steady-state emission quenching of photosensitizers and electron-transfer processes between sensitizer and WOC by nanosecond flash photolysis.

4.2 Results

4.2.1 Synthesis and Characterization

Trinuclear Ru(bda) macrocycles **MC3** and ***m*-CH_2NMe_2-MC3** were prepared as reported previously.[18, 20] Photosensitizers **PS1**[148] and **PS2**[149] were synthesized according to the literature procedures. The bichromophoric photosensitizer **PS3** was synthesized in four steps starting with 3-bromo-5-iodopyridine **41** and diborylated benzene **33** according to the route displayed in Scheme 3. Chemoselective Suzuki-coupling reaction between **41** and **33** afforded dibromobispyridylbenzene **42**, the latter was then converted to compound **43** by Miyaura borylation. Ligand **45** was then synthesized by Suzuki-coupling reaction of **43** with bromobipyridine **44**[150] and finally **PS3** was obtained by the complexation reaction of ligand **45** with $Ru(bpy)_2Cl_2$[151] in a mixture of ethanol/water 3:1. Detailed synthetic procedures and characterization data of new compounds are reported in the Experimental Section (Chapter 7).

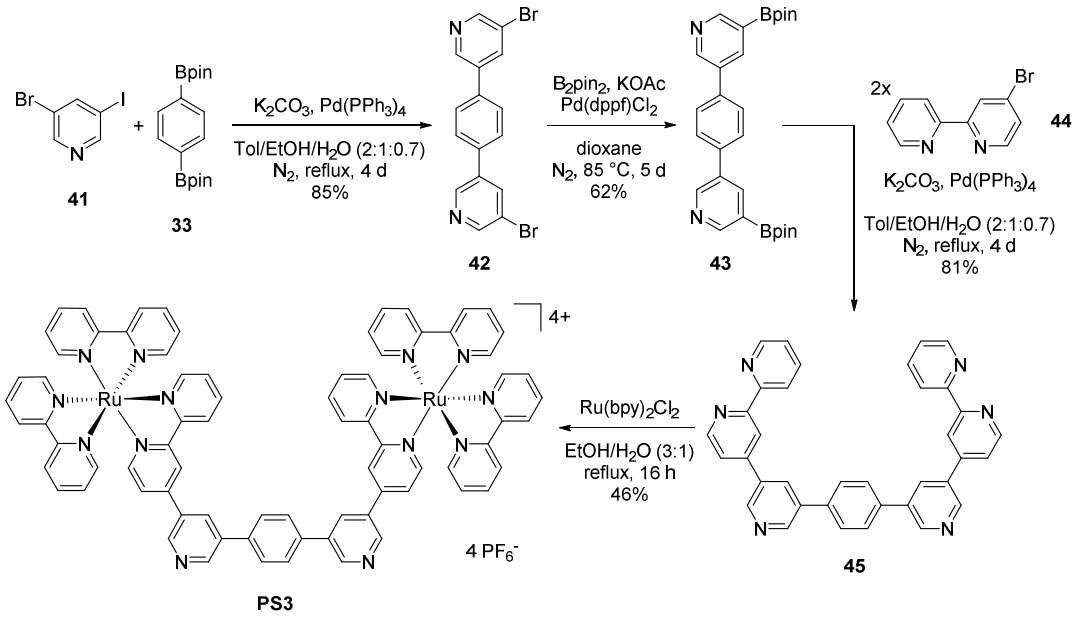

Scheme 3. Synthetic route to binuclear photosensitizer **PS3**.

4.2.2 Redox and Optical Properties

The redox properties of the Ru(bda) macrocycles **MC3** and ***m*-CH_2NMe_2-MC3** have been reported previously.[18-20, 130] The electrochemical properties of the sensitizers **PS0–3** were studied by cyclic voltammetry (CV) and differential pulse voltammetry (DPV) in phosphate buffered MeCN/H_2O (1:1) (Figure 38a) and pure water (Figure S60a, Chapter 8.2) at pH 7. As shown in Table 5, the changes in solvent composition have only a negligible effect on the redox properties of most of these sensitizers.

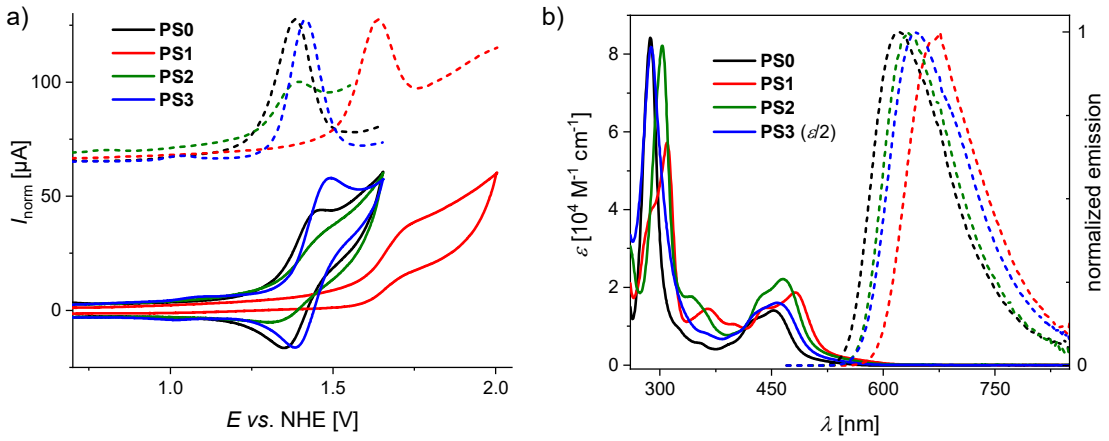

Figure 38. a) CV (solid lines) and DPV (dashed lines) traces of **PS0–3** in MeCN/H_2O 1:1 (pH 7, 50 mM phosphate buffer), c = 1-2 mM. b) UV/Vis absorption (solid lines) and emission (dashed lines) spectra of photosensitizers **PS0-3** in same solvent mixture, c_{abs} = 16 µM, c_{em} = 50 µM.

Table 5. Redox and optical properties of ruthenium tris(bipyridine) sensitizers **PS0–3** in aqueous media.

Sensitizer	MeCN/H_2O 1:1 [a]				H_2O [b]			
	E [V] [c]	$\lambda_{MLCT\ abs}$ [nm] [d]	$\lambda_{MLCT\ em}$ [nm] [e]	τ [ns] [e]	E [V] [c]	$\lambda_{MLCT\ abs}$ [nm] [d]	$\lambda_{MLCT\ em}$ [nm] [e]	τ [ns] [e]
PS0	+1.39	453	622	750 [f]	+1.40	453 [g]	622 [g]	570 [f,h]
PS1	+1.64	482	667	940	+1.63 [i]	483 [j]	667 [k]	560
PS2	+1.39	465	633	990	+1.49	466 [g,j]	633 [l]	670 [l]
PS3	+1.41	457	644	1020 (97%) 290 (3%)	--- [m]	--- [m]	--- [m]	--- [m]

[a] Measurements in MeCN/H_2O 1:1 (50 mM phosphate buffer, pH 7). [b] Measurements in 50 mM phosphate buffer (pH 7) in pure H_2O. [c] Oxidation potentials *vs*. NHE, *c* = 1-2 mM. [d] Absorption spectra were measured at rt, *c* = 16 µM. [e] Emission spectra and PL decay of samples degassed with argon were measured at rt, *c* = 50 µM. For these studies, compounds **PS0–3** were excited at their respective MLCT absorption maximum as indicated in the table. [f] Data in accordance with ref. [147]. [g] Data in accordance with ref. [149]. [h] Data in accordance with ref. [142]. [i] Data in accordance with ref. [72]. [j] Data in accordance with ref. [146a, 152]. [k] Data in accordance with ref. [153]. [l] Data in accordance with ref. [154]. [m] Could not be determined due to poor solubility of **PS3** in phosphate buffered water.

A single reversible $Ru^{III/II}$ oxidation process was observed for the individual sensitzers **PS0–3** in phosphate buffered MeCN/H_2O 1:1 as well as in pure water at pH 7. Notably, the four electron withdrawing carboxylic ester groups of **PS1** imparted a significant increase in the $Ru^{III/II}$ oxidation potential of about 250 mV compared to parent compound **PS0** (E_{PS0} = +1.39 *vs*. NHE) which complies with literature reported values.[72, 145b, 146a] The oxidation potential of **PS2** shows some dependency on the solvent composition since its value increased by 100 mV in the absence of organic co-solvent MeCN. This could be related to partly deprotonation of the carboxylic acid groups and kinetic barriers originating from the stronger hydrogen bonding in pure water as reported elsewhere.[155] Bichromophoric sensitizer **PS3** exhibits a very similar oxidation potential as the parent sensitizer **PS0** in MeCN/H_2O 1:1. Only one electrochemical wave was observed for the oxidation of the two Ru centers of this compound which are accordingly decoupled. This is in agreement with observations made on analogous ruthenium tris(bipyridine) binuclear systems reported by De Cola and co-workers.[156]

The optical properties of **PS0–3** were characterized by UV-vis absorption and steady-state emission spectroscopy in phosphate buffered MeCN/H_2O 1:1 and pure water (pH 7). For emission spectra, samples were degassed with argon to avoid quenching by oxygen. The absorption spectra of compounds **PS0–3** at room temperature show typical transitions characteristic of the ruthenium tris(bipyridine) moiety (Figures 38b and S60b).[135b] These are: (i) a π-π* bpy-ligand centered absorption band at around 300 nm, (ii) a Laporte forbidden

metal centered d-d transition at about 350 nm and (iii) a broad ^{1}MLCT band at 450 nm. The MLCT absorption maxima of the sensitizers are collected in Table 5, along with the corresponding ^{3}MLCT emission maxima and excited state lifetimes. The electron withdrawing groups of **PS1** and **PS2** led to significant bathochromic shifts in MLCT absorption (30 nm and 13 nm, respectively) and emission (45 nm and 11 nm, respectively) compared to parent compound **PS0** in both solvent mixtures. A minor red shift of 4 nm was observed for the MLCT absorption maximum of **PS3** compared to **PS0** while the MLCT emission of the former is red-shifted by 22 nm. This lowering in emission energy is in agreement with observations made for similar ruthenium tris(bipyridine) binuclear complexes as well as for analogous Ru-Os bimetallic systems.[156] A biexponential emission decay was revealed for the binuclear sensitizer **PS3** in MeCN/H_2O 1:1 with a predominant lifetime τ_1 of 1020 ns and a minor second component of τ_2 = 290 ns. Moreover, for **PS3** a larger median lifetime[157] $<\tau>$ of 1000 ns compared to that of the parent compound **PS0** (τ = 750 ns) was observed. In general, the absorption and emission maxima of the sensitizers are independent of the solvent composition. In contrast, the emission lifetime is affected by the used co-solvent as significantly higher lifetimes are observed in MeCN/H_2O 1:1 compared to those in pure water (Figures S61 and S62). For example, **PS1** showed a lifetime of 560 ns in buffered water, whereas in MeCN/H_2O 1:1 (pH 7) a lifetime of 950 ns was observed. This solvent dependency could be explained based on preferential solvation of the sensitizers by the organic co-solvent in MeCN/H_2O mixtures.[142, 147, 158]

4.2.3 Photocatalytic Water Oxidation

I have explored first the effects of light intensity as well as concentration of buffer and photosensitizer on light-driven water oxidation by Ru(bda) macrocycle **MC3**. As a light source a xenon lamp was used (λ = 400-1000 nm, Figure S63) and the generated oxygen was detected with a Clark electrode.

Using standard sensitizer **PS0** and sodium persulfate as sacrificial electron acceptor, the catalytic activity of macrocycle **MC3** was investigated in buffered MeCN/H_2O 1:1 (pH 7) at different phosphate buffer concentrations. As illustrated by the plot of the oxygen generation as a function of time (Figure 39a), under otherwise identical conditions (concentration of **PS0**, sodium persulfate and catalyst, light intensity and solvent composition), **MC3** performes around 25% higher TOF and TON values in 50 mM phosphate buffer compared to a more dilute 20 mM buffer solution (Table S6). While the pH at the end of catalysis remained constant in 50 mM phosphate buffer (pH 7), a reduction down to pH 5.5 was observed in the case of 20 mM solution. Accordingly, the higher catalytic activity at 50 mM buffer concentration

can be ascribed to a stronger buffering effect. The higher amount of phosphate anions might also facilitate atom-proton transfers (APT)[63] leading to efficient formation of Ru^{III}-hydroperoxo intermediates as it has been described for mononuclear Ru(bda) complexes in electrochemical water oxidation.[88] Note that after reaching a plateau of maximal oxygen concentration, some of the dissolved oxygen is released into the gas phase which results in a decrease in the amount of gas detected by the Clark electrode.

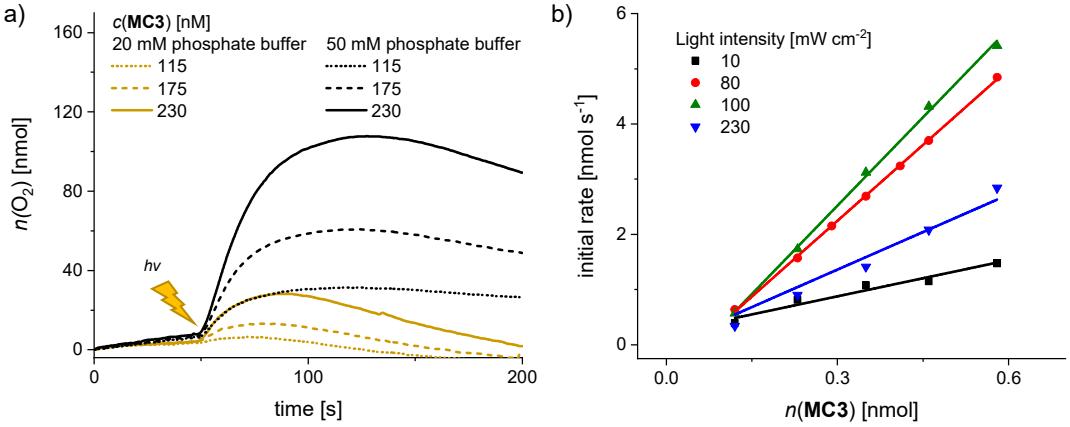

Figure 39. a) Catalyst concentration-dependent oxygen evolution curves of **MC3** in MeCN/H_2O 1:1 in 20 mM and 50 mM phosphate buffer solutions at pH 7, *c*(**PS0**) = 1.5 mM, *c*($Na_2S_2O_8$) = 37 mM. The lighting symbol indicates the start of sample irradiation at *t* = 50 s after sample preparation at a constant light intensity of 100 mW cm^{-2}. b) Initial rates of oxygen generation by **MC3** at variable light intensities. Experiments were performed in MeCN/H_2O 1:1 (50 mM phosphate buffer, pH 7), *c*(**PS0**) = 1.5 mM, *c*($Na_2S_2O_8$) = 37 mM.

As depicted in Figure 39b, the photocatalytic performance of WOC **MC3**, which is reflected in the initial rates of catalysis, is also strongly dependent on the used light intensity (Table S6, Figure S64). The highest TOF (10.9 s^{-1}) was obtained at 100 mW cm^{-2} (Table S6, entry 4) which is about the irradiance of the Sun at the Equator.[159] Decreasing light power down to 10 mW cm^{-2} led to a drastic loss in catalytic activity (TOF = 3.0 s^{-1}), presumably due to a slower activation of the sensitizer and corresponding photogeneration of PS^+.[160] Likewise, at a higher light power of 230 mW cm^{-2} TOF reduced to 5.3 s^{-1}.[6] This might be reasoned by a facile photodecomposition of the sensitizer under intense light exposure.[144a, 161] Further, I investigated the effect of light intensity on quantum yields Φ and chemical yields of oxygen production φ_{chem} (Table S6, see SI for details). The results indicate a correlation between the TONs and φ_{chem}, although for the latter due to the large excess $Na_2S_2O_8$ (*c* = 37 mM) only values below 1% were obtained. At 10 mW cm^{-2} the highest Φ of 7.9% was observed, corresponding to an overall quantum efficiency (QE) of 15.8%.[137b] At 100 mW cm^{-2} and

[6] Measurement at 230 mW cm^{-2} was performed by Dr. Valentin Kunz, Universität Würzburg.

230 mW cm^{-2} Φ decreased to 2.9% and 0.6%, respectively. These results comply well with recent observations that a careful adjustment of the photon flux is relevant towards the optimization of the light-driven catalytic response.[160, 162] The concentration of photosensitizer affects the catalytic activity of **MC3** as well. Increasing the concentration of **PS1** from 0.2 mM to 1.5 mM resulted in a significant increase of TOF and TON values (Table S6, entries 4 and 6, Figure 40). Notably, no oxygen was produced in the absence of the WOC neither at 0.2 mM nor 1.5 mM concentration of **PS0** as revealed by control experiments (Figure S65). Likewise, no oxygen generation was detected in the absence of the sensitizer. Accordingly, further experiments were conducted in MeCN/H_2O 1:1 containing 50 mM phosphate buffer (pH 7) at a light intensity of 100 mW cm^{-2} and in the presence of 1.5 mM of the respective PS.

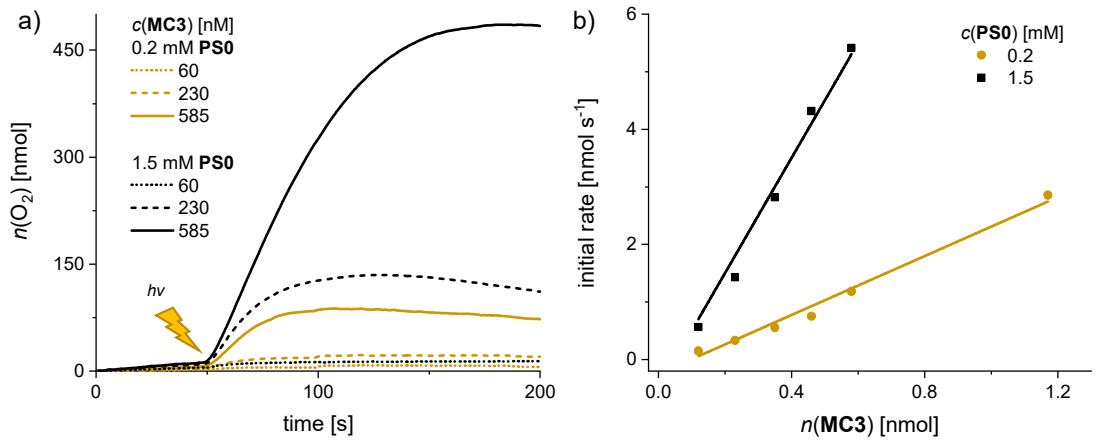

Figure 40. a) Catalyst concentration-dependent oxygen evolution curves of **MC3** in MeCN/H_2O 1:1 (50 mM phosphate buffer, pH 7), c(**PS0**) = 0.2 mM or 1.5 mM, c($Na_2S_2O_8$) = 37 mM. The lighting symbol indicates the start of sample irradiation at t = 50 s. b) Initial rates of oxygen generation for **MC3** at variable **PS0** concentrations.

Under the above-mentioned conditions, I have investigated the photocatalytic activities of **MC3** and functionalized WOC ***m*-CH_2NMe_2-MC3** using **PS0–3** as sensitizers in phosphate buffered MeCN/H_2O 1:1 (pH 7, Figures S66 and S67). These experiments showed that the catalytic activity of ***m*-CH_2NMe_2-MC3** in terms of TOFs, TONs, φ_{chem} and Φ is quite similar to **MC3** (Table 6). Hence, the catalytic efficiency of the functionalized Ru(bda) macrocycle is not considerably affected by the incorporated tertiary amino groups as observed for other trinuclear Ru(bda) macrocycles that are functionalized with methyl, methoxy or fluoro groups at the same position (Chapter 3).[130] This results indicate that the intrinsic catalytic activityies of macrocycles **MC3** and ***m*-CH_2NMe_2-MC3** are comparable. Since ***m*-CH_2NMe_2-MC3** is better soluble in aqueous mixtures, the catalytic activities of this WOC were further studied in 5% MeCN and the results are compared with those obtained in 50% MeCN for both WOCs (Table 6).

Table 6. Catalytic activities of **MC3** and ***m*-CH$_2$NMe$_2$-MC3** in photochemical water oxidation with **PS0–3** as sensitizers at varying MeCN content.

Sensitizer	**MC3** in 50% MeCN [a]				***m*-CH$_2$NMe$_2$-MC3** in 50% MeCN [b]				***m*-CH$_2$NMe$_2$-MC3** in 5% MeCN [c]			
	TOF [s^{-1}]	TON	Φ [%][d]	φ_{chem} [%][e]	TOF [s^{-1}]	TON	Φ [%][d]	φ_{chem} [%][e]	TOF [s^{-1}]	TON	Φ [%][d]	φ_{chem} [%][e]
PS0	10.9	430	2.9	1.6	9.5	550	2.6	2.3	2.9	270	2.0	0.5
PS1	2.8	220	0.3	0.6	2.2	180	0.4	0.8	10.8	320	3.0	0.7
PS2	0.5	170	0.1	0.3	0.4	100	0.1	0.4	0.7	100	0.3	0.3
PS3	5.9	350	1.6	1.6	5.8	400	1.5	1.8	--- [f]	--- [f]	--- [f]	--- [f]

[a] Measurements in MeCN/H_2O 1:1 (50 mM phosphate buffer, pH 7), *c*(PS) = 1.5 mM, *c*($Na_2S_2O_8$) = 37 mM, *c*(**MC3**) = 60 nM–2.5 µM. [b] Measurements in MeCN/H_2O 1:1 (50 mM phosphate buffer, pH 7), *c*(PS) = 1.5 mM, *c*($Na_2S_2O_8$) = 37 mM, *c*(***m*-CH$_2$NMe$_2$-MC3**) = 60 nM–2.5 µM. [c] Measurements in MeCN/H_2O 5:95 (50 mM phosphate buffer, pH 7), *c*(PS) = 0.2 mM, *c*($Na_2S_2O_8$) = 37 mM, *c*(***m*-CH$_2$NMe$_2$-MC3**) = 60 nM–2.5 µM. [d] Quantum yield of O_2 production determined for *c*(WOC) = 290 nM. [e] Chemical yield of O_2 production determined for *c*(WOC) = 880 nM. [f] Could not be determined due to poor solubility of **PS3** in phosphate buffered MeCN/H_2O 5:95.

Catalyst concentration-dependent studies of photocatalytic activity of **MC3** in 50% acetonitrile (Figure S66) revealed that the initial rates of catalysis (Figure 41a) as well as TOF and TON values of the WOC, φ_{chem} and Φ are strongly dependent on the choice of photosensitizer (Table 6). The highest catalytic activity of **MC3** was observed with the standard sensitizer **PS0** (TOF = 10.9 s^{-1}, TON = 430). A more moderate TOF of 5.9 s^{-1} was obtained for the bichromophoric sensitizer **PS3** under otherwise identical conditions, while with sensitizers **PS1** and **PS2** the photocatalytic activity of **MC3** decreased significantly to 2.8 s^{-1} and 0.5 s^{-1}, respectively. A similar trend was observed for Ru macrocycle ***m*-CH$_2$NMe$_2$-MC3** in the same solvent mixture (Figure S68). It should be noted that in all cases the initial rates of oxygen production plotted against the total amount of WOC follow a linear relationship. This is indicative of first order kinetics relative to the catalyst concentration and complies with the proposed WNA mechanism for WOC **MC3**.[18]

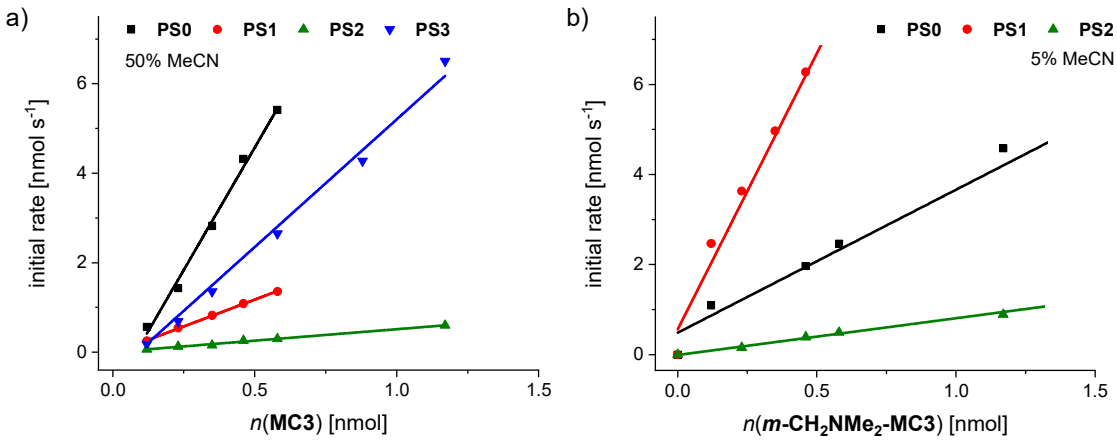

Figure 41. Catalytic performance of Ru(bda) macrocycles **MC3** (a) and ***m*-CH$_2$NMe$_2$-MC3** (b) in light-driven water oxidation using **PS0–3** as photosensitizers. The catalytic activity was analyzed by the initial rates of catalysis at variable WOC concentrations. Measurements were performed in (a) 1:1 or (b) 5:95 MeCN/H_2O mixtures (50 mM phosphate buffer, pH 7). Experiment conditions: (a) $c([Ru(bpy)_3]^{2+})$ = 1.5 mM, $c(Na_2S_2O_8)$ = 37 mM; (b) $c([Ru(bpy)_3]^{2+})$ = 0.2 mM, $c(Na_2S_2O_8)$ = 37 mM.

Interestingly, the trends in photocatalytic efficiency of ***m*-CH$_2$NMe$_2$-MC3** in combination with the present series of sensitizers are significantly different in 5% MeCN compared to 50% MeCN (Table 6, Figures 41b and S69). In 5:95 MeCN/H_2O mixture, WOC ***m*-CH$_2$NMe$_2$-MC3** reached the highest TOF of 10.8 s^{-1} with ester-functionalized sensitizer **PS1**, whereas with the parent sensitizer **PS0** a modest TOF value of 2.9 s^{-1} was observed. It is noteworthy that due to lower solubility of the sensitizers in 5% MeCN, a reduced PS concentration had to be used in this solvent mixture to study the photocatalytic activity of ***m*-CH$_2$NMe$_2$-MC3**. Notably, at this concentration distinctly lower TOF and TON values of 2.6 s^{-1} and 80 were obtained for the macrocycle **MC3** using **PS0** as sensitizer in MeCN/H_2O 1:1 (Figure S70) compared to the results obtained at c(**PS0**) = 1.5 mM (10.9 s^{-1} and 430, respectively). Accordingly, the TOF (10.8 s^{-1}) and TON (320) values obtained for the ***m*-CH$_2$NMe$_2$-MC3**/**PS1** system with a 0.2 mM concentration of **PS1** in 5% acetonitrile are remarkably high.[7] Catalytic samples of both Ru macrocycles **MC3** and ***m*-CH$_2$NMe$_2$-MC3** in MeCN:H_2O 1:1 and 5:95 were studied before and after catalysis by UV/vis absorption spectroscopy (Figure S72). These experiments revealed a significant degradation of the photosensitizers in both solvent mixtures that presumably explains the end of catalysis under the studied reaction conditions.

[7] For further comparison, the photocatalytic activity of parent **MC3** was also measured at c(**PS1**) = 0.2 mM in 50% acetonitrile (Figure S71). In this case, TOF and TON of **MC3** decreased to 1.1 s^{-1} and 45 compared to 2.8 s^{-1} and 220 observed at c(**PS1**) = 1.5 mM. These results clearly underline the significance of sensitizer concentration for photocatalytic water oxidation with Ru macrocycles.

4.2.4 Emission Quenching Studies

To get insights into the WOC activation by PS^+, which is generated by reaction of PS* with sodium persulfate ($Na_2S_2O_8$), I have explored the quenching efficiency of excited sensitizers by the electron acceptor sodium persulfate by Stern-Volmer analysis according to following equation.[142, 163]

$$\frac{I_0}{I} = 1 + \tau_0 k_q \, c(S_2O_8{}^{2-})$$

Here I_0 and I are the emission intensity in the absence and presence of quencher, respectively, τ_0 is the emission lifetime in the absence of quencher, k_q the bimolecular rate constant of the quenching process and $c(S_2O_8{}^{2-})$ the concentration of persulfate quencher. Emission spectra of photosensitizers **PS0–3** were measured at different concentrations of the quencher under inert conditions (see SI for experimental details). As exemplarily shown in Figure 42a for the emission quenching of parent sensitizer **PS0** in the presence of sodium persulfate in MeCN/H_2O 1:1 (see Figures S73 and S74 for emission quenching of sensitizers **PS0–3** in buffered sulutions of MeCN/H_2O 1:1 and 5:95, respectively), a decrease in emission intensity was clearly observed upon increasing the concentration of the electron acceptor. The ratio of I_0/I plotted against the concentration of persulfate for all sensitizers in both solvent mixtures followed a linear relationship as indicated by the Stern-Volmer plots (Figures 42b and S74d).

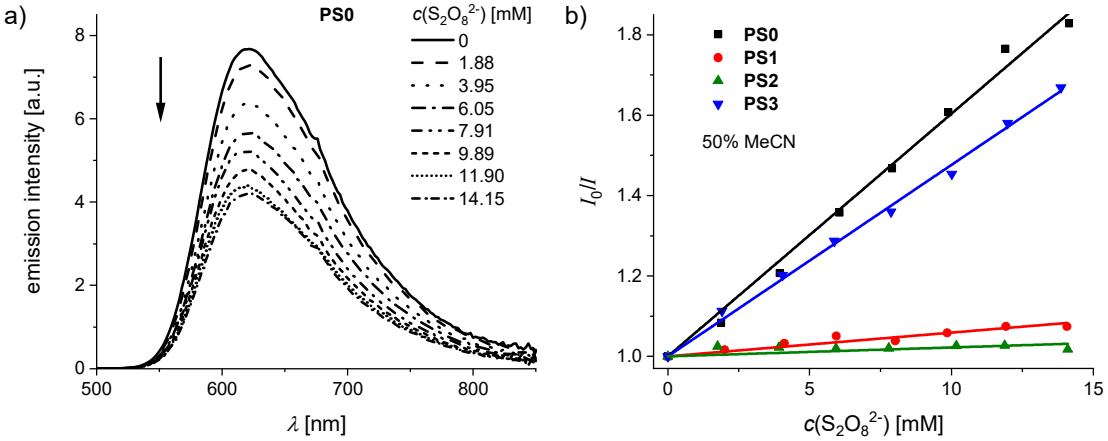

Figure 42. a) Emission spectra (λ_{ex} = 453 nm) of **PS0** in MeCN/H_2O 1:1 (phosphate buffer, pH 7) at varying concentrations of $Na_2S_2O_8$. The arrow indicates changes of emission spectra with increasing concentration of the persulfate quencher. b) Stern-Volmer plots showing linearly fitted curves for sensitizers **PS1–3** in buffered MeCN/H_2O 1:1 (pH 7). In all experiments, the concentration of the respective sensitizer was 50 µM.

As shown in Table 7 for sensitizers **PS0–3**, the rate constants k_q of emission quenching obtained from Stern-Volmer analysis are strongly dependent on the solvent system. For example, a high rate constant k_q of (1.8 ± 0.3) x 10^9 M^{-1} s^{-1} was observed for the quenching of **PS0** in MeCN/H_2O 5:95 while in MeCN/H_2O 1:1 k_q decreases by more than one order of magnitude to (8.1 ± 0.2) x 10^7 M^{-1} s^{-1}. The k_q value observed for **PS0** in MeCN/H_2O 5:95 is in excellent agreement with values reported in literature in water (k_q = 9.8 x 10^8 – 1.1 x 10^9 M^{-1} s^{-1})[142, 147, 164] and relates to a very fast, nearly diffusion controlled process. Also for **PS1**, k_q decreased by one order of magnitude upon increasing the MeCN content from 5% to 50% (Table 7). In contrast, such a solvent effect was not observed for the photosensitizer **PS2** bearing carboxylic acid groups as similar k_q values were obtained in both solvent mixtures. The relatively low quenching rates obtained for **PS2**, independent of the used MeCN content, point at an overall inefficient quenching of this photosensitizer by sodium persulfate. For bichromophoric sensitizer PS3, an intermediate quenching constant of (4.5 ± 0.6) x 10^9 M^{-1} s^{-1} was obtained.

Table 7. Rate of emission quenching of **PS0–3** by $Na_2S_2O_8$ determined by Stern-Volmer analysis.

Sensitizer	50% MeCN [a]		5% MeCN [b]	
	$\tau_0 k_q$ [M^{-1}]	k_q [$M^{-1}s^{-1}$]	$\tau_0 k_q$ [M^{-1}]	k_q [$M^{-1}s^{-1}$]
PS0	60.3 ± 1.1	(8.1 ± 0.2) x 10^7	1079.0 ± 16.8	(1.8 ± 0.3) x 10^9
PS1	5.9 ± 0.4	(6.3 ± 0.4) x 10^6	56.5 ± 0.6	(9.6 ± 0.1) x 10^7
PS2	2.2 ± 0.5	(2.2 ± 0.5) x 10^6	0.9 ± 0.3	(1.3 ± 0.5) x 10^6
PS3	47.6 ± 0.6	(4.5 ± 0.6) x 10^7	--- [c]	--- [c]

[a] Measurements in MeCN:H_2O 1:1 (phosphate buffer, pH 7), c(PS) = 50 µM, c($Na_2S_2O_8$) = 0–14 mM. [b] Measurements in MeCN:H_2O 5:95 (phosphate buffer, pH 7), c(PS) = 50 µM, c($Na_2S_2O_8$) = 0–14 mM. [c] Could not be determined due to poor solubility of **PS3** in phosphate buffered MeCN/H_2O 5:95.

4.2.5 Laser Flash Photolysis

I have then studied the electron transfer processes between sensitizers **PS0** and **PS1** and Ru macrocycles **MC3** and ***m*-CH_2NMe_2-MC3** by nanosecond laser flash photolysis in 1:1 and 5:95 MeCN/H_2O mixtures (phosphate buffer, pH 7). Both photosensitizers were excited close or at their respective MLCT absorption maximum ($\lambda_{ex\ PS0}$ = 460 nm, $\lambda_{ex\ PS1}$ = 482 nm) and oxidized using an excess of sodium persulfate. The formation of PS^+ was detected as a ground state bleach of the ^{1}MLCT absorption band at 455 nm. In the absence of a Ru macrocycle, the amount of oxidized PS^+ in MeCN:H_2O 1:1 remains appreciably constant within the time window of the experiment (black curves in Figures 43a and S75a). In MeCN:H_2O 5:95, a slow bleach recovery over a few ms is observed (black curves in Figure S75b,c). In the presence

of variable concentrations of Ru macrocycles **MC3** and ***m*-CH$_2$NMe$_2$-MC3**, changes in the ΔOD signal at 455 nm (bleaching recovery) indicate faster regeneration of the ground state of the sensitizers upon electron transfer from the catalyst to PS$^+$ (Figures 43a and S75). The residual negative absorption left upon recovery of the bleaching is consistent with oxidation of the macrocyclic WOC.[20] [8] The rates of the observed ΔOD changes (k_{obs}) for sensitizers **PS0** and **PS1** in MeCN/H$_2$O 1:1 plotted against the concentration of catalyst **MC3** follow a linear relationship (Figure 43b). Under pseudo-first order conditions due to excess of the WOC over photogenerated PS$^+$, bimolecular rate constants for the respective electron-transfer processes were determined from the slope of the linear correlation.[82, 137b, 143a] Thus, a k_{ET} constant of (3.5 ± 0.2) x 10^7 M^{-1} s^{-1} was obtained for the **PS0**/**MC3** system, while a one order of magnitude larger value of (3.3 ± 0.1) x 10^8 M^{-1} s^{-1} was observed for the electron transfer between **MC3** and **PS1**. This is in agreement with the larger thermodynamic driving force for the hole transfer process resulting from the introduction of electron withdrawing ester groups into **PS1** compared to **PS0**. For comparison, the electron transfer between ***m*-CH$_2$NMe$_2$-MC3** and photosensitizers **PS0** and **PS1** was studied in 50% MeCN as well (Figure S76). As expected, k_{ET} values comparable to those determined for **MC3** were obtained. These rate constants are in line with those reported for mononuclear ruthenium catalysts.[137b]

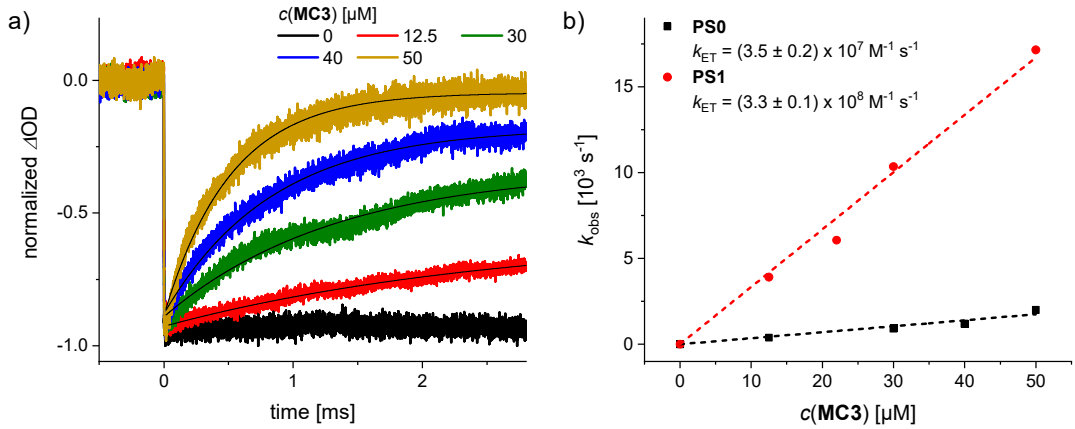

Figure 43. a) Kinetic traces at 455 nm of solutions of 50 µM **PS0** and 50 mM $Na_2S_2O_8$ in MeCN:H$_2$O 1:1 (50 mM phosphate buffer, pH 7) at variable concentrations of **MC3**. Exponential fits are shown in black. b) Plot of the observed rate constants k_{obs} for the electron transfer from **MC3** to oxidized sensitizers **PS0**$^+$ (black squares) and **PS1**$^+$ (red circles) *vs*. WOC concentration. k_{ET} is obtained from the slope of the linear correlation.

[8] Due to the overlying absorption between the sensitizers and the Ru macrocycles, the excitation light is partially absorbed by the catalysts. Nevertheless, control experiments with Ru macrocycles **MC3** and ***m*-CH$_2$NMe$_2$-MC3** in MeCN/H$_2$O 1:1 and 5:95 revealed that in the absence of photosensitizers no significant changes in ΔOD signal at 455 nm result from sample excitation at 460 nm or 482 nm (Figure S77).

The electron-transfer processes between functionalized Ru macrocycle ***m*-CH_2NMe_2-MC3** and sensitizers **PS0** and **PS1** were then studied in 5% MeCN (Figure S75b,c). In this case, a bimolecular k_{ET} constant of (7.3 ± 0.6) x 10^6 M^{-1} s^{-1} was obtained for the electron transfer between the WOC and **PS1** (Figure S75d), a value almost two orders of magnitude lower than in 50% MeCN. Moreover, k_{ET} for the **PS0**/***m*-CH_2NMe_2-MC3** system can be estimated to be lower than 10^6 M^{-1} s^{-1} according to the low response observed in the catalyst concentration-dependent measurements shown in Figure S75c (exact determination is indeed hampered by experimental constraints, i.e. available time-window and WOC solubility). Considering the similar oxidation potentials of both sensitizers and macrocycles in the presence of different amounts MeCN,[20] the systematic reduction of k_{ET} values for ***m*-CH_2NMe_2-MC3** in 5% MeCN compared to 50% MeCN is probably related to the presence of the organic co-solvent and preferential solvation effects on the electron transfer kinetics. Notwithstanding, in both solvent mixtures a faster electron transfer from the WOC to the oxidized photosensitizers is always observed using **PS2** compared to **PS1**. Furthermore, these studies revealed a very strong dependency of the efficiency of electron transfer on the amount of organic co-solvent used.

4.3 Discussion

I have studied the photocatalytic activities of trinuclear Ru(bda) macrocycles **MC3** and ***m*-CH_2NMe_2-MC3** using a series of ruthenium tris(bipyridine) **PS0–3** photosensitizers and sodium persulfate as electron acceptor in MeCN/H_2O mixtures containing varying amounts of MeCN as co-solvent to explore the effects of photosensitizers and co-solvent on catalytic efficiency of these WOCs. The experiments with **MC3** were performed in 50% MeCN, while studies with highly water-soluble ***m*-CH_2NMe_2-MC3** were conducted in 5% MeCN as well. The highest catalytic activity of Ru macrocycle **MC3** in 50% MeCN (TOF = 10.9 s^{-1}, TON = 430) was achieved with the standard ruthenium tris(bipyridine) sensitizer **PS0**. Similar catalytic activity (TOF = 9.5 s^{-1}, TON = 550) was observed for ***m*-CH_2NMe_2-MC3** with **PS0** under identical conditions. In contrast, in 5% MeCN ***m*-CH_2NMe_2-MC3** reached its best photocatalytic performance (TOF = 10.8 s^{-1}, TON = 320) with the ester functionalized sensitizer **PS1**. It is noteworthy that due to the lower solubility of the sensitizers in 5% MeCN, a reduced PS concentration (*c* = 0.2 mM) had to be used to study the photocatalytic activity of ***m*-CH_2NMe_2-MC3** in this solvent mixture. In control experiments I could show the significance of sensitizer concentration for light-driven water oxidation with Ru macrocycles. Accordingly, the efficiency of the ***m*-CH_2NMe_2-MC3**/**PS1** system is remarkably high for the low sensitizer concentration in 5% MeCN. Further, it should be mentioned that both Ru macrocycles exhibit higher photocatalytic activities than most homogeneous Ru WOCs,

including mononuclear Ru(bda) complexes that do not reach TOFs higher than 1 s^{-1}.[17] Both catalysts **MC3** and ***m*-CH_2NMe_2-MC3** performed very poorly with carboxylate-functionalized sensitizer **PS2** and a moderate catalytic activity was observed using bichromophoric photosensitizer **PS3**. Importantly, a linear relationship between the catalyst amount and the initial rates of catalysis was observed for **MC3** and ***m*-CH_2NMe_2-MC3** in all photocatalytic water oxidation experiments. This complies with the first order kinetics of the proposed WNA mechanism of water oxidation for the unsubstituted **MC3** WOC.[18] Therefore, the diverse trends observed in photocatalytic efficiency of the Ru macrocycles with different photosensitizers cannot be ascribed to a change in operating mechanism (WNA *vs*. I2M) of water oxidation, rather to the nature of the applied sensitizers and the solvent composition.

In photocatalytic water oxidation, the transfer of electrons to the sacrificial electron acceptor depends on the oxidation potentials of the components involved in the process and the resulting thermodynamic driving forces.[137b] In Figure 44 a schematic energy diagram with relevant oxidation potentials is shown for photocatalytic water oxidation with WOC **MC3**, photosensitizers **PS0** and **PS1**, and sodium persulfate as sacrificial electron acceptor. In general, the higher is the potential at which the catalyst reaches its active state (e.g. 1.00 V for oxidation of **MC3** to Ru^V state at pH 7), the lower is the driving force for electron transfer from the WOC to the oxidized sensitizer. At the same time, replacing standard sensitizer **PS0** with **PS1** is expected to increase the driving force for the oxidation of **MC3** into its active state due to the higher Ru^{III}/Ru^{II} oxidation potential of the latter sensitizer as shown in Figure 44. Indeed, Sun and co-workers have reported that sensitizer **PS1** leads to higher TOF and TON values compared to **PS0** in photocatalytic water oxidation with a water soluble Ru(bda) WOC in pure water.[145b] However, I have observed the opposite behavior, i.e. higher TOF and TON values with **PS0** than **PS1** in light-driven water oxidation using Ru(bda) macrocycles **MC3** and ***m*-CH_2NMe_2-MC3** in MeCN/H_2O 1:1 mixture (Table 6). Nevertheless, considering the comparable excited state energy for both ruthenium dyes, changing of the sensitizer from **PS0** to **PS1** leads to a decrease in driving force for excited state oxidative quenching by the persulfate anion.

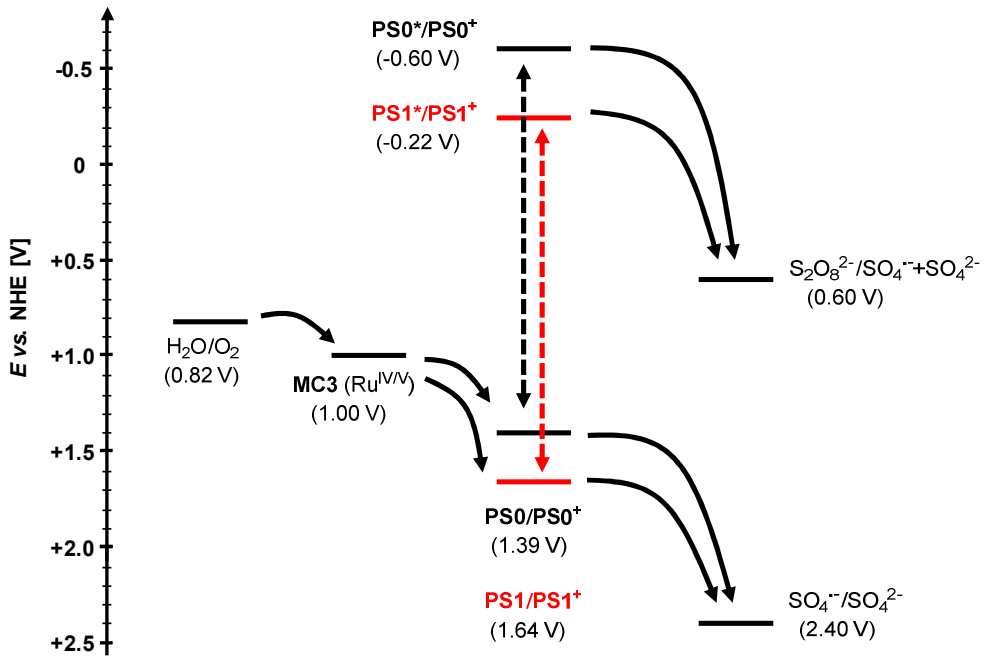

Figure 44. Energy scheme of photocatalytic water oxidation with **PS0** and **PS1** as photosensitizers, $Na_2S_2O_8$ as electron acceptor and trinuclear Ru(bda) macrocycle **MC3** as WOC (a similar situation applies for functionalized macrocycle ***m*-CH$_2$NMe$_2$-MC3**).[20] The potential for the oxidation of water to molecular oxygen at pH 7 was calculated by the Nernst equation: E = 1.23 - (0.059 x pH) V *vs.* NHE.[68b, 165] Oxidation potential of **MC3** was determined as described in Chapter 3.1. Oxidation potentials of the sensitizers in ground and excited states were determined by cyclic voltammetry measurements and calculated as reported elsewhere,[122b, 137b] respectively. Oxidation potentials of $Na_2S_2O_8$ according to eq. 2 and 3 in Figure 36 were obtained from literature references.[15, 137b, 166]

Photocatalytic water oxidation is usually dependent on the intrinsic catalytic ability of the WOC. However, the generation of the oxidized sensitizer PS^+ (by quenching of excited PS* by sodium persulfate) and the regeneration of ground state PS (by electron transfer from the WOC to PS^+) can also affect the efficiency of a photocatalytic system.[137] Thus, the fact that **PS1** did not lead to an increase in TOF and TON compared to **PS0** in MeCN/H_2O 1:1 can be related to the electron transfer from the WOC to the oxidized sensitizers not being the rate-determining step of photocatalysis in this solvent mixture. Nanosecond flash photolysis was used to study the efficiency of this electron transfer in 50% MeCN revealing k_{ET} rate constants in the range of 10^7 to 10^8 M^{-1} s^{-1}. Notably, a one order of magnitude larger value was observed for the **PS1**/**MC3** system compared to **PS0** as expected due to introduction of electron withdrawing ester groups into sensitizer **PS1**. Stern-Volmer analysis was used to determine the rate constants of emission quenching for **PS0–3** in 50% MeCN. Interestingly, the obtained k_q values of 10^6 – 10^7 M^{-1} s^{-1} relate very well to the trends observed for the photocatalytic activity of **MC3** with the series of functionalized sensitizers (**PS2** < **PS1** < **PS3** < **PS0**).

Considering that these experiments were performed with same WOC of invariant intrinsic catalytic ability (i.e. the "dark" catalytic steps related to the WNA water oxidation mechanism of **MC3** are not rate-determining) it can be concluded that the photocatalytic performance of **MC3** in MeCN/H_2O 1:1 is most probably limited by the rate of generation of the respective photooxidant PS^+. This is also in agreement with the increase in TOF values observed upon increasing the light intensity up to 100 mW cm^{-2} which suggest the presence of a light-limiting kinetic regime as it has been recently observed for Ir WOCs in light-driven water oxidation using **PS1** as photosensitizer.[160, 162] As a result, the different hole-transfer rates measured for the **PS0** and **PS1**/**MC3** systems did not considerably affect the efficiency of photocatalysis in 50% MeCN. The drastic decrease in TOF and TON values observed for the photosensitizer **PS2** can be explained by its inefficient quenching at pH 7 (in 50% MeCN and 5% as well) resulting from electrostatic repulsion between the negatively charged carboxylate groups of the sensitizer and the persulfate ions. This unfavorable situation might be avoided under strongly acidic conditions as suggested in a very recent publication by Concepcion and co-workers on the use of phosphonate functionalized ruthenium tris(bipyridine) derivatives as photosensitizers.[124]

Steady-state emission experiments further revealed that the quenching rates of excited photo-sensitizers **PS0*** and **PS1*** by sodium persulfate were significantly affected by the presence of the organic co-solvent. The respective k_q values were increased by one order of magnitude upon decreasing the content of MeCN from 50% to 5% (see Table 7). This effect may be related to a strong preferential solvation of the sensitizers by the organic co-solvent in MeCN/H_2O mixtures which could hinder an efficient quenching at higher MeCN contents.[147] It can be inferred that the larger thermodynamic driving force resulting from use of **PS1** as photosensitizer compared to **PS0** becomes effective upon reduction of the MeCN content since the generation of photooxidant PS^+ in MeCN/H_2O 5:95 is very efficient. Thus, this explains the higher TOF and TON values obtained for the **PS1**/***m*-CH_2NMe_2-MC3** system in 5% MeCN compared to **PS0**. However, in this solvent mixture a significant reduction in k_{ET} values of about two orders of magnitude was observed for both **PS0** and **PS1** photosensitizers compared to the values obtained in 50% MeCN. Although in the performed experiments only the primary hole-transfer from the oxidized sensitizers to the Ru macrocycles in their Ru^{II} oxidation state is investigated, subsequent hole-transfer processes to the oxidized WOCs are likely to be affected in a similar way. Therefore, it can be concluded that in MeCN/H_2O 5:95 the overall photocatalytic efficiencies of the Ru macrocycles in terms of TOF and TON values is most likely limited by the hole-transfer process from photogenerated PS^+ to the WOC.

To the best of my knowledge, the direct influence of the organic co-solvent on the photocatalytic performance of homogeneous Ru WOCs has solely been studied in one recent publication by Sun and co-workers.[125] They have reported an increase in photocatalytic TON values of the monomeric Ru(bda)(pic)$_2$ and a related dimeric catalyst using **PS0** as sensitizer upon increasing the MeCN content from 20% to 60% in phosphate buffered MeCN/H_2O mixtures. This finding was explained by an increase in the driving force for water oxidation provided by the photooxidized **PS0$^+$** sensitizer in solvent mixture containing higher amount of MeCN. In contrast, I observed an opposite trend using **PS0** in combination with the **MC3** macrocycle under otherwise identical conditions (TON $_{50\%\ MeCN}$ = 80, TON $_{5\%\ MeCN}$ = 270 at *c*(**PS0**) = 0.2 mM). Further, the performed investigations on the photocatalytic performance of trinuclear Ru(bda) macrocycle ***m*-CH_2NMe_2-MC3** revealed that with sensitizer **PS1** higher TOF and TON values can be achieved by reduction of MeCN content from 50% to 5%. This higher photocatalytic activity observed for the supramolecular WOCs at lower MeCN content is reasonable considering the ability of acetonitrile to competitively bind to the Ru centers of the WOC designed for coordination of water molecules.[87b] Indeed, Würthner and co-workers have previously demonstrated that upon increasing the MeCN content in MeCN/H_2O mixtures the catalytic efficiency of ***m*-CH_2NMe_2-MC3** and other trinuclear Ru(bda) macrocycles decreases in chemical water oxidation as well.[18, 20]

On a more general basis, the present work highlights how in complex photochemical reactions such as light-driven water oxidation, the use of photosensitizers with high oxidation potentials might become a powerful tool to boost photocatalysis, but only provided that catalyst activation represents the rate-determining step.[72, 82] In this respect, environmental factors such as use of organic co-solvents, solvent composition, type and concentration of buffer, etc. play a pivotal role and direct assessment of these experimental parameters is of high relevance for the application of PS/WOC couple towards efficient water oxidation catalysis.

4.4 Conclusions

The effects of photosensitizers and reaction media on the efficiency of photocatalytic water oxidation with trinuclear Ru(bda) macrocycles **MC3** and ***m*-CH_2NMe_2-MC3** have been elucidated using a series of ruthenium tris(bipyridine) photosensitizers and sodium persulfate as an electron acceptor. In addition, the kinetics of generation of photooxidant PS^+ and electron transfer from the trinuclear catalysts to the oxidized sensitizers have been explored to gain a deeper insight into the complex process of the photocatalytic water oxidation with Ru(bda) macrocycles.

In catalytic water oxidation with the present series of photosensitizers, diverse trends for the catalytic performance of **MC3** and ***m*-CH_2NMe_2-MC3** in MeCN/H_2O containing 50% and 5% of the organic co-solvent, respectively, were observed. Interestingly, the photocatalytic activities of both Ru macrocycles were significantly dependent on the applied sensitizer and amount of organic co-solvent used. In 50% MeCN, the highest TOF and TON values were reached by WOC **MC3** with the parent sensitizer **PS0**. In contrast, in 5% MeCN catalyst ***m*-CH_2NMe_2-MC3** exhibited its highest catalytic activity in combination with ester-functionalized sensitizer **PS1**, presumably due to the larger thermodynamic driving force for the electron transfer between WOC and sensitizer resulting from the introduction of the electron withdrawing groups. This became important only upon reduction of the MeCN content since in 50% MeCN the quenching of **PS1** by sodium persulfate and hence the generation of **$PS1^+$** is inefficient compared to parent compound **PS0**. As a result, an enhanced catalytic activity of functionalized macrocycle ***m*-CH_2NMe_2-MC3** was observed by using photosensitizer **PS1** upon decreasing the MeCN content from 50% to 5% which can also be related to the ability of MeCN to compete with water for binding sites of Ru WOCs. However, the performed studies revealed that the photocatalytic performance of the trinuclear Ru catalysts (in terms of TOFs and TONs) in either solvent mixture is not limited by their intrinsic catalytic abilities, which are related to the presence of preorganized water networks in their macrocyclic cavities, but rather by the efficiency of photogeneration of oxidant PS^+ and the ability of this species to act as an oxidizing agent to the WOCs. Therefore, it can be concluded that to increase the efficiency of Ru(bda) macrocycles in light-driven water oxidation the design of new photosensitizers would be required which are able to generate stable photooxidants in high yields in the presence of a minimum amount of organic co-solvents. High-performance photocatalytic systems for water splitting desired for application in solar fuel devices might be accessible with fully water-soluble WOCs in combination with properly functionalized photosensitizers.

Chapter 5 – Summary

In light of the rapidly increasing global demand of energy and the negative effects of climate change, innovative solutions that allow an efficient transition to a carbon-neutral economy are urgently needed. In this context, artificial photosynthesis is emerging as a promising technology to enable the storage of the fluctuating energy of sunlight in chemical bonds of transportable “solar fuels” (*Chapter 2.2*). Hereby, light-driven oxidation of water to molecular oxygen is expected to provide the reducing equivalents required for the production of those fuels. Thus, in recent years much efforts have been devoted to the development of robust water oxidation catalysts (WOCs) leading to the discovery of the highly reactive Ru(bda) (bda: 2,2’-**b**ipyridine-6,6’-**d**icarboxylic **a**cid) catalyst family (*Chapter 2.3*). Recently, following a supramolecular approach Würthner and co-workers designed macrocycle **MC3** (Figure 45a) bearing three catalytically active Ru(bda) units.[18] This supramolecular WOC showed an outstanding catalytic activity in chemical water oxidation. Based on theoretical simulations, this was ascribed to the formation of a hydrogen-bonded network of water molecules in the cavity of the macrocycle that facilitates cooperative proton abstractions during catalysis,[19] similar to catalytic processes by some enzymes and natural photosystem II.[37b, 141] Mechanistic studies based on kinetic analysis and ^{18}O labelling experiments revealed that **MC3** operates through a WNA (water nucleophilic attack) mechanism. The aim of this thesis was the study of chemical and photocatalytic water oxidation with functionalized **MC3** macrocycles to explore the impact of substituents on molecular properties and catalytic activities of the trinuclear macrocyclic Ru(bda) catalysts. A further objective of this thesis comprises the elucidation of factors that influence the light-driven water oxidation process with this novel class of supramolecular WOCs.

To explore the effects of substituents on catalytic water oxidation, a series of new trinuclear Ru(bda) macrocycles bearing methoxy, methyl or fluoro substituents either in the bridging or equatorial bda ligand was synthesized (Figure 45a) and their catalytic activities in chemical and photochemical water oxidation were thoroughly studied (Chapter 3). The hitherto unknown Ru complexes were adequately characterized by NMR spectroscopy, high resolution mass spectrometry and elemental analysis, and for the derivatives ***m*-F-MC3** and ***p*-F-MC3** single-crystal X-ray analysis could be performed that, for the first time, unequivocally confirmed the trinuclear macrocyclic structure of this class of WOCs (Figure 46a). Previous investigations on the mechanism of water oxidation with parent macrocycle **MC3** revealed that

the oxidation of Ru^{IV} to Ru^{V} is the rate-determining step.[18] Thus, the introduction of electron donating substituents into the macrocyclic structure was expected to increase the electron density at the Ru centers and, as a result, decrease the $Ru^{V/IV}$ oxidation potential and accelerate the rate of oxygen formation compared to **MC3**. Contrary to these expectations, cyclic and differential pulse voltammetry measurements of the functionalized Ru macrocycles revealed that the modification of the ligands did not result in desired tuning of the oxidation potentials of the macrocyclic complexes to modulate the formation of Ru^{V}.

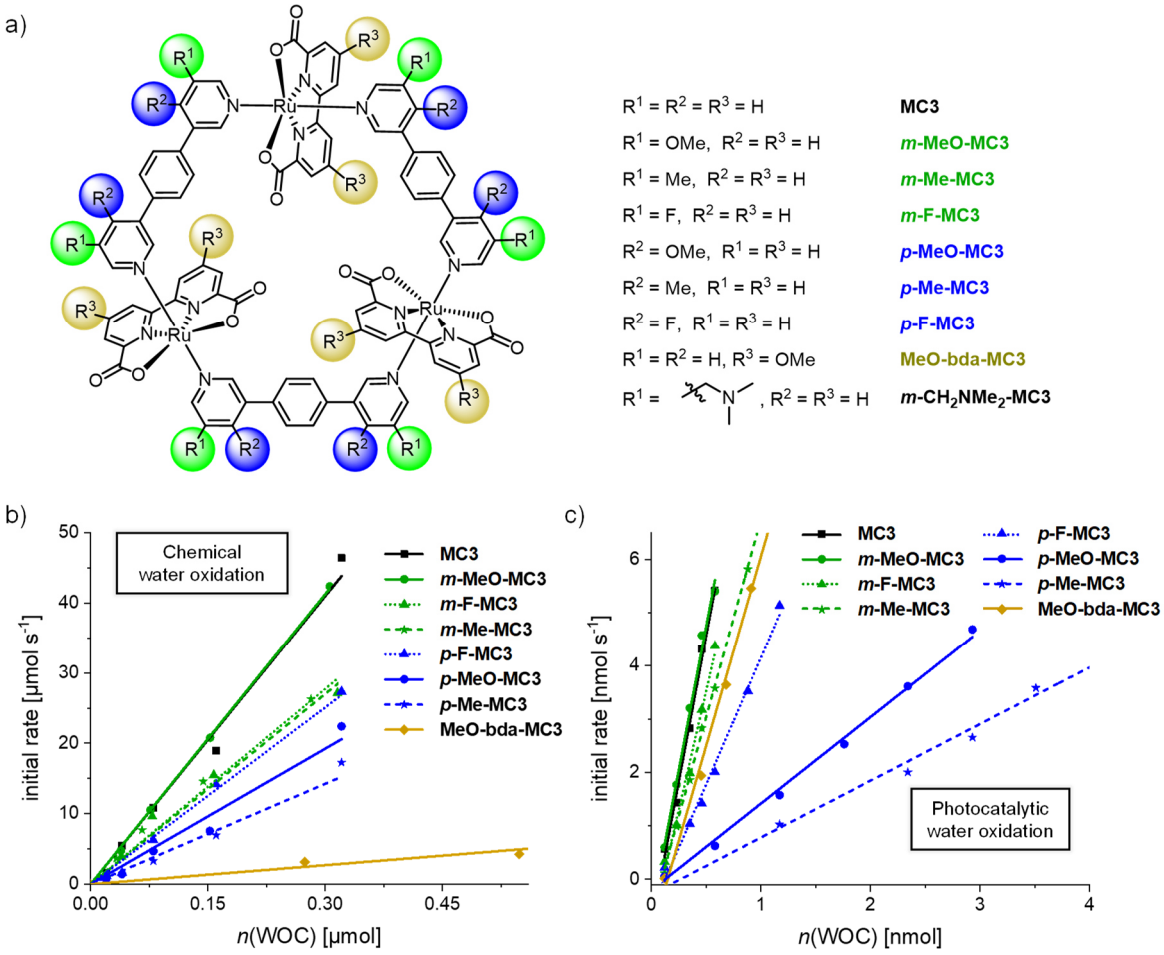

Figure 45. a) Chemical structures of trinuclear Ru(bda) macrocycles functionalized at the bda or bridging ligand in *meta* or *para*-position. b,c) Catalytic activities of functionalized macrocycles in (b) chemical (reagent: ceric ammonium nitrate) and (c) photocatalytic water oxidation (reagents: $[Ru(bpy)_3]Cl_2$, sodium persulfate) determined by analysis of initial rates of catalysis (see *Chapter 3* for details on experimental conditions).

Moreover, UV/vis absorption spectroscopy as well as spectroelectrochemistry studies showed that the substituents at bridging ligand had only a negligible effect on the optical properties of the WOCs. To characterize possible catalytic intermediates of the Ru macrocycles in their Ru^{III} and Ru^{IV} oxidation states, time-dependent EPR and X-ray absorption spectroscopy

studies were performed. These experiments, once again, confirmed the minor impact of the substituents on the molecular properties of the Ru macrocycles. An indirect confirmation for the preorganized water network in the macrocyclic cavity of the WOCs was obtained by extended X-ray absorption fine structure (EXAFS) as the measured Ru^{IV}-OH bond lengths of 1.88 Å, which were considerably shorter than 1.96 Å reported for mononuclear complex $Ru^{IV}(OH)(bda)(pic)_2$ (pic: picoline),[79] could only be explained under consideration of a hydrogen-bonded network between the Ru centers.

The catalytic activities of the functionalized macrocycles were then investigated in chemical water oxidation with ceric ammonium nitrate (CAN) as oxidant and under photochemical conditions using a three-component system based on a ruthenium tris(bipyridine) photosensitizer, sodium persulfate as sacrificial electron acceptor and the supramolecular catalysts. Interestingly, in both chemical and photocatalytic water oxidation the *meta*-functionalized macrocycles reached similar catalytic activities as parent **MC3** and higher turnover frequency (TOF) values than their *para*-substituted counterparts (Figure 45b,c). Therefore, the diverse trends observed in catalytic performance of the Ru macrocycles cannot be ascribed to the electronic nature of the introduced substituents, rather to the position at which these were introduced. Functionalization of the bda ligand with methoxy groups led to a decrease in catalytic efficiency of macrocycle **MeO-bda-MC3** of more than one order of magnitude compared to parent **MC3** in chemical water oxidation. However, under photocatalytic conditions the modified WOC reached a comparatively high TOF as illustrated in Figure 45b,c. This can be attributed to the higher lability of the methoxy bearing ligands under the acidic conditions required for chemical water oxidation using CAN. More importantly, the macrocyclic nature of the functionalized WOCs provided the unique opportunity to perform unprecedented studies on the role of steric effects on the catalytic activity of regioisomeric *meta* and *para*-substituted Ru(bda) catalysts. Detailed investigations by X-ray crystal structure analysis and theoretical simulations, the latter performed in collaboration with the group of Prof. Roland Mitrić (Institut für Physikalische und Theoretische Chemie, Universität Würzburg), showed that conformational changes imparted by the substituents were indeed responsible for the variation of the catalytic activities of the Ru macrocycles. For instance, functionalization at the *para*-position induces partial rotation of one of the catalytically active Ru(bda) centers with the open coordination site pointing to the outside of the macrocyclic cavity as it was observed in the crystal structure of ***p*-F-MC3** (Figure 46a). Nevertheless, according to the performed metadynamics simulations this rotation plays only a minor role in solution. Therefore, the reduced catalytic activity of the *para*-WOCs is better explained by the parallel orientation of the axial pyridyl ligands that leads to a restricted access of the 7th coordination site of Ru to water molecules. In contrast, in *meta*-substituted macrocycles and

parent **MC3** WOC a twisted orientation of the axial ligands results in permanently available Ru centers for coordination of water molecules.

As mentioned before, based on theoretical simulations the high catalytic efficiency of the **MC3** macrocycle has been previously ascribed to the presence of a hydrogen-bonded network of preorganized water molecules in its cavity.[18-19] In this thesis, for the first time, a direct experimental indication for the formation of such a water network was presented. This was obtained from the crystal structure of macrocycle ***m*-F-MC3** (Figure 46a). Presumably, the high hydrophilicity of the macrocyclic cavity resulting from rotation of the carboxylic groups of all Ru(bda) moieties to the inside of the cavity constitutes the driving force for the accumulation of water molecules from not dried solvent. In contrast, no ordered water network was found in the crystal structure of ***p*-F-MC3** containing carboxylic groups that are oriented to the outside of the cavity (Figure 46a). This finding indeed strengthens the hypothesis that hydrogen-bonded water networks in **MC3** and *meta*-substituted derivatives might facilitate efficient proton-coupled electron transfer (PCET) processes during catalysis following a Grotthuss-type mechanism (Figure 46b) and thus are responsible for the observed high catalytic activities of these Ru macrocycles in water oxidation.

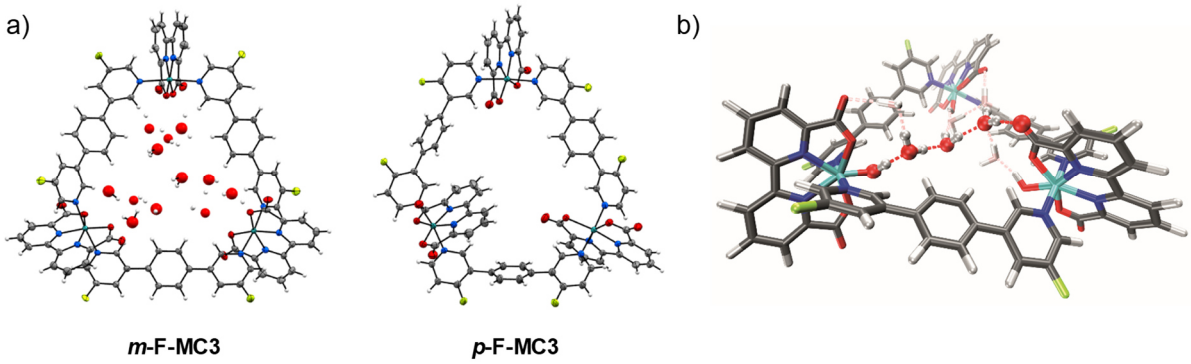

Figure 46. a) Crystal structures of ***m*-F-MC3** and ***p*-F-MC3** determined by single crystal X-ray diffraction (ORTEP diagram with thermal ellipsoids set at 50% probability). b) DFT-refined structure of ***m*-F-MC3** in Ru^{IV}_3 oxidation state showing network of preorganized water molecules connecting Ru centers. Grey: carbon, white: hydrogen, red: oxygen, blue: nitrogen, turquoise: ruthenium, green-yellow: fluorine.

Chapter 4 focuses on light-driven water oxidation with trinuclear Ru(bda) macrocycles **MC3** and ***m*-CH_2NMe_2-MC3** (Figure 45a) using a series of ruthenium tris(bipyridine) complexes **PS0–3** (Figure 47) under varied reaction conditions. Although, chemical water oxidation with ***m*-CH_2NMe_2-MC3** bearing six trialkylamine groups in axial ligands has been reported previously,[20] its catalytic activities under light-driven conditions remained unexplored. Here, control experiments showed that the photocatalytic activity of ***m*-CH_2NMe_2-MC3** is quite similar to **MC3** under identical conditions. Hence, the catalytic efficiency of ***m*-CH_2NMe_2-MC3** is not

considerably affected by the incorporated tertiary amino groups in *meta*-position in agreement with findings presented in *Chapter 3*. Thus, the photocatalytic activities of **MC3** and ***m*-CH_2NMe_2-MC3** were studied in a comparative manner. Photocatalytic experiments with **MC3** were performed in 50% MeCN, while studies with highly water-soluble ***m*-CH_2NMe_2-MC3** were conducted in 5% MeCN as well. Catalyst concentration-dependent experiments revealed that the photocatalytic activities of both Ru macrocycles are significantly affected by the choice of photosensitizer and reaction media, in addition to buffer concentration, light intensity and concentration of the sensitizer.

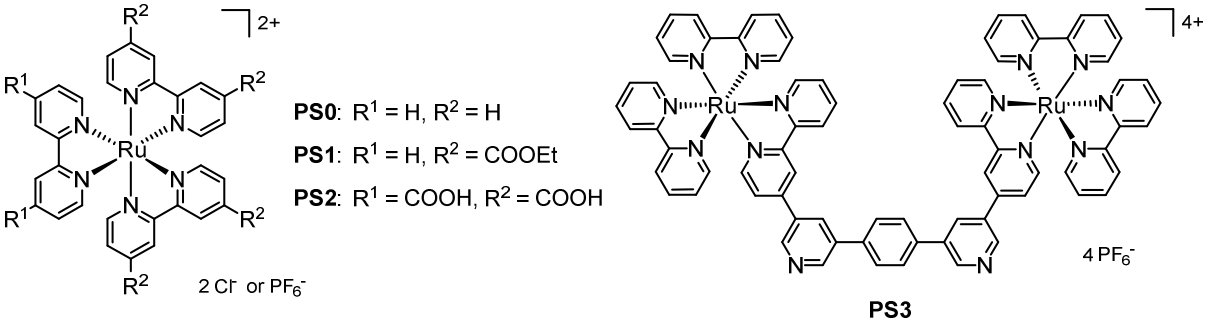

Figure 47. Chemical structures of ruthenium tris(bipyridine) photosensitizers **PS0–3** used in photocatalytic water oxidation with trinuclear Ru macrocycles **MC3** and ***m*-CH_2NMe_2-MC3**.

The kinetics of *in situ* generation of photooxidant $[Ru(bpy)_3]^{3+}$ and electron transfer from the trinuclear catalysts to the photooxidant were studied by steady-state emission quenching and nanosecond flash photolysis, respectively, to gain a deeper insight into the complex process of photocatalytic water oxidation with supramolecular Ru catalysts. These investigations revealed that under the studied conditions the photocatalytic performance of the trinuclear Ru(bda) macrocycles is not limited by their intrinsic catalytic abilities but rather by the efficiency of generation of $[Ru(bpy)_3]^{3+}$ and its ability to act as an oxidizing agent to the catalysts as both are strongly dependent on the choice of photosensitizer and the amount of employed organic co-solvent. Accordingly, in 50% MeCN the highest TOF and TON (**t**urn**o**ver **n**umber) values were reached by WOC **MC3** with photosensitizer **PS0**. In contrast, in 5% MeCN catalyst ***m*-CH_2NMe_2-MC3** exhibited its highest catalytic activity in combination with ester decorated sensitizer **PS1**, presumably due to the larger thermodynamic driving force for the electron transfer between WOC and sensitizer resulting from the introduction of the electron withdrawing groups. This became important only upon reduction of the MeCN content since in 50% MeCN the quenching of **PS1** by sodium persulfate and hence the generation of the respective $[Ru(bpy)_3]^{3+}$ oxidant is inefficient.

In conclusion, chemical and photocatalytic water oxidation with a broad series of trinuclear Ru(bda) macrocycles bearing different substituents at the axial or equatorial ligands was investigated within the scope of this thesis. The role of steric and electronic effects on the catalytic activity of regioisomeric Ru(bda) catalysts was elucidated and in-depth studies on photocatalytic water oxidation with this class of supramolecular WOCs were conducted. Furthermore, for the first time an experimental indication for the previously proposed network of preorganized water molecules in the cavity of the Ru macrocycles was obtained which is most probably responsible for their high catalytic efficiencies. The detailed studies of this thesis brought into the light that, not the electronic nature of the substituents, but their steric effects leading to conformational changes of the macrocycles are responsible for the substituent-dependent catalytic activities of this class of WOCs which was rather unexpected. Hence, the novel findings of this thesis will contribute to the rational design of new high-performance catalysts for water oxidation that are required for application in solar fuel devices.

Chapter 6 – Zusammenfassung

Innovative Ansätze zur Ermöglichung eines effizienten Übergangs zur CO_2-Neutralität werden angesichts der schnell steigenden Nachfrage nach Energie und der negativen Effekte des Klimawandels dringend gesucht. In diesem Zusammenhang hat das Konzept der künstlichen Photosynthese in den letzten Jahren für besondere Aufmerksamkeit gesorgt. Hierbei sollen unter Nutzung von Sonnenenergie chemische Energieträger, sogenannte „solare Brennstoffe“, produziert werden, welche sich speichern, lagern und transportieren lassen (*Kapitel 2.2*). Die dazu benötigten Reduktionsäquivalente sollen aus der Oxidation von Wasser zu molekularem Sauerstoff erhalten werden, wobei hierfür stabile Katalysatoren nötig sind. In dieser Hinsicht erscheinen in 2009 erstmals beschriebenen Ru(bda) (bda: 2,2'-bipyridin-6,6'-dicarbonsäure, engl.: 2,2'-**b**ipyridine-6,6'-**d**icarboxylic **a**cid) Wasseroxidations-katalysatoren besonders vielversprechend, welche sich durch eine erhöhte Reaktivität im Vergleich zu vorherigen Systemen auszeichnen (*Kapitel 2.3*). Würthner und Mitarbeiter verfolgten daraufhin einen supramolekularen Ansatz zur Entwicklung eines aus drei katalytisch aktiven Ru(bda) Einheiten bestehenden Makrozyklus.[18] Dieser **MC3** benannter Katalysator (Abbildung 45a) zeigt eine überaus hohe katalytische Aktivität in der chemischen Wasseroxidation, welche basierend auf theoretischen Simulationen auf die Ausbildung eines Wassernetzwerks in der Kavität des Makrozyklus mit einhergehenden kooperativen Protonenabstraktionen während der Katalyse zurückgeführt wird.[19] Ähnliche Vorgänge werden auch in einigen Enzymen sowie im natürlichen Photosystem II beobachtet.[37b, 141] Mittels kinetischer Untersuchungen und ^{18}O-Isotopenmarkierungsexperimenten wurde zudem festgestellt, dass **MC3** nach dem WNA (nukleophiler Wasserangriff, engl.: **w**ater **n**ucleophilic **a**ttack) Mechanismus agiert. Das Ziel dieser Forschungsarbeit war die Untersuchung von funktionalisierten **MC3** Makrozyklen in der chemischen und photokatalytischen Wasseroxidation, um den Einfluss der Substituenten in den Liganden auf molekulare Eigenschaften und katalytische Aktivitäten der Makrozyklen zu analysieren. Des Weiteren sollten Faktoren identifiziert werden, welche Einfluss auf die Effizienz der Photokatalyse mit dieser neuartigen Klasse von supramolekularen Katalysatoren ausüben.

Um den Einfluss von Substituenten in makrozyklischen WOCs auf die katalytische Wasseroxidation zu erforschen, wurde eine Reihe von neuen trinuklearen Ru(bda) Makrozyklen synthetisiert, deren äquatoriale oder Brückenliganden durch die Einführung von Methoxy-, Methyl- oder Fluorosubstituenten modifiziert wurden (Abbildung 45a). Die

katalytischen Aktivitäten dieser bisher unbekannten Makrozyklen wurden nach erfolgreicher Charakterisierung mittels NMR Spektroskopie, Massenspektrometrie und Elementaranalyse in der chemischen und photokatalytischen Wasseroxidation untersucht (Kapitel 3). Die fluorierten Derivate ***m*-F-MC3** und ***p*-F-MC3** konnten zudem mittels Röntgenkristallographie analysiert werden, wodurch zum ersten Mal die trinukleare Struktur der Makrozyklen dieser Klasse zweifelsfrei nachgewiesen werden konnte (Abbildung 46a). Vorausgegangene mechanistische Untersuchungen am **MC3** Makrozyklus zeigten, dass die Oxidation von Ru^{IV} zu Ru^{V} der geschwindigkeitsbestimmende Schritt der Wasseroxidationskatalyse mit diesem Ru Komplex darstellt.[18] Aus diesem Grund sollte durch die Einführung von elektronenschiebenden Substituenten die Elektronendichte am Ru erhöht werden, damit durch Erniedrigung des $Ru^{V/IV}$ Oxidationspotentials eine effizientere Sauerstoffproduktion im Vergleich zur Stammverbindung **MC3** erreicht wird. Cyclo- und differentialpuls-voltammetrische Untersuchungen zeigten jedoch, dass die Ligandenfunktionalisierung nicht zur gewünschten Anpassung der Redoxeigenschaften der Ru-Makrozyklen führte.

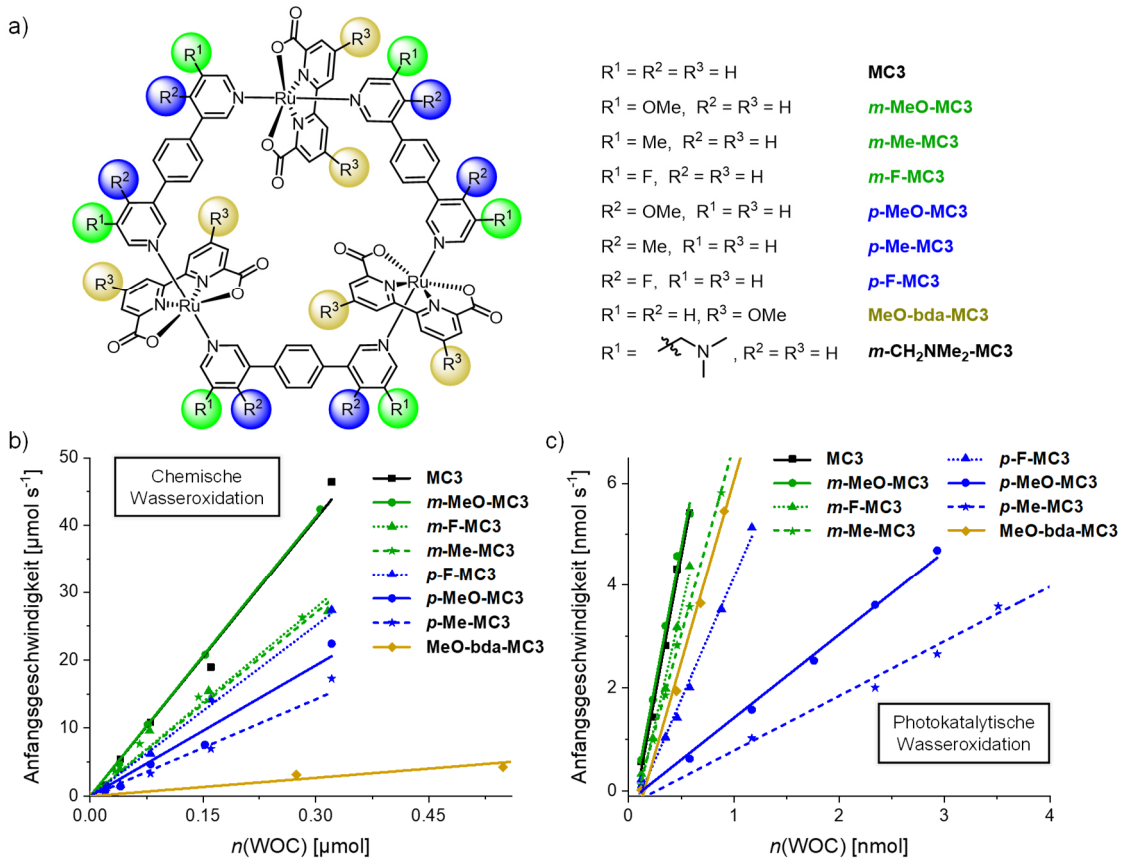

Abbildung 45. a) Chemische Struktur von trinuklearen Ru(bda) Makrozyklen mit funktionalisierten bda oder Brückenliganden. Letztere wurden durch die Einführung von Substituenten in der *meta*- oder *para*-Position modifiziert. b,c) Katalytische Aktivitäten der funktionalisierten Makrozyklen in der (b) chemischen (Reagens: Ammoniumcer(IV)-nitrat) und (c) photokatalytischen Wasseroxidation (Reagenzien: $[Ru(bpy)_3]Cl_2$, Natriumpersulfat). Aktivitäten wurden durch Analyse der Reaktions-Anfangsgeschwindigkeiten bestimmt (s. *Kapitel 3* für experimentelle Bedingungen).

Mittels UV/vis Absorptionsspektroskopie und Spektroelektrochemie wurde zudem ein geringer Effekt der Substituenten auf die optischen Eigenschaften der funktionalisierten Makrozyklen nachgewiesen. Darüber hinaus erfolgte die Charakterisierung von möglichen katalytischen Ru^{III} und Ru^{IV} Intermediaten der supramolekularen Ru Makrozyklen durch zeitabhängige EPR und Röntgenabsorptionsspektroskopie. Diese Studien zeigten erneut einen geringen Einfluss der Substituenten auf die molekularen Eigenschaften der Ru Makrozyklen. Mittels EXAFS (erweiterte Röntgenabsorption Feinstruktur, engl: **e**xtended **X**-ray **a**bsorption **f**ine **s**tructure) wurde ein indirekter Beweis für die Existenz eines präorganisierten Wassernetzwerks in der Kavität der Makrozyklen erhalten. Die für den oxidierten **MC3** Makrozyklus bestimmte Ru^{IV}-OH Bindungslänge von 1.88 Å ist tatsächlich deutlich kürzer als die entsprechende Bindungslänge des mononuklearen Komplexes $Ru^{IV}(OH)(bda)(pic)_2$ (pic: picoline) (1.96 Å).[79] Dieser erhebliche Unterschied kann nur durch die Anwesenheit eines wasserstoffverbrückten Wassernetzwerks in der makrozyklischen Kavität erklärt werden.

Anschließend wurden die katalytischen Aktivitäten der funktionalisierten Makrozyklen sowohl in der chemischen als auch in der photokatalytischen Wasseroxidation untersucht. Während bei der ersten Methode Ammoniumcer(IV)-nitrat (engl.: ceric ammonium nitrate, CAN) als chemisches Oxidationsmittel verwendet wird, findet für die Untersuchung der Photokatalyse ein drei-Komponenten-System Anwendung. Dieses besteht aus Tris(bipyridyl)ruthenium(II)-Komplexen als Photosensibilisatoren, Natriumpersulfat als Elektronenakzeptor und den Ru Makrozyklen als Wasseroxidationskatalysatoren. Als besonders interessant erwies sich, dass sowohl bei der chemischen als auch bei der photokatalytischen Wasseroxidation die *meta*-substituierten Makrozyklen eine hohe katalytische Aktivität vergleichbar mit der des Stammkomplexes **MC3** aufwiesen, während sie zugleich bedeutend höhere TOF Werte (TOF: Umsatzfrequenz, engl.: **t**urn**o**ver **f**requency) als die entsprechenden *para*-Derivate erzielten (Abbildung 45b,c). Dies deutete darauf hin, dass die katalytischen Aktivitäten der funktionalisierten Makrozyklen statt von elektronischen Effekten eher durch sterische Effekte der eingeführten Substituenten beeinflusst wurden. Die Funktionalisierung des bda Liganden mit Methoxygruppen führte ferner dazu, dass die katalytische Performance des **MeO-bda-MC3** Makrozyklus in der chemischen Wasseroxidation im Vergleich zur Stammverbindung **MC3** um mehr als eine Größenordnung reduziert wurde. Beide Makrozyklen erreichten jedoch ähnlich hohe TOF Werte in der photokatalytischen Wasseroxidation (Abbildung 45b,c). Dies kann als Folge der höheren Labilität der Methoxy-funktionalisierten Liganden unter den für die chemische Wasseroxidation unter Verwendung von CAN benötigten sauren Bedingungen erklärt werden.

Die makrozyklische Struktur der im Rahmen dieser Arbeit funktionalisierten Ru(bda) Komplexe ermöglichte die erstmalige Untersuchung von sterischen Effekten auf die katalytische Aktivität von *meta*- und *para*-Regioisomeren der supramolekularen Katalysatoren. Hierbei wurden mittels Röntgeneinkristallstrukturanalyse und theoretischer Simulationen, welche in Kooperation mit der Gruppe von Prof. Roland Mitrić (Institut für Physikalische und Theoretische Chemie, Universität Würzburg) durchgeführt wurden, aus der Einführung von Substituenten resultierende konformationelle Änderungen der Ru Makrozyklen erfasst. So wurde durch *para*-Funktionalisierung eine partielle Verdrehung einer der Ru(bda) Einheiten beobachtet, so dass die offene Koordinationsstelle am Ru nicht in die makrozyklische Kavität, sondern nach außen weist (Abbildung 46a). Diese unerwünschte Rotation der Ru Zentren sollte dennoch den metadynamischen Simulationen zufolge nur eine geringe Rolle in wässriger Lösung spielen. Als Ursache für die Unterschiede der katalytischen Aktivitäten der *meta*- und *para*-Makrozyklen wurde daher die Zugänglichkeit der Ru-Zentren für den Angriff von Wassermolekülen vorgeschlagen. Folglich tritt bei *para*-Substitution eine parallele Orientierung der axialen Pyridylliganden auf, welche zum erschwerten Zugang der Ru-Zentren für die Koordination von Wasser führt. Im Gegensatz dazu ergibt sich aus der *meta*-Substitution und im Fall des Stammkatalysators **MC3** eine verdrillte Orientierung dieser axialen Liganden, die dafür sorgt, dass die Ru-Zentren permanent für die Koordination von Wassermolekülen zur Verfügung stehen.

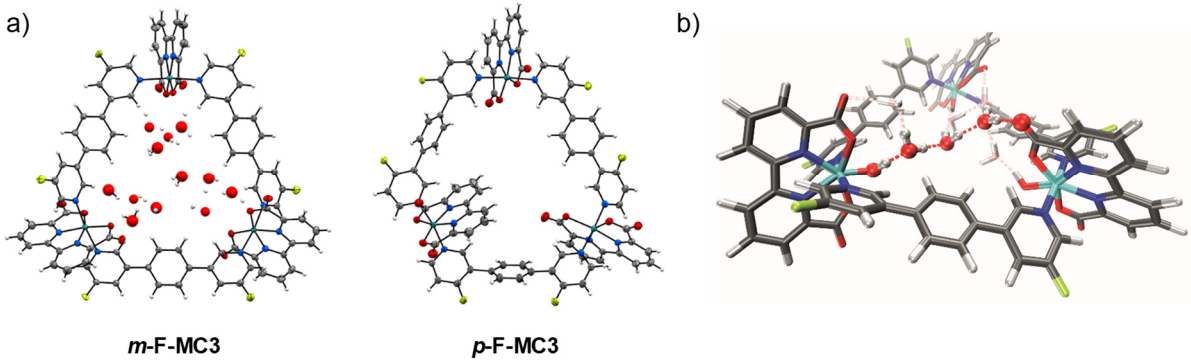

Abbildung 46. a) Einkristallröntgenstrukturanalyse von ***m*-F-MC3** und ***p*-F-MC3**, gezeigt als thermische Ellipsoide mit 50%-iger Wahrscheinlichkeit. b) DFT-optimierte Struktur von ***m*-F-MC3** in der Ru^{IV}_3 Oxidationsstufe zeigt ein präorganisiertes Wassernetzwerk zwischen den benachbarten Ru-Zentren. Grau: Kohlenstoff, weiß: Wasserstoff, rot: Sauerstoff, blau: Stickstoff, türkis: Ruthenium, gelbgrün: Fluor.

Wie bereits erwähnt lieferten zuvor berichtete theoretische Simulationen Hinweise auf die Bildung eines durch Wasserstoffbrücken stabilisierten Wassernetzwerks in der Kavität von **MC3**, welches seine hohe katalytische Aktivität für Wasseroxidation erklären könnte.[18-19] Im

Rahmen dieser Arbeit wurde zum ersten Mal die Existenz eines solchen Wassernetzwerks innerhalb der Kavität der trinuklearen Ru(bda) Makrozyklen experimentell belegt. Hierbei wurde bei der Röntgeneinkristallstrukturanalyse von ***m*-F-MC3** geordnete Restelektronendichte in der makrozyklischen Kavität gefunden, welche Wassermolekülen zugeordnet werden konnte (Abbildung 46a). Zu vermuten ist, dass die vorliegende Ausrichtung der drei Ru(bda)-Einheiten mit nach innen zeigenden Carbonsäuregruppen zu einer hohen Hydrophilizität der Kavität und einer daraus resultierenden Ansammlung von Wassermolekülen aus den nicht vorgetrockneten Lösungsmitteln geführt hat. Interessanterweise wurde kein geordnetes Wassernetzwerk in der Kavität von ***p*-F-MC3** gefunden, wobei in diesem Fall einige Ru(bda)-Carbonsäuregruppen nach außen zeigen (Abbildung 46a). Somit gewinnt die aufgestellte Hypothese der Erhöhung der katalytischen Aktivitäten von **MC3** und den *meta*-substituierten Makrozyklen durch Anwesenheit eines präorganisierten Wassernetzwerks in ihren Kavitäten weiter an Bedeutung. Dabei kann die hohe Wasseroxidationsaktivität dieser Makrozyklen vermutlich auf effiziente Protonen gekoppelte Elektronentransfer (engl.: proton-coupled electron transfer, PCET) Prozesse zurückgeführt werden, welche wie in Abbildung 46b gezeigt nach einem Grotthuss-Mechanismus stattfinden.

Kapitel 4 präsentiert die Ergebnisse einer detaillierten Studie über die lichtinduzierte Wasseroxidation mit den trinuklearen Ru(bda)-Makrozyklen **MC3** und ***m*-CH_2NMe_2-MC3** (Abbildung 45a) unter Verwendung von Tris(bipyridyl)ruthenium(II)-Komplexen **PS0–3** (Abbildung 47) als Photosensibilisatoren. Über die katalytische Aktivität von ***m*-CH_2NMe_2-MC3** in der chemischen Wasseroxidation wurde bereits berichtet.[20] Dennoch blieb bislang die photokatalytische Effizienz dieses über sechs Trialkylamin-Substituenten verfügenden Makrozyklus unerforscht. Kontrollexperimente zeigten, dass beide Ru Makrozyklen **MC3** und ***m*-CH_2NMe_2-MC3** unter identischen Bedingungen eine ähnliche photokatalytische Aktivität aufweisen. Dies ist in Übereinstimmung mit den Ergebnissen aus *Kapitel 3*, die bestätigten, dass die katalytischen Aktivitäten von trinuklearen Ru(bda)-Makrozyklen nur geringfügig durch das Einführen von Substituenten in der *meta*-Position beeinflusst werden. Die photokatalytischen Aktivitäten von **MC3** und ***m*-CH_2NMe_2-MC3** wurden daher vergleichend untersucht. Während Experimente mit **MC3** unter Verwendung von 50% MeCN als organisches Co-Lösungsmittel durchgeführt wurden, erfolgte die Studie der Photokatalyse mit dem wasserlöslichen Makrozyklus ***m*-CH_2NMe_2-MC3** auch unter Reduktion des MeCN Gehaltes auf 5%. Als besonders interessant erwies sich hierbei, dass die photokatalytischen Aktivitäten beider Makrozyklen erheblich durch die Auswahl des Photosensibilisators und des Reaktionsmediums beeinflusst werden. Zusätzlich wurde der Einfluss der Lichtintensität

sowie der Konzentration von Puffer und Photosensibilisator auf die Effizienz der Katalyse untersucht.

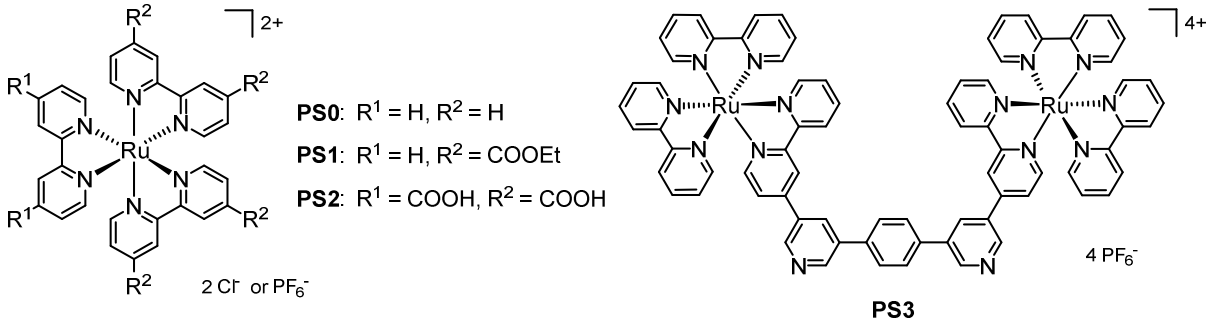

Abbildung 47. Chemische Struktur von Tris(bipyridyl)ruthenium(II)-Komplexen **PS0–3**, welche für die Untersuchung der photokatalytisichen Wasseroxidation mit trinuklearen Ru Makrozyklen **MC3** und ***m*-CH_2NMe_2-MC3** verwendet wurden.

Um einen tieferen Einblick in den komplexen Prozess der Photokatalyse mit den supramolekularen Ru-Katalysatoren zu gewinnen, wurde die Kinetik der *in situ* Photogenerierung des Oxidationsmittels $[Ru(bpy)_3]^{3+}$ sowie des Elektronentransfers zwischen den trinuklearen Katalysatoren und dem Photooxidans mittels Emissionslöschung im stationären Zustand und Nanosekunden-Blitzphotolyse analysiert. Es wurde festgestellt, dass unter den untersuchten Bedingungen die katalytische Effizienz der Ru(bda)-Makrozyklen nicht durch ihre intrinsischen katalytischen Eigenschaften begrenzt ist. Vielmehr wurden die katalytischen Aktivitäten der Ru-Makrozyklen durch die Effizienz der Generierung von $[Ru(bpy)_3]^{3+}$ sowie dessen Fähigkeit als Oxidationsmittel zu fungieren limitiert. Interessanterweise sind beide stark von der Auswahl des Photosensibilisators und der verwendeten Menge an organischem Co-Lösungsmittel abhängig. Während **MC3** die höchsten TOF- und TON-Werte (TON: Umsatzzahl, engl.: **t**urn**o**ver **n**umber) in 50% MeCN unter Verwendung von **PS0** erreichen konnte, wies ***m*-CH_2NMe_2-MC3** in 5% MeCN seine höchste Aktivität in Kombination mit dem Ester-funktionalisierten Sensibilisator **PS1**. In diesem Fall spielte vermutlich die höhere thermodynamische Triebkraft für den Elektronentransfer zwischen Katalysator und Sensibilisator eine Rolle, welche sich aus der Einführung von elektronenziehenden Substituenten ergibt. Da in 50% MeCN die Emissionslöschung von **PS1** durch Natriumpersulfat und dadurch die Bildung des entsprechenden $[Ru(bpy)_3]^{3+}$ Oxidans ineffizient sind, wird der Effekt der thermodynamischen Triebkraft nur bei Reduktion des MeCN Gehaltes beobachtet.

Zusammenfassend wurde in dieser Arbeit an der Entwicklung neuartiger trinuklearer Ru(bda)-Makrozyklen mit funktionalisierten axialen oder äquatorialen Liganden geforscht, welche Anwendung als molekulare Katalysatoren sowohl in der chemischen als auch in der

photokatalytischen Wasseroxidation finden. Dabei wurde die wichtige Rolle von sterischen und elektronischen Effekten auf die katalytischen Aktivitäten von *meta*- und *para*-Regioisomeren der supramolekularen Komplexe aufgeklärt und detaillierte Studien über die photokatalytische Wasseroxidation mit den Ru-Makrozyklen durchgeführt. Zusätzlich wurde zum ersten Mal ein experimenteller Hinweis für die Existenz eines präorganisierten Wassernetzwerks in der Kavität der Ru(bda)-Makrozyklen erhalten, welches vermutlich ihre hohe Aktivität in der Wasseroxidation erklärt. Die ausführlichen Untersuchungen, welche in dieser Arbeit präsentiert wurden, zeigten zudem, dass anstelle von elektronischen Einflüssen eher sterische Effekte der Substituenten zu konformationellen Änderungen der Makrozyklen führen und letztendlich die beobachtete Substituenten-Abhängigkeit der katalytischen Aktivitäten dieser Katalysator-Klasse erklären. Somit leisten die im Rahmen dieser Forschungsarbeit gewonnenen Erkenntnisse einen Beitrag zur Entwicklung neuer Hochleistungskatalysatoren für die Wasseroxidation, welche für die Fertigung von effizienten Vorrichtungen zur Produktion von solaren Brennstoffen gebraucht werden.

Chapter 7 – Experimental Section

7.1 Materials and Methods

Chemicals

Reagents and solvents, if not stated otherwise, were purchased from commercial sources and used as received. Compounds 2,2'-bipyridine-6,6'-dicarboxylic acid (H_2bda),[167] [$RuCl_2(dmso)_4$],[168] [Ru(bda)$(dmso)_2$] (**35**),[133] 6,6'-dibromo-4,4'-dimethoxy-2,2'-bipyridine (**36**),[131] 3-bromo-4-methoxypyridine,[151] [$Ru(bpy)_2Cl_2$],[169] [$Ru(bpy)_2$(bpy-4,4'-COOEt)]$(PF_6)_2$ (**PS1**),[148] [Ru(bpy-4,4'-$COOH)_3$]Cl_2 (**PS2**)[149] and 4-bromo-2,2'-bipyridine (**44**) [150] were synthesized according to literature procedures. Ligand 1,4-di(pyridin-3-yl)benzene (**bpb**)[18] and Ru macrocycles **MC3**[18] and ***m*-CH_2NMe_2-MC3**[20] were prepared as described in preceding publications by Würthner and co-workers.

Anhydrous DCM, THF, DMF and methanol were prepared using a Pure Solv MD-5 solvent purification system (Innovative Technology). All experiments in aqueous solutions were performed in either phosphate buffer pH 7 (Honeywell) or deionized water obtained from a Purelab Classic water purification system (ELGA).

Thin Layer Chromatography (TLC) and Column Chromatography

Analytical TLC was carried out on sheets pre-coated with silica gel (Alugram Xtra Sil G/UV_{254}, Macherey-Nagel) or aluminum oxide (Polygram Alox N/UV254, Macherey-Nagel). Compounds were purified, where specified, by column chromatography using silica gel (60M, 0.04-0.063 mm, Macherey-Nagel) or neutral aluminum oxide (EcoChrom MP Alumina N Act. V, MP Biomedicals).

Size Exclusion Chromatography

For size exclusion chromatography BioBeads particles (S-X3, Bio-Rad) suspended in a 9:1 mixture of DCM/MeOH were used.

NMR Spectroscopy

^{1}H-NMR spectra were recorded at 25 °C, unless otherwise noted, at 400 MHz or 600 MHz using a Bruker Avance III HD 400 or Bruker Avance III HD 600 spectrometer, respectively. Proton decoupled ^{13}C-NMR spectra were recorded at 100 MHz or 150 MHz using the same spectrometers, respectively. Chemical shifts δ are indicated in parts per million (ppm) relative to residual undeuterated solvent signals[170] and coupling constants J in Hz. Signal multiplicity is described using the following abbreviations: s = singlet, d = doublet, t = triplet and m = multiplet. 2D-NMR spectra (COSY, NOESY, HSQC and HMBC) were recorded to allow for a correct interpretation of the 1D-NMR spectra of novel compounds.

Mass Spectrometry

HR-ESI mass spectra were recorded on an ESI micrOTOF focus mass spectrometer (Bruker Daltonics). HR-MALDI spectra were measured on an Autoflex II spectrometer (Bruker Daltonics). All spectra were recorded in positive ion mode. DCTB was used as matrix for MALDI measurements.

Elemental Analysis

Elemental analysis was performed at the Institute of Inorganic Chemistry of the University of Würzburg using a Vario MICRO cube (Elementar Analysensysteme). For elemental analysis samples were dried under high vacuum for 12 h at 60 °C. Samples were then prepared in the Glovebox (Braun) under inert atmosphere.

Determination of Melting Points

Melting points were determined using a B-545 melting point apparatus (Büchi) or a BX41 optical microscope (Olympus) and are uncorrected.

X-ray Crystallography

Single crystals of ***m*-F-MC3** and ***p*-F-MC3** were obtained by slow evaporation of a DCM/MeOH solution of the macrocycles under an argon atmosphere. X-ray data was recorded at 100 K on a Bruker D8 Quest Kappa diffractometer using Cu K_α radiation (λ = 1.54178 Å) from an Incoatec IμS microsource with Montel multi layered mirror with a Photon II CPAD detector. The structures were solved using direct methods, expanded with Fourier techniques and refined with the software package SHELX.[171] Non-hydrogen atoms were refined

anisotropically. Hydrogen atoms were included in the structure factor calculation on geometrically idealized positions.

***m*-F-MC3**: The macrocyclic structure was refined as a two-component twin. Diffuse electron density originating from solvent molecules was located inside the macrocyclic cavity. Water molecules were assigned to the maxima of electron density, although the origin of these Q-peaks could not be elucidated unambiguously. However, the resulting hydrogen bonding network is in good agreement with molecular dynamics simulations. Remaining Q-peaks below 1 have not been assigned to water molecules anymore which could have been acceptor sides for H42A and H42B.

Crystal data for ***m*-F-MC3**: Mr = 2086.81, trigonal space group R-3, a = 23.4927(5) Å, α = 90°, b = 23.4927(5) Å, β = 90°, c = 32.5166(7) Å, γ = 120°, V = 15541.8(7) Å^3, Z = 6, ρ = 1.338 g cm^{-3}, μ = 4.194 mm^{-1}, $F_{(000)}$ = 6352.0, $GooF(F^2)$ = 1.157, R = 0.0385, wR^2 = 0.1181, 6705 unique reflections [$\theta \leq$ 72.421°] with a completeness of 100% and 452 parameters.

***p*-F-MC3**: The macrocyclic structure was refined as a two-component twin. Residual electron density resulting solvent molecules could not be modeled satisfactorily. Therefore, the PLATON squeeze routine was applied to remove the respective electron density.[172] The remaining structure could be refined nicely.

Crystal data for ***p*-F-MC3**: Mr = 1834.56, triclinic space group P-1, a = 15.9552(3) Å, α = 65.145(1)°, b = 18.9386(4) Å, β = 87.292(1)°, c = 21.0317(4) Å, γ = 76.631(1)°, V = 5601.2(2) Å^3, Z = 2, ρ = 1.088 g cm^{-3}, μ = 3.742 mm^{-1}, $F_{(000)}$ = 1836.0, $GooF(F^2)$ = 1.026, R = 0.0407, wR^2 = 0.0997, 18147 unique reflections [$\theta \leq$ 72.520°] with a completeness of 99.5% and 1054 parameters.

Crystallographic data have been deposited with the Cambridge Crystallographic Data Centre as supplementary publication no. CCDC 1985319 (***m*-F-MC3**) and 1985320 (***p*-F-MC3**). These data can be obtained free of charge from the Cambridge Crystallographic Data Centre via www.ccdc.ac.uk/data.request/cif.

Powder X-ray diffraction (PXRD)

PXRD was performed in reflection mode on a Bruker D8 Discovery diffractometer with position-sensitive 1D-Lynxeye detector using Cu-Kα radiation. Crystalline samples of ***m*-F-MC3** were dried under high vacuum at 60 °C.

Electrochemistry

A Cell Stand C3 (BAS Epsilon) with a standard three-electrode configuration was used to perform cyclic voltammetry (CV) and differential pulse voltammetry (DPV). For measurements in organic media, samples were dissolved in anhydrous DCM (c = 0.25 mM) and tetrabutylammonium hexafluorophosphat was added as electrolyte (c = 0.1 M). A platinum disk and wire as well as a Ag/AgCl electrode were used as working, auxiliary and pseudo-reference electrodes, respectively. Ferrocene (Fc) was added at the end of each experiment as an internal standard (Fc^+/Fc = +0.63 V *vs*. NHE).[173] For measurements in aqueous media, glassy carbon was used as working electrode, a Platinum wire as counter electrode and a Ag/AgCl (3 M KCl) electrode as reference electrode (Ag^+/Ag = +0.21 V *vs*. NHE).[174] Samples were dissolved in aqueous mixtures with acetonitrile or TFE as organic cosolvents (c = 0.25 – 2 mM). If not otherwise stated, CV and DPV were recorded at a scan rate of 100 mV s^{-1} and 20 mV s^{-1}, respectively.

Spectroelectrochemistry

Spectroelectrochemistry in reflexion mode was perfomed using a Agilent Cary 5000 spectrometer in combination with a home-built sample compartment consisting of a cylindrical PTFE cell with a sapphire window and an adjustable three-in-one electrode (6 mm Platinum disk working electrode, 1 mm Platinum counter and pseudo-reference electrode). All experiments were carried out at a sample concentration of c = 0.24 mM in 1:1 acetonitrile/water (pH 7, phosphate buffer) with a layer thickness of about 100 µm. The potential was referenced to the first oxidation event as it was determined by DPV.

Stopped-Flow Sample Preparation

A SFM-20 Stopped-Flow System (BioLogic Science Instruments) was used to prepare freeze-quenched samples for EPR and X-ray absorption spectroscopy. At the end of the aging loop, the aged reaction mixtures were sprayed into precooled pentane at -120 °C.

EPR Spectroscopy

Low-temperature X-band EPR spectra were recorded at 7 K using a Bruker EMX X-band spectrometer equipped with a X-Band CW microwave bridge and an Air Products LTR liquid helium cryostat. Measurements were performed at microwave frequency 9.47 GHz, field modulation amplitude 10 G at 100 kHz and microwave power 30 mW.

X-ray Absorption Spectroscopy

X-ray absorption spectra were collected at the Advanced Photon Source APS at Argonne National Laboratory on bending magnet beamline 20 at 23 keV incident photoelectron energy and 100 mA average current. The radiation was monochromatized by a Si(110) crystal and the intensity of the X-rays monitored by three ion chambers (I_0, I_1, I_2). I_0 was filled with 80% nitrogen and 20% argon and was placed in front of the sample, while I_1 and I_2 were filled with 100% nitrogen and placed behind the sample. The absorption of a Ruthenium metal foil placed between I_1 and I_2 was recorded with each scan for energy calibration. The X-ray energy was calibrated by setting the first maximum in the derivative of the Ru metal K-edge XANES spectrum to 22117 eV.

EXAFS data were analyzed using the Athena software package.[175] Data was background-corrected, normalized, deglitched if needed, then converted to wave vector space (*k*-space) and weighted by k^3. Before Fourier transformation *k*-space data was truncated near zero crossings. Artemis software package was used for curve fitting. The fitting model consisted of either the first or first and second coordination shells around Ru. In order to decrease the number of variables, the first shell was modelled as six nitrogen atoms and the second shell as ten (8 + 2 or 6 + 4) carbon atoms. EXAFS peaks were either isolated and fitted individually or fitted in groups depending on the model used. *Ab initio* calculated phases and amplitudes from the FEFF8 code[176] were applied for curve fitting using the EXAFS equation:

$$\chi(k) = S_0^2 \sum_j \frac{N_j}{kR_j^2} f_{eff_j}(\pi, k, R_j) e^{-2\sigma_j^2 k^2} e^{-\frac{2R_j}{\lambda_j(k)}} \sin(2kR_j + \phi_{ij}(k))$$

where N_j is the number of atoms in the j^{th} shell and R_j is the mean distance between the absorbing atom and the other atoms in the j^{th} shell. f_{eff_j} is the calculated amplitude function. The Debye-Waller term $e^{-2\sigma 2k2}$ and the term $e^{-2R/\lambda(k)}$ account for damping caused by thermal disorder and losses resulting from inelastic scattering, respectively. $\lambda_j(k)$ is the electron mean free path, Φ_{ij} the calculated phase function and S_0^2 the amplitude reduction factor.

Fit quality was evaluated by the *R*-factor and the reduced X^2 value.

Chemical Water Oxidation

Chemical water oxidation experiments were performed at 20 °C in reaction vessels connected to SSCDANN030PAAA5 pressure sensors (Honeywell, absolute pressure, 0 to 30 psi). For each measurement, 1 g (1.82 mmol) ceric ammonium nitrate (CAN) was dissolved in 3 mL of

aqueous mixtures (pH 1, triflic acid) with acetonitrile as organic cosolvent. 400 µL of the catalyst stock solution was then injected through a septum using a Hamilton syringe. To determine the gas composition at the end of gas evolution, 500 µL of the gas head space was injected into a gas chromatograph GC-2010 Plus (Shimadzu, thermal conductivity detector at 30 mA, argon as carrier gas) using a gas tight Hamilton syringe.

TON was calculated based on the total amount of oxygen evolved during catalysis divided by the amount of catalyst injected. The amount of evolved oxygen was determined by the pressure increase in the reaction vessel using the ideal gas law:

$$\Delta p\, V = R\, T\, \Delta n$$

where T = 293.15 K, R = 8.314 J K^{-1} mol^{-1}, V = 20.6 mL.

In concentration-dependent experiments a TON was calculated for each concentration and the highest TON is reported.

For calculation of TOF, the initial rate of catalysis was determined again at each concentration by the linear regression of the oxygen evolution curve during the first two seconds of reaction. TOF was then determined from the slope of the plot of the initial rates *vs.* catalyst amount.

Photocatalytic Water Oxidation

An Oxygraph Plus Clark-electrode system (Hansatech Instruments) was used for oxygen detection in photocatalytic water oxidation experiments. Samples were irradiated using a 150 W xenon lamp (Newport) equipped with a 400 nm cutoff filter. Irradiation was calibrated to 100 mW cm^{-1}, unless otherwise stated, using a PM 200 optical power meter with a S121C sensor (Thorlabs) in combination with a CCS 200/M wide range spectrometer (Thorlabs). For each measurement, a stock solution of the respective PS and sodium persulfate in the indicated solvent mixture was prepared in the dark. An aliquot of this solution was then mixed with the catalyst at variable concentrations (2.0 mL total volume) and transferred to the transparent reaction chamber while kept in the dark. Irradiation was started at 50 s to allow thermal equilibration of the sample in the temperature-controlled chamber at 20 °C. For TON determination, the maximum amount of oxygen evolved during catalysis was divided by the amount of catalyst used. In concentration-dependent experiments, a TON was calculated for each concentration and the highest TON is reported. For calculation of TOF, the initial rate of catalysis was determined at each concentration by linear regression of the oxygen evolution curve in the first five to ten seconds of catalysis (after an initial induction period of about 1 s).

The reported TOF was determined from the slope of the plot of the initial rates *vs.* catalyst amount.

The quantum yield (Φ) of oxygen production, defined according to equation (S1),[165, 177] has been estimated according to equation (S2).

$$\Phi = \frac{(moles\ of\ O_2\ produced)}{(moles\ of\ absorbed\ photons)} \quad \text{(S1)}$$

$$\Phi = \frac{R_{O_2}}{F} \quad \text{(S2)}$$

where R_{O_2} [O_2-molecules·s^{-1}] is the initial rate of oxygen generation and *F* [photons·s^{-1}] is the absorbed photon flux determined according to equation (S3) in which *A* (1.96 x 10^{-4} m^2) is the irradiated surface area, P_{Xe} [photons·s^{-1}·nm^{-1}·m^{-2}] is the spectral irradiance of the irradiation source, and *LHE* the light-harvesting efficiency estimated from equation (S4) considering the absorbance (abs) of each sensitizer under photoreaction conditions.

$$F = A \cdot \int P_{Xe}\, LHE\, d\lambda \quad \text{(S3)}$$

$$LHE = 1 - 10^{-abs} \quad \text{(S4)}$$

The chemical yield φ of oxygen production was calculated by dividing the maximum amount of oxygen produced by half the amount of sodium persulfate.[178]

Molecular dynamics simulations

For the metadynamics simulations the electronic structure of the trinuclear Ru macrocycles has been described by the semiempirical PM6 method[179] using the MOPAC2016 program package[180] version 17.279L. The Newtonian equations of motion were integrated for a total of 1 ns in time steps of 2 fs using the velocity Verlet algorithm.[181] During the dynamics, the temperature was kept constant using a velocity-rescaling thermostat at 300 K allowing for canonical sampling.[182] For the evaluation of the torsional distortion of the axial bridging ligands, the two torsion angles between the aromatic rings in one of the bridging ligands have been used as collective variables. Gaussians of 20° width and 0.1 kcal mol^{-1} height were added to the metadynamics potential every 200 time steps. For the rotation of the Ru(bda) moieties according to the collective variable visualized in Figure 58 (see Appendix Chapter 3), Gaussians with a width of 7.5° and a height of 0.015 kcal mol^{-1} were added every 1000 time steps. In order to account for the slower energy deposition rate, total trajectory lengths of 2 ns have been realized in this case. All metadynamics simulations were performed using the

metaFALCON python package.[183] Additionally, structure optimizations have been performed on the semiempirical level as described before, as well as using density functional theory (DFT) in Turbomole V7.0[184] employing the PBE exchange-correlation functional[185] together with the def2-SVP basis set[186] and the corresponding effective core potentials (ECP)[187] on ruthenium atoms. In all calculations, solvation was treated implicitly using the COSMO model for water.[188]

UV/Vis Absorption Spectroscopy

UV/Vis absorption spectra were recorded at 25 °C using a Jasco V-670 spectrometer. Samples prepared with spectroscopic grade solvents were measured in 1 cm quartz cuvettes.

Emission Spectroscopy

Steady-state emission and lifetime measurements were recorded at 25 °C on a FLS980 spectrometer (Edinburgh Instruments). Lifetime measurements were performed with a pulsed laser diode (λ_{ex} = 405 nm). Samples in acetonitrile/water mixtures were thoroughly degassed with argon in 1 cm quartz Schlenk cuvettes to prevent emission quenching by oxygen.

Stern-Volmer experiments: A stock solution of the photosensitizer in the respective solvent mixture was prepared under argon in the dark (c = 50 µM). Sodium persulfate was added to an aliquot of the solution to reach a concentration between 0–14 mM. The obtained mixtures were then carefully degassed with argon in Schlenk cuvettes prior to each measurement.

Laser Flash Photolysis

Laser flash photolysis was performed at 25 °C using a Edinburgh LP920 Laser flash photolysis/Transient absorption spectrometer equipped with a 450 W ozone-free Xe arc lamp including a photomultiplier (Hamamatsu R955) and a digital storage oscilloscope (Tektronix TD3012B). Samples were prepared with spectroscopic grade solvents and degassed with argon in 1 cm quartz Schlenk cuvettes. For sample excitation a NT340 Nd:YAG laser (EKSPLA) with integrated optical parametric oscillator was used (5 ns pulse length). Samples of photosensitizers **PS0** and **PS1** were excited with 25 mJ pulses at 460 nm or 482 nm, respectively. For measurements, Xe lamp was used in continuous wave mode to provide a stable light intensity.

7.2 Synthesis and Characterization

Synthesis of Ru macrocycles functionalized at bridging ligand

1,4-bis(4,4,5,5-tetramethyl-1,3,2-dioxaborolan-2-yl)benzene (33)

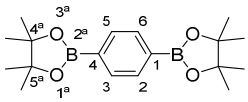

1,4-Dibromobenzene (3.00 g, 12.7 mmol, 1.0 equiv), bis(pinacolato)diboron (9.69 g, 38.2 mmol, 3.0 equiv) and potassium acetate (7.49 g, 76.3 mmol, 6.0 equiv) were dissolved in degassed dioxane (120 mL) under nitrogen. After addition of $Pd(dppf)Cl_2$ (0.93 g, 1.3 mmol, 0.1 equiv), the mixture was heated at 85 °C for 17.5 h. Afterwards, water (250 mL) was added and the organic phase extracted with ethyl acetate (4 x 100 mL). The combined organic phases were washed with brine and dried over anhydrous Na_2SO_4. The residue was purified by column chromatography (SiO_2, hexane/EtOAc 10:1) and washed with MeOH to yield **33** as a white solid (3.17 g, 9.61 mmol, 76%).

Melting point: 244 °C. ^{1}H-NMR (400 MHz, $CDCl_3$): δ [ppm] = 7.80 (s, 4H, *H*-2,3,5,6), 1.35 (s, 24H, C*H*$_3$).

Analytical data in accordance with literature reported values.[189]

***m*-MeO-bpb**

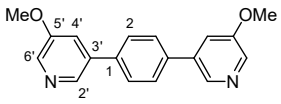

3-Bromo-5-methoxypyridine (239 mg, 1.27 mmol, 2.1 equiv) and **33** (200 mg, 606 µmol, 1.0 equiv) were dissolved in a degassed mixture of toluene (2.4 mL), ethanol (0.6 mL) and 2 M Na_2CO_3 (2.4 mL) under a nitrogen atmosphere. After addition of $Pd(PPh_3)_4$ (70 mg, 60 µmol, 0.1 equiv), the mixture was heated under reflux (105 °C) for 5 days. Afterwards, the solvent was removed under reduced pressure and the residue purified by column chromatography (SiO_2, DCM/EtOAc 5:1 to 1:1) to yield ***m*-MeO-bpb** as a white solid (147 mg, 503 µmol, 83%).

Melting point: 217 °C (decomposition). ^{1}H-NMR (400 MHz, CD_2Cl_2): δ [ppm] = 8.50 (d, $^4J_{H\text{-}H}$ = 1.6 Hz, 2H, *H*-2'), 8.30 (d, $^4J_{H\text{-}H}$ = 2.7 Hz, 2H, *H*-6'), 7.73 (s, 4H, *H*-2), 7.45 (dd, $^4J_{H\text{-}H}$ = 2.7 Hz, $^4J_{H\text{-}H}$ = 1.6 Hz, 2H, *H*-4'), 3.93 (s, 6H, O-C*H*$_3$). ^{13}C-NMR (100 MHz,

CD_2Cl_2/CD_3OD): δ [ppm] = 156.3, 140.9, 137.9, 136.9, 136.8, 128.2, 119.0, 56.1. HR-MS (ESI$^+$, MeCN/$CHCl_3$ 1:1): *m*/*z* calculated for $[M+H]^+$ ($[C_{18}H_{17}N_2O_2]^+$): 293.1285, found: 293.1281 (error: 1.4 ppm). Elemental analysis (%): calculated for $C_{18}H_{16}N_2O_2$: C 73.95, H 5.52, N 9.58, found: C 73.55, H 5.56, N 9.70.

***m*-F-bpb**

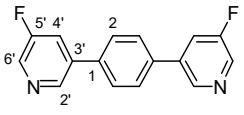

3-Bromo-5-fluoropyridine (660 mg, 3.74 mmol, 2.5 equiv) was dissolved in dry THF (40 mL) under nitrogen. 2 M Na_2CO_3 (7.6 mL) was then added. The mixture was degassed for 10 min before **33** (500 mg, 1.51 mmol, 1.0 equiv) and $Pd(PPh_3)_4$ (175 mg, 151 µmol, 0.1 equiv) were added. The resulting mixture was heated under reflux (70 °C) for 24 h. After cooling to rt, the white crystalline product was collected by vacuum filtration and washed with water to remove Na_2CO_3 traces. The remaining residue was purified by column chromatography (SiO_2, DCM/EtOAc 10:1 to 1:1) to yield ***m*-F-MC3** as a white solid (362 mg, 1.35 mmol, 89%).

Melting point: 193 °C (decomposition). ^{1}H-NMR (400 MHz, CD_2Cl_2): δ [ppm] = 8.73 (t, $^4J_{H\text{-}H}$ = 1.8 Hz, 2H, *H*-2'), 8.48 (d, $^4J_{H\text{-}H}$ = 2.7 Hz, 2H, *H*-6'), 7.75 (s, 4H, *H*-2), 7.68 (ddd, $^3J_{H\text{-}F}$ = 9.7 Hz, $^4J_{H\text{-}H}$ = 2.7 Hz, $^4J_{H\text{-}H}$ = 1.8 Hz, 2H, *H*-4'). ^{13}C-NMR (100 MHz, CD_2Cl_2/CD_3OD): δ [ppm] = 160.2 (d, $^1J_{C\text{-}F}$ = 254.0 Hz), 144.5 (d, $^4J_{C\text{-}F}$ = 3.8 Hz), 137.6 (d, $^3J_{C\text{-}F}$ = 4.0 Hz), 137.3 (d, $^2J_{C\text{-}F}$ = 23.1 Hz), 137.1 (d, $^4J_{C\text{-}F}$ = 1.0 Hz), 128.4, 121.2 (d, $^2J_{C\text{-}F}$ = 18.7 Hz). HR-MS (ESI$^+$, MeCN/$CHCl_3$ 1:1): *m*/*z* calculated for $[M+H]^+$ ($[C_{16}H_{11}F_2N_2]^+$): 269.0885, found: 269.0885 (error: -0.1 ppm). Elemental analysis (%): calculated for $C_{16}H_{10}F_2N_2$: C 71.64, H 3.76, N 10.44, found: C 71.14, H 4.03, N 9.94.

***m*-Me-bpb**

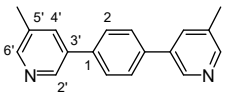

3-Bromo-5-methylpyridine (1.09 g, 6.36 mmol, 2.1 equiv) and **33** (1.00 g, 3.03 mmol, 1.0 equiv) were dissolved in a degassed mixture of toluene (12 mL), ethanol (3 mL) and 2 M Na_2CO_3 (12 mL) under nitrogen. After addition of $Pd(PPh_3)_4$ (350 mg, 303 µmol, 0.1 equiv), the mixture was heated under reflux (105 °C) for 5 days. Afterwards, the solvent was removed *in vacuo* and the residue purified by column chromatography (SiO_2, DCM/EtOAc 5:1 to 1:1) to yield ***m*-Me-bpb** as a white solid (560 mg, 2.15 mmol, 71%).

Melting point: 206 °C. ^{1}H-NMR (400 MHz, CD_2Cl_2): δ [ppm] = 8.69 (d, $^{4}J_{H\text{-}H}$ = 2.1 Hz, 2H, *H*-2'), 8.42 (dd, $^{4}J_{H\text{-}H}$ = 2.1 Hz, $^{4}J_{H\text{-}H}$ = 0.7 Hz, 2H, *H*-6'), 7.76 (ddd, $^{4}J_{H\text{-}H}$ = 2.1 Hz, $^{4}J_{H\text{-}H}$ = 2.1 Hz, $^{4}J_{H\text{-}H}$ = 0.7 Hz, 2H, *H*-4'), 7.72 (s, 4H, *H*-2), 2.41 (d, $^{4}J_{H\text{-}H}$ = 0.7 Hz, 2H, C*H*$_3$). ^{13}C-NMR (100 MHz, CD_2Cl_2): δ [ppm] = 149.2, 145.7, 138.0, 135.6, 135.0, 133.6, 128.0, 18.6. HR-MS (ESI$^+$, MeOH/$CHCl_3$ 1:1): *m*/*z* calculated for $[M+H]^+$ ($[C_{18}H_{17}N_2]^+$): 261.1386, found: 261.1390 (error: -1.6 ppm). Elemental analysis (%): calculated for $C_{18}H_{16}N_2$: C 83.04, H 6.19, N 10.76, found: C 82.60, H 6.30, N 10.90.

p-MeO-bpb

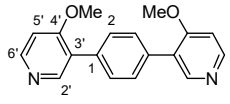

3-Bromo-4-methoxypyridine (1.2 g, 6.36 mmol, 2.1 equiv) and **33** (1.00 g, 3.03 µmol, 1.0 equiv) were dissolved in a degassed mixture of toluene (12 mL), ethanol (3 mL) and 2 M Na_2CO_3 (12 mL) under a nitrogen atmosphere. After addition of $Pd(PPh_3)_4$ (350 mg, 303 µmol, 0.1 equiv), the mixture was heated under reflux (105 °C) for 5 days. Afterwards, the solvent was removed under reduced pressure and the residue purified by column chromatography (SiO_2, EtOAc/MeOH 100:0 to 98:2) to yield ***p*-MeO-bpb** as a white solid (561 mg, 1.92 mmol, 63%).

Melting point: 225 °C (decomposition). ^{1}H-NMR (400 MHz, CD_2Cl_2): δ [ppm] = 8.47 (d, $^{3}J_{H\text{-}H}$ = 5.7 Hz, 2H, *H*-6'), 8.45 (s, 2H, *H*-2'), 7.58 (s, 4H, *H*-2), 6.94 (d, $^{3}J_{H\text{-}H}$ = 5.7 Hz, 2H, *H*-5'), 3.90 (s, 6H, O-C*H*$_3$). ^{13}C-NMR (100 MHz, CD_2Cl_2): δ [ppm] = 162.9, 151.0, 151.0, 134.7, 129.7, 126.3, 106.9, 55.8. HR-MS (ESI$^+$, MeCN/$CHCl_3$ 1:1): *m*/*z* calculated for $[M+H]^+$ ($[C_{18}H_{17}N_2O_2]^+$): 293.1285, found: 293.1287 (error: -1.0 ppm). Elemental analysis (%): calculated for $C_{18}H_{16}N_2O_2$: C 73.95, H 5.52, N 9.58, found: C 73.97, H 5.63, N 9.56.

p-F-bpb

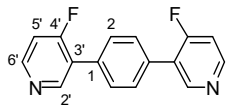

3-Bromo-4-fluoropyridine (1.00 g, 5.68 mmol, 2.5 equiv) was dissolved in dry THF (60 mL) under nitrogen. 2 M Na_2CO_3 (11.4 mL) was then added. The mixture was degassed for 15 min before **33** (750 mg, 2.27 mmol, 1.0 equiv) and $Pd(PPh_3)_4$ (262 mg, 227 µmol, 0.1 equiv) were added. The resulting mixture was heated under reflux (70 °C) for 24 h. After cooling to rt, the

residue was purified by column chromatography (SiO_2, DCM/EtOAc 5:1 to 1:1) to yield ***p*-F-MC3** as a white solid (372 mg, 1.39 mmol, 61%).

Melting point: 177 °C (decomposition). ^{1}H-NMR (400 MHz, CD_2Cl_2): δ [ppm] = 8.74 (d, $^4J_{H\text{-}F}$ = 10.4 Hz, 2H, *H*-2'), 8.57 (dd, $^4J_{H\text{-}F}$ = 7.4 Hz, $^3J_{H\text{-}H}$ = 5.7 Hz, 2H, *H*-6'), 7.70 (s, 4H, *H*-2), 7.18 (dd, $^4J_{H\text{-}F}$ = 10.4 Hz, $^3J_{H\text{-}H}$ = 5.7 Hz, 2H, *H*-5'). ^{13}C-NMR (100 MHz, CD_2Cl_2): δ [ppm] = 165.9 (d, $^1J_{C\text{-}F}$ = 262.0 Hz), 152.4 (d, $^3J_{C\text{-}F}$ = 2.8 Hz), 151.7 (d, $^3J_{C\text{-}F}$ = 7.3 Hz), 132.8, 129.8 (d, $^4J_{C\text{-}F}$ = 2.6 Hz), 125.1 (d, $^2J_{C\text{-}F}$ = 9.6 Hz), 112.1 (d, $^2J_{C\text{-}F}$ = 17.7 Hz). HR-MS (ESI$^+$, MeCN/$CHCl_3$ 1:1): *m*/*z* calculated for $[M+H]^+$ ($[C_{16}H_{11}F_2N_2]^+$): 269.0885, found: 269.0884 (error: 0.1 ppm). Elemental analysis (%): calculated for $C_{16}H_{10}F_2N_2$: C 71.64, H 3.76, N 10.44, found: C 71.57, H 3.71, N 10.71.

***p*-Me-bpb**

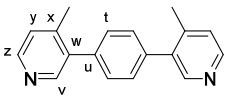

3-Bromo-4-methylpyridine (1.09 g, 6.36 mmol, 2.1 equiv) and **33** (1.00 g, 3.03 mmol, 1.0 equiv) were dissolved in a degassed mixture of toluene (12 mL), ethanol (3 mL) and 2 M Na_2CO_3 (12 mL) under a nitrogen atmosphere. After addition of $Pd(PPh_3)_4$ (350 mg, 303 µmol, 0.1 equiv), the mixture was heated under reflux (105 °C) for 5 days. Afterwards, the solvent was removed *in vacuo* and the residue purified by column chromatography (SiO_2, DCM/EtOAc 5:1 to 1:1) to yield ***p*-Me-bpb** as a white solid (500 mg, 1.92 mmol, 63%).

Melting point: 202 °C. ^{1}H-NMR (400 MHz, CD_2Cl_2): δ [ppm] = 8.46 (d, $^5J_{H\text{-}H}$ = 0.3 Hz, 2H, *H*-2'), 8.44 (d, $^3J_{H\text{-}H}$ = 5.0 Hz, $^5J_{H\text{-}H}$ = 0.3 Hz, 2H, *H*-6'), 7.44 (s, 4H, *H*-2), 7.23 (dq, $^3J_{H\text{-}H}$ = 5.0 Hz, $^4J_{H\text{-}H}$ = 0.7 Hz, 2H, *H*-5'), 2.35 (t, $^5J_{H\text{-}H}$ = 0.3 Hz, 2H, CH_3). ^{13}C-NMR (100 MHz, CD_2Cl_2): δ [ppm] = 150.3, 148.8, 144.9, 137.7, 137.6, 129.7, 125.6, 20.0. HR-MS (ESI$^+$, MeOH/$CHCl_3$ 1:1): *m*/*z* calculated for $[M+H]^+$ ($[C_{18}H_{17}N_2]^+$): 261.1386, found: 261.1389 (error: -1.2 ppm). Elemental analysis (%): calculated for $C_{18}H_{16}N_2$: C 83.04, H 6.19, N 10.76, found: C 82.77, H 6.18, N 10.95.

m-MeO-MC3

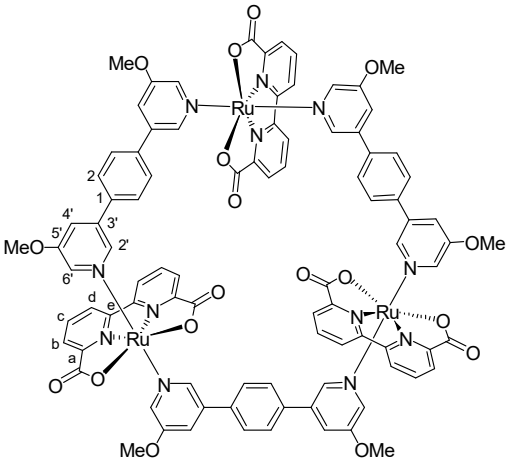

Ru(bda)(dmso)$_2$ (100 mg, 200 µmol, 1.1 equiv) and ***m*-MeO-bpb** (53 mg, 182 µmol, 1.0 eq) were dissolved in a degassed mixture of chloroform (55 mL) and methanol (11 mL) and stirred for 16.5 h at 60 °C. After cooling to rt, the solvent was removed under reduced pressure and the residue purified by column chromatography (Al_2O_3 15% w/w H_2O, DCM/MeOH 6:1 and subsequently SiO_2, DCM/MeOH 10:1 to 2:1) and precipitation with hexane to yield ***m*-MeO-MC3** as a dark brown solid (41 mg, 22 µmol, 36%).

Melting point: >300 °C. ^{1}H-NMR (400 MHz, CD_2Cl_2/CD_3OD): δ [ppm] = 8.52 (dd, $^3J_{H\text{-}H}$ = 7.9 Hz, $^4J_{H\text{-}H}$ = 1.1 Hz, 6H, *H*-d), 8.10 (dd, $^3J_{H\text{-}H}$ = 7.9 Hz, $^4J_{H\text{-}H}$ = 1.1 Hz, 6H, *H*-b), 8.05 (d, $^4J_{H\text{-}H}$ = 1.6 Hz, 6H, *H*-2'), 7.92 (t, $^3J_{H\text{-}H}$ = 7.9 Hz, 6H, *H*-c), 7.50 (s, 12H, *H*-2), 7.27 (dd, $^4J_{H\text{-}H}$ = 2.5 Hz, $^4J_{H\text{-}H}$ = 1.6 Hz, 6H, *H*-6'), 7.08 (d, $^4J_{H\text{-}H}$ = 2.5 Hz, 6H, *H*-4'), 3.72 (s, 18H, O-C*H*$_3$). ^{13}C-NMR (100 MHz, CD_2Cl_2/CD_3OD): δ [ppm] = 173.8, 160.1, 157.7, 156.7, 144.0, 138.8, 137.9, 136.9, 132.3, 128.4, 126.5, 125.0, 119.6, 56.2. HR-MS (ESI$^+$, MeOH/$CHCl_3$ 1:1): *m*/*z* calculated for $[M]^{2+}$ ($[C_{90}H_{66}N_{12}O_{18}Ru_3]^{2+}$): 954.0869, found: 954.0920 (error: -2.7 ppm). Elemental analysis (%): calculated for $C_{90}H_{66}N_{12}O_{18}Ru_3 \cdot 3\,H_2O$: C 55.13, H 3.70, N 8.57, found: C 55.44, H 3.82, N 8.36.

m-F-MC3

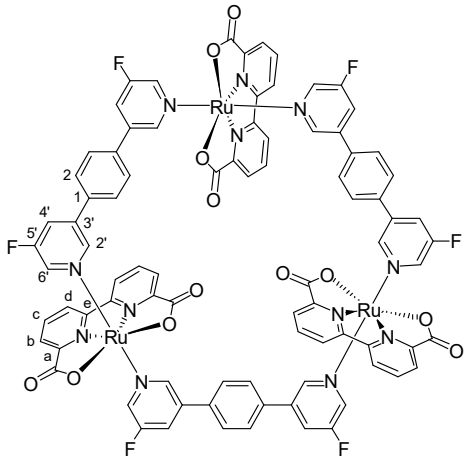

Ru(bda)(dmso)$_2$ (250 mg, 500 µmol, 1.1 equiv) and ***m*-F-bpb** (122 mg, 455 µmol, 1.0 equiv) were dissolved in a degassed mixture of chloroform (138 mL) and methanol (28 mL) and stirred for 16.5 h at 60 °C. After cooling to rt, the solvent was removed *in vacuo* and the residue purified by column chromatography (SiO_2, DCM/MeOH 10:1 to 3:1) and precipitation with hexane to yield ***m*-F-MC3** as a dark brown solid (104 mg, 57 µmol, 38%).

Melting point: >300 °C. ^{1}H-NMR (600 MHz, CD_2Cl_2/CD_3OD): δ [ppm] = 8.56 (dd, $^{3}J_{H\text{-}H}$ = 7.9 Hz, $^{4}J_{H\text{-}H}$ = 1.1 Hz, 6H, *H*-d), 8.41 (d, $^{4}J_{H\text{-}H}$ = 1.7 Hz, 6H, *H*-2'), 8.13 (dd, $^{3}J_{H\text{-}H}$ = 7.9 Hz, $^{4}J_{H\text{-}H}$ = 1.1 Hz, 6H, *H*-b), 7.98 (t, $^{3}J_{H\text{-}H}$ = 7.9 Hz, 6H, *H*-c), 7.59 (ddd, $^{3}J_{H\text{-}F}$ = 8.5 Hz, $^{4}J_{H\text{-}H}$ = 2.4 Hz, $^{4}J_{H\text{-}H}$ = 1.7 Hz, 6H, *H*-4'), 7.57 (s, 12H, *H*-2), 7.28 (t, $^{4}J_{H\text{-}H}$ = 2.4 Hz, 6H, *H*-6'). ^{13}C-NMR (151 MHz, CD_2Cl_2/CD_3OD): δ [ppm] = 173.7, 159.8 (d, $^{1}J_{C\text{-}F}$ = 254.8 Hz), 159.8, 157.5, 148.6 (d, $^{4}J_{C\text{-}F}$ = 3.2 Hz), 139.4 (d, $^{2}J_{C\text{-}F}$ = 30.7 Hz), 138.8 (d, $^{3}J_{C\text{-}F}$ = 6.2 Hz), 136.1 (d, $^{4}J_{C\text{-}F}$ = 1.7 Hz), 133.2, 128.7, 126.8, 125.4, 122.5 (d, $^{2}J_{C\text{-}F}$ = 19.1 Hz). HR-MS (ESI^{+}, MeOH/$CHCl_3$ 1:1): *m*/*z* calculated for $[M+2Na]^{2+}$ ($[C_{84}H_{48}F_6N_{12}Na_2O_{12}Ru_3]^{2+}$): 941.0167, found: 941.0176 (error: -1.6 ppm). Elemental analysis (%): calculated for $C_{84}H_{48}F_6N_{12}O_{12}Ru_3 \cdot H_2O$: C 54.46, H 2.72, N 9.07, found: C 54.53, H 3.27, N 9.42.

***m*-Me-MC3**

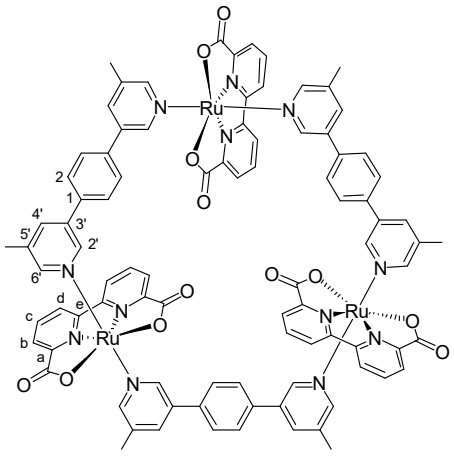

Ru(bda)(dmso)$_2$ (100 mg, 200 µmol, 1.1 equiv) and ***m*-Me-bpb** (47 mg, 182 µmol, 1.0 equiv) were dissolved in a degassed mixture of chloroform (55 mL) and methanol (11 mL) and stirred for 16.5 h at 60 °C. After cooling to rt, the solvent was removed under reduced pressure and the residue purified by column chromatography (Al_2O_3 15% w/w H_2O, DCM/MeOH 6:1, two consecutive times and subsequently SiO_2, DCM/MeOH 10:1 to 4:1) and precipitation with hexane to yield ***m*-Me-MC3** as a dark brown solid (31 mg, 17 µmol, 28%).

Melting point: >300 °C. ^{1}H-NMR (400 MHz, CD_2Cl_2/CD_3OD): δ [ppm] = 8.52 (dd, $^{3}J_{H\text{-}H}$ = 7.9 Hz, $^{4}J_{H\text{-}H}$ = 1.0 Hz, 6H, *H*-d), 8.27 (d, $^{4}J_{H\text{-}H}$ = 1.7 Hz, 6H, *H*-2'), 8.10 (dd, $^{3}J_{H\text{-}H}$ = 7.9 Hz, $^{4}J_{H\text{-}H}$ = 1.0 Hz, 6H, *H*-b), 7.91 (t, $^{3}J_{H\text{-}H}$ = 7.9 Hz, 6H, *H*-c), 7.58 (d, $^{4}J_{H\text{-}H}$ = 0.7 Hz, 6H, *H*-4'), 7.50 (s, 12H, *H*-2), 7.16 (s, 6H, *H*-6'), 2.13 (s, 18H, O-CH_3). ^{13}C-NMR (100 MHz, CD_2Cl_2/CD_3OD): δ [ppm] = 173.9, 160.2, 157.6, 150.3, 148.9, 137.0, 136.8, 135.9, 135.6, 132.0, 128.3, 126.5, 124.9, 18.5. HR-MS (ESI^{+}, MeOH/$CHCl_3$ 1:1): *m*/*z* calculated for $[M]^{+}$ ($[C_{90}H_{66}N_{12}O_{12}Ru_3]^{+}$): 1812.2048, found: 1812.2094 (error: -0.3 ppm). Elemental analysis (%): calculated for $C_{90}H_{66}N_{12}O_{18}Ru_3 \cdot 3\ H_2O$: C 57.97, H 3.89, N 9.01, found: C 58.45, H 4.54, N 9.12.

***p*-MeO-MC3:**

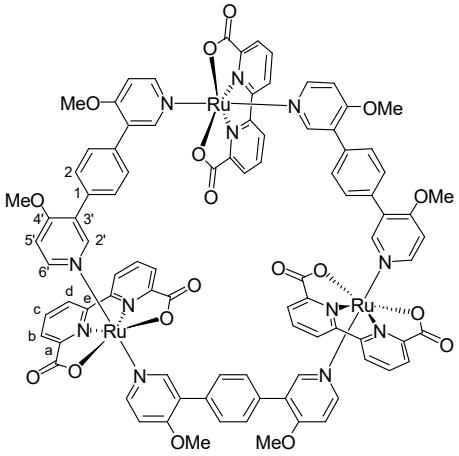

Ru(bda)(dmso)$_2$ (100 mg, 200 µmol, 1.1 equiv) and ***p*-MeO-bpb** (53 mg, 182 µmol, 1.0 equiv) were dissolved in a degassed mixture of chloroform (55 mL) and methanol (11 mL) and stirred for 16.5 h at 60 °C. After cooling to rt, the solvent was removed under reduced pressure and the residue purified by column chromatography (Al_2O_3 15% w/w H_2O, DCM/MeOH 6:1 and subsequently SiO_2, DCM/MeOH 10:1 to 2:1) and precipitation with hexane to yield ***p*-MeO-MC3** as a dark brown solid (37 mg, 19 µmol, 32%).

Melting point: >300 °C. ^{1}H-NMR (400 MHz, CD_2Cl_2/CD_3OD): δ [ppm] = 8.42 (dd, $^3J_{H\text{-}H}$ = 7.9 Hz, $^4J_{H\text{-}H}$ = 1.1 Hz, 6H, *H*-d), 8.11 (dd, $^3J_{H\text{-}H}$ = 7.9 Hz, $^4J_{H\text{-}H}$ = 1.1 Hz, 6H, *H*-b), 7.86 (t, $^3J_{H\text{-}H}$ = 7.9 Hz, 6H, *H*-c), 7.72 (d, $^4J_{H\text{-}H}$ = 1.0 Hz, 6H, *H*-2'), 7.41 (dd, $^4J_{H\text{-}H}$ = 6.7 Hz, $^4J_{H\text{-}H}$ = 1.0 Hz, 6H, *H*-6'), 7.27 (s, 12H, *H*-2), 6.72 (d, $^4J_{H\text{-}H}$ = 6.7 Hz, 6H, *H*-5'), 3.76 (s, 18H, O-CH_3). ^{13}C-NMR (100 MHz, CD_2Cl_2/CD_3OD): δ [ppm] = 174.0, 163.6, 160.5, 157.7, 152.2, 152.1, 133.5, 131.5, 129.6, 127.8, 126.5, 124.6, 108.7, 56.4. HR-MS (ESI$^+$, MeOH/$CHCl_3$ 1:1): *m*/*z* calculated for $[M]^{2+}$ ($[C_{90}H_{66}N_{12}O_{18}Ru_3]^{2+}$): 954.0869, found: 954.0906 (error: -1.2 ppm). Elemental analysis (%): calculated for $C_{90}H_{66}N_{12}O_{18}Ru_3 \cdot 3\ H_2O$: C 55.13, H 3.70, N 8.57, found: C 55.29, H 3.92, N 8.14.

***p*-F-MC3:**

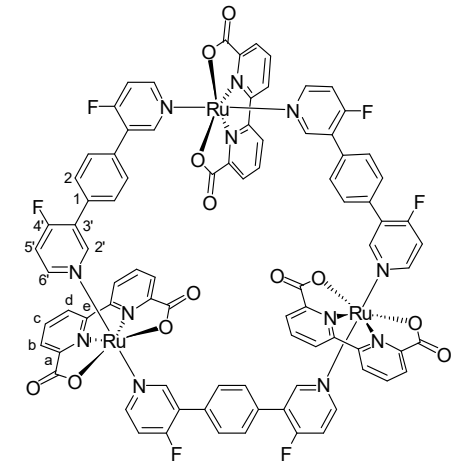

Ru(bda)(dmso)$_2$ (250 mg, 500 µmol, 1.1 equiv) and ***p*-F-bpb** (122 mg, 455 µmol, 1.0 equiv) were dissolved in a degassed mixture of chloroform (138 mL) and methanol (28 mL) and stirred for 16.5 h at 60 °C. After cooling to rt, the solvent was removed *in vacuo* and the residue purified by column chromatography (SiO_2, DCM/MeOH 10:1 to 3:1) and precipitation with hexane to yield ***p*-F-MC3** as a dark brown solid (154 mg, 84 µmol, 55%).

Melting point: >300 °C. ^{1}H-NMR (600 MHz, CD_2Cl_2/CD_3OD): δ [ppm] = 8.50 (dd, $^{3}J_{H\text{-}H}$ = 7.9 Hz, $^{4}J_{H\text{-}H}$ = 0.9 Hz, 6H, *H*-d), 8.28 (d, $^{4}J_{H\text{-}F}$ = 8.1 Hz, 6H, *H*-2'), 8.12 (dd, $^{3}J_{H\text{-}H}$ = 7.9 Hz, $^{4}J_{H\text{-}H}$ = 0.9 Hz, 6H, *H*-b), 7.93 (t, $^{3}J_{H\text{-}H}$ = 7.9 Hz, 6H, *H*-c), 7.48 (s, 12H, *H*-2), 7.41 (t, $^{3}J_{H\text{-}H}$ = 6.3 Hz, 6H, *H*-6'), 6.98 (dd, $^{3}J_{H\text{-}F}$ = 8.7 Hz, $^{4}J_{H\text{-}H}$ = 6.3 Hz, 6H, *H*-5'). ^{13}C-NMR (151 MHz, CD_2Cl_2/CD_3OD): δ [ppm] = 173.8, 166.0 (d, $^{1}J_{C\text{-}F}$ = 270.0 Hz), 160.1, 157.6, 155.3 (d, $^{3}J_{C\text{-}F}$ = 4.5 Hz), 153.1 (d, $^{3}J_{C\text{-}F}$ = 9.0 Hz), 132.6, 131.7, 129.9 (d, $^{4}J_{C\text{-}F}$ = 1.5 Hz), 127.0 (d, $^{2}J_{C\text{-}F}$ = 12.0 Hz), 126.7, 125.1, 114.2 (d, $^{2}J_{C\text{-}F}$ = 20.0 Hz). HR-MS (ESI^{+}, MeOH/$CHCl_3$ 1:1): *m*/*z* calculated for $[M]^{2+}$ ($[C_{84}H_{48}F_6N_{12}O_{12}Ru_3]^{2+}$): 918.0269, found: 918.0309 (error: -1.7 ppm). Elemental analysis (%): calculated for $C_{84}H_{48}F_6N_{12}O_{12}Ru_3$: C 54.99, H 2.64, N 9.16, found: C 55.36, H 2.91, N 9.16.

***p*-Me-MC3:**

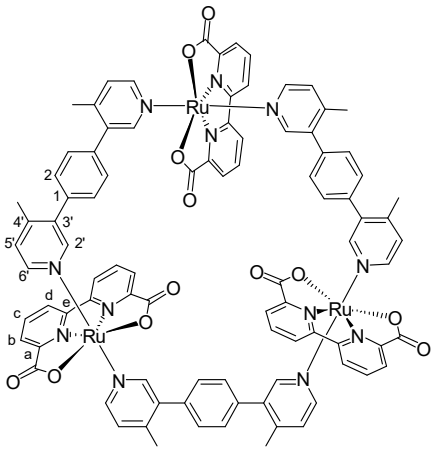

Ru(bda)(dmso)$_2$ (100 mg, 200 µmol, 1.1 equiv) and ***p*-Me-bpb** (47 mg, 182 µmol, 1.0 equiv) were dissolved in a degassed mixture of chloroform (55 mL) and methanol (11 mL) and stirred for 16.5 h at 60 °C. After cooling to rt, the solvent was removed under reduced pressure and the residue purified by column chromatography (Al_2O_3 15% w/w H_2O, DCM/MeOH 6:1, two consecutive times and subsequently SiO_2, DCM/MeOH 10:1 to 4:1) and precipitation with hexane to yield ***p*-Me-MC3** as a dark brown solid (23 mg, 13 µmol, 21%).

Melting point: >300 °C. ^{1}H-NMR (400 MHz, CD_2Cl_2/CD_3OD): δ [ppm] = 8.45 (dd, $^{3}J_{H\text{-}H}$ = 7.9 Hz, $^{4}J_{H\text{-}H}$ = 1.0 Hz, 6H, *H*-d), 8.08 (dd, $^{3}J_{H\text{-}H}$ = 7.9 Hz, $^{4}J_{H\text{-}H}$ = 1.0 Hz, 6H, *H*-b), 7.87 (t, $^{3}J_{H\text{-}H}$ = 7.9 Hz, 6H, *H*-c), 7.80 (s, 6H, *H*-2'), 7.38 (d, $^{4}J_{H\text{-}H}$ = 5.9 Hz, 6H, *H*-6'), 7.16 (s, 12H, *H*-2), 6.98 (d, $^{4}J_{H\text{-}H}$ = 5.9 Hz, 6H, *H*-5'), 2.18 (s, 18H, O-CH_3). ^{13}C-NMR (100 MHz, CD_2Cl_2/CD_3OD): δ [ppm] = 174.1, 160.4, 157.5, 152.1, 150.0, 146.9, 138.8, 136.4, 132.0, 129.8, 127.1, 126.5, 125.0, 19.8. HR-MS (ESI^{+}, MeOH/DCM 1:1): *m*/*z* calculated for $[M]^{+}$ ($[C_{90}H_{66}N_{12}O_{12}Ru_3]^{+}$): 1812.2048, found: 1812.2069 (error: -1.6 ppm). Elemental analysis (%): calculated for $C_{90}H_{66}N_{12}O_{18}Ru_3 \cdot H_2O$: C 59.11, H 3.75, N 9.19, found: C 59.05, H 3.38, N 9.00.

Synthesis of Ru macrocycle functionalized at equatorial ligand

4,4'-Dimethoxy-6,6'-divinyl-2,2'-bipyridine (38)

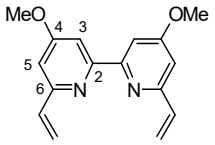

6,6'-Dibromo-4,4'-dimethoxy-2,2'-bipyridine **36** (780 mg, 2.09 mmol, 1.0 equiv) and 2,4,6-trivinylcyclotriboroxane **37** (602 mg, 2.50 mmol, 1.2 equiv) were suspended in a degassed mixture of DME (10 mL) and 2 M K_2CO_3 (5 mL) under nitrogen. After addition of $Pd(PPh_3)_4$ (483 mg, 418 µmol, 0.2 equiv), the mixture was heated under reflux (105 °C) for 16 h. Afterwards, the solvent was removed *in vacuo* and the residue redissolved in EtOAc, filtered and purified by column chromatography (SiO_2, cyclohexane/EtOAc 49:1) to yield **38** as a white solid (382 mg, 1.42 mmol, 68%).

Melting point: 84 °C. ^{1}H-NMR (400 MHz, $CDCl_3$): δ [ppm] = 7.99 (d, $^4J_{H\text{-}H}$ = 2.4 Hz, 2H, *H*-3), 6.87 (d, $^4J_{H\text{-}H}$ = 2.4 Hz, 2H, *H*-5), 6.89 (dd, $^3J_{H\text{-}H}$ = 17.4 Hz, $^3J_{H\text{-}H}$ = 10.7 Hz, 2H, Ar-*H*=CH_2), 6.33 (dd, $^3J_{H\text{-}H}$ = 17.4 Hz, $^4J_{H\text{-}H}$ = 1.5 Hz, 2H, CH=CH_2), 5.50 (dd, $^3J_{H\text{-}H}$ = 10.7 Hz, $^4J_{H\text{-}H}$ = 1.5 Hz, 2H, CH=CH_2), 3.96 (s, 6H, OCH_3). ^{13}C-NMR (100 MHz, $CDCl_3$): δ [ppm] = 167.2, 157.4, 156.3, 137.0, 118.2, 108.3, 105.4, 55.3. HR-MS (ESI^+, MeOH/$CHCl_3$ 1:1): *m*/*z* calculated for $[M+H]^+$ ($[C_{16}H_{17}N_2O_2]^+$): 269.1290, found: 269.1286 (error: 1.5 ppm). Elemental analysis (%): calculated for $C_{16}H_{16}N_2O_2$: C 71.62, H 6.01, N 10.44, found: C 71.38, H 6.23, N 10.31.

4,4'-dimethoxy-[2,2'-bipyridine]-6,6'-dicarboxylic acid (39)

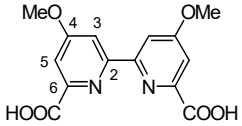

38 (380 mg, 1.42 mmol, 1.0 equiv) was dissolved in concentrated sulfuric acid (10 mL) and added dropwise to a solution of $K_2Cr_2O_7$ (1.25 g, 4.25 mmol, 3.0 equiv) in water (15 mL). The mixture was stirred at 65 °C for 16 h and then poured into ice. Afterwards, the solid was collected by centrifugation and washed with water to yield **39** as a white solid (258 mg, 0.85 mmol, 60%).

Melting point: 245 °C. ^{1}H-NMR (400 MHz, DMSO-d_6): δ [ppm] = 13.24 (s, 2H, COO*H*), 8.32 (d, $^4J_{H\text{-}H}$ = 2.5 Hz, 2H, *H*-3), 7.65 (d, $^4J_{H\text{-}H}$ = 2.5 Hz, 2H, *H*-5), 4.01 (s, 6H, OCH_3). ^{13}C-NMR

(100 MHz, DMSO-d_6): δ [ppm] = 167.9, 166.1, 156.3, 150.1, 111.7, 110.5, 56.6. HR-MS (ESI^+, MeOH/$CHCl_3$ 1:1): *m*/*z* calculated for $[M+Na]^+$ ($[C_{14}H_{12}N_2NaO_6]^+$): 327.0588, found: 327.0592 (error: -1.5 ppm).

Ru(MeO-bda)(dmso)$_2$ (40)

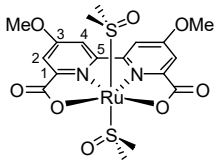

39 (109 mg, 358 µmol, 1.0 equiv) and $RuCl_2(dmso)_4$ (190 mg, 394 µmol, 1.1 equiv) were dissolved in a degassed mixture of anhydrous methanol (20 mL) and triethylamine (1 mL) under nitrogen. The mixture was heated under reflux (75 °C) for 16 h. Afterwards, the solid was collected by centrifugation and washed with methanol to yield **40** as a brown solid (112 mg, 200 µmol, 56%).

Melting point: 185-190 °C (decomposition). ^{1}H-NMR (400 MHz, 399 K, DMSO-d_6): δ [ppm] = 8.24 (s, 2H, *H*-4), 7.56 (d, $^4J_{H\text{-}H}$ = 2.3 Hz, 2H, *H*-2), 4.09 (s, 6H, O*CH*$_3$), 2.54 (s, 12H, O=S(*CH*$_3$)$_2$). HR-MS (ESI^+, MeCN/H_2O 1:1): *m*/*z* calculated for $[M\text{-dmso }+MeCN+H]^+$ ($[C_{18}H_{20}N_3O_7RuS]^+$): 524.0060, found: 524.0042 (error: 3.4 ppm).

MeO-bda-MC3

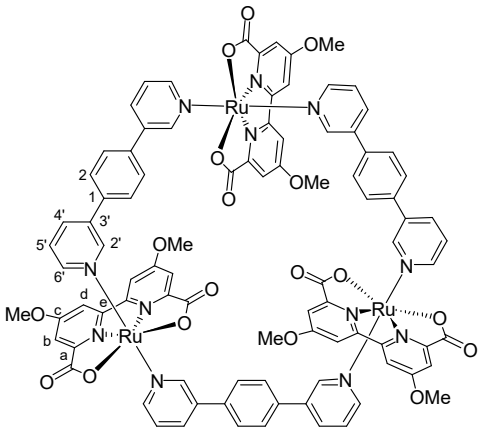

40 (35 mg, 63 µmol, 1.0 equiv) and **bpb** (14.5 mg, 63 µmol, 1.0 eq) were dissolved in a degassed mixture of chloroform (37.5 mL) and methanol (7.5 mL) and stirred for 16.5 h at 60 °C. After cooling to rt, the solvent was removed under reduced pressure and the residue purified by column chromatography (Al_2O_3 15% w/w H_2O, DCM/MeOH 9:1) to yield **MeO-bda-MC3** as a dark brown solid (34 mg, 18 µmol, 28%).

Melting point: >300 °C. ^{1}H-NMR (400 MHz, CD_2Cl_2/CD_3OD + ascorbic acid): δ [ppm] = 8.58 (t, $^4J_{H\text{-}H}$ = 2.3 Hz, 6H, *H*-d), 8.21 (d, $^4J_{H\text{-}H}$ = 2.3 Hz, 6H, *H*-b), 7.81 (ddd, $^3J_{H\text{-}H}$ = 7.8 Hz, $^4J_{H\text{-}H}$ = 2.3 Hz, $^5J_{H\text{-}H}$ = 1.2 Hz, 6H, *H*-4'), 7.71 (d, $^4J_{H\text{-}H}$ = 2.3 Hz, 6H, *H*-2'), 7.61 (d, $^3J_{H\text{-}H}$ = 5.5 Hz, 6H, *H*-6'), 7.58 (d, $^5J_{H\text{-}H}$ = 1.2 Hz, 12H, *H*-2), 7.16 (dd, $^3J_{H\text{-}H}$ = 7.8 Hz, $^3J_{H\text{-}H}$ = 5.5 Hz, 6H, *H*-5'), 4.08 (s, 18H, O*CH*$_3$). ^{13}C-NMR (100 MHz, CD_2Cl_2/CD_3OD + ascorbic acid): δ [ppm] = 173.9,

165.5, 160.7, 160.5, 158.2, 153.0, 150.8, 137.4, 137.0, 134.8, 128.5, 125.4, 113.3, 57.2. HR-MS (MALDI$^+$, MeOH/$CHCl_3$ 1:1): *m*/*z* calculated for $[M]^+$ ($[C_{90}H_{66}N_{12}O_{18}Ru_3]^+$): 1908.1743, found: 1908.1790 (error: -2.5 ppm).

Synthesis of ruthenium tris(bipyridine) photosensitizer **PS3**

1,4-bis(5-bromopyridin-3-yl)benzene (42)

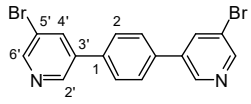

3-Bromo-5-iodopyridine **41** (5.00 g, 17.6 mmol, 2.2 equiv), 1,4-bis(4,4,5,5-tetramethyl-1,3,2-dioxolan-2-yl)benzene **33** (2.64 g, 8.0 mmol, 1.0 equiv) and potassium carbonate (3.32 g, 24.0 mmol, 3.0 equiv) were dissolved in a degassed mixture of toluene (19 mL), ethanol (10 mL) and water (6.4 mL) under a nitrogen atmosphere. After addition of $Pd(PPh_3)_4$ (930 mg, 800 µmol, 0.1 equiv), the mixture was heated under reflux (105 °C) for 4 days. Afterwards, the originated precipitate was collected by vacuum filtration and washed with DCM (100 mL) and water (100 mL) to yield **42** as a white solid (2.65 g, 6.79 mmol, 85%).

Melting point: 188 °C. ^{1}H-NMR (400 MHz, CD_2Cl_2): *δ* [ppm] = 8.81 (d, $^4J_{H\text{-}H}$ = 2.1 Hz, 2H, *H*-2'), 8.67 (d, $^4J_{H\text{-}H}$ = 2.1 Hz, 2H, *H*-6'), 8.11 (t, $^4J_{H\text{-}H}$ = 2.1 Hz, 2H, *H*-4'), 7.73 (s, 4H, *H*-2). ^{13}C-NMR (100 MHz, CD_2Cl_2): *δ* [ppm] = 150.1, 146.7, 137.6, 137.1, 137.0, 128.3, 121.3. HR-MS (ESI$^+$, MeOH/$CHCl_3$): *m*/*z* calculated for $[M+H]^+$ ($[C_{16}H_{11}N_2O_2]^+$): 388.9283, found: 388.9270 (error: 3.4 ppm). Elemental analysis (%): calculated for $C_{16}H_{10}N_2O_2$: C 49.27, H 2.58, N 7.18, found: C 49.12, H 2.69, N 7.07.

1,4-bis(5-(4,4,5,5-tetramethyl-1,3,2-dioxaborolan-2-yl)pyridin-3-yl)benzene (43)

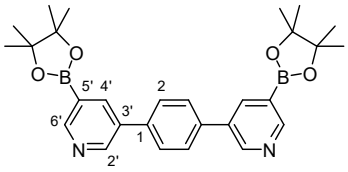

42 (1.60 g, 4.10 mmol, 1.0 equiv), bis(pinacolato)diboron (3.12 g, 12.3 mmol, 3.0 equiv) and potassium acetate (2.42 g, 24.6 mmol, 6.0 equiv) were dissolved in degassed dioxane (19 mL) under nitrogen. After addition of $Pd(dppf)Cl_2$ (300 mg, 410 µmol, 0.1 equiv), the mixture was heated at 85 °C for 3 days. Afterwards, water (100 mL) was added and the organic phase extracted with ethyl acetate (4 x 100 mL). The combined organic phases were

dried over anhydrous Na_2SO_4. The residue was purified by column chromatography (SiO_2, EtOAc to EtOAc/MeOH 95:5) and washed with EtOAc to yield **43** as a white solid (1.24 g, 2.55 mmol, 62%).

Melting point: >300 °C. ^{1}H-NMR (400 MHz, $CDCl_3$): δ [ppm] = 8.95 (d, $^4J_{H\text{-}H}$ = 2.5 Hz, 2H, *H*-2'), 8.94 (d, $^4J_{H\text{-}H}$ = 1.6 Hz, 2H, *H*-6'), 8.31 (dd, $^4J_{H\text{-}H}$ = 2.5 Hz, $^4J_{H\text{-}H}$ = 1.6 Hz, 2H, *H*-4'), 7.73 (s, 4H, *H*-2), 1.39 (s, 24H, C*H*$_3$). ^{13}C-NMR (100 MHz, $CDCl_3$): δ [ppm] = 154.5, 150.6, 140.6, 137.6, 135.3, 127.9, 124.0, 84.5, 25.0. HR-MS (ESI$^+$, MeOH/$CHCl_3$ 1:1): *m*/*z* calculated for $[M+H]^+$ ($[C_{28}H_{35}B_2N_2O_4]^+$): 485.2777, found: 485.2781 (error: -1.2 ppm). Elemental analysis (%): calculated for $C_{28}H_{34}B_2N_2O_4$: C 69.45, H 7.08, N 5.79, found: C 69.70, H 7.20, N 5.85.

1,4-di([2,2':4',3''-terpyridin]-5''-yl)benzene (45)

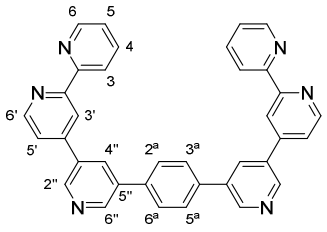

4-Bromo-2,2'-bipyridine **44** (713 mg, 3.04 mmol, 2.2 equiv), **43** (668 mg, 1.38 mmol, 1.0 equiv) and potassium carbonate (572 mg, 4.14 mmol, 3.0 equiv) were dissolved in a degassed mixture of toluene (4.0 mL), ethanol (1.8 mL) and water (1.3 mL) under a nitrogen atmosphere. After addition of $Pd(PPh_3)_4$ (318 mg, 276 µmol, 0.2 equiv), the mixture was heated under reflux (105 °C) for 4 days. Afterwards, the solvent was removed *in vacuo* and the residue resuspended in water (100 mL). The remaining solid was collected by vacuum filtration and washed with EtOAc (100 mL) and DCM (10 mL) to yield **45** as a light-yellow solid (604 mg, 1.12 mmol, 81%).

Melting point: 288 °C. ^{1}H-NMR (400 MHz, 330 K, $CDCl_3$): δ [ppm] = 9.01 (d, $^4J_{H\text{-}H}$ = 2.2 Hz, 2H, *H*-2''), 9.00 (d, $^4J_{H\text{-}H}$ = 2.2 Hz, 2H, *H*-6''), 8.82 (dd, $^3J_{H\text{-}H}$ = 5.1 Hz, $^5J_{H\text{-}H}$ = 0.6 Hz, 2H, *H*-6'), 8.79 (dd, $^4J_{H\text{-}H}$ = 1.8 Hz, $^5J_{H\text{-}H}$ = 0.6 Hz, 2H, *H*-3'), 8.72 (ddd, $^3J_{H\text{-}H}$ = 4.8 Hz, $^4J_{H\text{-}H}$ = 1.8 Hz, $^5J_{H\text{-}H}$ = 1.0 Hz, 2H, *H*-6), 8.52 (dd, $^3J_{H\text{-}H}$ = 8.0 Hz, $^5J_{H\text{-}H}$ = 1.0 Hz, 2H, *H*-3), 8.27 (t, $^4J_{H\text{-}H}$ = 2.2 Hz, 2H, *H*-4''), 7.85 (dt, $^3J_{H\text{-}H}$ = 8.0 Hz, $^4J_{H\text{-}H}$ = 1.8 Hz, 2H, *H*-4), 7.84 (s, 4H, *H*-2ª,3ª,5ª,6ª), 7.61 (dd, $^3J_{H\text{-}H}$ = 5.1 Hz, $^4J_{H\text{-}H}$ = 1.8 Hz, 2H, *H*-5'), 7.34 (ddd, $^3J_{H\text{-}H}$ = 8.0 Hz, $^3J_{H\text{-}H}$ = 4.8 Hz, $^4J_{H\text{-}H}$ = 1.0 Hz, 2H, *H*-5). ^{13}C-NMR (100 MHz, 330 K, $CDCl_3$): δ [ppm] = 157.2, 156.2, 150.2, 149.4, 148.8, 147.5, 146.4, 137.8, 137.1, 136.4, 134.6, 133.0, 128.4, 124.2, 121.7, 121.6, 119.4. HR-MS (ESI$^+$, MeOH/$CHCl_3$ 1:1): *m*/*z* calculated for $[M+H]^+$ ($[C_{36}H_{25}N_6]^+$): 541.2135,

found: 541.2144 (error: -1.5 ppm). Elemental analysis (%): calculated for $C_{36}H_{24}N_6$: C 79.98, H 4.47, N 15.55, found: C 79.64, H 4.59, N 15.49.

PS3

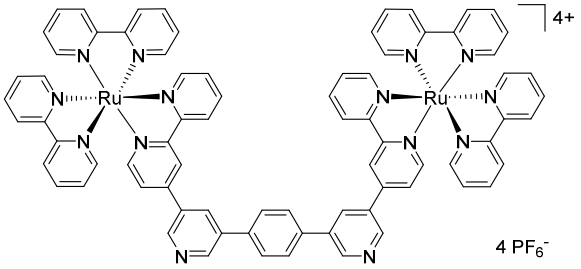

45 (100 mg, 185 µmol, 1.0 equiv) and $[Ru(bpy)_2Cl_2]$ (188 mg, 388 µmol, 2.1 equiv) were suspended in a mixture of ethanol (27 mL) and water (9 mL) and heated under reflux (100 °C) for 16 h. Afterwards, the solvent was removed *in vacuo* and the residue purified by column chromatography (SiO_2, MeCN/H_2O/3 N KNO_3 40:4:1). The dried product fraction was washed with cold water to remove the excess of KNO_3. The residue was then dissolved in water and a saturated aqueous solution of NH_4PF_6 added. The resulting precipitate was isolated by vacuum filtration, washed with water and Et_2O and dried under reduced pressure at 60 °C to yield **PS3** as a red solid (224 mg, 85.6 mmol, 46%).

Melting point: 297 °C. ^{1}H-NMR (400 MHz, CDCN): δ [ppm] = 9.09 (d, $^4J_{H\text{-}H}$ = 2.2 Hz, 2H), 9.06 (d, $^4J_{H\text{-}H}$ = 2.2 Hz, 2H), 8.87 (d, $^4J_{H\text{-}H}$ = 1.5 Hz, 2H), 8.73 (d, $^3J_{H\text{-}H}$ = 8.0 Hz, 2H), 8.54-8.50 (m, 10H), 8.14-8.04 (m, 10H), 8.00 (s, 4H), 7.85-7.72 (m, 14H), 7.47-7.38 (m, 10H). ^{13}C-NMR (100 MHz, CDCN): δ [ppm] = 158.7, 158.0, 157.9, 157.9, 157.9, 153.0, 152.8, 152.8, 152.7, 152.6, 152.6, 150.5, 148.4, 147.5, 138.9, 138.8, 138.1, 136.8, 134.0, 132.7, 129.1, 128.8, 128.6, 128.6, 128.6, 126.1, 125.6, 125.3, 123.3. HR-MS (ESI$^+$, MeCN): *m*/*z* calculated for $[M\text{-}PF_6]^+$ ($[C_{76}H_{56}F_{18}N_{14}P_3Ru_2]^+$): 1803.1819, found: 1803.1812 (error: 2.3 ppm). Elemental analysis (%): calculated for $C_{76}H_{56}F_{24}N_{14}P_4Ru_2$: C 46.88, H 2.90, N 10.07, found: C 46.50, H 3.05, N 9.77.

Chapter 8 – Appendix

8.1 Supporting Information for Chapter 3

X-ray Crystal Structure Analysis

Table S1. Summary of X-ray crystal structure analysis of ***m*-F-MC3** (CCDC 1985319) and ***p*-F-MC3** (CCDC 1985320).

	***m*-F-MC3**	***p*-F-MC3**		
		Ru^1	Ru^2	Ru^3
O-Ru-O [°]	122.8(2)	123.1(1)	121.9(1)	123.0(1)
N_{ax}-Ru-N_{ax} [°]	172.5(2)	176.3(1)	175.1(1)	171.1(1)
d(Ru-N_{ax}) [Å]	2.081(5)	2.089(3)	2.080(2)	2.075(3)
	2.084(4)	2.118(3)	2.099(2)	2.067(3)
Torsion py_{ax}-Ru-py_{ax} [°]	48.7	47.5	29.1	18.0
Torsion py_{ax}-ph-py_{ax} [°]	54.8	71.8	5.3	2.0

Redox Properties

Table S2. Redox properties of the macrocyclic **MC3** derivatives under neutral conditions.[a]

Macrocycle	*E vs.* NHE [V]		
	Ru^{III}_3/Ru^{II}_3	Ru^{IV}_3/Ru^{III}_3	Ru^{V}_3/Ru^{IV}_3
MC3	+0.66	+0.82	+1.00
***m*-MeO-MC3**	+0.66	+0.83	+1.02
***m*-F-MC3**	+0.68	+0.83	+1.06
***m*-Me-MC3**	+0.66	+0.84	+1.02
***p*-F-MC3**	+0.65	+0.84	+1.04
***p*-MeO-MC3**	+0.61	+0.81	+0.98
***p*-Me-MC3**	+0.63	+0.81	+1.00
MeO-bda-MC3	+0.57	+0.80	+0.97

[a] CV and DPV measurements were performed in TFE/H_2O 1:1 (phosphate buffer, pH 7), *c* = 0.25 mM.

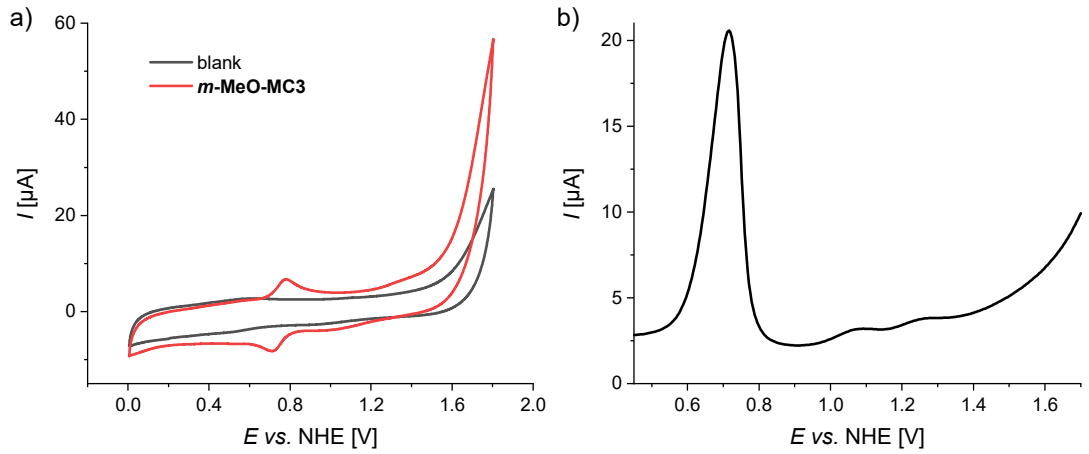

Figure S1. CV (a) and DPV (b) of ***m*-MeO-MC3** in TFE/H_2O 1:1 (pH 1, triflic acid), *c* = 0.25 mM.

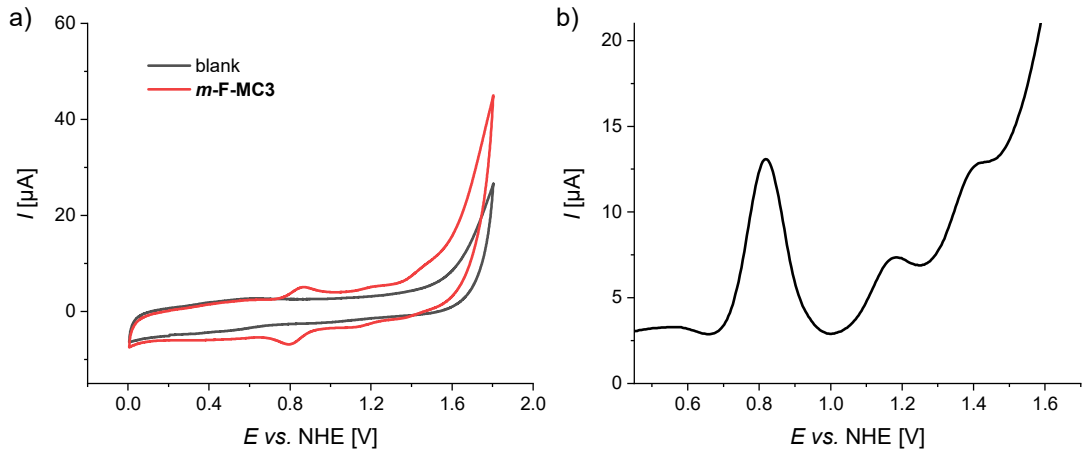

Figure S2. CV (a) and DPV (b) of ***m*-F-MC3** in TFE/H_2O 1:1 (pH 1, triflic acid), *c* = 0.25 mM.

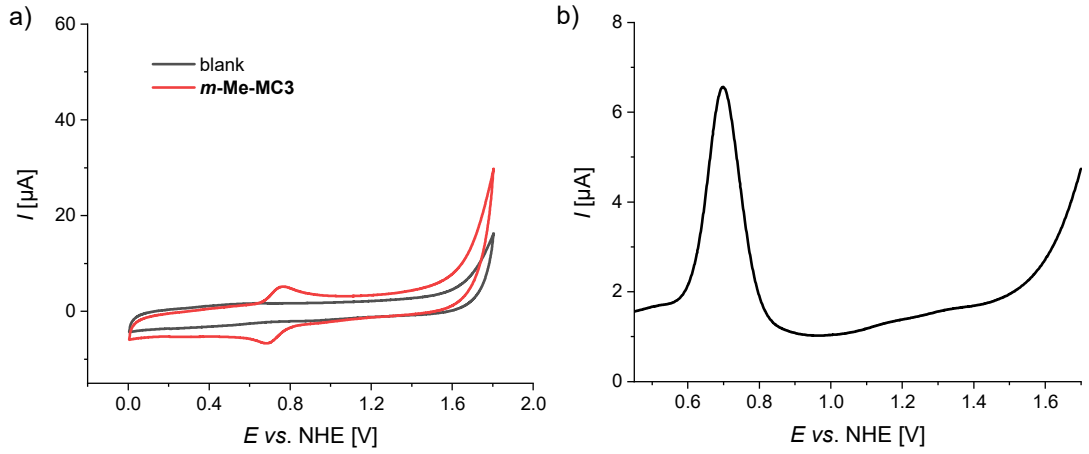

Figure S3. CV (a) and DPV (b) of ***m*-Me-MC3** in TFE/H_2O 1:1 (pH 1, triflic acid), *c* = 0.25 mM.

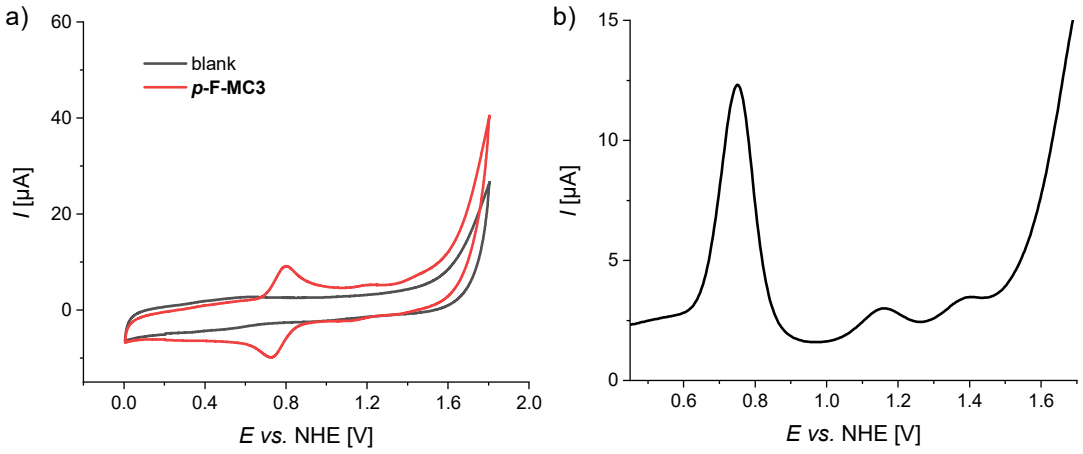

Figure S4. CV (a) and DPV (b) of ***p*-F-MC3** in TFE/H_2O 1:1 (pH 1, triflic acid), *c* = 0.25 mM.

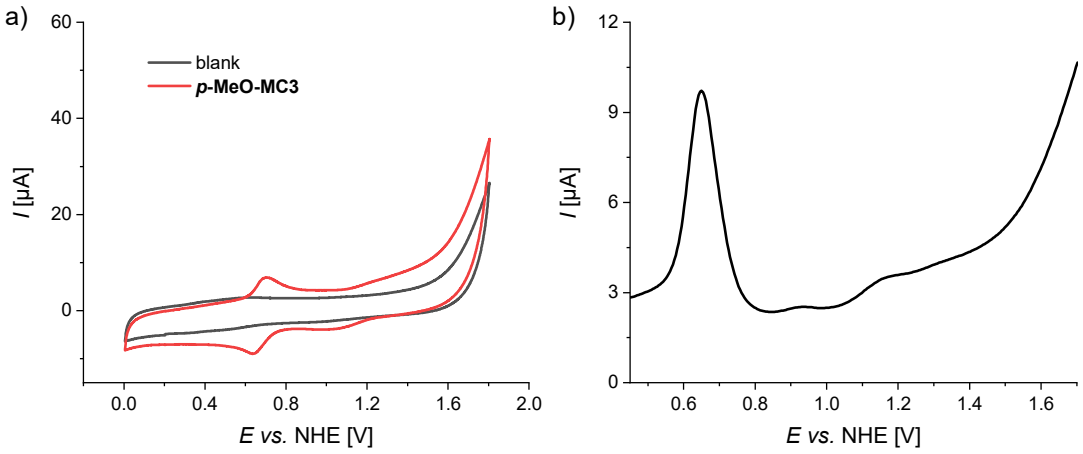

Figure S5. CV (a) and DPV (b) of ***p*-MeO-MC3** in TFE/H_2O 1:1 (pH 1, triflic acid), *c* = 0.25 mM.

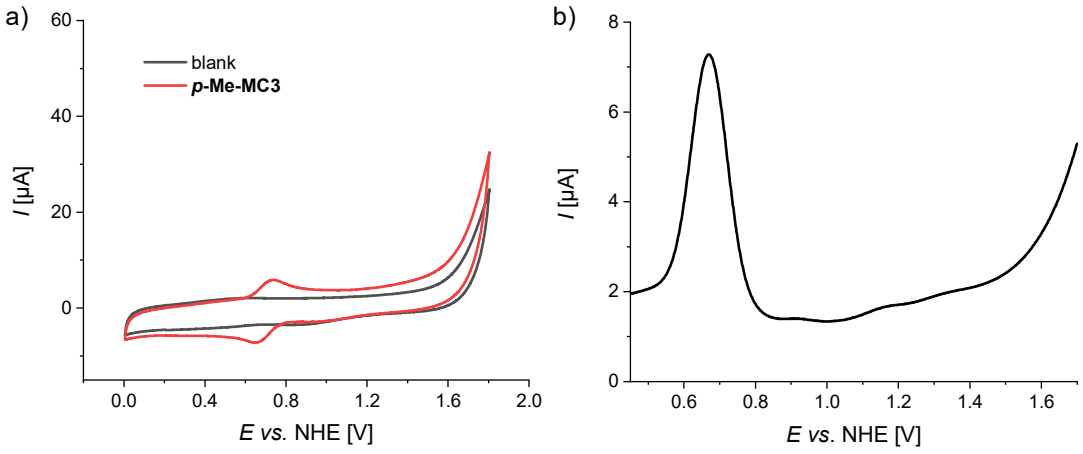

Figure S6. CV (a) and DPV (b) of ***p*-Me-MC3** in TFE/H_2O 1:1 (pH 1, triflic acid), *c* = 0.25 mM.

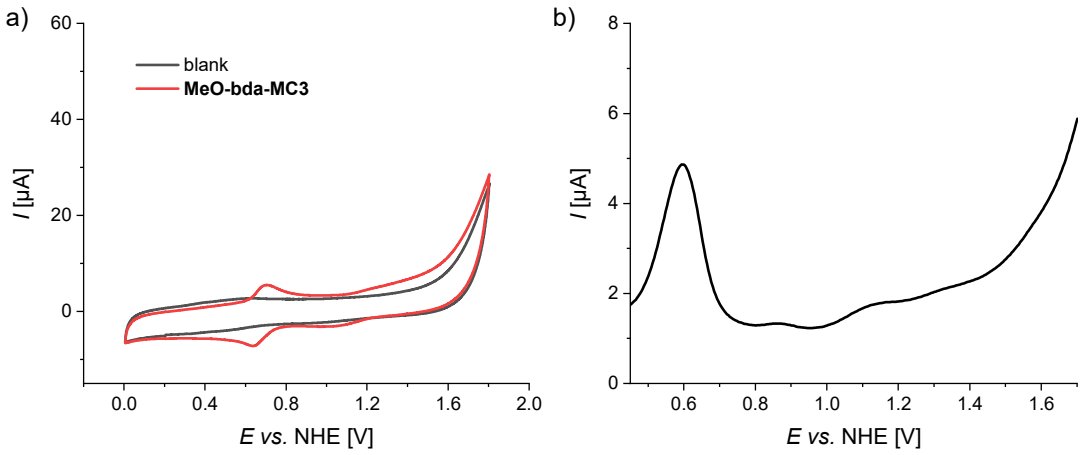

Figure S7. CV (a) and DPV (b) of **MeO-bda-MC3** in TFE/H_2O 1:1 (pH 1, triflic acid), *c* = 0.25 mM.

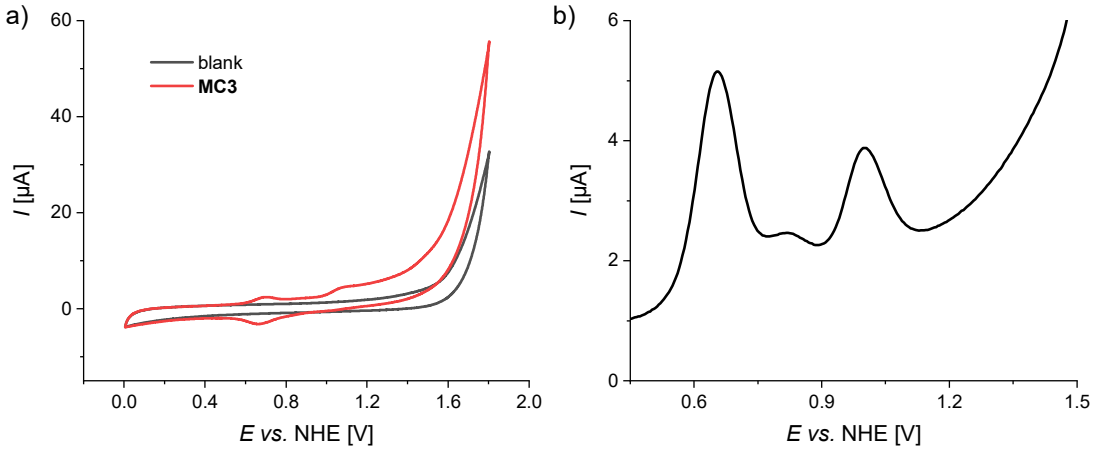

Figure S8. CV (a) and DPV (b) of **MC3** in TFE/H_2O 1:1 (pH 7, phosphate buffer), *c* = 0.25 mM.

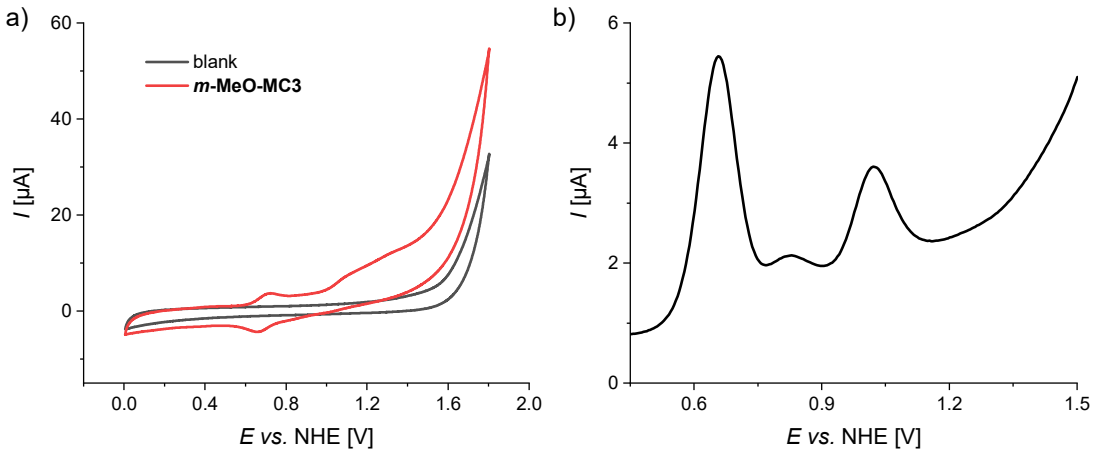

Figure S9. CV (a) and DPV (b) of ***m*-MeO-MC3** in TFE/H_2O 1:1 (pH 7, phosphate buffer), *c* = 0.25 mM.

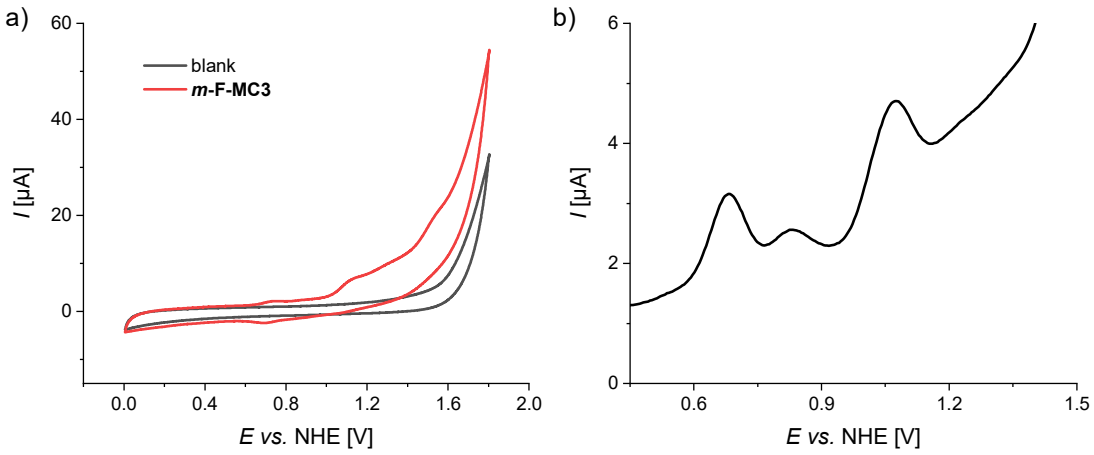

Figure S10. CV (a) and DPV (b) of ***m*-F-MC3** in TFE/H_2O 1:1 (pH 7, phosphate buffer), *c* = 0.25 mM.

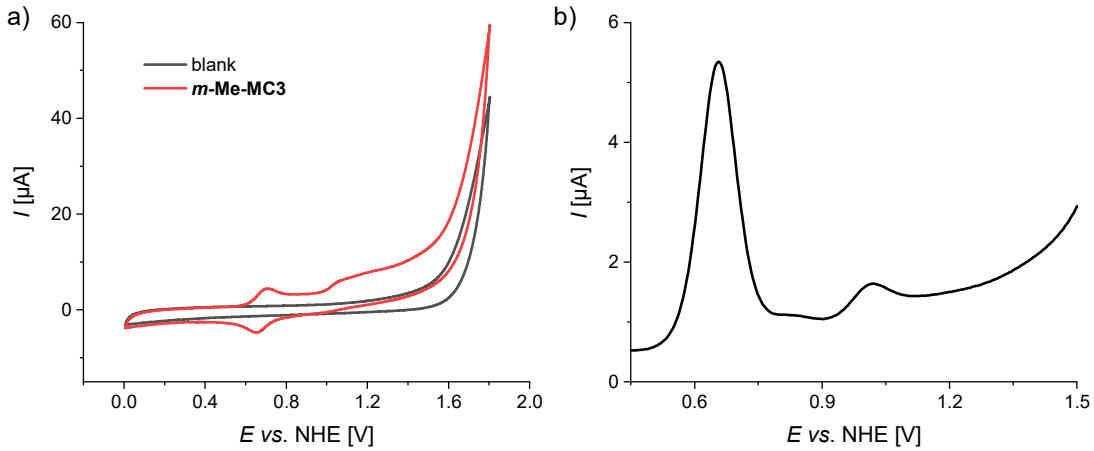

Figure S11. CV (a) and DPV (b) of ***m*-Me-MC3** in TFE/H_2O 1:1 (pH 7, phosphate buffer), *c* = 0.25 mM.

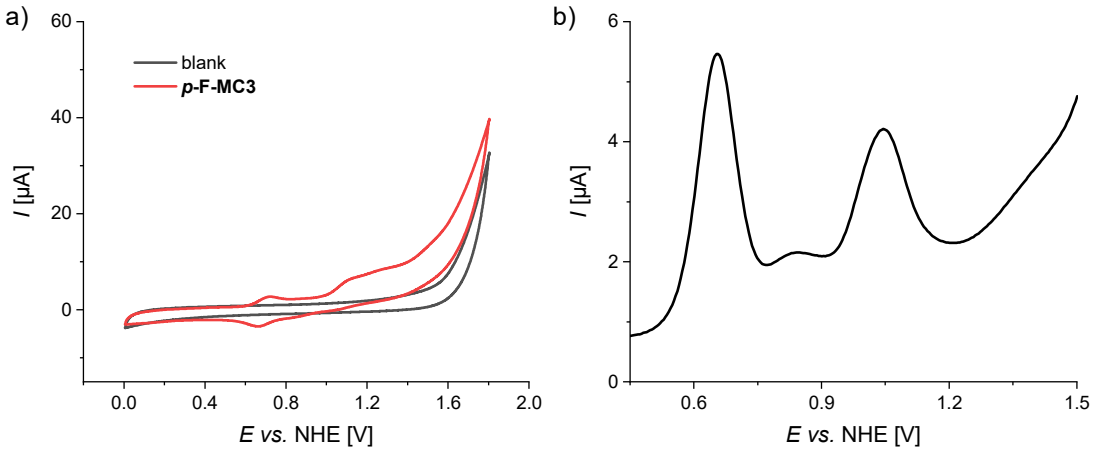

Figure S12. CV (a) and DPV (b) of ***p*-F-MC3** in TFE/H_2O 1:1 (pH 7, phosphate buffer), *c* = 0.25 mM.

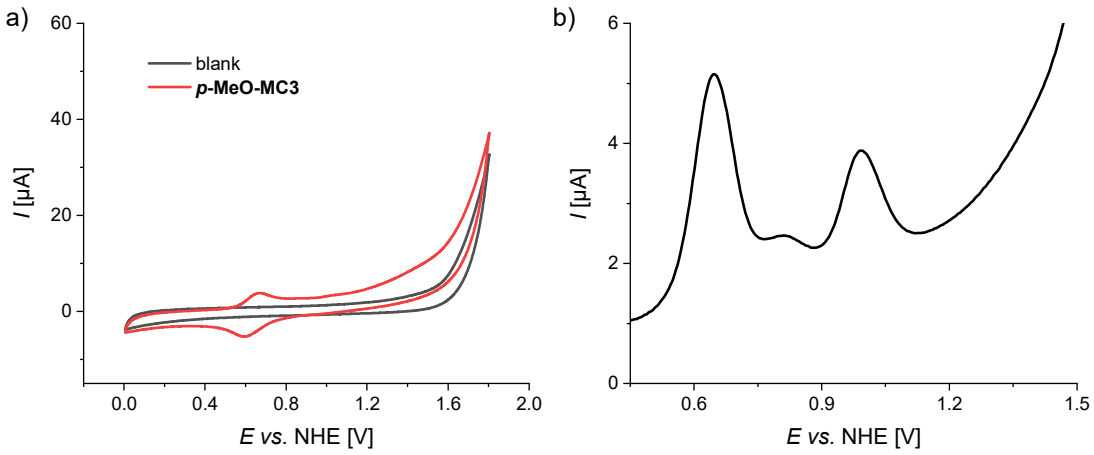

Figure S13. CV (a) and DPV (b) of ***p*-MeO-MC3** in TFE/H_2O 1:1 (pH 7, phosphate buffer), *c* = 0.25 mM.

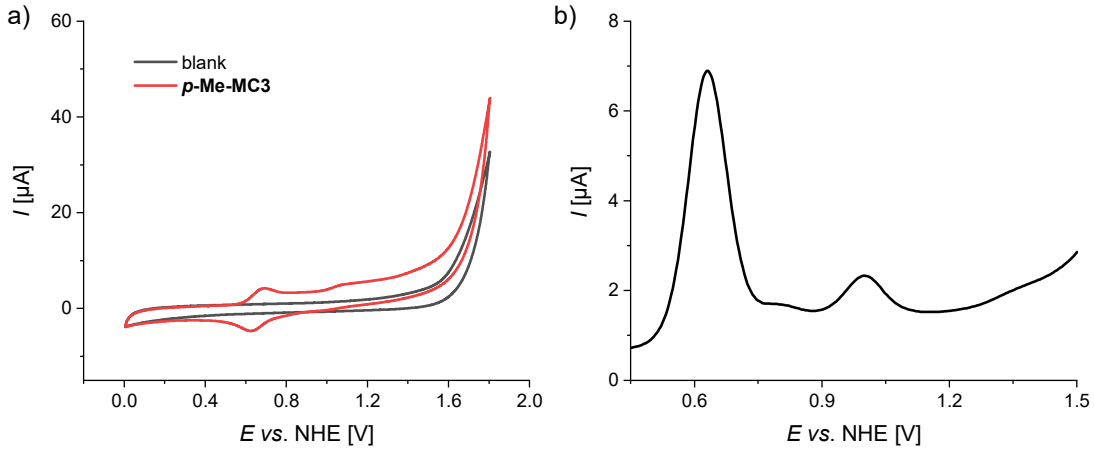

Figure S14. CV (a) and DPV (b) of ***p*-Me-MC3** in TFE/H_2O 1:1 (pH 7, phosphate buffer), *c* = 0.25 mM.

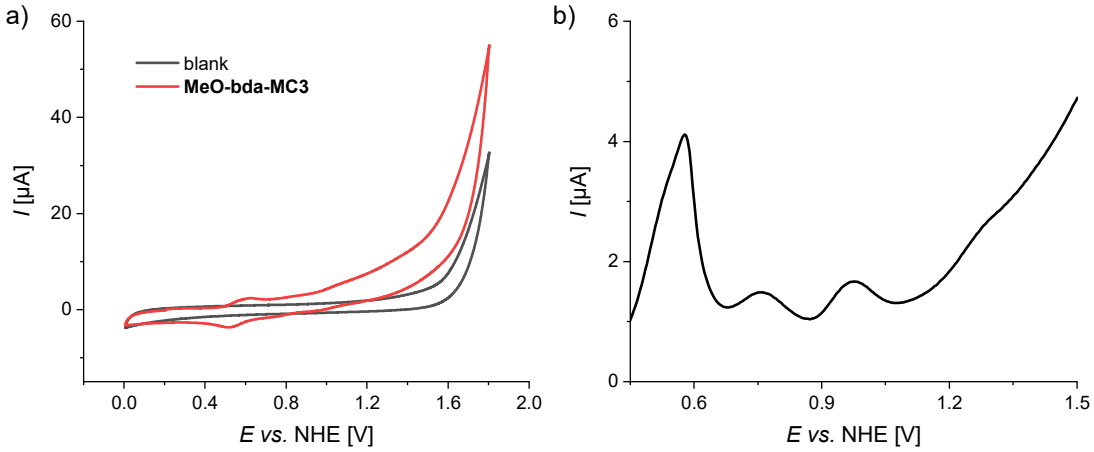

Figure S15. CV (a) and DPV (b) of **MeO-bda-MC3** in TFE/H_2O 1:1 (pH 7, phosphate buffer), *c* = 0.25 mM.

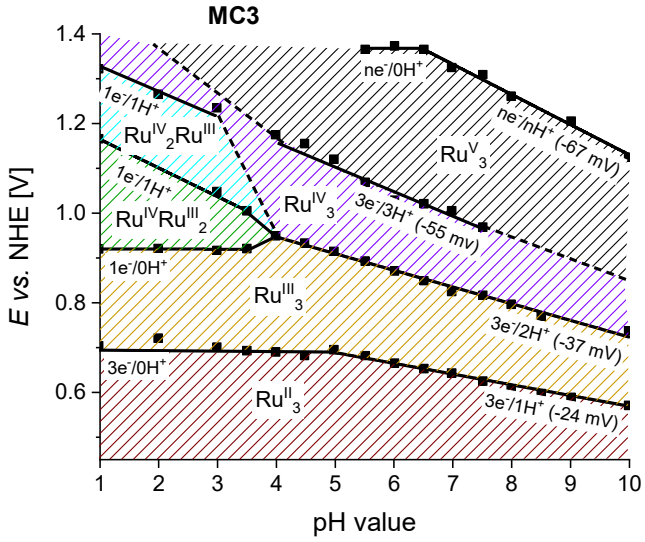

Figure S16. Pourbaix diagram of **MC3**. DPV measurements were performed in TFE/H_2O 1:1 (phosphate buffer at different pH values). In a previous publication (ref. [18]) a different Pourbaix diagram of **MC3** was published. The discrepancy is presumably due to some differences in experimental procedure. In ref. [18], the pH value of a starting acidic solution of the macrocycle was adjusted by successive addition of sodium hydroxide disregarding any control over the ionic strength. Here, several solutions of **MC3** were prepared at a constant ionic strength of 0.1 M.

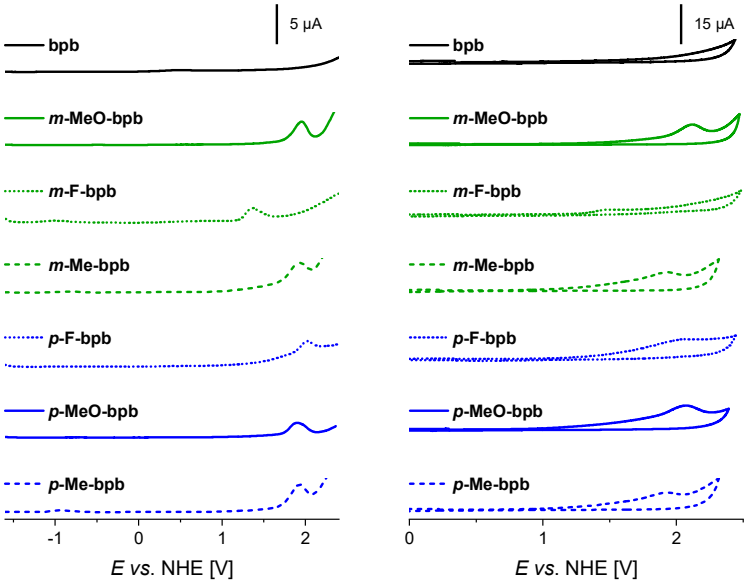

Figure S17. CV (left) and DPV (right) of functionalized bpb bridging ligands in DCM, ^{n}Bu$_4$NPF$_6$ (0.1 M), *c* = 0.25 mM.

Spectroelectrochemistry

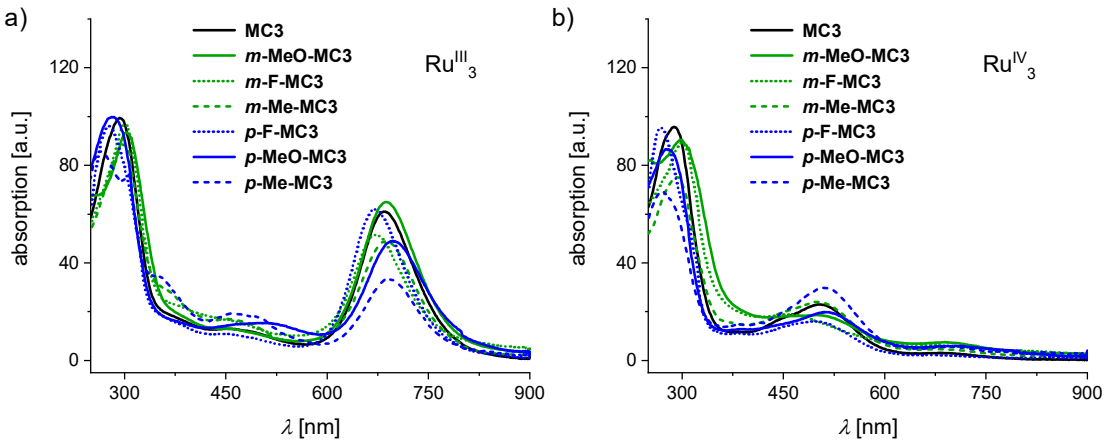

Figure S18. UV/Vis absorption spectra of the macrocyclic **MC3** derivatives at the Ru^{III}_3 (a) and Ru^{IV}_3 (b) states in MeCN/H_2O 1:1 (phosphate buffer, pH 7), *c* = 0.24 mM. Oxidized Ru species were generated by application of an increasing voltage from 500 mV to 1100 mV.

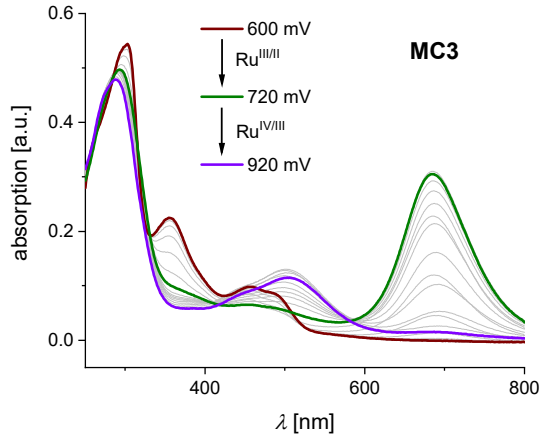

Figure S19. Spectroelectrochemistry of **MC3** in MeCN/H_2O 1:1 (phosphate buffer, pH 7), *c* = 0.24 mM. Starting from Ru^{II}_3 (brown), Ru^{III}_3 (green) and Ru^{IV}_3 (purple) species were generated by application of an increasing voltage as indicated in the inset.

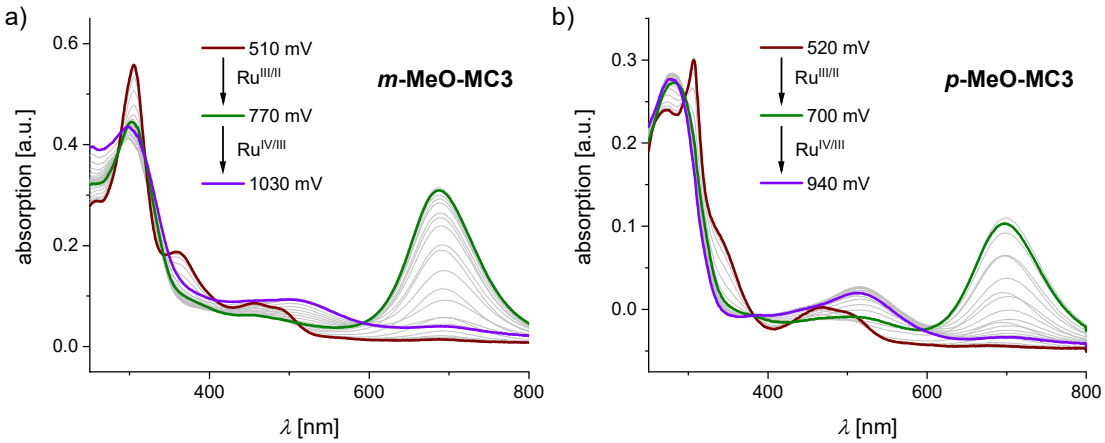

Figure S20. Spectroelectrochemistry of (a) ***m*-MeO-MC3** and (b) ***p*-MeO-MC3** in MeCN/H_2O 1:1 (phosphate buffer, pH 7), c = 0.24 mM. Starting from Ru^{II}_3 (brown), Ru^{III}_3 (green) and Ru^{IV}_3 (purple) species were generated by application of an increasing voltage as indicated in the insets.

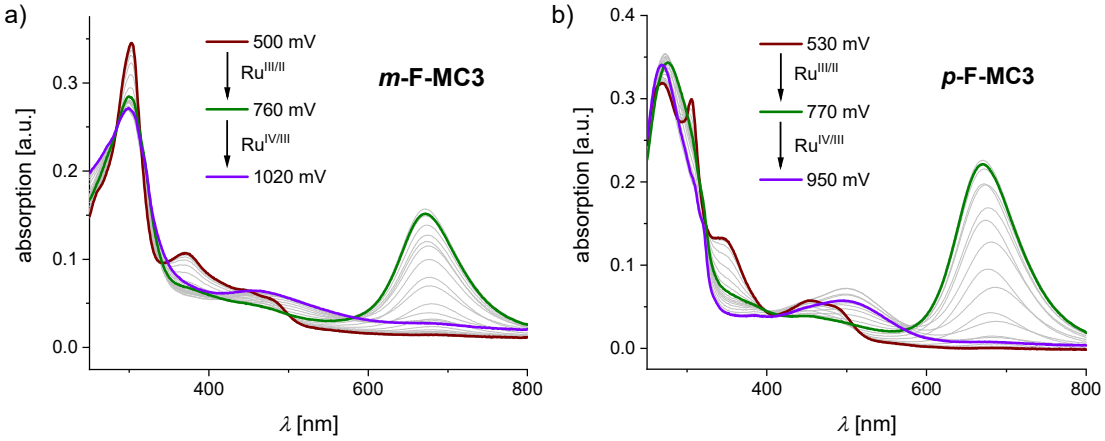

Figure S21. Spectroelectrochemistry of (a) ***m*-F-MC3** and (b) ***p*-F-MC3** in MeCN/H_2O 1:1 (phosphate buffer, pH 7), c = 0.24 mM. Starting from Ru^{II}_3 (brown), Ru^{III}_3 (green) and Ru^{IV}_3 (purple) species were generated by application of an increasing voltage as indicated in the insets.

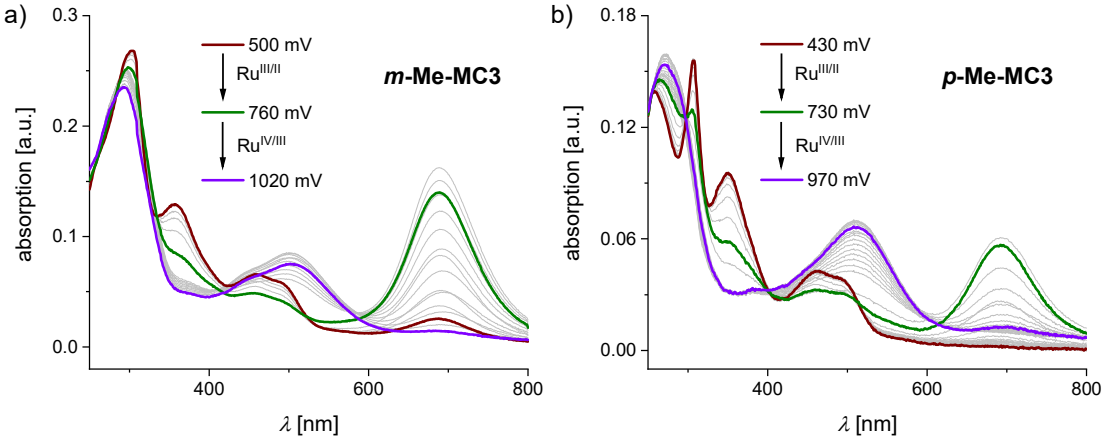

Figure S22. Spectroelectrochemistry of (a) ***m*-Me-MC3** and (b) ***p*-Me-MC3** in MeCN/H_2O 1:1 (phosphate buffer, pH 7), c = 0.24 mM. Starting from Ru^{II}_3 (brown), Ru^{III}_3 (green) and Ru^{IV}_3 (purple) species were generated by application of an increasing voltage as indicated in the insets.

EPR Experiments

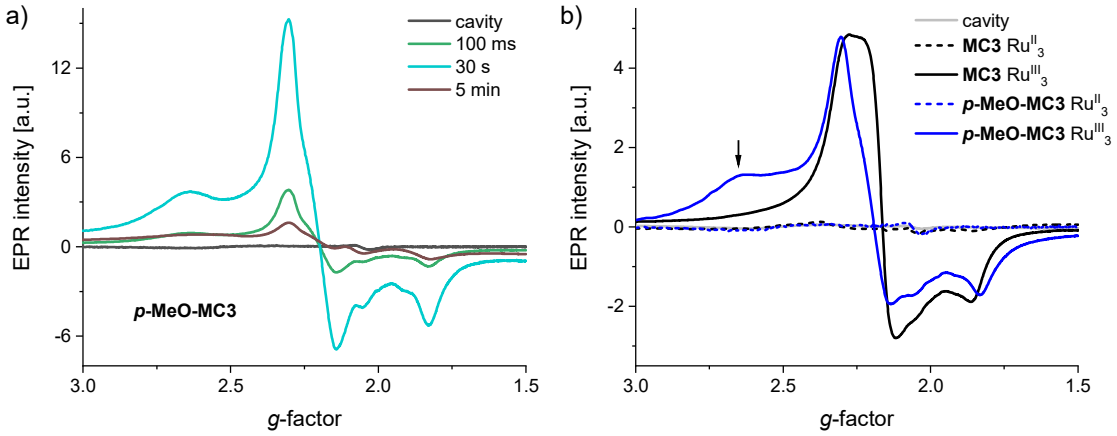

Figure S23. a) Time-dependent EPR spectra (9.47 GHz) of ***p*-MeO-MC3** after addition of excess CAN. Measurements in MeCN/H_2O 1:1 (pH 1, nitric acid), *c*(**MC3**) = 1 mM, *c*(CAN) = 20 mM. b) EPR spectra of **MC3** and ***p*-MeO-MC3** at Ru^{II}_3 and Ru^{III}_3 states. Oxidized form was prepared by addition of 3 equiv CAN per macrocycle to a 1 mM solution of the respective **MC3** derivative in MeCN/H_2O 1:1 (pH 1, nitric acid). The arrow indicates *g* = 2.64, which according to Sun and co-workers[90] can be assigned to a seven-coordinated Ru^{III}(bda) species with a solvent molecule attached to Ru.

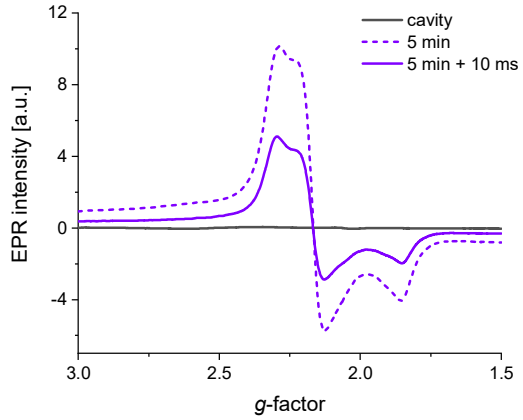

Figure S24. a) EPR spectra (9.47 GHz) of **MC3** after addition of excess CAN. Measurements in MeCN/H_2O 1:1 (pH 1, nitric acid), *c*(**MC3**) = 1 mM, *c*($CAN_{10\ min}$) = 20 mM, *c*($CAN_{10\ min\ +\ 10\ ms}$) = 25 mM.

EXAFS Fits[9]

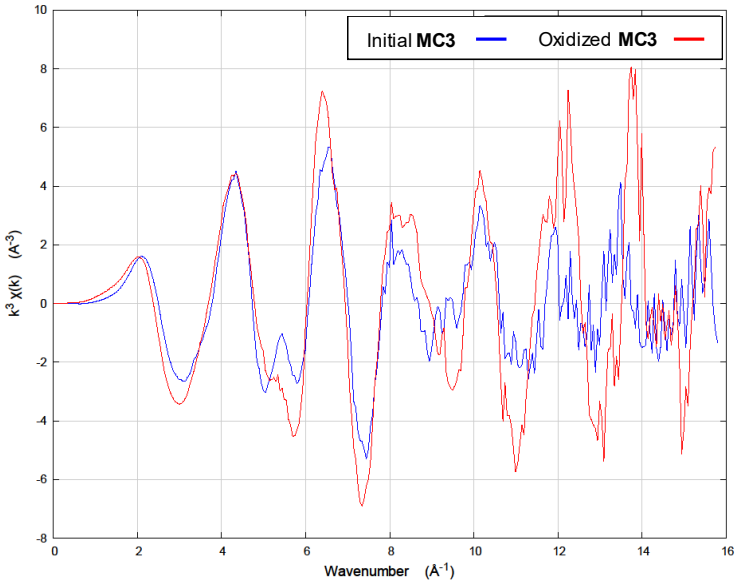

Figure S25. Raw EXAFS data of **MC3** in its initial and oxidized states. Measurements in MeCN/H_2O 1:1 (pH 1, nitric acid), *c*(**MC3**) = 1 mM, *c*($CAN_{oxidized\ sample}$) = 25 mM.

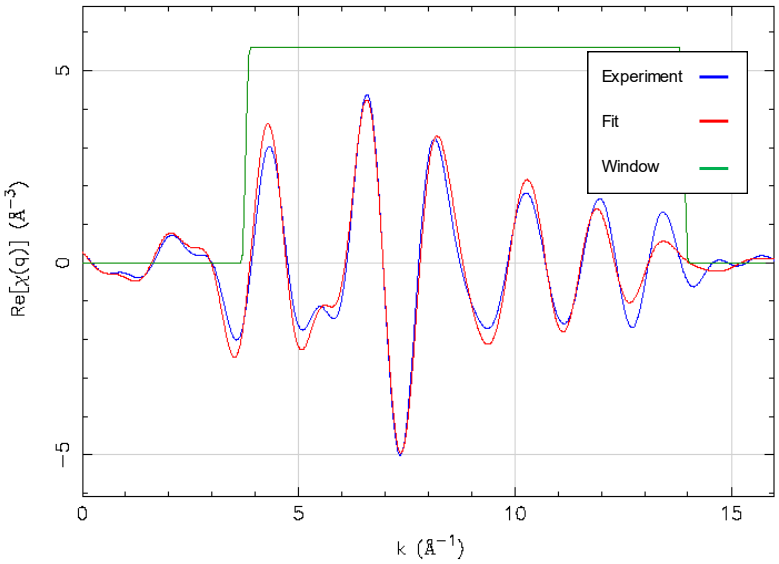

Figure S26. EXAFS Fit 3 (see Table 2) of initial **MC3** Ru^{II}; 3.8-13.9 *k*-space.

[9] EXAFS fits were performed by Prof. Dr. Yulia Pushkar, Purdue University.

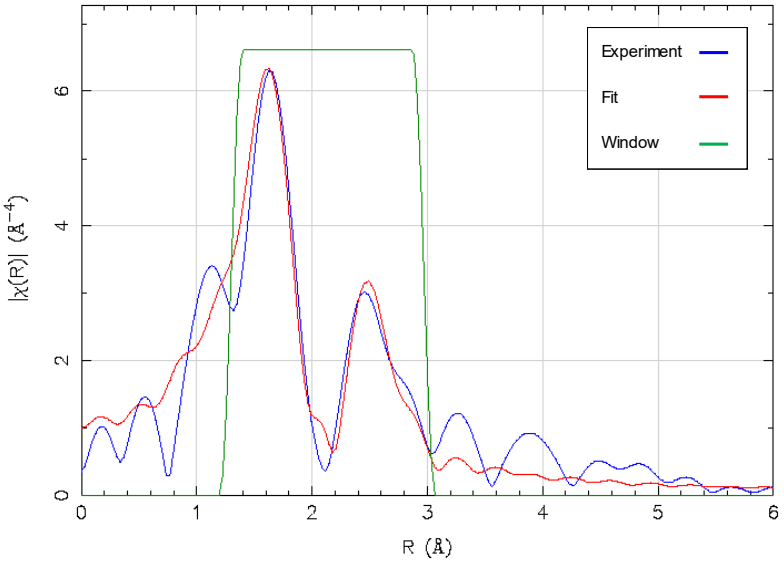

Figure S27. EXAFS Fit 3 (see Table 2) of initial **MC3** Ru^{II}; 1.3-3.0 *R*-space.

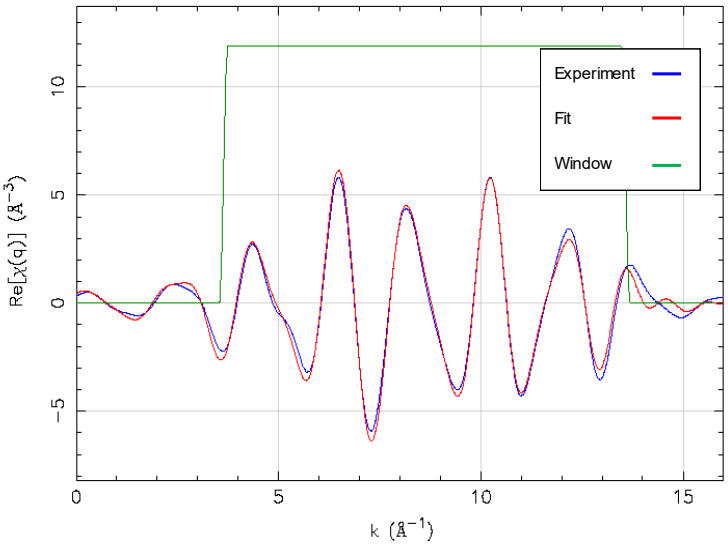

Figure S28. EXAFS Fit 7 (see Table 2) of oxidized **MC3** Ru^{IV}; 3.6-14.2 *k*-space.

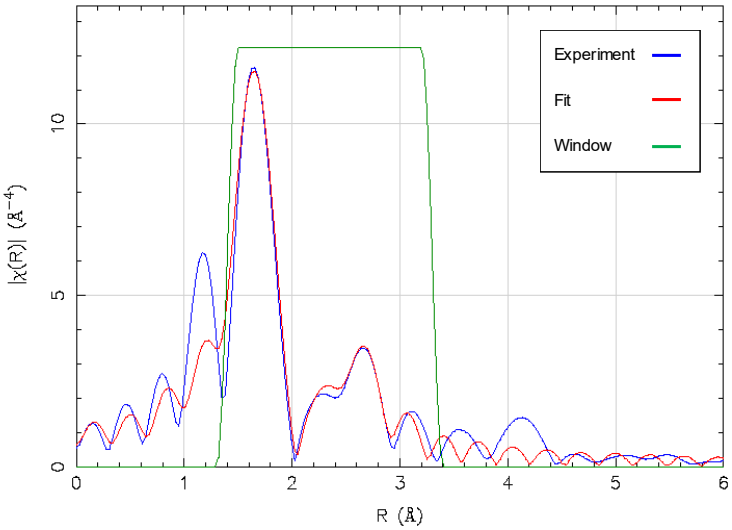

Figure S29. EXAFS Fit 7 (see Table 2) of oxidized **MC3** Ru^{IV}; 1.4-3.2 *R*-space.

Chemical Water Oxidation

Table S3. Catalytic activity of **MC3** derivatives in chemical water oxidation with varying MeCN content.[a]

MeCN content	**MC3**		***m*-MeO-MC3**		***m*-F-MC3**		***m*-Me-MC3**	
	TOF [s^{-1}]	TON	TOF [s^{-1}]	TON	TOF [s^{-1}]	TON	TOF [s^{-1}]	TON
30%	23	1600	21	600	24	1500	10	400
40%	102	3100	127	750	87	2150	60	2300
50%	136	5300	138	1300	90	4700	90	3700
60%	150	7400	102	3900	84	4500	60	3000
70%	72	5200	104	1300	44	550	40	2600

MeCN content	***p*-F-MC3**		***p*-MeO-MC3**		***p*-Me-MC3**	
	TOF [s^{-1}]	TON	TOF [s^{-1}]	TON	TOF [s^{-1}]	TON
30%	18	250	22	450	26	650
40%	51	900	44	1200	37	1900
50%	80	2500	60	2200	60	2300
60%	64	3150	20	1800	20	1100
70%	38	2550	17	1000	6	600

[a] Experiments in MeCN/H_2O mixtures (pH 1, triflic acid), *c*(CAN) = 0.6 M, *c*(WOC) = 24 µM.

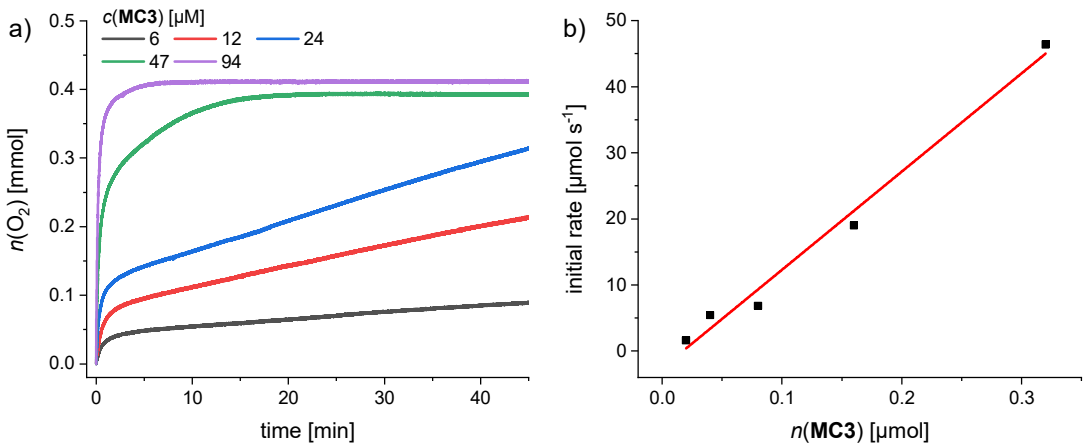

Figure S30. a) Concentration-dependent experiments with **MC3** as WOC in MeCN/H_2O 1:1 (pH 1, triflic acid). b) Plot of initial rates *vs.* catalyst amount with linear regression for the determination of TOF.

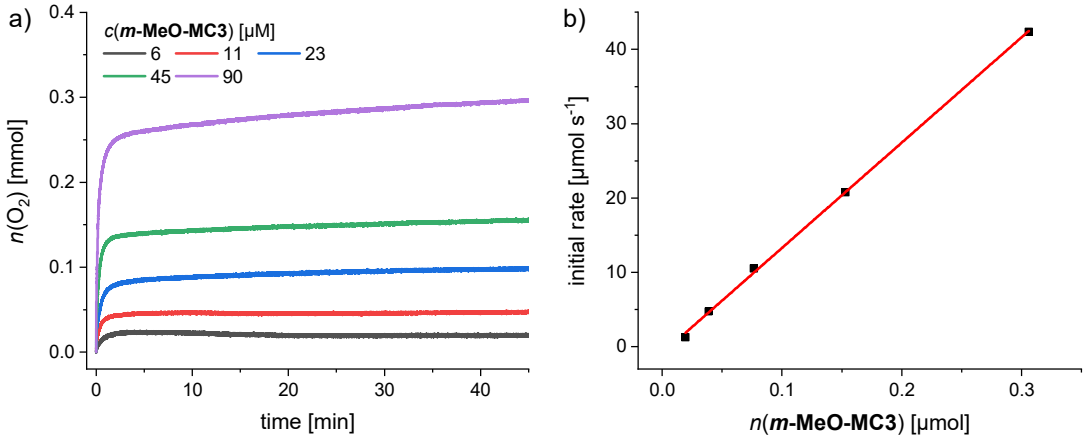

Figure S31. a) Concentration-dependent experiments with ***m*-MeO-MC3** as WOC in MeCN/H_2O 1:1 (pH 1, triflic acid). b) Plot of initial rates *vs.* catalyst amount with linear regression for the determination of TOF.

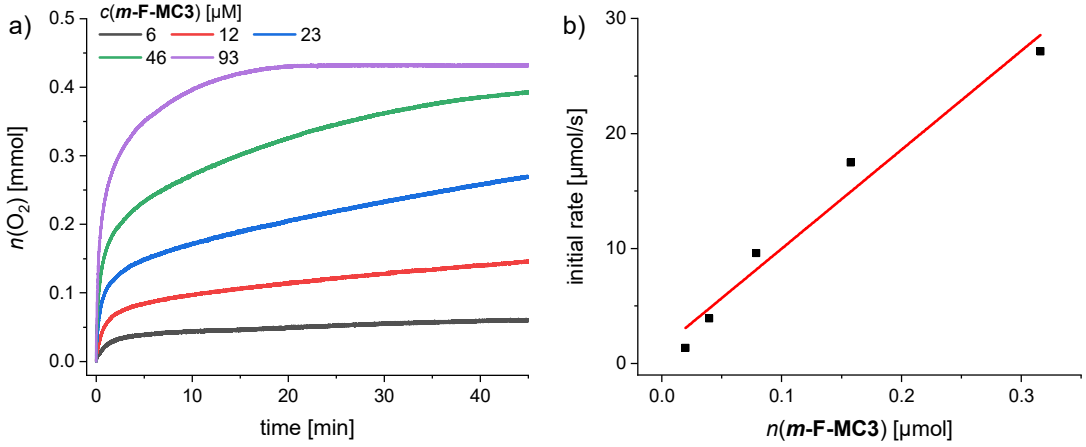

Figure S32. a) Concentration-dependent experiments with ***m*-F-MC3** as WOC in MeCN/H_2O 1:1 (pH 1, triflic acid). b) Plot of initial rates *vs.* catalyst amount with linear regression for the determination of TOF.

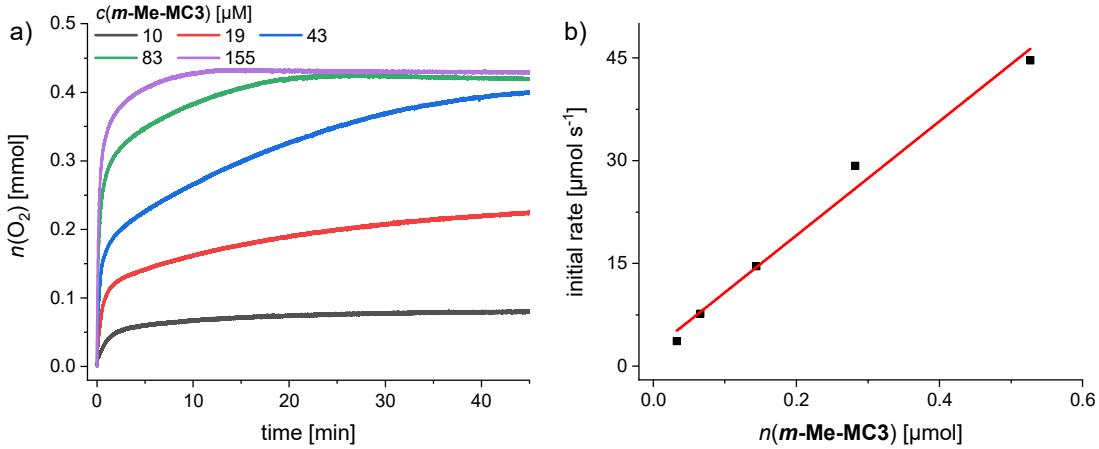

Figure S33. a) Concentration-dependent experiments with ***m*-Me-MC3** as WOC in MeCN/H_2O 1:1 (pH 1, triflic acid). b) Plot of initial rates *vs.* catalyst amount with linear regression for the determination of TOF.

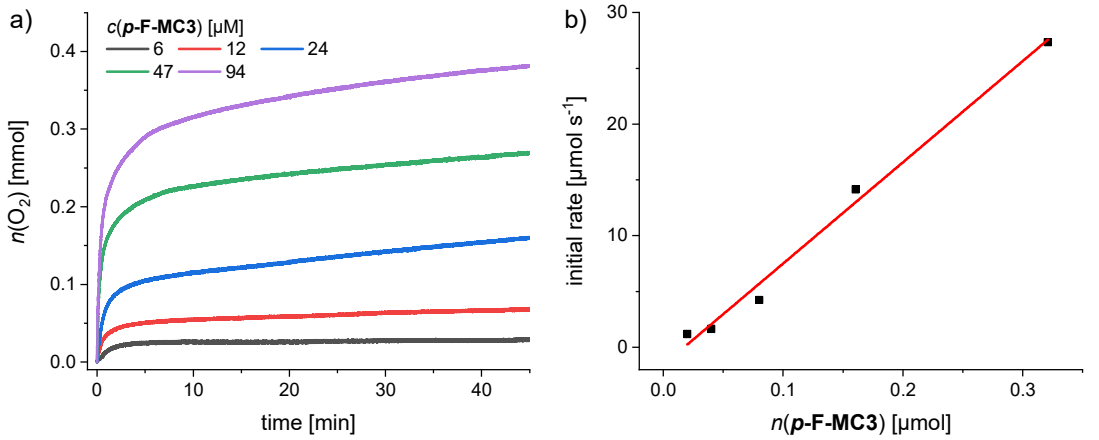

Figure S34. a) Concentration-dependent experiments with ***p*-F-MC3** as WOC in MeCN/H_2O 1:1 (pH 1, triflic acid). b) Plot of initial rates *vs.* catalyst amount with linear regression for the determination of TOF.

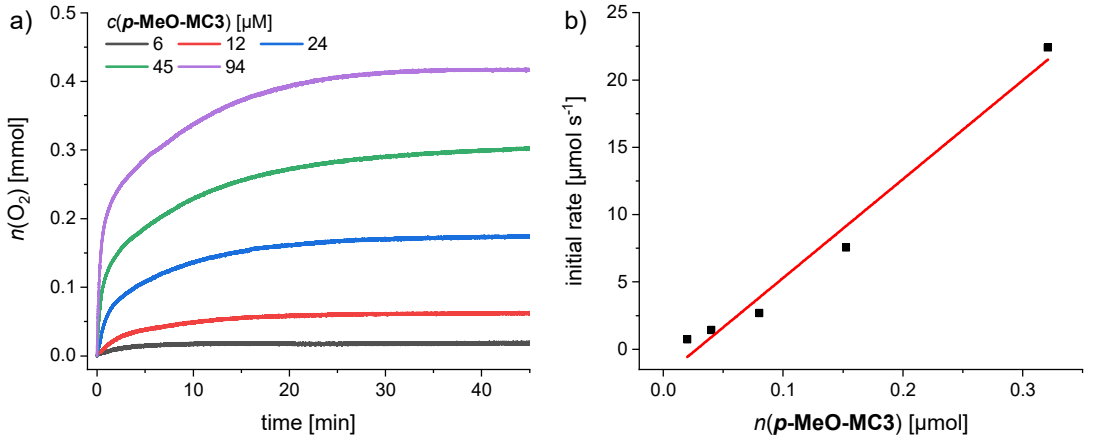

Figure S35. a) Concentration-dependent experiments with ***p*-MeO-MC3** as WOC in MeCN/H_2O 1:1 (pH 1, triflic acid). b) Plot of initial rates *vs.* catalyst amount with linear regression for the determination of TOF.

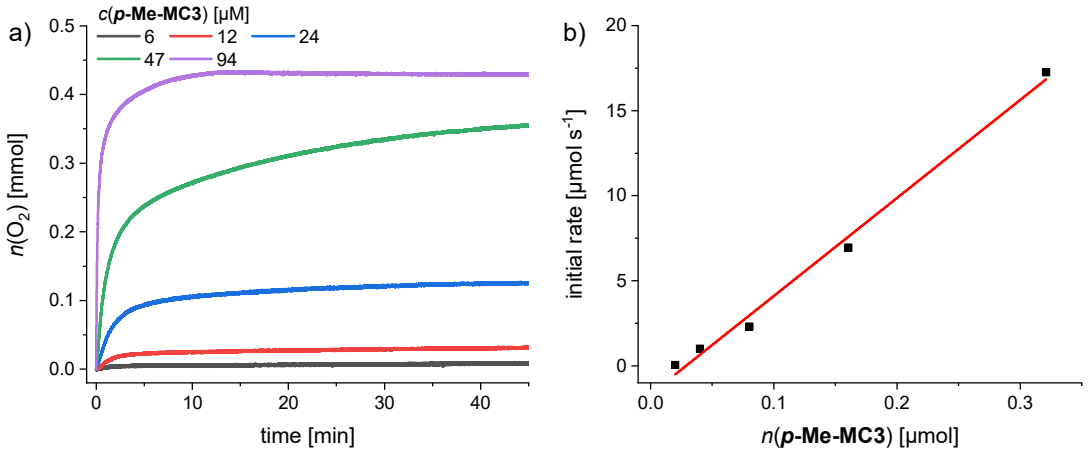

Figure S36. a) Concentration-dependent experiments with ***p*-Me-MC3** as WOC in MeCN/H_2O 1:1 (pH 1, triflic acid). b) Plot of initial rates *vs.* catalyst amount with linear regression for the determination of TOF.

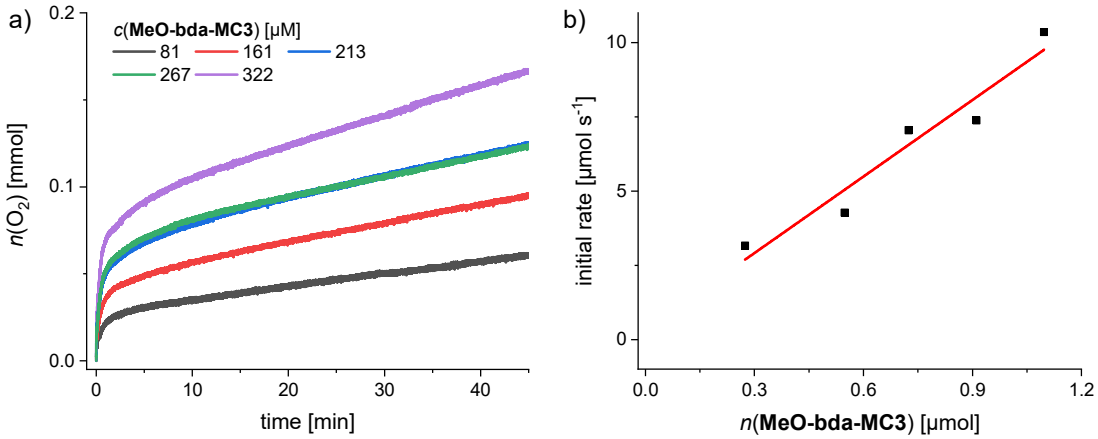

Figure S37. a) Concentration-dependent experiments with **MeO-bda-MC3** as WOC in MeCN/H_2O 1:1 (pH 1, triflic acid). b) Plot of initial rates *vs.* catalyst amount with linear regression for the determination of TOF.

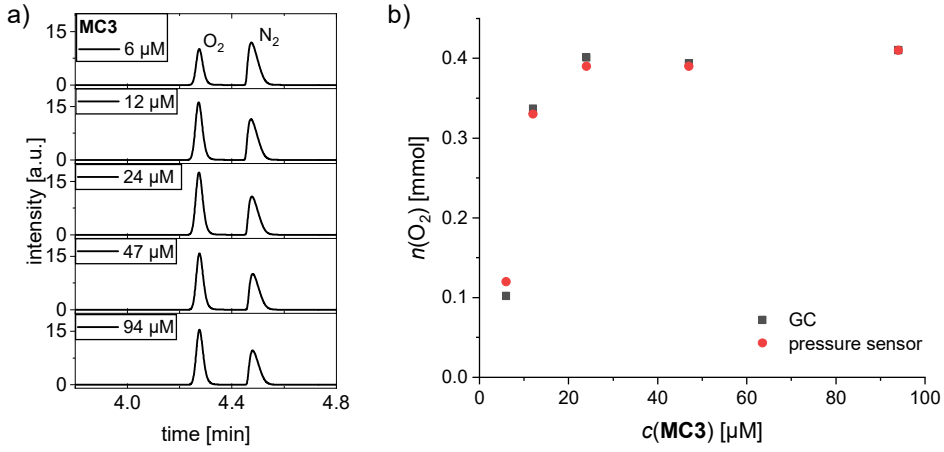

Figure S38. a) Chromatogram of headspace at the end of water oxidation experiments with **MC3** as WOC. b) Comparison of amount of evolved oxygen determined by GC or with pressure sensors.

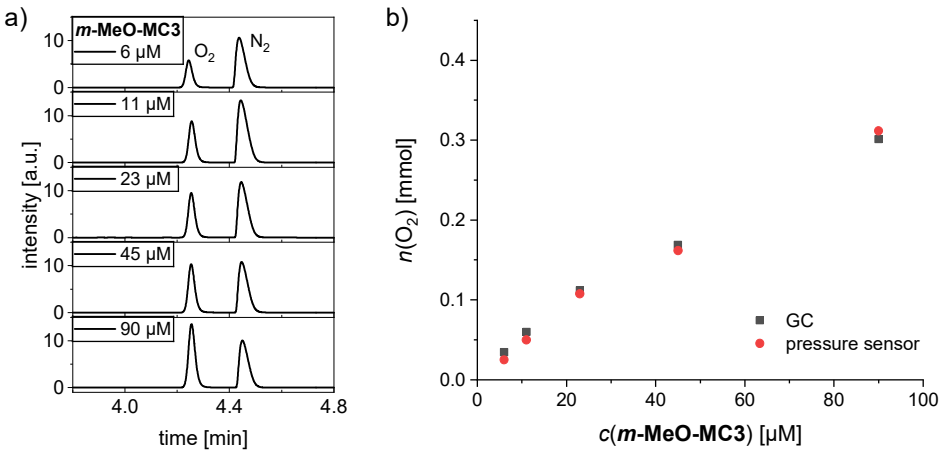

Figure S39. a) Chromatogram of headspace at the end of water oxidation experiments with ***m*-MeO-MC3** as WOC. b) Comparison of amount of evolved oxygen determined by GC or with pressure sensors.

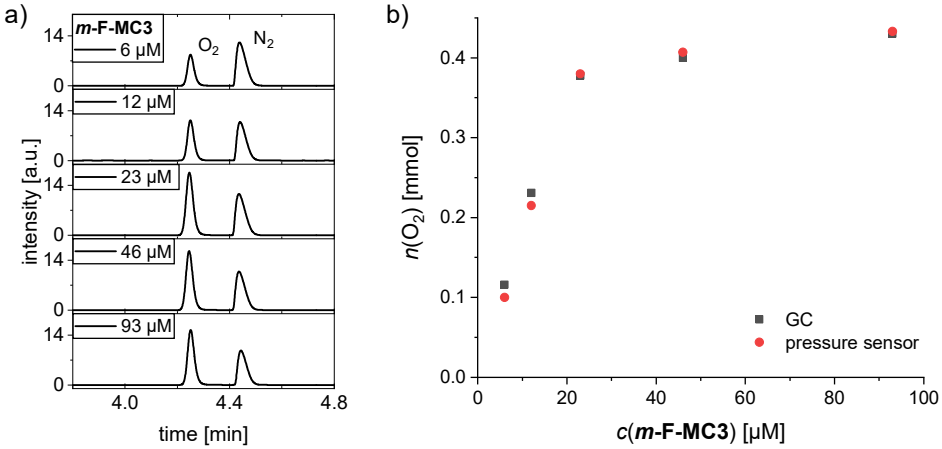

Figure S40. a) Chromatogram of headspace at the end of water oxidation experiments with ***m*-F-MC3** as WOC. b) Comparison of amount of evolved oxygen determined by GC or with pressure sensors.

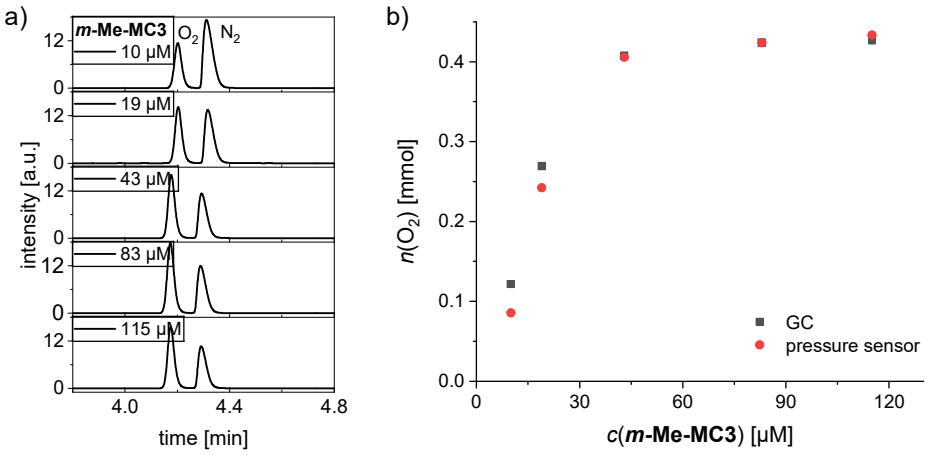

Figure S41. a) Chromatogram of headspace at the end of water oxidation experiments with ***m*-Me-MC3** as WOC. b) Comparison of amount of evolved oxygen determined by GC or with pressure sensors.

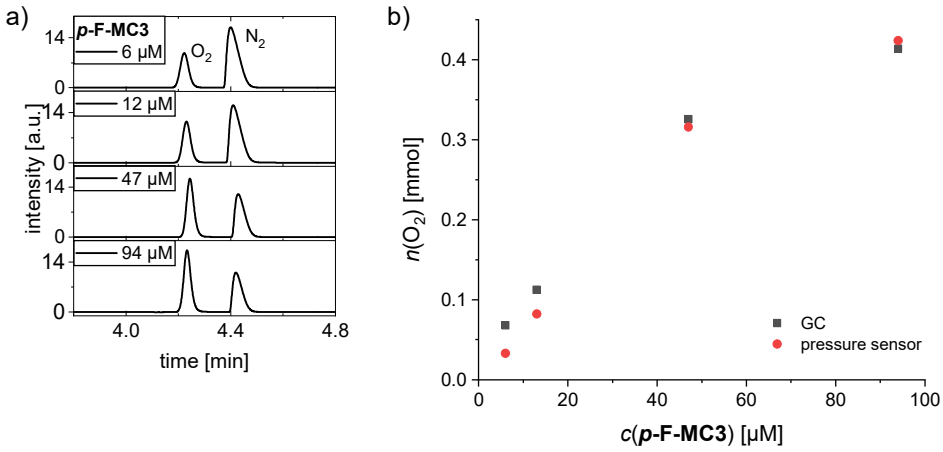

Figure S42. a) Chromatogram of headspace at the end of water oxidation experiments with ***p*-F-MC3** as WOC. b) Comparison of amount of evolved oxygen determined by GC or with pressure sensors.

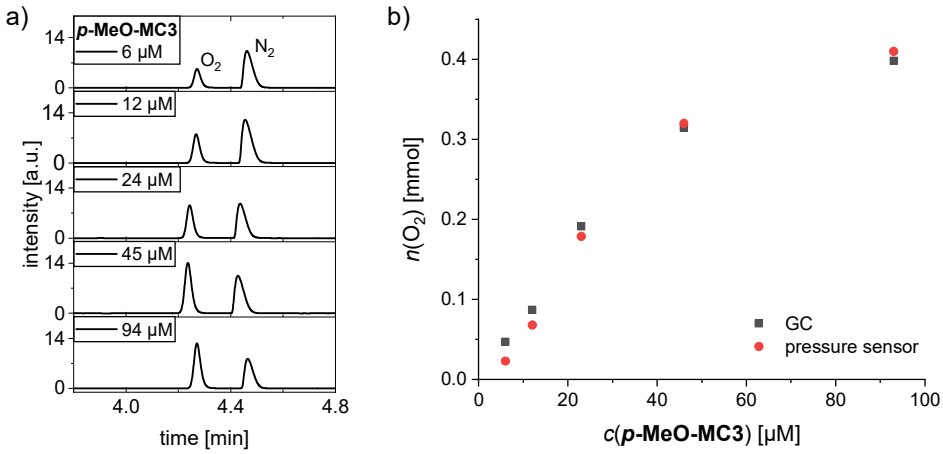

Figure S43. a) Chromatogram of headspace at the end of water oxidation experiments with ***p*-MeO-MC3** as WOC. b) Comparison of amount of evolved oxygen determined by GC or with pressure sensors.

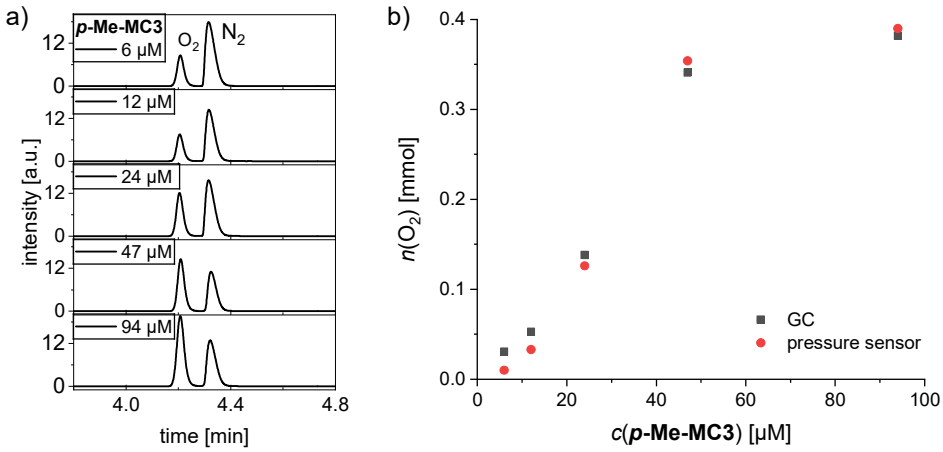

Figure S44. a) Chromatogram of headspace at the end of water oxidation experiments with ***p*-Me-MC3** as WOC. b) Comparison of amount of evolved oxygen determined by GC or with pressure sensors.

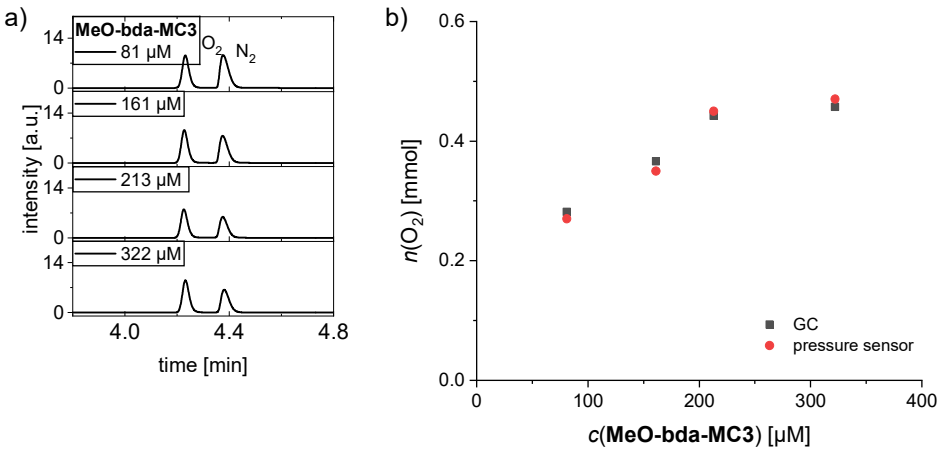

Figure S45. a) Chromatogram of headspace at the end of water oxidation experiments with **MeO-bda-MC3** as WOC. b) Comparison of amount of evolved oxygen determined by GC or with pressure sensors.

Photocatalytic Water Oxidation

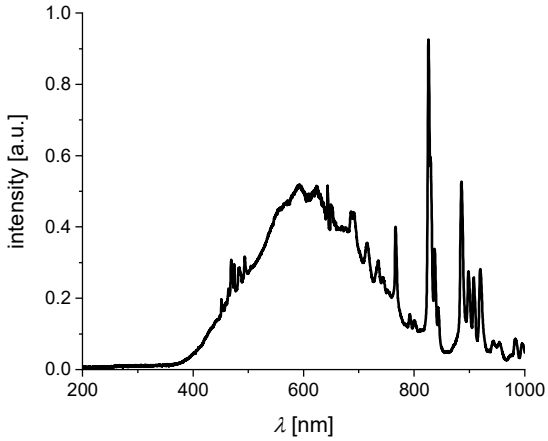

Figure S46. Emission profile of xenon lamp used for photocatalytic water oxidation experiments.

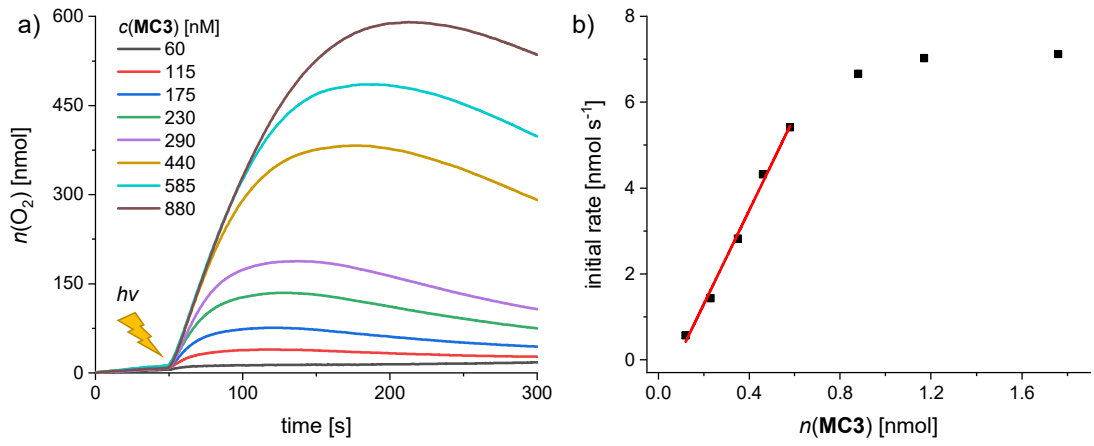

Figure S47. a) Concentration-dependent experiments with **MC3** as WOC in MeCN/H_2O 1:1 (phosphate buffer, pH 7). b) Plot of initial rates *vs.* catalyst amount with linear regression for the determination of TOF.

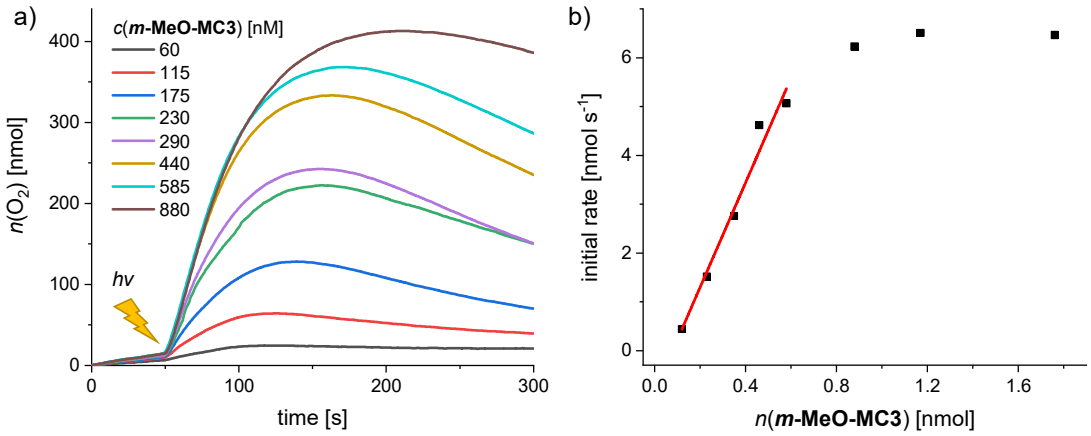

Figure S48. a) Concentration-dependent experiments with ***m*-MeO-MC3** as WOC in MeCN/H_2O 1:1 (phosphate buffer, pH 7). b) Plot of initial rates *vs.* catalyst amount with linear regression for the determination of TOF.

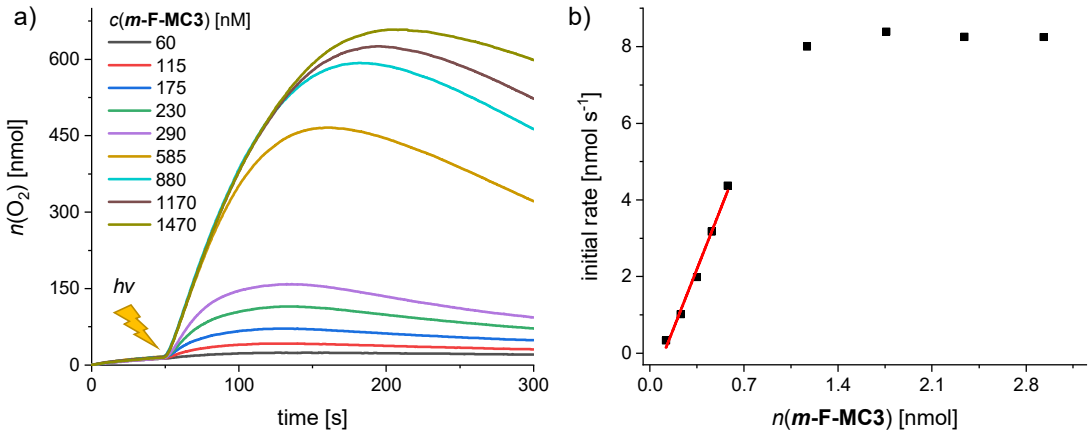

Figure S49. a) Concentration-dependent experiments with ***m*-F-MC3** as WOC in MeCN/H_2O 1:1 (phosphate buffer, pH 7). b) Plot of initial rates *vs.* catalyst amount with linear regression for the determination of TOF.

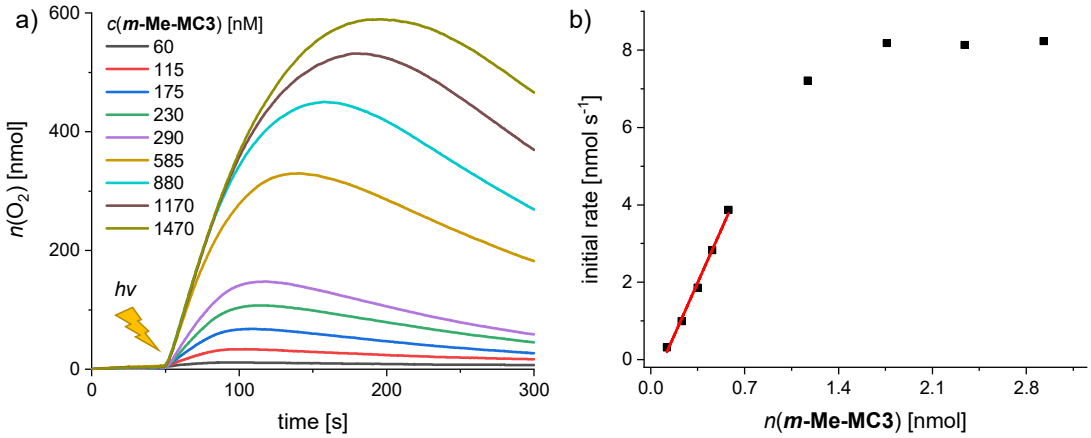

Figure S50. a) Concentration-dependent experiments with ***m*-Me-MC3** as WOC in MeCN/H_2O 1:1 (phosphate buffer, pH 7). b) Plot of initial rates *vs.* catalyst amount with linear regression for the determination of TOF.

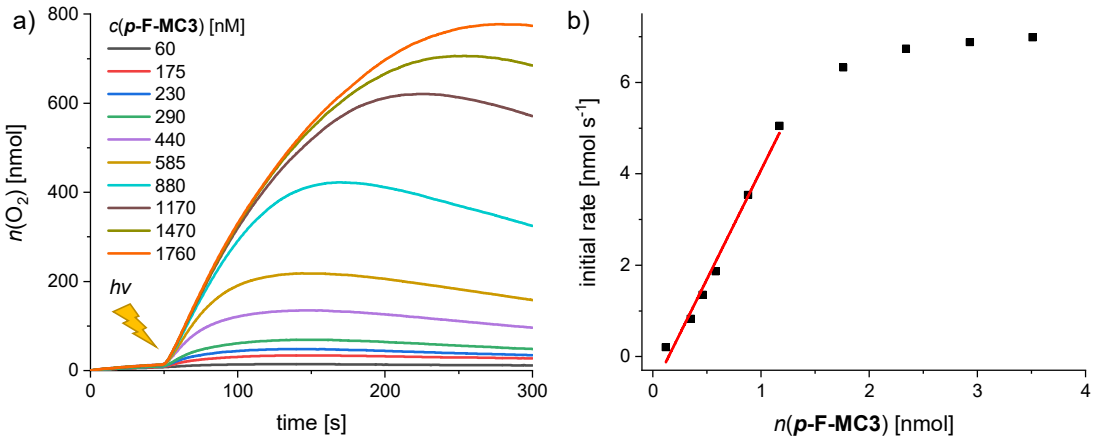

Figure S51. a) Concentration-dependent experiments with ***p*-F-MC3** as WOC in MeCN/H_2O 1:1 (phosphate buffer, pH 7). b) Plot of initial rates *vs.* catalyst amount with linear regression for the determination of TOF.

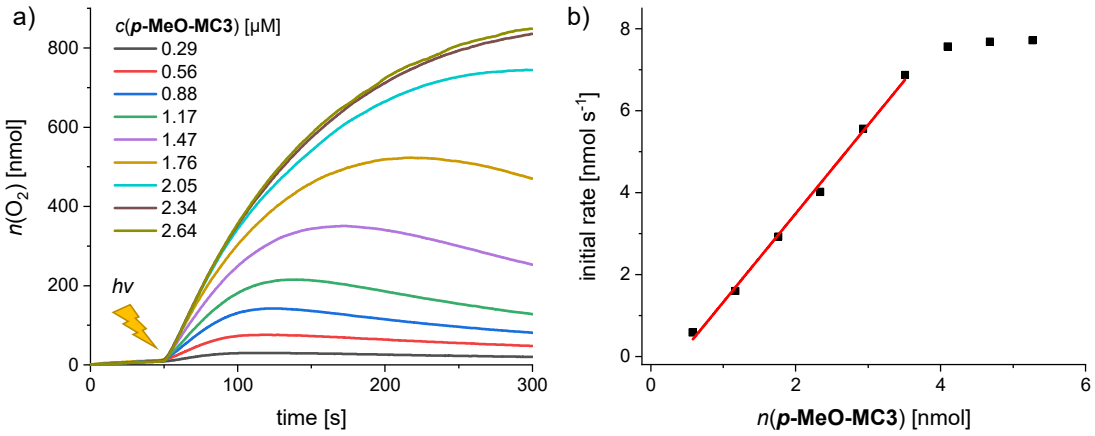

Figure S52. a) Concentration-dependent experiments with ***p*-MeO-MC3** as WOC in MeCN/H_2O 1:1 (phosphate buffer, pH 7). b) Plot of initial rates *vs.* catalyst amount with linear regression for the determination of TOF.

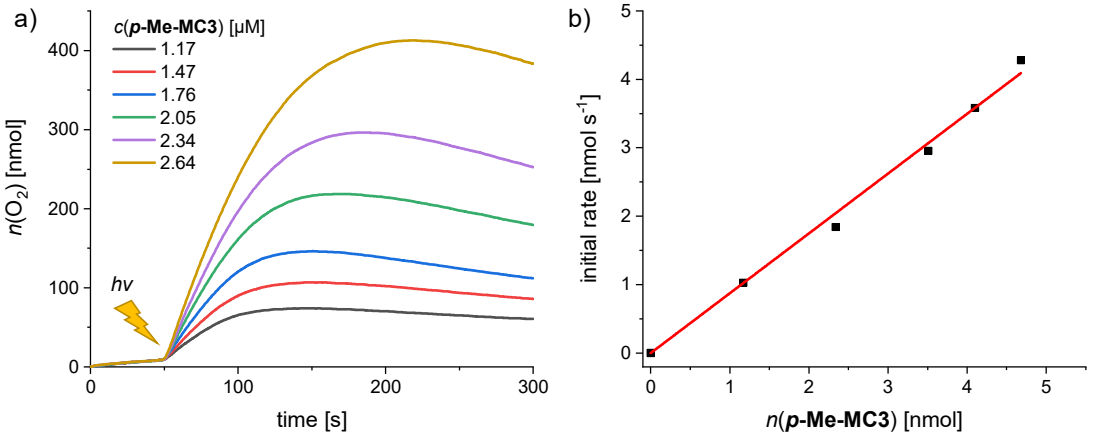

Figure S53. a) Concentration-dependent experiments with ***p*-Me-MC3** as WOC in MeCN/H_2O 1:1 (phosphate buffer, pH 7). b) Plot of initial rates *vs.* catalyst amount with linear regression to determine TOF.

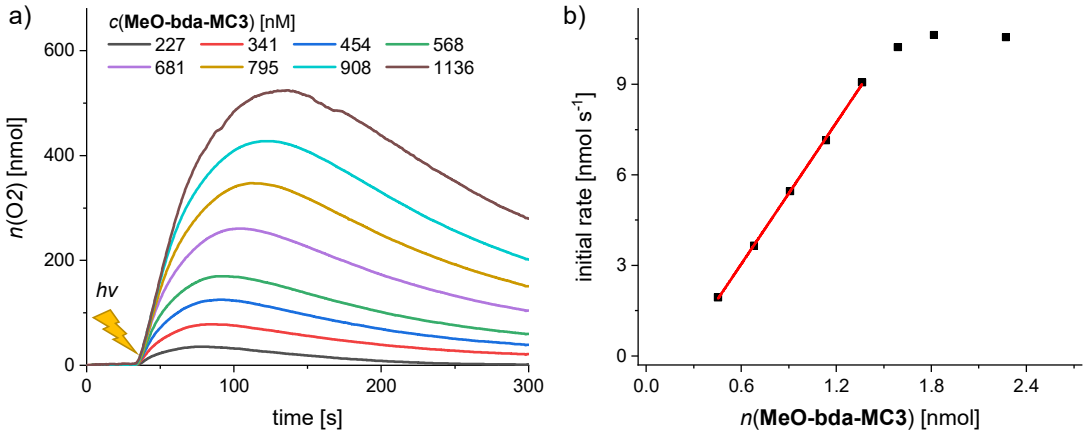

Figure S54. Concentration-dependent experiments with **MeO-bda-MC3** as WOC in MeCN/H_2O 1:1 (phosphate buffer, pH 7). b) Plot of initial rates *vs.* catalyst amount with linear regression for the determination of TOF.

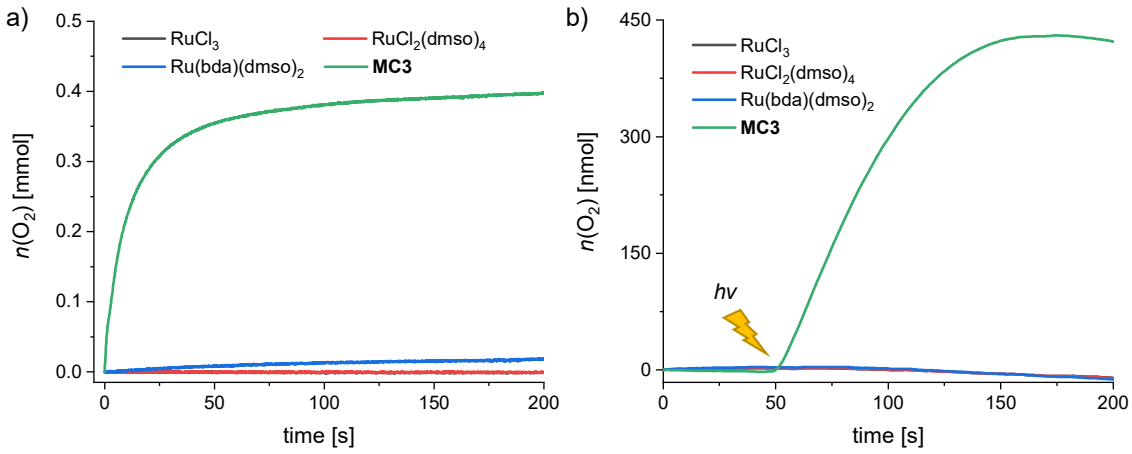

Figure S55. Catalytic activities of $RuCl_3$, $RuCl_2(dmso)_4$, $Ru(bda)(dmso)_2$ and **MC3** in a) chemical and b) photochemical water oxidation. Experimental conditions: a) MeCN/H_2O 1:1 (pH 1, triflic acid), *c*(CAN) = 0.6 M, *c*(**MC3**) = 94 µM, *c*($RuCl_3$) = *c*($RuCl_2(dmso)_4$) = *c*($Ru(bda)(dmso)_2$) = 282 µM. b) MeCN/H_2O (pH 7, phosphate buffer), *c*($[Ru(bpy)_3]^{2+}$) = 1.5 mM, *c*($Na_2S_2O_8$) = 37 mM, *c*(**MC3**) = 585 nM, *c*($RuCl_3$) = *c*($RuCl_2(dmso)_4$) = *c*($Ru(bda)(dmso)_2$) = 1755 nM. The lighting symbol indicates the start of sample irradiation at *t* = 50 s.

Theoretical Studies[10]

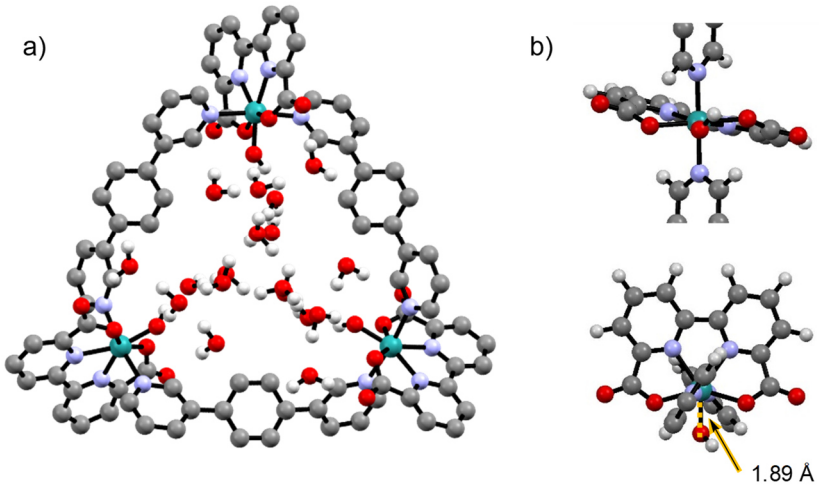

Figure S56. a) Optimized DFT structure of **MC3** at $[Ru^{IV}\text{-}OH]_3$ state including 18 explicit water molecules (optimization method: PBE/def2-SVP). The hydrogen atoms of the macrocycle were omitted for clarity. b) Close-up of one Ru center of the macrocycle with Ru–OH bond distance of 1.89 Å marked in yellow (grey: carbon, white: hydrogen, red: oxygen, purple: nitrogen, turquoise: ruthenium).

Table S4. Energy of optimized structures of **MC3** and methylated derivatives.[a]

Conformation	Optimized structure energy [kJ mol^{-1}]		
	***m*-Me-MC3**	**MC3**	***p*-Me-MC3**
A	0	0	0
B	-22.5	-18.5	0.8
C	---	---	136.5
D	55.1	63.2	53.4

[a] Optimized structures of **MC3** and methylated macrocycles in conformations **A–D** (as depicted in Figure 34) at Ru^{II}_3 oxidation state were determined on the basis of PM6/COSMO model.

[10] Molecular dynamics simulations were performed by Dr. Joachim O. Lindner, Universität Würzburg.

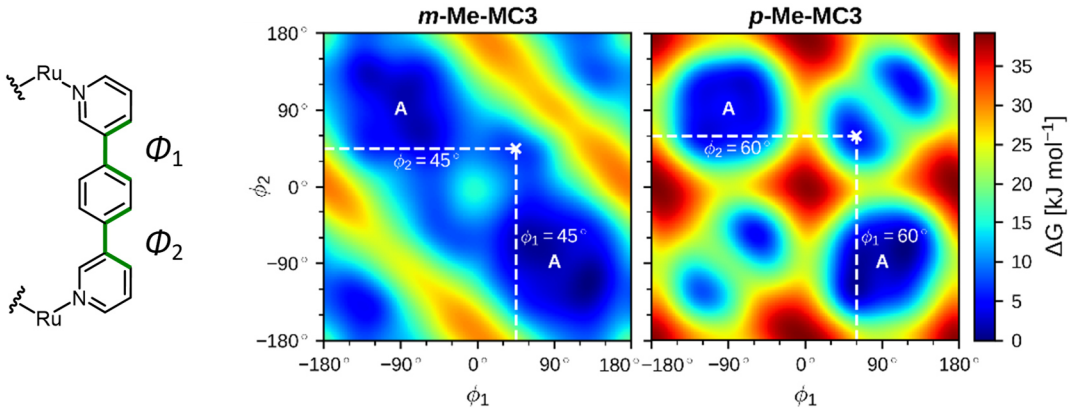

Figure S57. Free energy surfaces of ***m*-Me-MC3** (left) and ***p*-Me-MC3** (right) obtained from metadynamic studies on the distortion of one of the bridging ligands starting from conformation **A** in aqueous solution. $\Phi_{1,2}$ are the torsion angles within the bridging ligand which were used as collective variables. The white cross indicates exemplary $\mathbf{A_2B}$ configuration of each macrocycle.

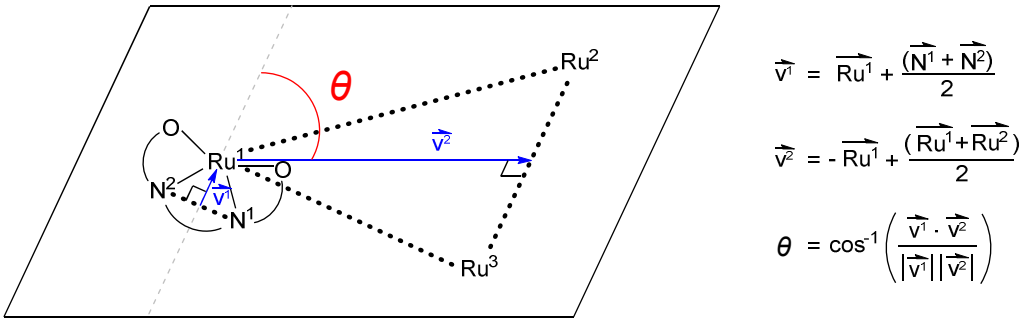

Figure S58. Definition of the angle θ used as collective variable to assess the rotation of the Ru(bda) unit within the macrocyclic structure.

Table S5. Energy of optimized structures of **MC3** at Ru^{II}_3 and Ru^{IV}_3 oxidation states.[a]

Conformation	Optimized structure energy [kJ mol^{-1}]	
	Ru^{II}_3	**Ru^{IV}_3**
A	0	0
B	-19.7	-35.0
C	---	120.4
D	23.2	115.8

[a] Optimized structures of **MC3** in conformations **A–D** (as depicted in Figure 34) at Ru^{II}_3 and Ru^{IV}_3 oxidation states determined by PBE/COSMO model.

PXRD[11]

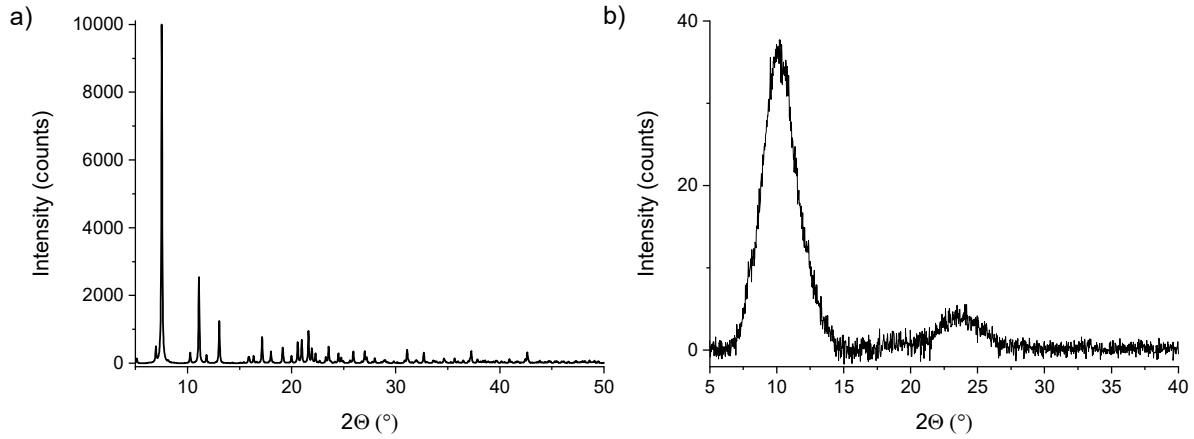

Figure S59. a) Calculated powder diffraction pattern for single crystals of ***m*-F-MC3**. b) Experimental diffraction pattern obtained for vacuum-dried crystals of ***m*-F-MC3**.

To determine whether the solid-state structure of ***m*-F-MC3** remained porous after removal the solvent molecules, crystals of this macrocycle were dried under high vacuum prior to analysis by PXRD. As shown in Figure S59, the crystal packing of ***m*-F-MC3** clearly depended on the presence of solvent molecules, since upon their removal a collapse of the ordered structure was observed by comparison with the calculated pattern from the X-ray structure of this compound.

[11] PXRD measurement of vacuum dried crystals of ***m*-F-MC3** were performed by Markus Hecht, Universität Würzburg.

8.2 Supporting Information for Chapter 4

Redox and Optical Properties

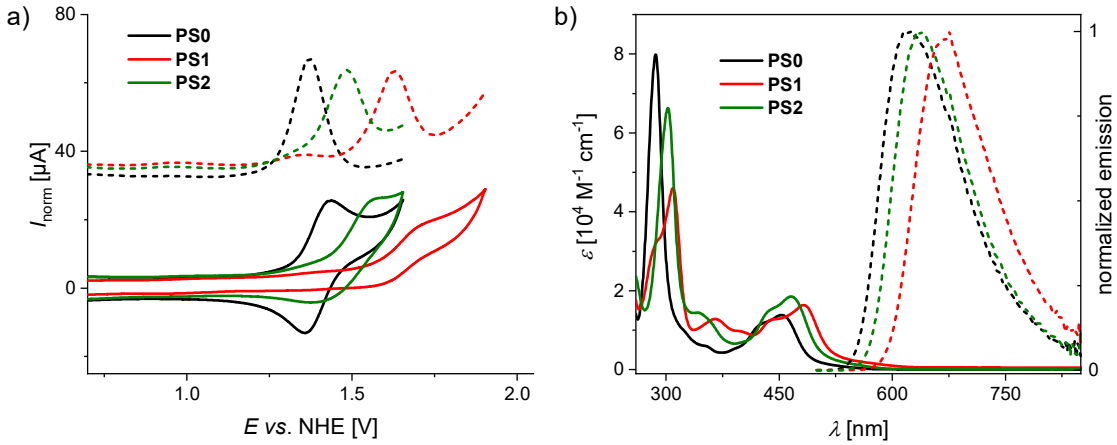

Figure S60. a) CV (solid lines) and DPV (dashed lines) traces of **PS0–3** in 50 mM phosphate buffer (pH 7), c = 1–2 mM. b) UV/Vis absorption (solid lines) and emission (dashed lines) spectra of photosensitizers **PS0–3** in same solvent mixture, c_{Abs} = 16 µM, c_{Em} = 50 µM.

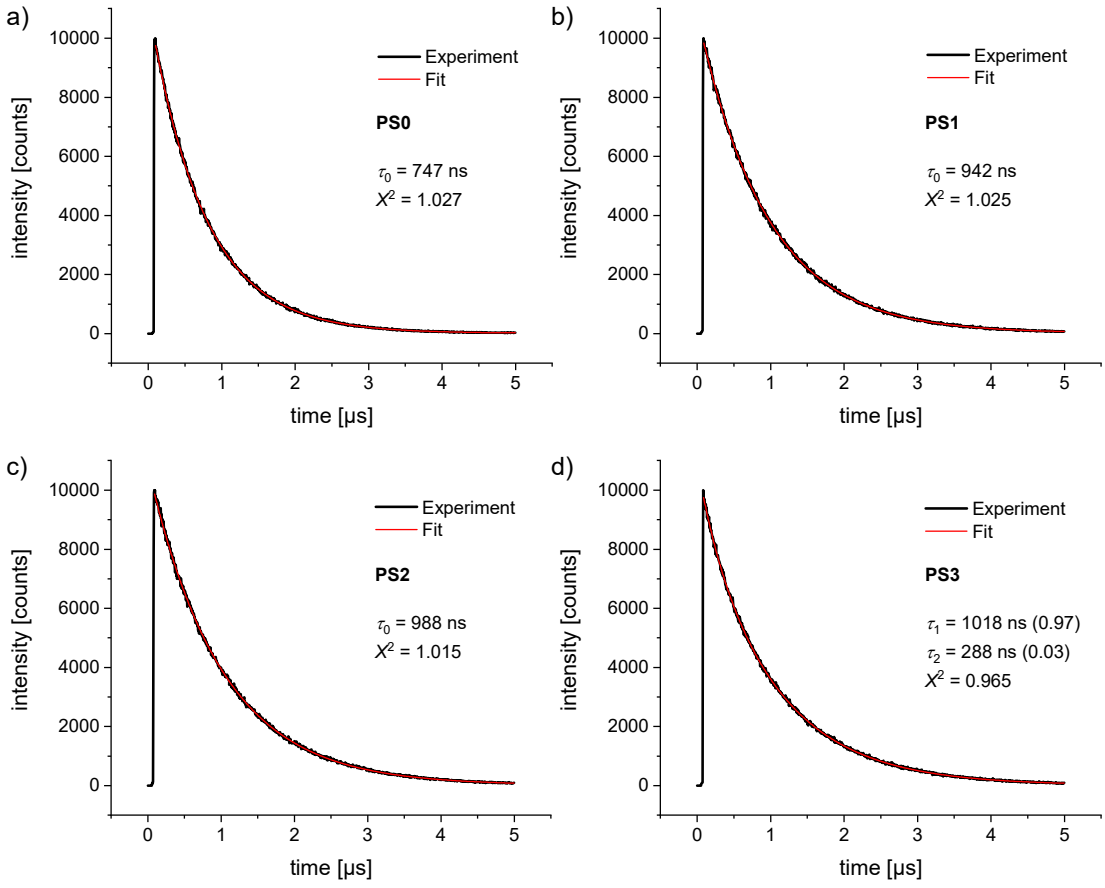

Figure S61. Time-resolved emission decay of **PS0–3** in MeCN/H_2O 1:1 (50 mM phosphate buffer, pH 7), λ_{ex} = 405 nm. The emission decay was detected at the emission maximum of each sensitizer (Table 5).

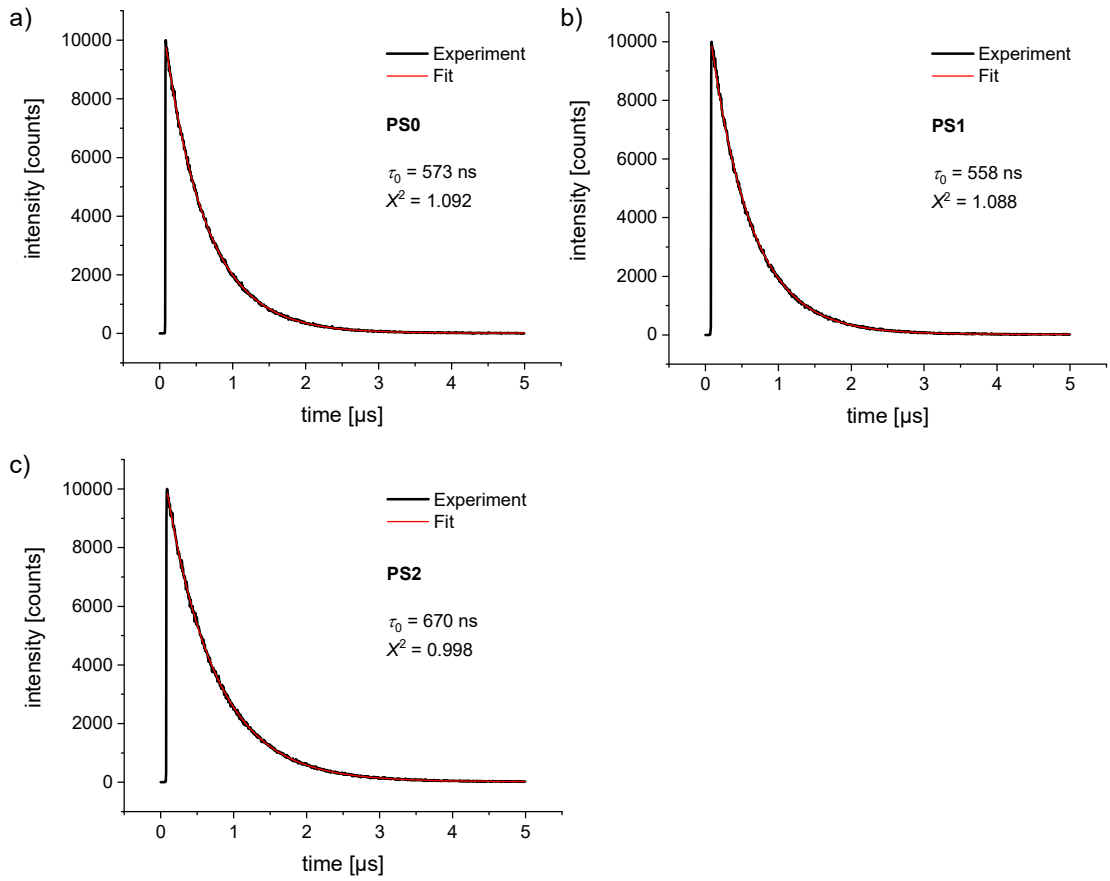

Figure S62. Time-resolved emission decay of **PS0–2** in 50 mM phosphate buffer (pH 7), λ_{ex} = 405 nm. The emission decay was detected at the emission maximum of each sensitizer (Table 5).

Photocatalytic Water Oxidation

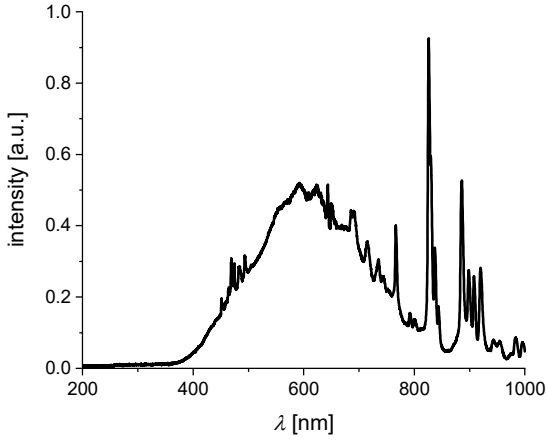

Figure S63. Emission profile of xenon lamp used for photocatalytic water oxidation experiments.

Table S6. Photocatalytic water oxidation with **MC3** and **PS0** in MeCN/H_2O 1:1.[a]

Entry	Light intensity [mW cm^{-2}]	*c* (buffer) [mM]	*c* (**PS0**) [mM]	TOF [s^{-1}]	TON	Φ [%] [b]	φ_{chem} [%] [c]
1	10	50	1.5	3.0	280	7.9	0.4
2	80	50	1.5	9.2	280	3.1	0.4
3	230	50	1.5	5.3	440	0.6	0.7
4	100	50	1.5	10.9	430	2.9	0.6
5	100	20	1.5	8.6	350	1.0	0.1
6	100	50	0.2	2.6	80	1.1	0.2

[a] Phosphate buffer pH 7, *c*($Na_2S_2O_8$) = 37 mM, *c*(**MC3**) = 60 nM–2.5 µM. [b] Photochemical quantum yield of O_2 production determined for *c*(**MC3**) = 290 nM. [c] Chemical yield of O_2 production determined for *c*(**MC3**) = 290 nM.

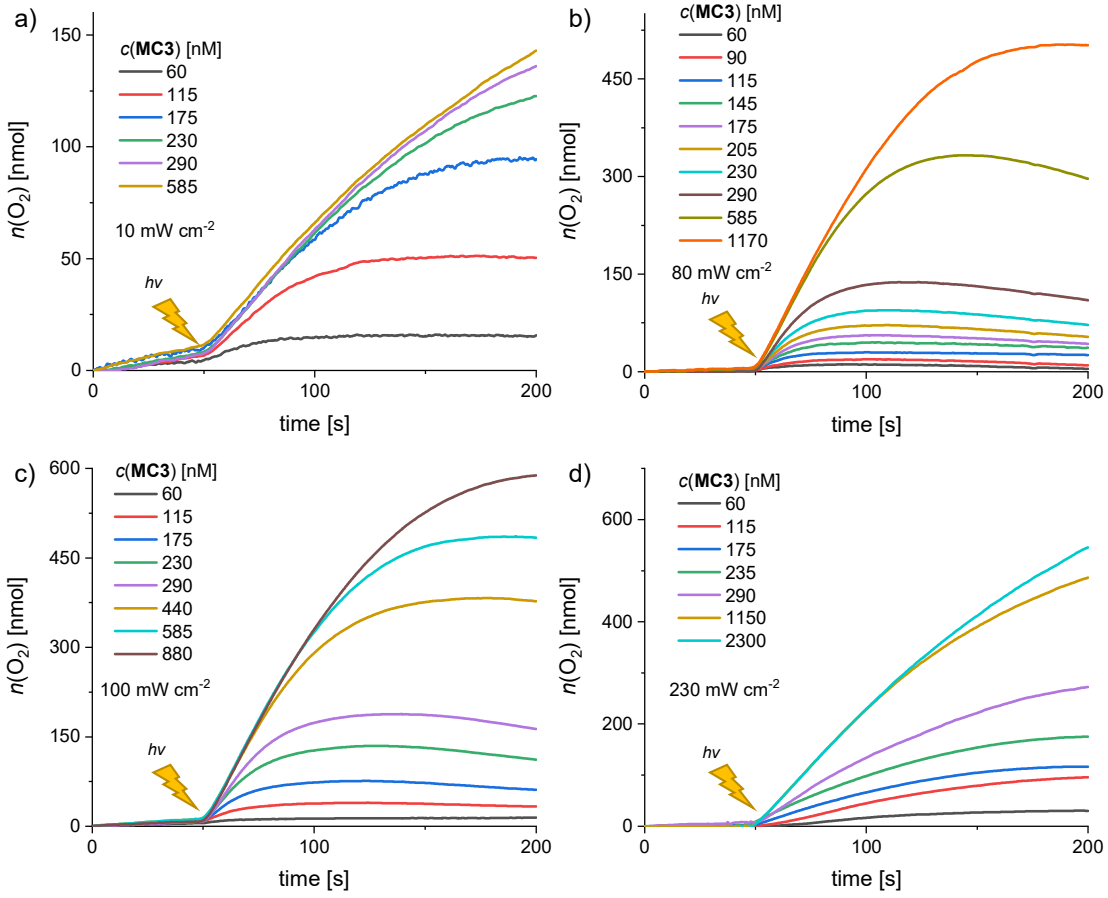

Figure S64. Concentration-dependent oxygen evolution curves of **MC3** in MeCN/H_2O 1:1 (50 mM phosphate buffer, pH 7) at variable light intensities, *c*(**PS0**) = 1.5 mM, *c*($Na_2S_2O_8$) = 37 mM. The lighting symbol indicates the start of sample irradiation at *t* = 50 s.

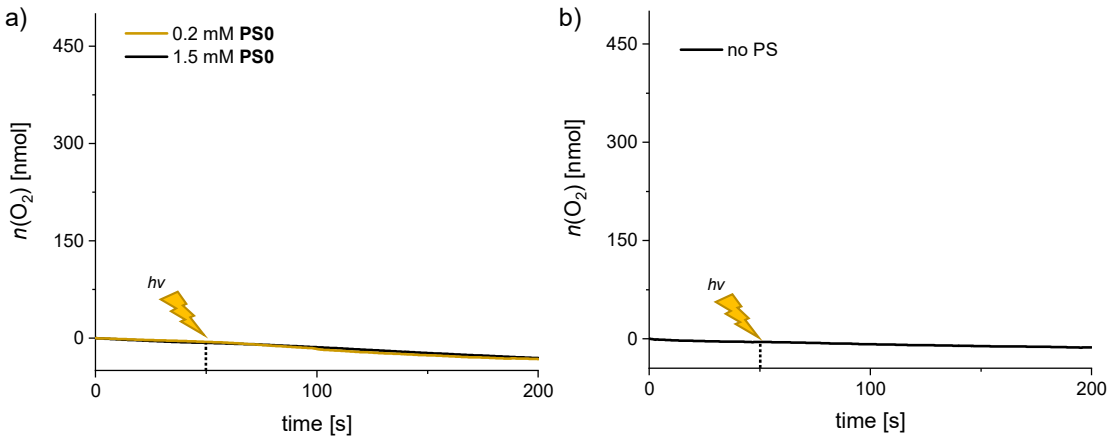

Figure S65. Control experiments with a) no WOC and b) no PS in MeCN/H_2O 1:1 (phosphate buffer, pH 7) using **PS0** as sensitizer and **MC3** as WOC. Experimental conditions: a) *c*(**PS0**) = 0.2 or 1.5 mM, *c*($Na_2S_2O_8$) = 37 mM, b) *c*(**MC3**) = 290 nM, *c*($Na_2S_2O_8$) = 37 mM. The lighting symbol indicates the start of sample irradiation at *t* = 50 s.

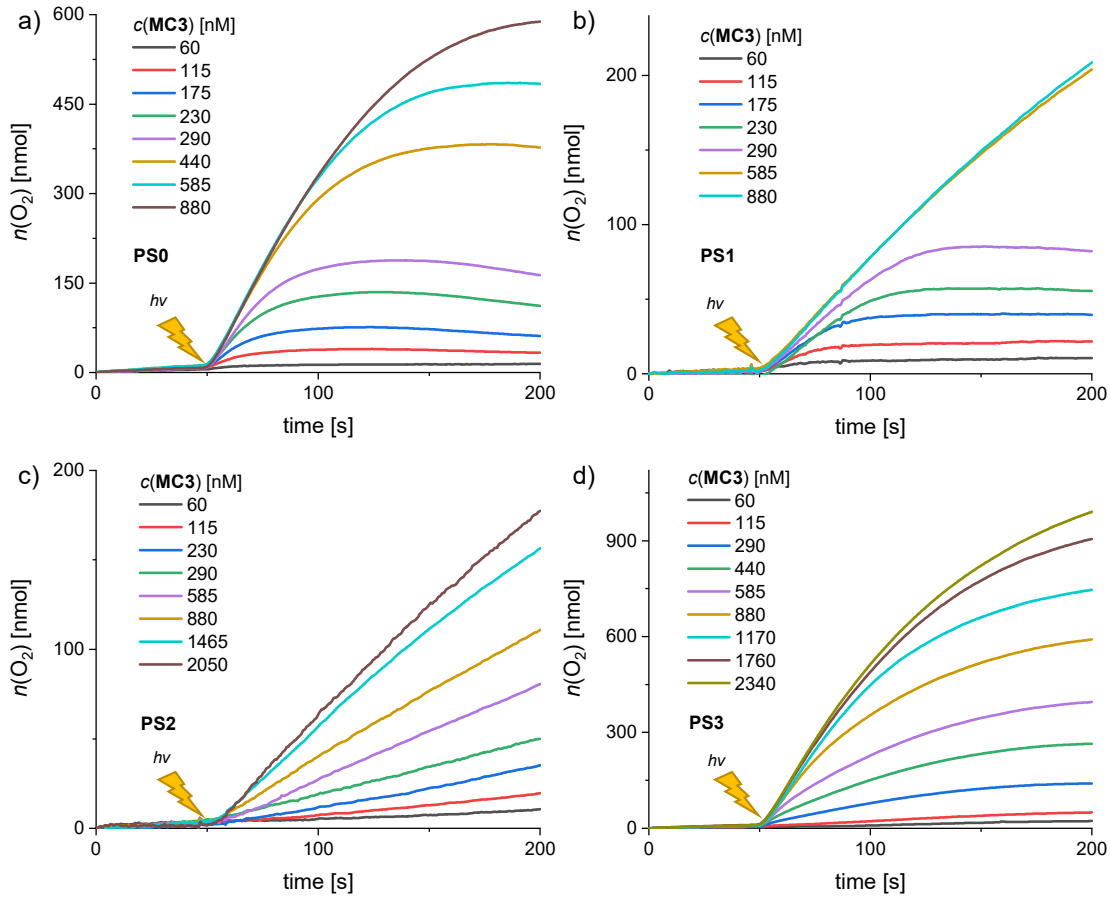

Figure S66. Concentration-dependent oxygen evolution curves of **MC3** in MeCN/H_2O 1:1 (50 mM phosphate buffer, pH 7) using **PS0–3** as photosensitizers, *c*(PS) = 1.5 mM, *c*($Na_2S_2O_8$) = 37 mM. The lighting symbol indicates the start of sample irradiation at *t* = 50 s.

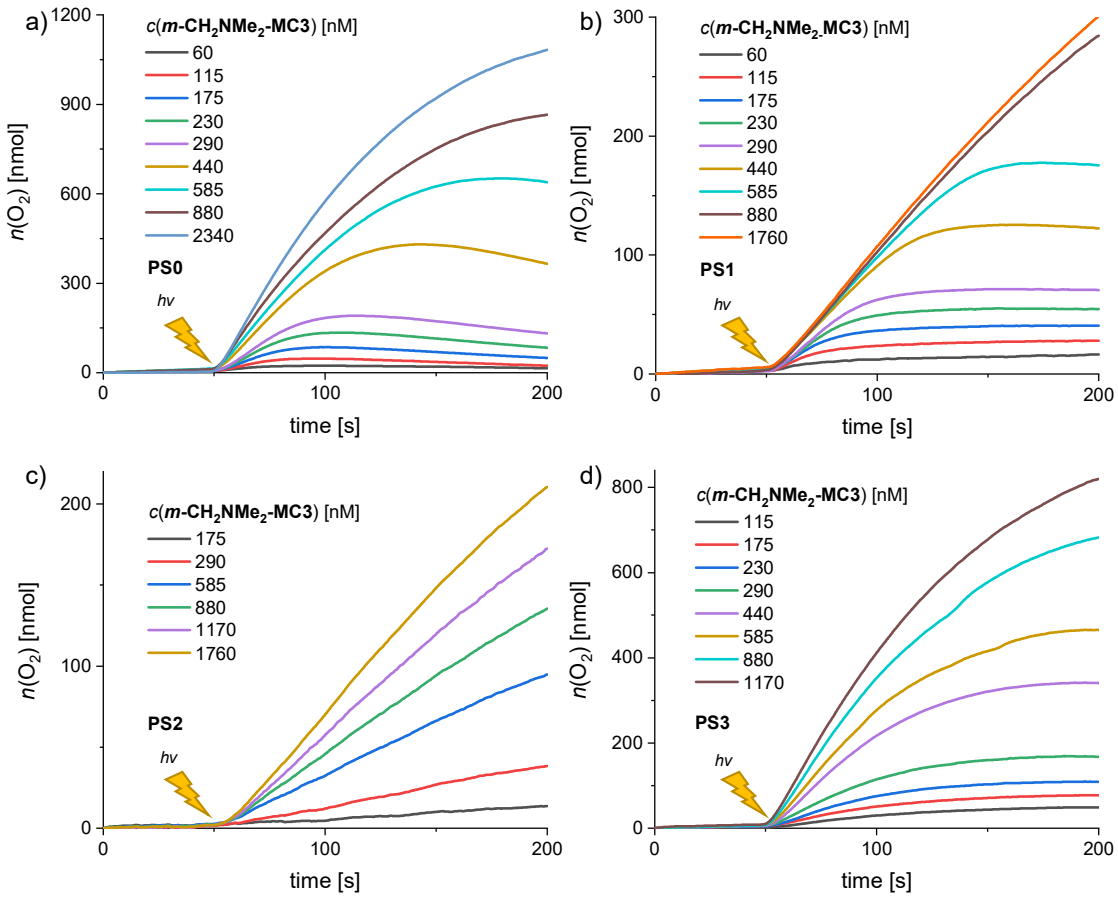

Figure S67. Concentration-dependent oxygen evolution curves of ***m*-CH_2NMe_2-MC3** in MeCN/H_2O 1:1 (50 mM phosphate buffer, pH 7) using **PS0–3** as photosensitizers, *c*(PS) = 1.5 mM, *c*($Na_2S_2O_8$) = 37 mM. The lighting symbol indicates the start of sample irradiation at *t* = 50 s.

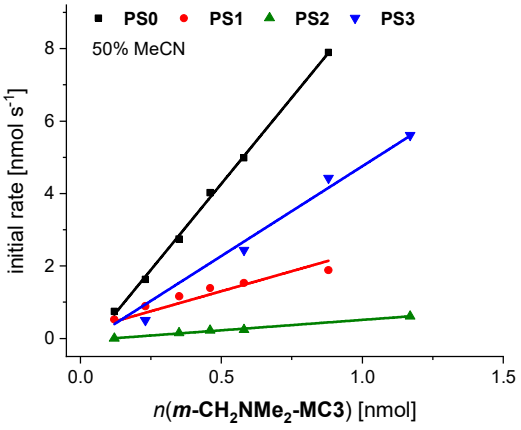

Figure 68. Catalytic performance of ***m*-CH_2NMe_2-MC3** in light-driven water oxidation using **PS0–3** as photosensitizers. The catalytic activity was analyzed by the initial rates of catalysis at variable WOC concentrations. Measurements were performed in 1:1 MeCN/H_2O mixtures (50 mM phosphate buffer, pH 7). Experiment conditions: *c*($[Ru(bpy)_3]^{2+}$) = 1.5 mM, *c*($Na_2S_2O_8$) = 37 mM, *c*(***m*-CH_2NMe_2-MC3**) = 60–585 nM.

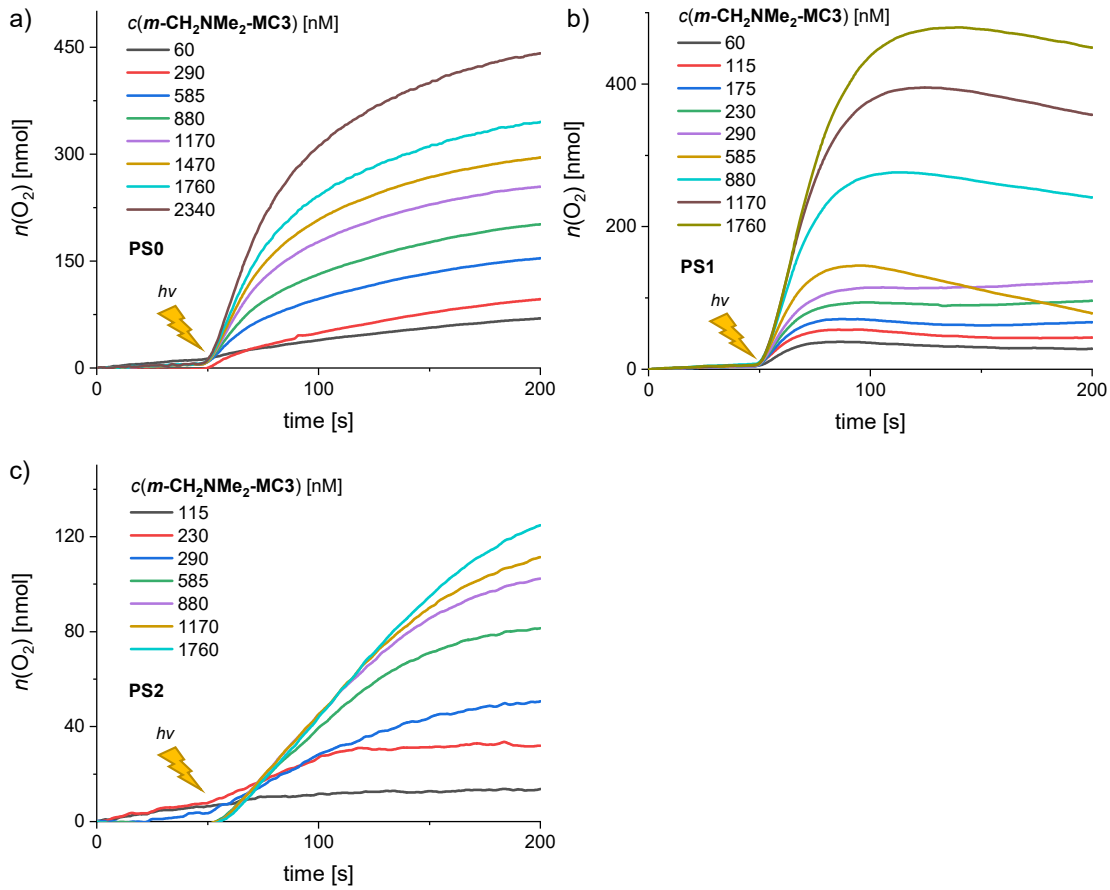

Figure S69. Concentration-dependent oxygen evolution curves of ***m*-CH$_2$NMe$_2$-MC3** in MeCN/H_2O 5:95 (50 mM phosphate buffer, pH 7) using **PS0–2** as photosensitizers, *c*(PS) = 0.2 mM, *c*($Na_2S_2O_8$) = 37 mM. The lighting symbol indicates the start of sample irradiation at *t* = 50 s.

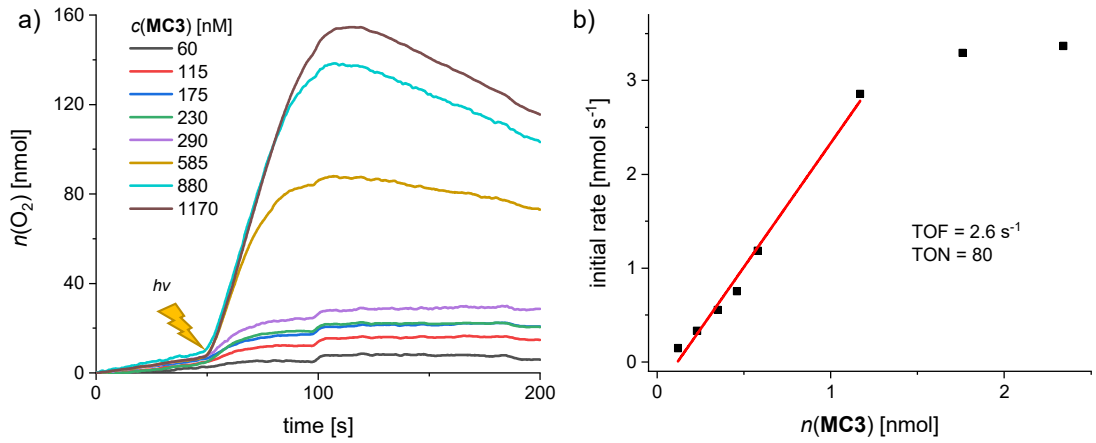

Figure S70. a) Catalyst concentration-dependent oxygen evolution curves of **MC3** in MeCN/H_2O 1:1 (phosphate buffer, pH 7) using **PS0** as sensitizer, *c*(**PS0**) = 0.2 mM, *c*($Na_2S_2O_8$) = 37 mM. The lighting symbol indicates the start of sample irradiation at *t* = 50 s. b) Initial rates of oxygen generation at variable **MC3** concentrations.

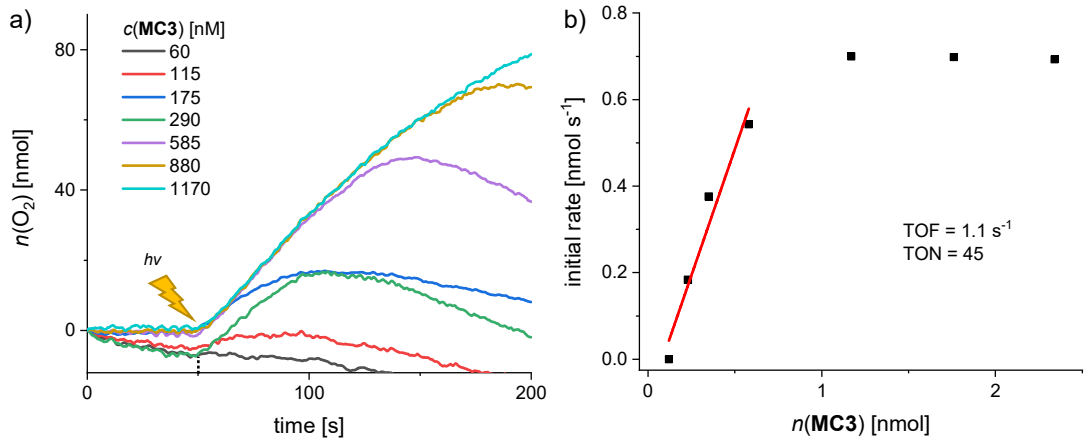

Figure S71. a) Concentration-dependent oxygen evolution curves of **MC3** in MeCN/H_2O 1:1 (phosphate buffer, pH 7) using **PS1** as sensitizer, c(**PS1**) = 0.2 mM, c($Na_2S_2O_8$) = 37 mM. The lighting symbol indicates the start of sample irradiation at t = 50 s. b) Initial rates of oxygen generation at variable **MC3** concentrations.

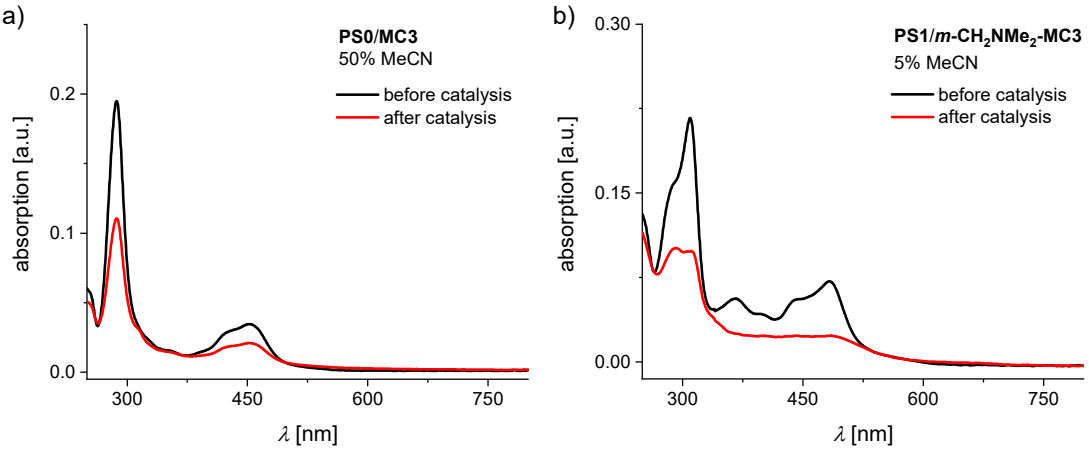

Figure S72. UV/Vis absorption spectra of catalytic mixtures before and after irradiation. a) MeCN/H_2O 1:1 (phosphate buffer, pH 7), c(**PS0**) = 1.5 mM, c($Na_2S_2O_8$) = 37 mM, c(**MC3**) = 1 µM. b) MeCN/H_2O 5:95 (phosphate buffer, pH 7), c(**PS1**) = 0.2 mM, c($Na_2S_2O_8$) = 37 mM, c(***m*-CH_2NMe_2-MC3**) = 1 µM.

Emission Quenching Studies

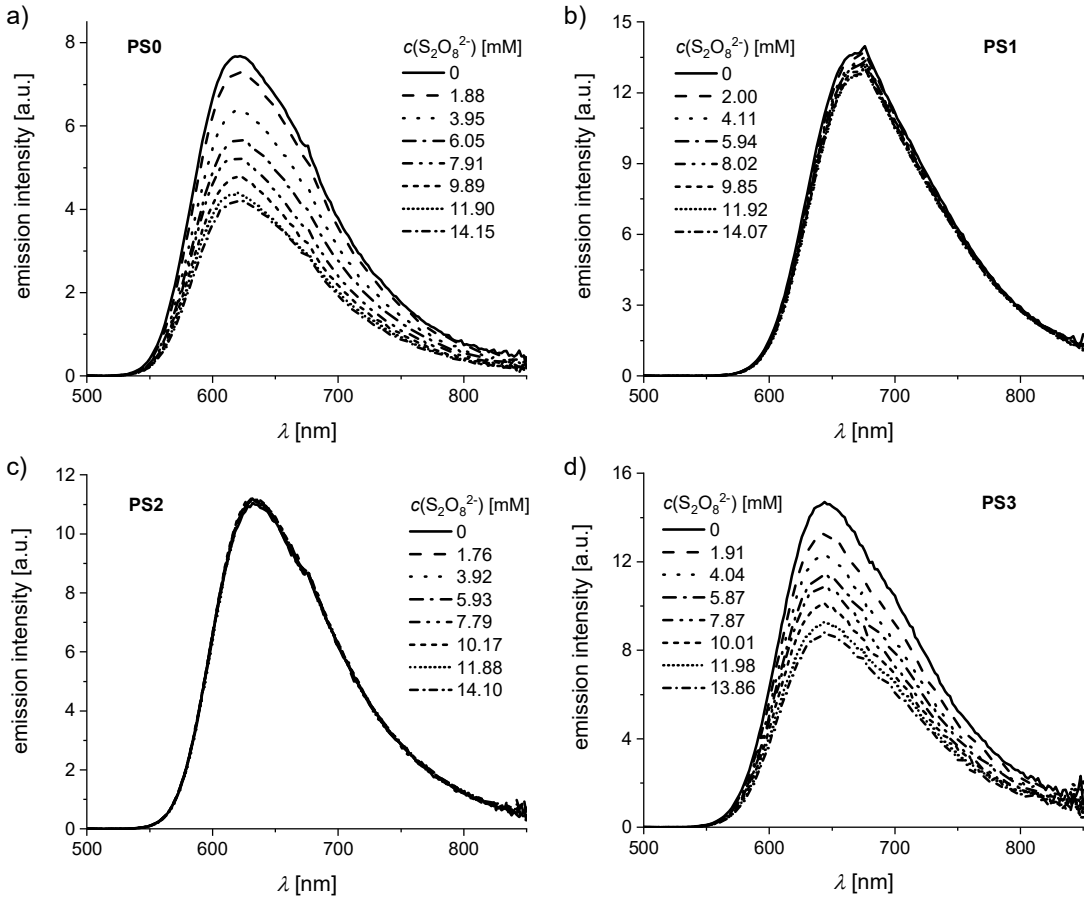

Figure S73. Emission spectra of **PS0–3** in MeCN/H_2O 1:1 (phosphate buffer, pH 7) at varying concentrations of electron acceptor $Na_2S_2O_8$. **PS0-3** were excited at their respective MLCT absorption maximum, $c([Ru(bpy)_3]^{2+})$ = 50 µM.

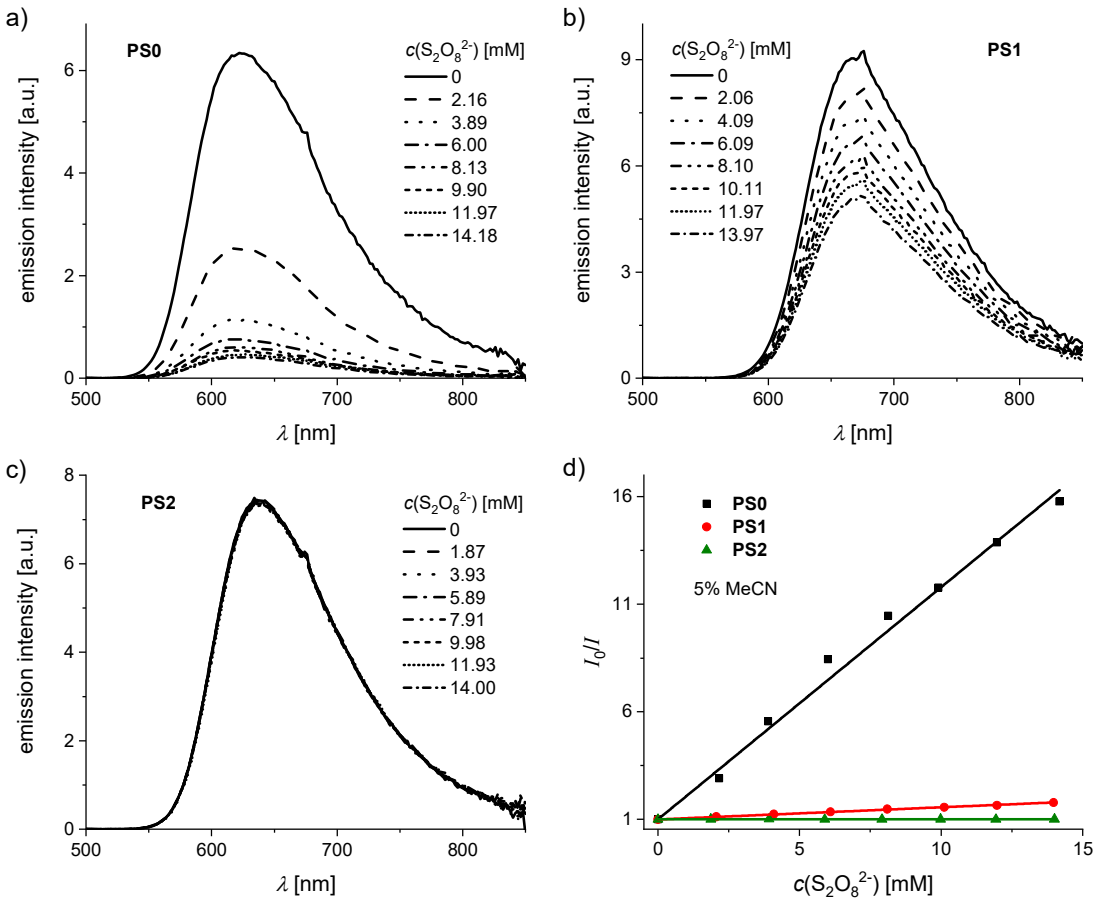

Figure S74. a-c) Emission spectra of **PS0–2** in MeCN/H_2O 5:95 (phosphate buffer, pH 7) at varying concentrations of electron acceptor $Na_2S_2O_8$. **PS0–2** were excited at their respective MLCT absorption maximum, $c([Ru(bpy)_3]^{2+})$ = 50 µM. d) Stern-Volmer plots for **PS0–2** in phosphate buffered MeCN/H_2O 5:95.

Laser Flash Photolysis

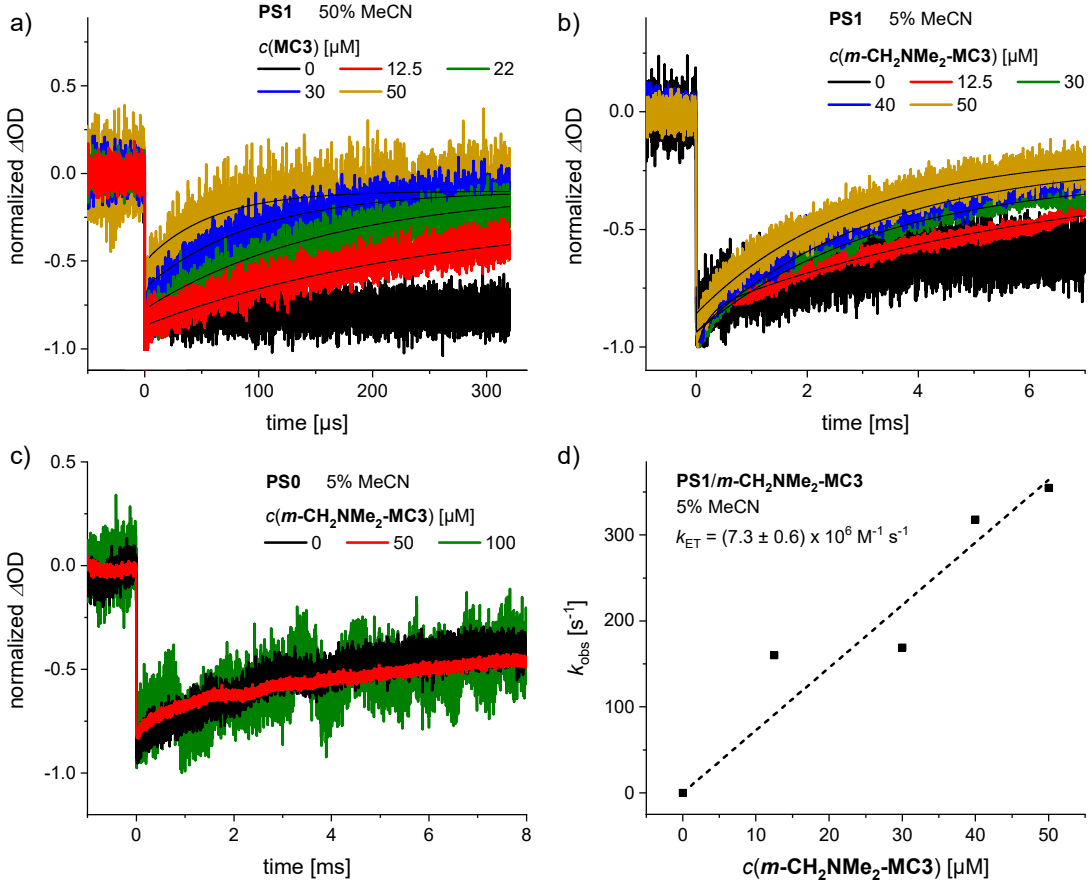

Figure S75. a,b,c) Kinetic traces at 455 nm of solutions of 50 mM $Na_2S_2O_8$ and (a,b) 50 µM **PS1**, (c) 50 µM **PS0** in (a) 1:1 and (b,c) 5:95 MeCN:H_2O (50 mM phosphate buffer, pH 7) at variable concentrations of WOCs (a) **MC3** and (b,c) ***m*-CH$_2$NMe$_2$-MC3**. Exponential fits are shown in black. d) Plot of the observed rate constants k_{obs} for the electron transfer from ***m*-CH$_2$NMe$_2$-MC3** to **PS1**$^+$ in 5% MeCN *vs*. WOC concentration. k_{ET} is obtained from the slope of the linear correlation.

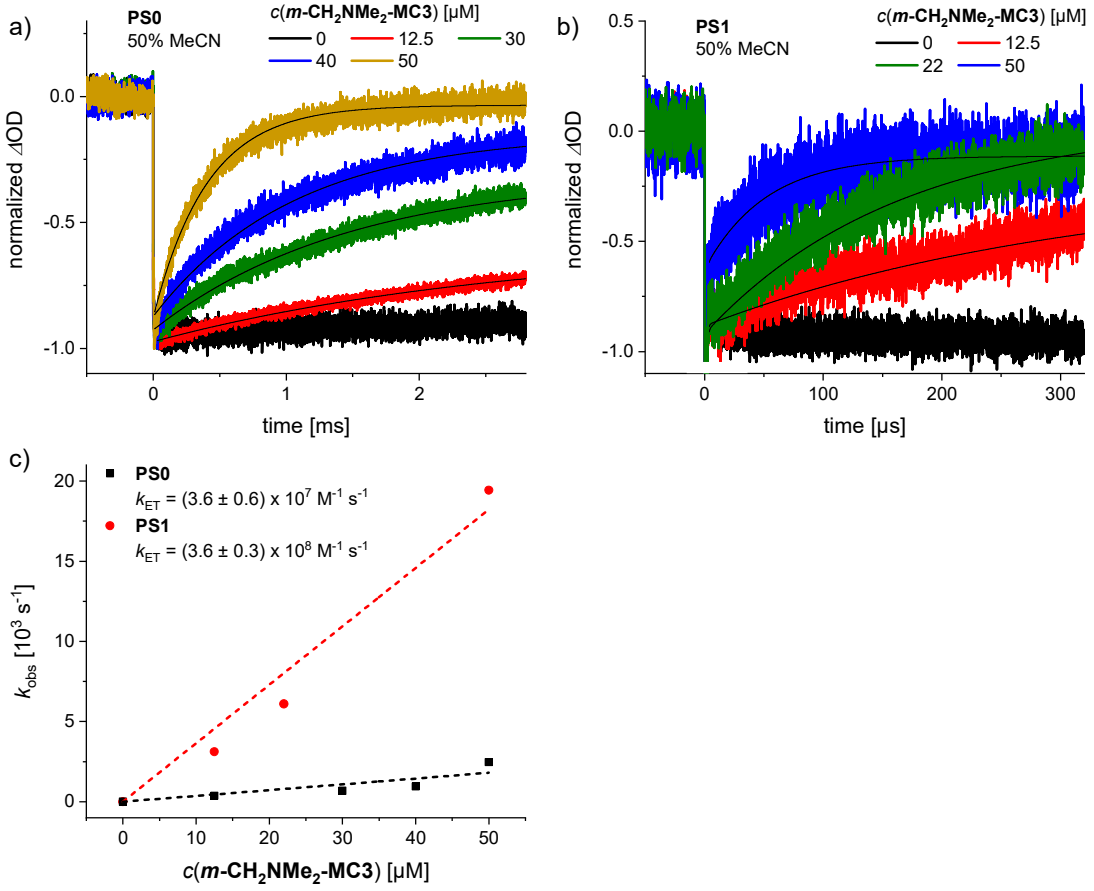

Figure S76. a,b) Kinetic traces at 455 nm of solutions of 50 mM $Na_2S_2O_8$ and (a) 50 μM **PS0**, (b) 50 μM **PS1** in 1:1 MeCN:H_2O (50 mM phosphate buffer, pH 7) at variable concentrations of ***m*-CH$_2$NMe$_2$-MC3**. Exponential fits are shown in black. d) Plot of the observed rate constants k_{obs} for the electron transfer from ***m*-CH$_2$NMe$_2$-MC3** to oxidized sensitizers **PS0$^+$** (black squares) and **PS1$^+$** (red circles) *vs*. WOC concentration. k_{ET} is obtained from the slope of the linear correlation.

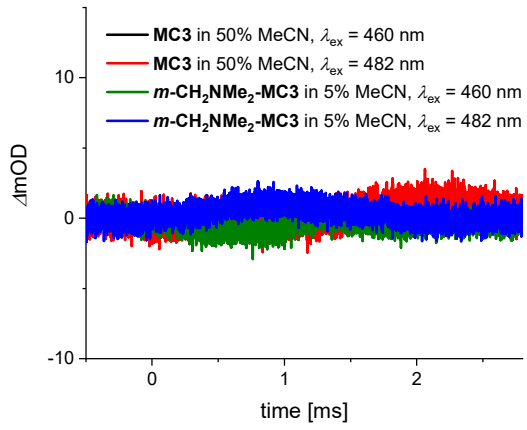

Figure S77. Kinetic traces at 455 nm of solutions of 50 mM $Na_2S_2O_8$ and 50 μM of WOCs **MC3** and ***m*-CH$_2$NMe$_2$-MC3** in 1:1 and 5:95 MeCN:H_2O (50 mM phosphate buffer, pH 7), respectively. Samples were excited at 460 nm and 482 nm

References

[1] G. Ciamician, *Science* **1912**, *36*, 385-394.

[2] a) acatech – National Academy of Science and Engineering, German National Academy of Sciences Leopoldina, Union of the German Academies of Sciences and Humanities, in *Artificial Photosynthesis*, Munich, **2018**, 1-74; b) D. R. Whang, D. H. Apaydin, *ChemPhotoChem* **2018**, *2*, 148-160.

[3] BP p.l.c., in *BP Statistical Review of World Energy 2019*, London, **2019**, 1-61.

[4] a) The Royal Society of Chemistry, in *Solar Fuels and Artificial Photosynthesis: Science and innovation to change our future energy options*, Cambridge, London, **2012**, 1-23; b) European Association of Chemical and Molecular Sciences (EuCheMS), in *Solar-Driven Chemistry. A vision for sustainable chemistry production*, Brussels, **2016**, 1-18.

[5] The International Renewable Energy Agency (IRENA), in *Renewable Energy Statistics 2019*, Abu Dhabi, **2019**, 1-382.

[6] Enerdata, *Global Energy Statistical Yearbook 2019*, Grenoble, **2019**.

[7] World Energy Council, in *World Energy Insights Brief 2019*, London, **2019**, 1-33.

[8] B. Zhang, L. Sun, *Chem. Soc. Rev.* **2019**, *48*, 2216-2264.

[9] P. Li, R. Zhao, H. Chen, H. Wang, P. Wei, H. Huang, Q. Liu, T. Li, X. Shi, Y. Zhang, M. Liu, X. Sun, *Small* **2019**, *15*, 1805103.

[10] B. M. Hunter, H. B. Gray, A. M. Müller, *Chem. Rev.* **2016**, *116*, 14120-14136.

[11] a) P. Garrido-Barros, C. Gimbert-Suriñach, R. Matheu, X. Sala, A. Llobet, *Chem. Soc. Rev.* **2017**, *46*, 6088-6098; b) M. Schilling, S. Luber, *Water Oxidation Catalysis* in *Advances in Inorganic Chemistry,* Academic Press, Cambridge, San Diego, Oxford, London **2019**, *74*, 61-114.

[12] S. W. Gersten, G. J. Samuels, T. J. Meyer, *J. Am. Chem. Soc.* **1982**, *104*, 4029-4030.

[13] a) J. D. Blakemore, R. H. Crabtree, G. W. Brudvig, *Chem. Rev.* **2015**, *115*, 12974-13005; b) M. D. Kärkäs, B. Åkermark, *Dalton Trans.* **2016**, *45*, 14421-14461; c) L. Wang, L. Duan, R. B. Ambre, Q. Daniel, H. Chen, J. Sun, B. Das, A. Thapper, J. Uhlig, P. Dinér, L. Sun, *J. Catal.* **2016**, *335*, 72-78; d) R. Matheu, P. Garrido-Barros, M. Gil-Sepulcre, M. Z. Ertem, X. Sala, C. Gimbert-Suriñach, A. Llobet, *Nat. Rev. Chem.* **2019**, *3*, 331-341.

[14] a) L. Duan, F. Bozoglian, S. Mandal, B. Stewart, T. Privalov, A. Llobet, L. Sun, *Nat. Chem.* **2012**, *4*, 418-423; b) L. Duan, C. M. Araujo, M. S. G. Ahlquist, L. Sun, *Proc. Natl. Acad. Sci.* **2012**, *109*, 15584-15588.

[15] A. R. Parent, R. H. Crabtree, G. W. Brudvig, *Chem. Soc. Rev.* **2013**, *42*, 2247-2252.

[16] M. D. Kärkäs, O. Verho, E. V. Johnston, B. Åkermark, *Chem. Rev.* **2014**, *114*, 11863-12001.

[17] L.-X. Xue, T.-T. Meng, W. Yang, K.-Z. Wang, *J. Photochem. Photobiol. B* **2015**, *152*, 95-105.

[18] M. Schulze, V. Kunz, P. D. Frischmann, F. Würthner, *Nat. Chem.* **2016**, *8*, 576-583.

[19] V. Kunz, J. O. Lindner, M. Schulze, M. I. S. Röhr, D. Schmidt, R. Mitrić, F. Würthner, *Energy Environ. Sci.* **2017**, *10*, 2137-2153.

[20] V. Kunz, M. Schulze, D. Schmidt, F. Würthner, *ACS Energy Lett.* **2017**, *2*, 288-293.

[21] V. Kunz, D. Schmidt, M. I. S. Röhr, R. Mitrić, F. Würthner, *Adv. Energy Mater.* **2017**, *7*, 1602939.

[22] J. M. Berg, J. L. Tymoczko, L. Stryer, in *Stryer Biochemie*, Springer Berlin Heidelberg, Berlin, Heidelberg, **2013**, 569-591.

[23] A. Stirbet, D. Lazár, Y. Guo, G. Govindjee, *Ann. Bot.* **2019**, mcz171.

[24] J. A. Bassham, M. Calvin, The path of carbon in photosynthesis in *Die CO_2-Assimilation / The Assimilation of Carbon Dioxide. Handbuch der Pflanzenphysiologie*, Springer Berlin Heidelberg, Berlin, Heidelberg, **1960**, 884-922.

[25] J. Gao, H. Wang, Q. Yuan, Y. Feng, *Front. Plant Sci.* **2018**, *9*, 1-7.

[26] a) X. Qin, M. Suga, T. Kuang, J.-R. Shen, *Science* **2015**, *348*, 989-995; b) X. Wei, X. Su, P. Cao, X. Liu, W. Chang, M. Li, X. Zhang, Z. Liu, *Nature* **2016**, *534*, 69-74.

[27] P. D. Frischmann, K. Mahata, F. Würthner, *Chem. Soc. Rev.* **2013**, *42*, 1847-1870.

[28] M. M. Najafpour, G. Renger, M. Hołyńska, A. N. Moghaddam, E.-M. Aro, R. Carpentier, H. Nishihara, J. J. Eaton-Rye, J.-R. Shen, S. I. Allakhverdiev, *Chem. Rev.* **2016**, *116*, 2886-2936.

[29] W. Lubitz, M. Chrysina, N. Cox, *Photosynth. Res.* **2019**, *142*, 105-125.

[30] Y. Umena, K. Kawakami, J.-R. Shen, N. Kamiya, *Nature* **2011**, *473*, 55-60.

[31] F. A. Armstrong, *Philos. Trans. R. Soc. B* **2008**, *363*, 1263-1270.

[32] G. W. Brudvig, *Philos. Trans. R. Soc. B* **2008**, *363*, 1211-1219.

[33] T. Lohmiller, N. Cox, J.-H. Su, J. Messinger, W. Lubitz, *J. Biol. Chem.* **2012**, *287*, 24721-24733.

[34] F. H. M. Koua, Y. Umena, K. Kawakami, J.-R. Shen, *Proc. Natl. Acad. Sci.* **2013**, *110*, 3889-3894.

[35] a) J. S. Kanady, E. Y. Tsui, M. W. Day, T. Agapie, *Science* **2011**, *333*, 733-736; b) S. Mukherjee, J. A. Stull, J. Yano, T. C. Stamatatos, K. Pringouri, T. A. Stich, K. A. Abboud, R. D. Britt, V. K. Yachandra, G. Christou, *Proc. Natl. Acad. Sci.* **2012**, *109*, 2257-2262; c) J. S. Kanady, P.-H. Lin, K. M. Carsch, R. J. Nielsen, M. K. Takase, W. A. Goddard, T. Agapie, *J. Am. Chem. Soc.* **2014**, *136*, 14373-14376.

[36] C. Zhang, C. Chen, H. Dong, J.-R. Shen, H. Dau, J. Zhao, *Science* **2015**, *348*, 690-693.

[37] a) L. Vogt, D. J. Vinyard, S. Khan, G. W. Brudvig, *Curr. Opin. Chem. Biol.* **2015**, *25*, 152-158; b) J. Kern, R. Chatterjee, I. D. Young, F. D. Fuller, L. Lassalle, M. Ibrahim, S. Gul, T. Fransson, A. S. Brewster, R. Alonso-Mori, R. Hussein, M. Zhang, L. Douthit, C. de Lichtenberg, M. H. Cheah, D. Shevela, J. Wersig, I. Seuffert, D. Sokaras, E. Pastor, C. Weninger, T. Kroll, R. G. Sierra, P. Aller, A. Butryn, A. M. Orville, M. Liang, A. Batyuk, J. E. Koglin, S. Carbajo, S. Boutet, N. W. Moriarty, J. M. Holton, H. Dobbek, P. D. Adams, U. Bergmann, N. K. Sauter, A. Zouni, J. Messinger, J. Yano, V. K. Yachandra, *Nature* **2018**, *563*, 421-425.

[38] S. Vassiliev, T. Zaraiskaya, D. Bruce, *Biochim. Biophys. Acta* **2012**, *1817*, 1671-1678.

[39] K. Reiss, U. N. Morzan, A. T. Grigas, V. S. Batista, *Inorganics* **2019**, *7*, 39.

[40] a) D. J. Vinyard, G. M. Ananyev, G. Charles Dismukes, *Annu. Rev. Biochem.* **2013**, *82*, 577-606; b) M. M. Najafpour, I. Zaharieva, Z. Zand, S. Maedeh Hosseini, M. Kouzmanova, M. Hołyńska, I. Tranca, A. W. Larkum, J.-R. Shen, S. I. Allakhverdiev, *Coord. Chem. Rev.* **2020**, *409*, 213183.

[41] B. Kok, B. Forbush, M. McGloin, *Photochem. Photobiol.* **1970**, *11*, 457-475.

[42] K. N. Ferreira, T. M. Iverson, K. Maghlaoui, J. Barber, S. Iwata, *Science* **2004**, *303*, 1831-1838.

[43] M. Suga, F. Akita, K. Hirata, G. Ueno, H. Murakami, Y. Nakajima, T. Shimizu, K. Yamashita, M. Yamamoto, H. Ago, J.-R. Shen, *Nature* **2015**, *517*, 99-103.

[44] J. Yano, J. Kern, K. Sauer, M. J. Latimer, Y. Pushkar, J. Biesiadka, B. Loll, W. Saenger, J. Messinger, A. Zouni, V. K. Yachandra, *Science* **2006**, *314*, 821-825.

[45] a) S. Luber, I. Rivalta, Y. Umena, K. Kawakami, J.-R. Shen, N. Kamiya, G. W. Brudvig, V. S. Batista, *Biochemistry* **2011**, *50*, 6308-6311; b) A. Grundmeier, H. Dau, *Biochim. Biophys. Acta* **2012**, *1817*, 88-105; c) D. A. Pantazis, W. Ames, N. Cox, W. Lubitz, F. Neese, *Angew. Chem. Int. Ed.* **2012**, *51*, 9935-9940.

[46] J. Barber, *Nat. Plants* **2017**, *3*, 17041.

[47] D. J. Vinyard, G. W. Brudvig, *Annu. Rev. Phys. Chem.* **2017**, *68*, 101-116.

[48] V. L. Pecoraro, M. J. Baldwin, M. T. Caudle, W.-Y. Hsieh, N. A. Law, *Pure Appl. Chem.* **1998**, *70*, 925-929.

[49] a) P. E. M. Siegbahn, *Acc. Chem. Res.* **2009**, *42*, 1871-1880; b) P. E. M. Siegbahn, *Proc. Natl. Acad. Sci.* **2017**, *114*, 4966-4968.

[50] a) B. Zhang, L. Sun, *Dalton Trans.* **2018**, *47*, 14381-14387; b) B. Zhang, L. Sun, *ChemSusChem* **2019**, *12*, 3401-3404.

[51] S. Berardi, S. Drouet, L. Francàs, C. Gimbert-Suriñach, M. Guttentag, C. Richmond, T. Stoll, A. Llobet, *Chem. Soc. Rev.* **2014**, *43*, 7501-7519.

[52] V. Balzani, A. Credi, M. Venturi, *Curr. Opin. Chem. Biol.* **1997**, *1*, 506-513.

[53] H. L. Tuller, *Mater. Renew. Sustain. Energy* **2017**, *6*, 1-16.

[54] a) J. R. McKone, N. S. Lewis, H. B. Gray, *Chem. Mater.* **2014**, *26*, 407-414; b) J. H. Montoya, L. C. Seitz, P. Chakthranont, A. Vojvodic, T. F. Jaramillo, J. K. Nørskov, *Nat. Mater.* **2017**, *16*, 70-81.

[55] J. Hessels, R. J. Detz, M. T. M. Koper, J. N. H. Reek, *Chem. Eur. J.* **2017**, *23*, 16413-16418.

[56] a) C. Hu, L. Zhang, J. Gong, *Energy Environ. Sci.* **2019**, *12*, 2620-2645; b) N. Yuan, Q. Jiang, J. Li, J. Tang, *Arab. J. Chem.* **2020**, *13*, 4294-4309.

[57] S. Fukuzumi, D. Hong, *Eur. J. Inorg. Chem.* **2014**, *2014*, 645-659.

[58] a) M. Kondo, S. Masaoka, *Chem. Lett.* **2016**, *45*, 1220-1231; b) R. Matheu, M. Z. Ertem, C. Gimbert-Suriñach, X. Sala, A. Llobet, *Chem. Rev.* **2019**, *119*, 3453-3471.

[59] a) S. M. Lauinger, Q. Yin, Y. V. Geletii, C. L. Hill, *Polyoxometalate Chemistry* in *Advances in Inorganic Chemistry*, Academic Press, Cambridge, San Diego, Oxford, London, **2017**, *69*, 117-154; b) J. Lin, Q. Han, Y. Ding, *Chem. Rec.* **2018**, *18*, 1531-1547; c) D. Gao, I. Trentin, L. Schwiedrzik, L. González, C. Streb, *Molecules* **2020**, *25*, 157.

[60] a) K. R. Yang, A. J. Matula, G. Kwon, J. Hong, S. W. Sheehan, J. M. Thomsen, G. W. Brudvig, R. H. Crabtree, D. M. Tiede, L. X. Chen, V. S. Batista, *J. Am. Chem. Soc.* **2016**, *138*, 5511-5514; b) T. K. Michaelos, D. Y. Shopov, S. B. Sinha, L. S. Sharninghausen, K. J. Fisher, H. M. C. Lant, R. H. Crabtree, G. W. Brudvig, *Acc. Chem. Res.* **2017**, *50*, 952-959.

[61] M. Okamura, M. Kondo, R. Kuga, Y. Kurashige, T. Yanai, S. Hayami, V. K. K. Praneeth, M. Yoshida, K. Yoneda, S. Kawata, S. Masaoka, *Nature* **2016**, *530*, 465-468.

[62] D. Wang, J. T. Groves, *Proc. Natl. Acad. Sci.* **2013**, *110*, 15579-15584.

[63] D. R. Weinberg, C. J. Gagliardi, J. F. Hull, C. F. Murphy, C. A. Kent, B. C. Westlake, A. Paul, D. H. Ess, D. G. McCafferty, T. J. Meyer, *Chem. Rev.* **2012**, *112*, 4016-4093.

[64] P. Garrido-Barros, C. Gimbert-Suriñach, D. Moonshiram, A. Picón, P. Monge, V. S. Batista, A. Llobet, *J. Am. Chem. Soc.* **2017**, *139*, 12907-12910.

[65] a) J. P. Collin, J. P. Sauvage, *Inorg. Chem.* **1986**, *25*, 135-141; b) K. Nagoshi, S. Yamashita, M. Yagi, M. Kaneko, *J. Mol. Catal. A* **1999**, *144*, 71-76.

[66] N. N. Greenwood, A. Earnshaw, in *Chemistry of the Elements*, Butterworth-Heinemann, Oxford, **1997**, 1070-1112.

[67] a) R. A. Binstead, C. W. Chronister, J. Ni, C. M. Hartshorn, T. J. Meyer, *J. Am. Chem. Soc.* **2000**, *122*, 8464-8473; b) F. Liu, J. J. Concepcion, J. W. Jurss, T. Cardolaccia, J. L. Templeton, T. J. Meyer, *Inorg. Chem.* **2008**, *47*, 1727-1752; c) D. Moonshiram, J.

W. Jurss, J. J. Concepcion, T. Zakharova, I. Alperovich, T. J. Meyer, Y. Pushkar, *J. Am. Chem. Soc.* **2012**, *134*, 4625-4636; d) D. Moonshiram, I. Alperovich, J. J. Concepcion, T. J. Meyer, Y. Pushkar, *Proc. Natl. Acad. Sci.* **2013**, *110*, 3765-3770.

[68] a) L. Tong, R. P. Thummel, *Chem. Sci.* **2016**, *7*, 6591-6603; b) M. D. Kärkäs, B. Åkermark, *Chem. Rec.* **2016**, *16*, 940-963; c) M. J. Kamdar, B. D. Grotjahn, *Molecules* **2019**, *24*, 494.

[69] C. Sens, I. Romero, M. Rodríguez, A. Llobet, T. Parella, J. Benet-Buchholz, *J. Am. Chem. Soc.* **2004**, *126*, 7798-7799.

[70] a) S. Romain, F. Bozoglian, X. Sala, A. Llobet, *J. Am. Chem. Soc.* **2009**, *131*, 2768-2769; b) F. Bozoglian, S. Romain, M. Z. Ertem, T. K. Todorova, C. Sens, J. Mola, M. Rodríguez, I. Romero, J. Benet-Buchholz, X. Fontrodona, C. J. Cramer, L. Gagliardi, A. Llobet, *J. Am. Chem. Soc.* **2009**, *131*, 15176-15187.

[71] S. Neudeck, S. Maji, I. López, S. Meyer, F. Meyer, A. Llobet, *J. Am. Chem. Soc.* **2014**, *136*, 24-27.

[72] S. Berardi, L. Francàs, S. Neudeck, S. Maji, J. Benet-Buchholz, F. Meyer, A. Llobet, *ChemSusChem* **2015**, *8*, 3688-3696.

[73] R. Zong, R. P. Thummel, *J. Am.Chem. Soc.* **2005**, *127*, 12802-12803.

[74] H.-W. Tseng, R. Zong, J. T. Muckerman, R. Thummel, *Inorg. Chem.* **2008**, *47*, 11763-11773.

[75] a) D. E. Polyansky, J. T. Muckerman, J. Rochford, R. Zong, R. P. Thummel, E. Fujita, *J. Am. Chem. Soc.* **2011**, *133*, 14649-14665; b) Y. M. Badiei, D. E. Polyansky, J. T. Muckerman, D. J. Szalda, R. Haberdar, R. Zong, R. P. Thummel, E. Fujita, *Inorg. Chem.* **2013**, *52*, 8845-8850.

[76] D. Moonshiram, Y. Pineda-Galvan, D. Erdman, M. Palenik, R. Zong, R. Thummel, Y. Pushkar, *J. Am. Chem. Soc.* **2016**, *138*, 15605-15616.

[77] T. Norrby, A. Börje, B. Åkermark, L. Hammarström, J. Alsins, K. Lashgari, R. Norrestam, J. Mårtensson, G. Stenhagen, *Inorg. Chem.* **1997**, *36*, 5850-5858.

[78] Y. Xu, T. Åkermark, V. Gyollai, D. Zou, L. Eriksson, L. Duan, R. Zhang, B. Åkermark, L. Sun, *Inorg. Chem.* **2009**, *48*, 2717-2719.

[79] L. Duan, A. Fischer, Y. Xu, L. Sun, *J. Am. Chem. Soc.* **2009**, *131*, 10397-10399.

[80] L. Wang, L. Duan, B. Stewart, M. Pu, J. Liu, T. Privalov, L. Sun, *J. Am. Chem. Soc.* **2012**, *134*, 18868-18880.

[81] R. Matheu, M. Z. Ertem, J. Benet-Buchholz, E. Coronado, V. S. Batista, X. Sala, A. Llobet, *J. Am. Chem. Soc.* **2015**, *137*, 10786-10795.

[82] L. Francàs, R. Matheu, E. Pastor, A. Reynal, S. Berardi, X. Sala, A. Llobet, J. R. Durrant, *ACS Catal.* **2017**, *7*, 5142-5150.

[83] N. Vereshchuk, R. Matheu, J. Benet-Buchholz, M. Pipelier, J. Lebreton, D. Dubreuil, A. Tessier, C. Gimbert-Suriñach, M. Z. Ertem, A. Llobet, *J. Am. Chem. Soc.* **2020**, *142*, 5068-5077.

[84] L. Duan, L. Wang, F. Li, F. Li, L. Sun, *Acc. Chem. Res.* **2015**, *48*, 2084-2096.

[85] B. Zhang, L. Sun, *J. Am. Chem. Soc.* **2019**, *141*, 5565-5580.

[86] J. J. Concepcion, D. K. Zhong, D. J. Szalda, J. T. Muckerman, E. Fujita, *Chem. Commun.* **2015**, *51*, 4105-4108.

[87] a) L. Duan, L. Wang, A. K. Inge, A. Fischer, X. Zou, L. Sun, *Inorg. Chem.* **2013**, *52*, 7844-7852; b) L. Wang, L. Duan, Y. Wang, M. S. G. Ahlquist, L. Sun, *Chem. Commun.* **2014**, *50*, 12947-12950.

[88] N. Song, J. J. Concepcion, R. A. Binstead, J. A. Rudd, A. K. Vannucci, C. J. Dares, M. K. Coggins, T. J. Meyer, *Proc. Natl. Acad. Sci.* **2015**, *112*, 4935-4940.

[89] R. Matheu, A. Ghaderian, L. Francas, P. Chernev, M. Ertem, J. Benet-Buchholz, V. Batista, M. Haumann, C. Gimbert-Suriñach, X. Sala, A. Llobet, *Chem. Eur. J.* **2018**, *24*, 12838-12847.

[90] Q. Daniel, P. Huang, T. Fan, Y. Wang, L. Duan, L. Wang, F. Li, Z. Rinkevicius, F. Mamedov, M. S. G. Ahlquist, S. Styring, L. Sun, *Coord. Chem. Rev.* **2017**, *346*, 206-215.

[91] D. W. Shaffer, Y. Xie, J. J. Concepcion, *Chem. Soc. Rev.* **2017**, *46*, 6170-6193.

[92] D. W. Shaffer, Y. Xie, D. J. Szalda, J. J. Concepcion, *J. Am. Chem. Soc.* **2017**, *139*, 15347-15355.

[93] A. F. Holleman, N. Wiberg, E. Wiberg, G. Fischer, in *Lehrbuch der Anorganischen Chemie*, De Gruyter, Berlin, Boston, **2007**, 1315-1399.

[94] R. Matheu, S. Neudeck, F. Meyer, X. Sala, A. Llobet, *ChemSusChem* **2016**, *9*, 3361-3369.

[95] L. Duan, Y. Xu, P. Zhang, M. Wang, L. Sun, *Inorg. Chem.* **2010**, *49*, 209-215.

[96] J. Nyhlén, L. Duan, B. Åkermark, L. Sun, T. Privalov, *Angew. Chem. Int. Ed.* **2010**, *49*, 1773-1777.

[97] D. Lebedev, Y. Pineda-Galvan, Y. Tokimaru, A. Fedorov, N. Kaeffer, C. Copéret, Y. Pushkar, *J. Am. Chem. Soc.* **2018**, *140*, 451-458.

[98] S. Zhan, D. Mårtensson, M. Purg, S. C. L. Kamerlin, M. S. G. Ahlquist, *Angew. Chem. Int. Ed.* **2017**, *56*, 6962-6965.

[99] a) T. Fan, S. Zhan, M. S. G. Ahlquist, *ACS Catal.* **2016**, *6*, 8308-8312; b) S. Zhan, R. Zou, M. S. G. Ahlquist, *ACS Catal.* **2018**, *8*, 8642-8648.

[100] a) Y. Jiang, F. Li, F. Huang, B. Zhang, L. Sun, *Chin. J. Catal.* **2013**, *34*, 1489-1495; b) Y. Sato, S.-Y. Takizawa, S. Murata, *Eur. J. Inorg. Chem.* **2015**, *2015*, 5495-5502.

[101] a) Y. Xie, D. W. Shaffer, J. J. Concepcion, *Inorg. Chem.* **2018**, *57*, 10533-10542; b) C. J. Richmond, S. Escayola, A. Poater, *Eur. J. Inorg. Chem.* **2019**, *2019*, 2101-2108.

[102] C. J. Richmond, R. Matheu, A. Poater, L. Falivene, J. Benet-Buchholz, X. Sala, L. Cavallo, A. Llobet, *Chem. Eur. J.* **2014**, *20*, 17282-17286.

[103] T.-T. Li, W.-L. Zhao, Y. Chen, F.-M. Li, C.-J. Wang, Y.-H. Tian, W.-F. Fu, *Chem. Eur. J.* **2014**, *20*, 13957-13964.

[104] Z. Liu, Y. Gao, Z. Yu, M. Zhang, J. Liu, *Chin. J. Catal.* **2015**, *36*, 1742-1749.

[105] D. W. Shaffer, Y. Xie, D. J. Szalda, J. J. Concepcion, *Inorg. Chem.* **2016**, *55*, 12024-12035.

[106] Q. Daniel, L. Wang, L. Duan, F. Li, L. Sun, *Dalton Trans.* **2016**, *45*, 14689-14696.

[107] R. Staehle, L. Tong, L. Wang, L. Duan, A. Fischer, M. S. G. Ahlquist, L. Sun, S. Rau, *Inorg. Chem.* **2014**, *53*, 1307-1319.

[108] B. Li, F. Li, S. Bai, Z. Wang, L. Sun, Q. Yang, C. Li, *Energy Environ. Sci.* **2012**, *5*, 8229-8233.

[109] L. Tong, L. Duan, Y. Xu, T. Privalov, L. Sun *Angew. Chem. Int. Ed.* **2011**, *50*, 445-449.

[110] F. Yu, D. Poole Iii, S. Mathew, N. Yan, J. Hessels, N. Orth, I. Ivanović-Burmazović, J. N. H. Reek, *Angew. Chem. Int. Ed.* **2018**, *57*, 11247-11251.

[111] V. Kunz, V. Stepanenko, F. Würthner, *Chem. Commun.* **2015**, *51*, 290-293.

[112] B. Yang, X. Jiang, Q. Guo, T. Lei, L.-P. Zhang, B. Chen, C.-H. Tung, L.-Z. Wu, *Angew. Chem. Int. Ed.* **2016**, *55*, 6229-6234.

[113] T. Zheng, L. Li, *New J. Chem.* **2018**, *42*, 2526-2536.

[114] T. Zheng, M. Zhu, M. Waqas, A. Umair, M. Zaheer, J. Yang, X. Duan, L. Li, *RSC Adv.* **2018**, *8*, 38818-38830.

[115] J. Zhang, J. Du, J. Wang, Y. Wang, C. Wei, M. Li, *Angew. Chem. Int. Ed.* **2018**, *57*, 16698-16702.

[116] a) F. Ding, L. Duan, Y. Gao, *Inorg. Chem. Commun.* **2016**, *70*, 129-131; b) A. Bhunia, B. A. Johnson, J. Czapla-Masztafiak, J. Sá, S. Ott, *Chem. Commun.* **2018**, *54*, 7770-7773.

[117] Z. Liu, Y. Gao, M. Zhang, J. Liu, *Inorg. Chem. Commun.* **2015**, *55*, 56-59.

[118] Y. Jiang, F. Li, B. Zhang, X. Li, X. Wang, F. Huang, L. Sun, *Angew. Chem. Int. Ed.* **2013**, *52*, 3398-3401.

[119] L. L. Zhang, Y. Gao, Z. Liu, X. Ding, Z. Yu, L. C. Sun, *Dalton Trans.* **2016**, *45*, 3814-3819.

[120] Y. Dong, J. Zhang, J. Ma, in *Bimetallic Ru supramolecular macrocyclic compound, synthetic method and application thereof*, Patent CN104558050A, **2015**.

[121] P. Garrido-Barros, R. Matheu, C. Gimbert-Suriñach, A. Llobet, *Curr. Opin. Electrochem.* **2019**, *15*, 140-147.

[122] a) S. Campagna, F. Puntoriero, F. Nastasi, G. Bergamini, V. Balzani, in *Photochemistry and Photophysics of Coordination Compounds I*, Springer Berlin Heidelberg, Berlin, Heidelberg, **2007**, 117-214; b) F. Puntoriero, S. Serroni, G. La Ganga, A. Santoro, M. Galletta, F. Nastasi, E. La Mazza, A. M. Cancelliere, S. Campagna, *Eur. J. Inorg. Chem.* **2018**, *2018*, 3887-3899.

[123] a) B. Zhang, F. Li, R. Zhang, C. Ma, L. Chen, L. Sun, *Chem. Commun.* **2016**, *52*, 8619-8622; b) Y. Tsubonouchi, S. Lin, A. R. Parent, G. W. Brudvig, K. Sakai, *Chem. Commun.* **2016**, *52*, 8018-8021.

[124] L. Wang, D. W. Shaffer, G. F. Manbeck, D. E. Polyansky, J. J. Concepcion, *ACS Catal.* **2020**, *10*, 580-585.

[125] F. Li, C. Xu, X. Wang, Y. Wang, J. Du, L. Sun, *Chin. J. Catal.* **2018**, *39*, 446-452.

[126] L. Wang, M. Mirmohades, A. Brown, L. Duan, F. Li, Q. Daniel, R. Lomoth, L. Sun, L. Hammarström, *Inorg. Chem.* **2015**, *54*, 2742-2751.

[127] Y. Gao, L. Duan, Z. Yu, X. Ding, L. Sun, *Faraday Discuss.* **2014**, *176*, 225-232.

[128] F. Li, Y. Jiang, B. Zhang, F. Huang, Y. Gao, L. Sun, *Angew. Chem. Int. Ed.* **2012**, *51*, 2417-2420.

[129] H. Li, F. Li, B. Zhang, X. Zhou, F. Yu, L. Sun, *J. Am. Chem. Soc.* **2015**, *137*, 4332-4335.

[130] A.-L. Meza-Chincha, J. O. Lindner, D. Schindler, D. Schmidt, A.-M. Krause, M. I. S. Röhr, R. Mitrić, F. Würthner, *Chem. Sci.* **2020**, DOI: 10.1039/D0SC01097A.

[131] U. Neumann, F. Vögtle, *Chem. Ber.* **1989**, *122*, 589-591.

[132] C. L. M. Bolli, B. Mathys, C. Mueller, O. Nayler, B. Steiner, J. Velker, in *Pyridine derivatives as S1P1/EDG1 receptor modulators*, Patent WO2009024905, **2009**.

[133] a) F. Li, B. Zhang, X. Li, Y. Jiang, L. Chen, Y. Li, L. Sun, *Angew. Chem. Int. Ed.* **2011**, *50*, 12276-12279; b) Y. Gao, X. Ding, J. Liu, L. Wang, Z. Lu, L. Li, L. Sun, *J. Am. Chem. Soc.* **2013**, *135*, 4219-4222.

[134] M. V. Sheridan, B. D. Sherman, Z. Fang, K.-R. Wee, M. K. Coggins, T. J. Meyer, *ACS Catal.* **2015**, *5*, 4404-4409.

[135] a) K. Kalyanasundaram, *Coord. Chem. Rev.* **1982**, *46*, 159-244; b) A. Juris, V. Balzani, F. Barigelletti, S. Campagna, P. Belser, A. von Zelewsky, *Coord. Chem. Rev.* **1988**, *84*, 85-277.

[136] W. Rabten, M. D. Kärkäs, T. Åkermark, H. Chen, R.-Z. Liao, F. Tinnis, J. Sun, P. E. M. Siegbahn, P. G. Andersson, B. Åkermark, *Inorg. Chem.* **2015**, *54*, 4611-4620.

[137] a) B. Limburg, E. Bouwman, S. Bonnet, *ACS Catal.* **2016**, *6*, 5273-5284; b) M. Natali, F. Nastasi, F. Puntoriero, A. Sartorel, *Eur. J. Inorg. Chem.* **2019**, *2019*, 2027-2039.

[138] L. Vigara, M. Z. Ertem, N. Planas, F. Bozoglian, N. Leidel, H. Dau, M. Haumann, L. Gagliardi, C. J. Cramer, A. Llobet, *Chem. Sci.* **2012**, *3*, 2576-2586.

[139] J. Lin, X. Liang, X. Cao, N. Wei, Y. Ding, *Chem. Commun.* **2018**, *54*, 12515-12518.

[140] N. Agmon, *Chem. Phys. Lett.* **1995**, *244*, 456-462.

[141] a) M. Bommer, A.-N. Bondar, A. Zouni, H. Dobbek, H. Dau, *Biochemistry* **2016**, *55*, 4626-4635; b) H. Singh, S. K. Vasa, H. Jangra, P. Rovó, C. Päslack, C. K. Das, H. Zipse, L. V. Schäfer, R. Linser, *J. Am. Chem. Soc.* **2019**, *141*, 19276-19288.

[142] A. Lewandowska-Andralojc, D. E. Polyansky, *J. Phys. Chem. A* **2013**, *117*, 10311-10319.

[143] a) A. Lewandowska-Andralojc, D. E. Polyansky, R. Zong, R. P. Thummel, E. Fujita, *Phys. Chem. Chem. Phys.* **2013**, *15*, 14058-14068; b) M. Natali, M. Orlandi, S. Berardi, S. Campagna, M. Bonchio, A. Sartorel, F. Scandola, *Inorg. Chem.* **2012**, *51*, 7324-7331.

[144] a) P. K. Ghosh, B. S. Brunschwig, M. Chou, C. Creutz, N. Sutin, *J. Am. Chem. Soc.* **1984**, *106*, 4772-4783; b) P. Comte, M. K. Nazeeruddin, F. P. Rotzinger, A. J. Frank, M. Grätzel, *J. Mol. Catal.* **1989**, *52*, 63-84; c) N. D. Morris, M. Suzuki, T. E. Mallouk, *J. Phys. Chem. A* **2004**, *108*, 9115-9119.

[145] a) M. Hara, C. C. Waraksa, J. T. Lean, B. A. Lewis, T. E. Mallouk, *J. Phys. Chem. A* **2000**, *104*, 5275-5280; b) L. Wang, L. Duan, L. Tong, L. Sun, *J. Catal.* **2013**, *306*, 129-132.

[146] a) Y. Xu, L. Duan, L. Tong, B. Akermark, L. Sun, *Chem. Commun.* **2010**, *46*, 6506-6508; b) M. N. Kushner-Lenhoff, J. D. Blakemore, N. D. Schley, R. H. Crabtree, G. W. Brudvig, *Dalton Trans.* **2013**, *42*, 3617-3622.

[147] H. S. White, W. G. Becker, A. J. Bard, *J. Phys. Chem.* **1984**, *88*, 1840-1846.

[148] a) M. R. Norris, J. J. Concepcion, C. R. K. Glasson, Z. Fang, A. M. Lapides, D. L. Ashford, J. L. Templeton, T. J. Meyer, *Inorg. Chem.* **2013**, *52*, 12492-12501; b) Y.-J. Hou, P.-H. Xie, B.-W. Zhang, Y. Cao, X.-R. Xiao, W.-B. Wang, *Inorg. Chem.* **1999**, *38*, 6320-6322; c) B. H. Farnum, J. J. Jou, G. J. Meyer, *Proc. Natl. Acad. Sci.* **2012**, *109*, 15628-15633.

[149] M. Zhou, G. P. Robertson, J. Roovers, *Inorg. Chem.* **2005**, *44*, 8317-8325.

[150] a) D. Wenkert, R. B. Woodward, *J. Org. Chem.* **1983**, *48*, 283-289; b) T. Mizuno, M. Takeuchi, I. Hamachi, K. Nakashima, S. Shinkai, *J. Chem. Soc. Perkin Trans. 2* **1998**, 2281-2288.

[151] a) A. S. Wagman, H. E. Moser, in *Carbacephem β-lactam antibiotics*, Patent WO2010030811, **2010**; b) D. O. Kirsanov, N. E. Borisova, M. D. Reshetova, A. V. Ivanov, L. A. Korotkov, I. I. Eliseev, M. Y. Alyapyshev, I. G. Spiridonov, A. V. Legin, Y. G. Vlasov, V. A. Babain, *Russ. Chem. Bull.* **2012**, *61*, 881-890.

[152] W. M. Ward, B. H. Farnum, M. Siegler, G. J. Meyer, *J. Phys. Chem. A* **2013**, *117*, 8883-8894.

[153] D. Bürßner, H.-J. Wolff, E. Steiner Ulrich, *Z. Phys. Chem.* **1993**, *182*, 297-308.

[154] K. Kalyanasundaram, M. K. Nazeeruddin, M. Grätzel, G. Viscardi, P. Savarino, E. Barni, *Inorg. Chim. Acta* **1992**, *198-200*, 831-839.

[155] a) V. Gutmann, G. Gritzner, K. Danksagmuller, *Inorg. Chim. Acta* **1976**, *17*, 81-86; b) D. Ajloo, B. Yoonesi, A. Soleymanpour, *Int. J. Electrochem. Sci.* **2010**, *5*, 459-477.

[156] a) S. Welter, N. Salluce, A. Benetti, N. Rot, P. Belser, P. Sonar, A. C. Grimsdale, K. Müllen, M. Lutz, A. L. Spek, L. De Cola, *Inorg. Chem.* **2005**, *44*, 4706-4718; b) A. D'Aléo, S. Welter, E. Cecchetto, L. De Cola, *Pure Appl. Chem.* **2005**, *77*, 1035-1050.

[157] G. Leem, S. Keinan, J. Jiang, Z. Chen, T. Pho, Z. A. Morseth, Z. Hu, E. Puodziukynaite, Z. Fang, J. M. Papanikolas, J. R. Reynolds, K. S. Schanze, *Polym. Chem.* **2015**, *6*, 8184-8193.

[158] J. V. Caspar, T. J. Meyer, *J. Am. Chem. Soc.* **1983**, *105*, 5583-5590.

[159] J. Blanco-Gálvez, S. Malato-Rodríguez, E. Delyannis, V. G. Belessiotis, S. C. Bhattacharya, S. Kumar, in *Solar Energy Conversion and Photoenergy Systems: Thermal Systems and Desalination Plants Vol. III*, EOLSS Publications, **2010**, 186-226.

[160] A. Volpe, C. Tubaro, M. Natali, A. Sartorel, G. W. Brudvig, M. Bonchio, *Inorg. Chem.* **2019**, *58*, 16537-16545.

[161] a) A. Vaidyalingam, P. K. Dutta, *Anal. Chem.* **2000**, *72*, 5219-5224; b) S. G. Farina, W. Yuey, C. Ambrose, P. E. Hoggard, *Inorg. Chim. Acta* **1988**, *148*, 97-100; c) C. T. Lin, W. Boettcher, M. Chou, C. Creutz, N. Sutin, *J. Am. Chem. Soc.* **1976**, *98*, 6536-6544.

[162] A. Volpe, M. Natali, C. Graiff, A. Sartorel, C. Tubaro, M. Bonchio, *Dalton Trans.* **2020**, *49*, 2696-2705.

[163] a) O. Stern, M. Volmer, *Phys. Z.* **1919**, *20*, 183-188; b) P. Thordarson, *Chem. Soc. Rev.* **2011**, *40*, 1305-1323.

[164] A. Harriman, G. Porter, P. Walters, *J. Chem. Soc. Faraday Trans. 2* **1981**, *77*, 2373-2383.

[165] F. Puntoriero, A. Sartorel, M. Orlandi, G. La Ganga, S. Serroni, M. Bonchio, F. Scandola, S. Campagna, *Coord. Chem. Rev.* **2011**, *255*, 2594-2601.

[166] A. Harriman, G. Porter, P. Walters, *J. Chem. Soc. Faraday Trans. 1* **1983**, *79*, 1335-1350.

[167] a) C. L. Donnici, D. H. Máximo-Filho, L. L. Cruz-Moreira, G. Teixeira-dos-Reis, E. Santos-Cordeiro, I. M. Ferreira-de-Oliveira, S. Carvalho, E. B. Paniago, *J. Braz. Chem. Soc.* **1998**, *9*, 455-460; b) F. H. Burstall, *J. Chem. Soc.* **1938**, 1662-1672.

[168] a) I. P. Evans, A. Spencer, G. Wilkinson, *J. Chem. Soc. Dalton Trans.* **1973**, 204-209; b) E. Alessio, G. Balducci, M. Calligaris, G. Costa, W. M. Attia, G. Mestroni, *Inorg.*

Chem. **1991**, *30*, 609-618; c) E. Dulière, M. Devillers, J. Marchand-Brynaert, *Organometallics* **2003**, *22*, 804-811.

[169] a) G. Wolfbauer, A. M. Bond, D. R. MacFarlane, *Inorg. Chem.* **1999**, *38*, 3836-3846; b) W. Zhang, B. Li, H. Ma, L. Zhang, Y. Guan, Y. Zhang, X. Zhang, P. Jing, S. Yue, *ACS Appl. Mater. Interfaces* **2016**, *8*, 21465-21471; c) N. D. McClenaghan, F. Barigelletti, B. Maubert, S. Campagna, *Chem. Commun.* **2002**, *6*, 602-603.

[170] G. R. Fulmer, A. J. M. Miller, N. H. Sherden, H. E. Gottlieb, A. Nudelman, B. M. Stoltz, J. E. Bercaw, K. I. Goldberg, *Organometallics* **2010**, *29*, 2176-2179.

[171] G. Sheldrick, *Acta Crystallograph. Sect. A* **2008**, *64*, 112-122.

[172] A. Spek, *Acta Crystallograph. Sect. A* **1990**, *46*, c34.

[173] V. V. Pavlishchuk, A. W. Addison, *Inorg. Chim. Acta* **2000**, *298*, 97-102.

[174] S. Gawęda, G. Stochel, K. Szaciłowski, *J. Phys. Chem. C* **2008**, *112*, 19131-19141.

[175] B. Ravel, M. Newville, *J. Synchrotron Radiat.* **2005**, *12*, 537-541.

[176] J. J. Rehr, R. C. Albers, *Rev. Mod. Phys.* **2000**, *72*, 621-654.

[177] A. Sartorel, M. Bonchio, S. Campagna, F. Scandola, *Chem. Soc. Rev.* **2013**, *42*, 2262-2280.

[178] G. La Ganga, F. Puntoriero, S. Campagna, I. Bazzan, S. Berardi, M. Bonchio, A. Sartorel, M. Natali, F. Scandola, *Faraday Discuss.* **2012**, *155*, 177-190.

[179] J. J. P. Stewart, *J. Mol. Model.* **2007**, *13*, 1173-1213.

[180] MOPAC2016, Version: 17.279L, J. J. P. Stewart, Stewart Computational Chemistry, web: http://OpenMopac.net.

[181] W. C. Swope, H. C. Andersen, P. H. Berens, K. R. Wilson, *J. Chem. Phys.* **1982**, *76*, 637-649.

[182] G. Bussi, D. Donadio, M. Parrinello, *J. Chem. Phys.* **2007**, *126*, 014101.

[183] J. O. Lindner, K. Sultangaleeva, M. I. S. Röhr, R. Mitrić, *J. Chem. Theory Comput.* **2019**, *15*, 3450-3460.

[184] TURBOMOLE V.7.0, **2015**, a development of University of Karlsruhe and Forschungszentrum Karlsruhe GmbH, 1989-2007, TURBOMOLE GmbH, since 2007, available from http://www.turbomole.com.

[185] J. P. Perdew, K. Burke, M. Ernzerhof, *Phys. Rev. Lett.* **1996**, *77*, 3865-3868.

[186] F. Weigend, R. Ahlrichs, *Phys. Chem. Chem. Phys.* **2005**, *7*, 3297-3305.

[187] D. Andrae, U. Häußermann, M. Dolg, H. Stoll, H. Preuß, *Theor. Chim. Acta* **1990**, *77*, 123-141.

[188] A. Klamt, G. Schüürmann, *J. Chem. Soc. Perkin Trans. 2* **1993**, 799-805.

[189] M. Jiang, H. Yang, H. Fu, *Org. Lett.* **2016**, *18*, 5248-5251.

Danksagung

Mein besonderer Dank gilt meinem Doktorvater Prof. Dr. Frank Würthner für die Aufnahme in seinen Arbeitskreis und für das Überlassen dieses spannenden und zukunftsorientierten Themas. Weiterhin möchte ich mich für die fachlichen Diskussionen und die Bereitstellung hervorragender Arbeitsbedingungen bedanken. Darüber hinaus danke ich ihm für seine Unterstützung für meine Bewerbung um ein Kekulé-Stipendium als auch für die Ermöglichung eines fünfwöchigen Forschungsaufenthalts an der Purdue University in den USA.

Der Stiftung Stipendien-Fonds des Verbandes der Chemische Industrie e.V. danke ich für die Gewährung eines Kekulé-Stipendiums.

Prof. Dr. Yulia Pushkar danke ich für die Aufnahme in ihren Arbeitskreis im Rahmen des oben genannten Forschungsaufenthalts am Institut für Physik und Astronomie der Purdue University. Dank ihrer Geduld und Expertise war es mir möglich, innerhalb der kurzen Zeit wichtige neue Einblicke in die molekularen Eigenschaften meiner Ru Makrozyklen zu gewinnen. Ich bedanke mich zudem bei Alireza Karbakhsh, Dr. Scott Jensen, Dr. Roman Ezhov und Pavani Devabathini für die gute Zusammenarbeit und angenehme Atmosphäre sowohl im Labor als auch während der Synchrotronzeit am Argonne National Laboratory.

Prof. Dr. Roland Mitrić, Dr. Merle Röhr, Dr. Joachim Lindner und Prof. Dr. Mirco Natali danke ich für die ausgezeichnete Zusammenarbeit im Rahmen unserer Kooperationsprojekte, welche zur erfolgreichen Publikation der erhaltenen Ergebnisse geführt hat.

Prof. Dr. Christoph Lambert danke ich für die Möglichkeit, spektroelektrochemische Untersuchungen und transiente Absorptionsexperimente in seinem Arbeitskreis durchführen zu dürfen. Zudem möchte ich mich bei Michael Moos und David Mims für ihre sehr freundliche Art und Unterstützung bei der Durchführung der Experimente bedanken.

Dr. Chantu R. Saha-Möller danke ich für das Korrekturlesen dieser Arbeit und die Überarbeitung der zwei Publikationsentwürfe über die hier präsentierten Ergebnisse. Ich bedanke mich für die erfolgreiche Zusammenarbeit und die wertvollen wissenschaftlichen Diskussionen. Zusätzlich möchte ich ihm dafür danken, dass er mich immer motiviert und ermutigt hat.

Dr. David Schmidt danke ich für die wissenschaftlichen Diskussionen und die Unterstüztung sowohl zu Beginn meiner Promotionszeit als auch in der Zeit nachdem er von Würzburg weg gezogen ist. Zusätzlich bedanke ich mich für die Messung und Auswertung einer der in dieser

Arbeit vorgestellten Kristallstrukturen. Ana-Maria Krause danke ich für die Messung und Auswertung der zweiten Kristallstruktur.

Weiterhin möchte ich mich bei Dr. Matthias Stolte für seine Hilfe mit der Kalibierung der in der photokatalytischen Wasseroxidation verwendeten Xenonlampe und für seine Unterstützung bei weiteren Anliegen bedanken.

Sarah Bullnheimer, Christiana Toussaint und Eleonore Klaus danke ich herzlich für ihre sehr freundliche Art und immerwährende Unterstützung bei organisatorischen Anliegen. Ferner möchte ich mich bei Dr. Matthias Grüne und Patricia Altenberger für die Durchführung von NMR-Experimenten am 600 MHz Spektrometer bedanken. Dr. Michael Büchner und Juliane Adelmann danke ich für die Hilfsbereitschaft bei Fragen und Problemen bezüglich der massenspektrometrischen Untersuchungen meiner Verbindungen.

Den Mitgliedern des Ru-Teams Dorothee Schindler, Niklas Noll, Dr. Joachim Lindner, Dr. Suvendu Karak und Maximilian Roth, danke ich für die sehr schöne Arbeitsatmosphäre und die gute Zusammenarbeit. Dabei möchte ich mich besonders bei Maximilian Roth für seine wichtige Unterstützung bei synthetischen Anliegen bedanken. Zusätzlich danke ich meinen Masterpraktikanten Wiebke Daul und Martin Luff, meiner Bachelorstudentin Maria Lupp und meiner Auszubildenden Jennifer Walter für die gute Zusammenarbeit. Dr. Valentin Kunz und Dr. Marcus Schulze, ehemaligen Mitgliedern des Ru-Teams, danke ich für die Unterstützung beim Einstieg in dieses Arbeitsgebiet.

Petra Seufert-Baumbach und Anja Rausch danke ich für ihre immer freundliche Art und Hilfsbereitschaft. Markus Hecht danke ich für das Messen von PXRD Proben. Zudem danke ich allen weiteren Mitgliedern des AK Würthners ich für die gute Zusammenarbeit und die schöne Zeit.

Zuletzt ein paar Worte auf Spanisch:

Gracias a mi familia alemana, Dagi, Heinz y Doro, por todo lo que han hecho por mi en los últimos años.

Gracias mamá, papá y Eduardo. Ha sido un largo camino, gracias por haber estado siempre conmigo.